Development of a screening tool for risk assessment of groundwater infiltration into sewer systems

- Including capillary fringe induced rapid groundwater rise during rain

MASTER'S THESIS

DEPARTMENT OF THE BUILT ENVIRONMENT
AALBORG UNIVERSITY

JUNE 2024

AALBORG UNIVERSITY

AALBORG UNIVERSITY

Department of the Built Environment
Water and Environmental Engineering
Thomas Manns vej 23
9220 Aalborg Øst
https://www.build.aau.dk

Title:

Development of a screening tool for risk assessment of groundwater infiltration into sewer systems - including capillary fringe induced rapid groundwater rise during rain

Project:

Master's thesis

Project period:

September 2023 - June 2024

Authors:

Emil Bom Pedersen
Gustav Ditlev Pedersen
Maiken í Dali Nørlund

Supervisors:

Per Møldrup
Rasmus Vest Nielsen
Søren Liedtke Thorndal

Page number: 166
Appendix pages: 7
Finished: June 2024

Abstract:

The issue with extraneous water has come into increased focus in recent years due to its effect on wastewater loads. Therefore, the project Ternært Vand was started in 2022 and focused on the part of extraneous water originating from groundwater infiltration. Being part of the second year of the Ternært Vand project, this Master's thesis worked with the hypothesis of groundwater infiltrating into pipes due to increases in the groundwater table. To aid decision-makers in risk assessment of groundwater infiltration this Master's thesis developed a screening tool using the Danish city Beder as a case area. Here, the infiltration was hypothesised to originate from a capillary fringe induced rapid water table rise submerging the sewer system during a rain event. The increase was modelled with a 1D numerical model of water flow and groundwater rise in unsaturated soil. In addition to being used for the screening tool the 1D model was also expanded to a 2D model. Both the 1D and 2D model were calibrated and validated against sandbox experiments which investigated disproportionate increases in the groundwater table and a subsequent infiltration into a buried pipe. One out of five of the experiments showed a distinct disproportionate rise. The remaining four experiments were also considered to have shown disproportionate increases but due to the experiment setup it could not be definitively concluded. Both models of the sandbox showed a sufficient fit with the measured data where the 1D and 2D model could estimate rapid and disproportional groundwater rise and the 2D model could also estimate the infiltrated amount of water. Overall, this Master's thesis concluded that the screening tool could not be validated for Beder, but showed the expected dynamics in the case area and could be used in practical applications as a supplemental approach.

Synopsis på dansk

Problemet med uvedkommende vand er kommet i stigende fokus i de seneste år på grund af dets effekt på spildevandsmængder. Derfor blev projektet Ternært Vand startet i 2022, hvor projektet fokuserede på den del af uvedkommende vand, der stammer fra grundvandsinfiltration. Under andet år af Ternært Vand-projektet arbejdede denne kandidatafhandling med hypotesen om, at grundvand infiltrerer ind i afløbssytemet pga. stigninger i grundvandsspejlet. For at hjælpe beslutningstagere med risikovurdering af grundvandsinfiltration udviklede denne kandidatafhandling et screeningsværktøj, hvor den danske by Beder blev brugt som caseområde. Her var hypotesen, at infiltrationen skyldtes hurtigt stigende grundvand som steg op til afløbssystemet under en regnhændelse grundet dynamikker i kapillærzonen. Grundvandsstigningen blev modelleret med en 1D numerisk model for vandføring og grundvandsstigning i umættet jord. Udover at blive brugt i screeningsværktøjet blev 1D modellen også udvidet til en 2D model. Begge modeller blev kalibrerede og validerede mod sandboksforsøg, som undersøgte disproportional grundvandstigning og den resulterende infiltration ind i et nedgravet rør. Ét af de fem eksperimenter viste en tydelig disproportional stigning, hvor de resterende fire også blev betragtet som at have vist disproportionale stigninger, men pga. eksperimentets udformning kunne det ikke definitivt konkluderes. Begge modeller viste et tilstrækkeligt fit til de målte data, hvor både 1D og 2D modellen kunne estimere hurtig og disproportional grundvandsstigning og 2D-modellen kunne yderligere estimere den infiltrerede mængde vand. Alt i alt konkluderede denne kandidatafhandling at screeningsværktøjet ikke kunne valideres for caseområdet, dog viste værktøjet de forventede dynamikker i Beder og det konkluderedes derfor, at det kan bruges i praktiske applikationer som et supplement i dimensioneringsprocessen.

Preface

This Master's thesis was written on the 3rd and 4th semester on the Master program "Water and Environmental Engineering" by three students at Aalborg University. It was written in conjunction with the second year of the project group "Ternært Vand", which was a collaboration between Aalborg University, the water utility Aarhus Vand A/S, Aarhus Municipality and the consulting engineering company NIRAS A/S [Ternært Vand project group 2024].

For the knowledgeable collaboration, useful insight and overall constructive guidance, a big thank you goes out to the supervisors Per Møldrup, Rasmus Vest Nielsen and Søren Liedtke Thorndahl. A thank you also goes to Anette Næslund Pedersen, Engineer Constructor at the Department of the Built Environment for advice and guidance for the preparation of the sandbox experiments. Another thank you goes to Henrik Koch, Assistant Engineer at the Department of the Built Environment for technical advice and help with the development and creation of the temperature spears.

Reading Guide

Multiple sources and references are used throughout this Master's thesis. References were documented using the Harvard method [Author last name, Year]. All cited sources and their necessary details are included in the bibliography at the end of the project. Throughout this Master's thesis figures, equations, and tables are numbered according to their respective chapter. Thus, the first figure in Chapter 1 is Figure 1.1, the second is Figure 1.2, etc.

In this project, multiple datasets are based on on elevation data. The global reference for all geocoded datasets in this project is the Danish DVR90. For multiple maps presented in this project the background map "Skærmkort - dæmpet" from Dataforsyningen [2024a] was used. The main models employed in this Master's thesis are uploaded with the thesis.


Emil Bom Pedersen

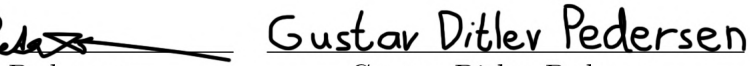
Gustav Ditlev Pedersen

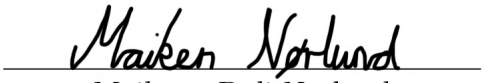
Maiken í Dali Nørlund

Table of Contents

Part I :

Introduction to extraneous water dynamics and capillary fringe induced rapid groundwater rise, its effect on urban drainage systems and current knowledge of the phenomenon

1 Introduction to extraneous water, its causes and effects on the urban drainage system

Changing patterns in precipitation and extreme temperature due to climate change are expected to alter the recharge and discharge of groundwater resources worldwide [Taylor et al. 2012]. In Denmark, annual precipitation is expected to increase towards the year 2100, especially during winter. In combination with the projected rise of oceans towards year 2100, this will likely increase groundwater recharge and groundwater levels in Denmark. However, groundwater levels in Denmark are already high, especially during winter and spring, causing problems with ponding in agricultural areas, moist basements and undermining of infrastructure, etc. Furthermore, increases in the groundwater table will submerge parts of the sewer system and allow groundwater to infiltrate through leaky pipes [Olesen et al. 2014; Rasmussen et al. 2022]. Infiltrating groundwater into sewer systems has been a known issue for decades, but the problem is expected to increase due to climate change [Karpf and Krebs 2004; Awad et al. 2018].

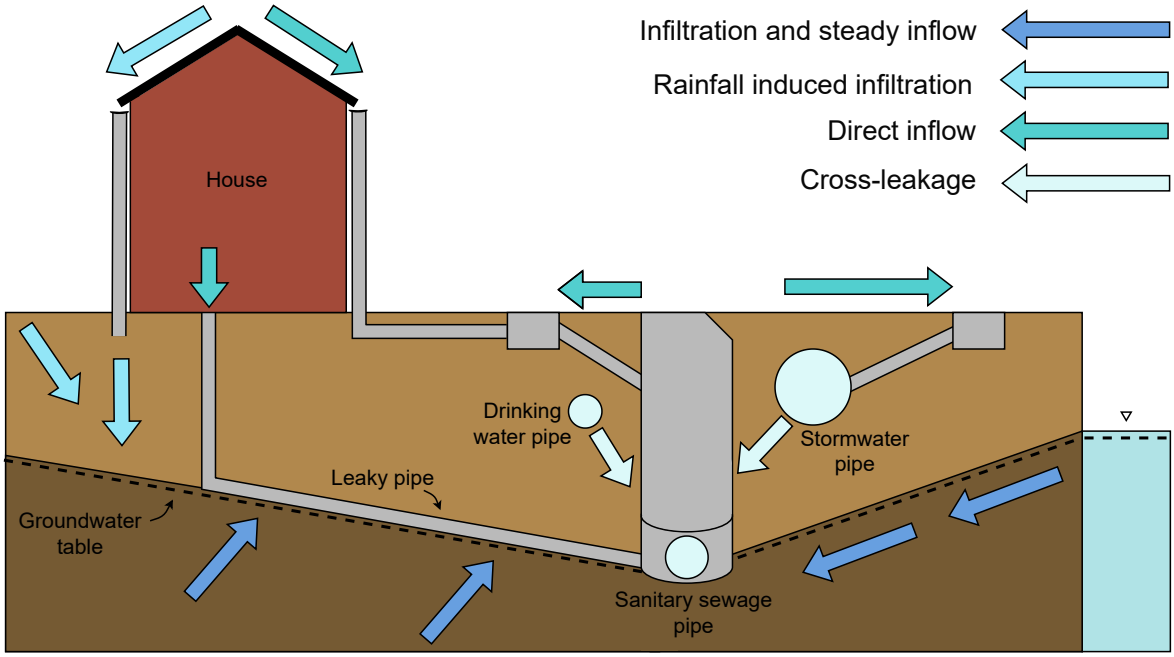

Figure 1.1: Sources of water into the sewer system, where cross-leakage, infiltration and steady inflow are extraneous water. Inspired by Dakša, Dejus, and Rubulis [2022].

According to Bassø et al. [2021] water that does not belong in the sewer system, denoted "extraneous water", is a major issue in sewer systems across the globe. Here, extraneous water enters the sewer system through misconnections, leaky manhole covers, infiltration, return flow from recipients, etc. The fraction of extraneous water is difficult to quantify, but Bassø et al. [2021] estimates that 50% of the flow in sewer systems is extraneous water, where the

maximum flow peak during precipitation is 400% of the wastewater flow. Moreover, based on data from 2016 Andersen and Getreuer [2018] estimate that extraneous water ranges from 25-30% of the total water volume treated at the waste water treatment plants in Denmark, corresponding to 150-200 million m^3 annually [Andersen and Getreuer 2018]. Figure 1.1 shows examples of how water enters the sewer system, where some contributions are of external origin. Infiltrating groundwater is generally the major constituent of extraneous water [Andersen and Getreuer 2018].

1.1 Effects of extraneous water

According to Rasmussen et al. [2022] the amounts of infiltrating groundwater can exceed the amount from runoff during rain events and Andersen and Getreuer [2018] mentions that 1-2 days of combined sewer overflow has been experienced during dry weather. Not surprisingly, the issue of extraneous water in the sewer systems has received increasing attention from Danish water utilities in recent years due to its effect on wastewater treatment cost and environmental impacts [Bassø et al. 2021]. Extraneous water dilutes the wastewater and decreases its temperature, thus reducing the effect of the biological efficiency at the wastewater treatment plant [Karpf and Krebs 2013]. This results in higher loads of e.g. nutrients in the effluent, but also an increased frequency of overflows to recipients due to the treatment plants being designed for smaller wastewater volumes. Besides the environmental impacts, this also increases the cost per treated m^3 for the consumers due to enlarged costs of pumping, wear of the system and lower treatment efficiency [Andersen and Getreuer 2018; Bassø et al. 2021].

Infiltrating water in sewer systems does have positive effects. For instance increased self-cleansing of pipes and reduced issues with hydrogen sulphide [Andersen and Getreuer 2018]. Moreover, the infiltration of water lowers the groundwater table. This can mitigate issues in low lying areas by reducing damage done to infrastructure and reducing flooding of basements, while also ensuring faster transport of water during for instance flooding [Karpf and Krebs 2004; Karpf and Krebs 2013; Thorndahl, Balling, and Larsen 2016]. However, despite not having quantified the environmental impacts, Andersen and Getreuer [2018] estimates that extraneous water overall has a negative environmental impact.

1.2 Extraneous water in the municipality of Aarhus

Negative impacts of extraneous water is evident in the Danish municipality of Aarhus where the water utility Aarhus Vand A/S has struggled with capacity at their wastewater treatment plants (WWTP), partly due to extraneous water and urban expansion [Bassø et al. 2021; Aarhus Kommune 2022]. Aarhus Vand A/S estimates that 30% of the annual water volume at their plants is of external origin [Andersen and Getreuer 2018]. Consequently, high levels of precipitation in the fall of 2023 led to increased amounts of water to Viby WWTP. Combining this with the increased water levels of the receiving stream, the flow of the effluent was too constrained and thus Aarhus Vand A/S was forced to urgently tear down a bridge crossing the recipient to avoid flooding of the plant [Aarhus Vand 2023; Aarhus Kommune 2022].

Part of the catchment area of Viby WWTP is the sewer system in the city of Beder, which is identified by Aarhus Vand A/S as one of the regions in the catchment area with the greatest

contribution of extraneous water [Bassø et al. 2021]. Here, the extraneous water is identified based on observations of rain induced runoff in the sewers, despite the entire sewer system in Beder being separately sewered as shown in figure 1.2.

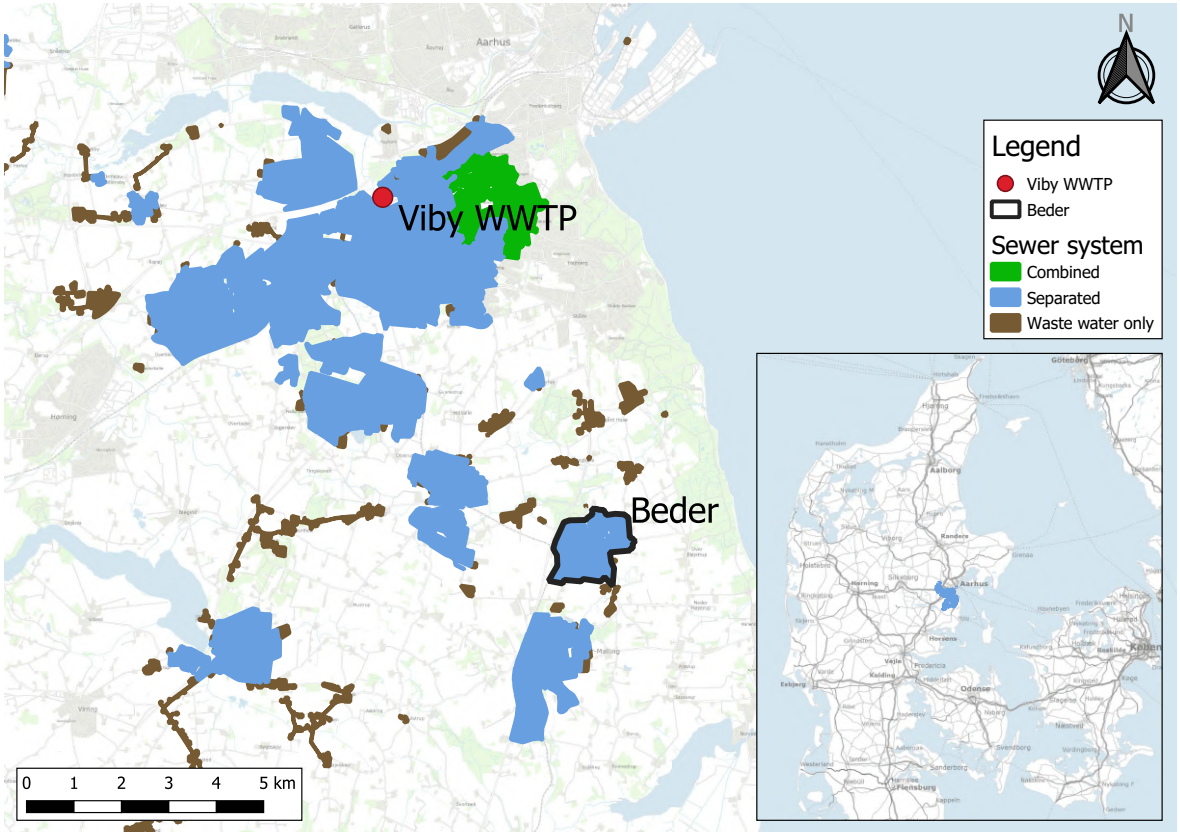

Figure 1.2: Sewer systems in the catchment area of Viby waste water treatment plant (WWTP) and the city of Beder. Shown in relation to its location in Denmark. Based on data from Aarhus Kommune [2024] and Aarhus Kommune [2022].

1.2.1 Monitoring of groundwater levels and rise patterns in the city of Beder

The extraneous water in Beder originates from infiltrating groundwater due to high groundwater levels and thus periodic submersion of the sewer system. Moreover, monitoring of the groundwater levels in 7 borings across Beder from 2023 show dynamics where millimeters of added rain turns into many centimeters of increase in the groundwater table. For instance, as shown in figure 1.3 where a rain event of 40 mm on the 25th of August 2023 caused a peak in groundwater level of 53 cm, which is more than a tenfold increase compared to the amount of rain. Furthermore, the groundwater level reached the surface at the end of October and did not decrease for the rest of the measuring period (not shown in figure). Such dynamics of rapid increases in groundwater combined with slow decreases enable groundwater to infiltrate through leaky pipes and contribute a considerable volume to the sewer system [Ternært Vand project group 2024].

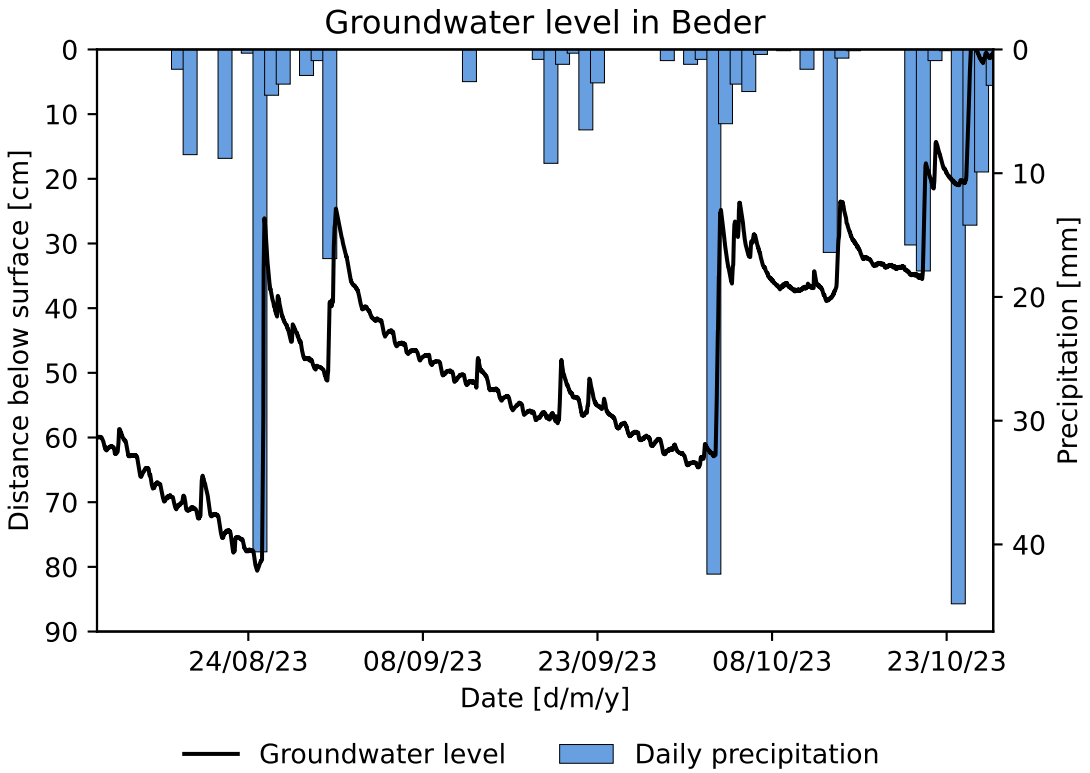

Figure 1.3: Precipitation and concurrent rise in groundwater table combined with a slow decrease at the monitoring boring B6 in the Danish city of Beder [Ternært Vand project group 2024].

1.3 Strategies to handle extraneous water

Current strategies to mitigate extraneous water involve removal of point sources and wrong connections as well as renovation of pipes [Andersen and Getreuer 2018]. Experience from water utilities in Denmark shows that extraneous water is more frequently present in old concrete or ceramic pipes due to defects [Thorndahl, Balling, and Larsen 2016; Andersen and Getreuer 2018]. However, renovation of old pipes has shown varying effects. In some areas, tightening of pipes has increased groundwater levels and instead enabled infiltration from private pipes from houses. Therefore, Andersen and Getreuer [2018] concluded that efforts to decrease extraneous water in the sewer systems generally are not economically viable. However, environmental impacts must also be considered why solutions must be identified. According to Bassø et al. [2021] current practice when dimensioning the sewer systems do not account for extraneous water originating from precipitation. Therefore, Bassø et al. [2021] suggests that more knowledge of geographical and seasonal variations in the origin of extraneous water would improve the dimensioning of sewer systems. Therefore, the goal of this Master's thesis was to improve knowledge of the interactions between the soil matrix and leaky pipe along with the development of a tool for screening areas with high risk of rain induced groundwater infiltration into already existing or planned sewer systems.

2 | Scope of Master's thesis and problem statement

Using the Danish city of Beder as a case area, a 3-year project 'Ternært Vand' was started in 2022 with the goal of gaining knowledge of infiltrating groundwater into pipes. The project was a collaboration between Aalborg University, the water utility Aarhus Vand A/S, Aarhus Municipality and the consulting engineering company NIRAS A/S [Ternært Vand project group 2024]. Previous knowledge of the dynamics stated that infiltration of groundwater happens when the groundwater level is high as well as during heavy rain due to infiltration while percolating through the soil [Miljøstyrelsen 1992]. To test this, Ternært Vand project group [2024] outlined three working hypothesises of the origin of the infiltrating water:

1. Percolation through the unsaturated zone and storage during winter (water from above)
2. Local increase in groundwater table after a rain event (water from beneath)
3. Groundwater flow due to horizontal pressure gradients (water from the side)

The second hypothesis of water originating from below was assessed by Hedevang and Sørensen [2023] in the first year of the Ternært Vand project. Here, Hedevang and Sørensen [2023] excluded that the water infiltrates from above and concluded that the infiltration happens when groundwater rises above the holes in the pipe.

This Master's thesis was initiated in the second year of the Ternært Vand project and was a continuation of the work started by Hedevang and Sørensen [2023]. Due to a very limited amount of repetitions of the experiments conducted by Hedevang and Sørensen [2023], this Master's thesis continued working with the second hypothesis and the experiment setup. Here, the goal with the experiments in this Master's thesis was to attempt to replicate the dynamics where millimeters of added rain turns into centimeters of groundwater rise as observed in Beder which enable groundwater to infiltrate through leaky pipes. As the disproportional rise in groundwater table is caused by dynamics of the capillary fringe as reported by Khaled et al. [2011], Novakowski and Gillham [1988], Miyazaki, Ibrahimi, and Nishimura [2012], Heliotis and Dewitt [1987], and Zheng, liu, and Yang [2022], improvement of the knowledge of these dynamics was focused on in the second year of the Ternært Vand project and therefore also in this Master's thesis. Consequently, this Master's thesis was not oriented towards attaining a solution for removal of extraneous water, but rather on increasing knowledge. This knowledge of the dynamics was necessary for the development of the screening tool for assessing areas with risk of rain induced groundwater infiltration due to submersion of the sewer system.

2.1 Problem statement

All of the above leads to the following problem statement:

How can capillary fringe induced disproportional groundwater rise and subsequent infiltration be replicated experimentally and numerically, and how can the numerical model be utilized to evaluate the risk of infiltration into a sewer system?

The problem statement above was answered through the following sub-questions:

1. Which dynamics in the soil matrix cause disproportional groundwater rise?
2. How can a sandbox experiment be used to assess the hypothesis of water infiltrating from below and how can it be used to replicate disproportional groundwater rise?
3. Utilizing experimental results, how can a 1D and 2D numerical model of water flow and groundwater rise in unsaturated soil be employed to model the dynamics of the sandbox experiments?
4. How can the risk of groundwater infiltration into the sewer system in Beder be assessed by integrating the 1D model into a screening tool?

An overview of how the questions above are answered throughout this Master's thesis along with the scope of the project within the Ternært Vand project group [2024] is shown in figure 2.1.

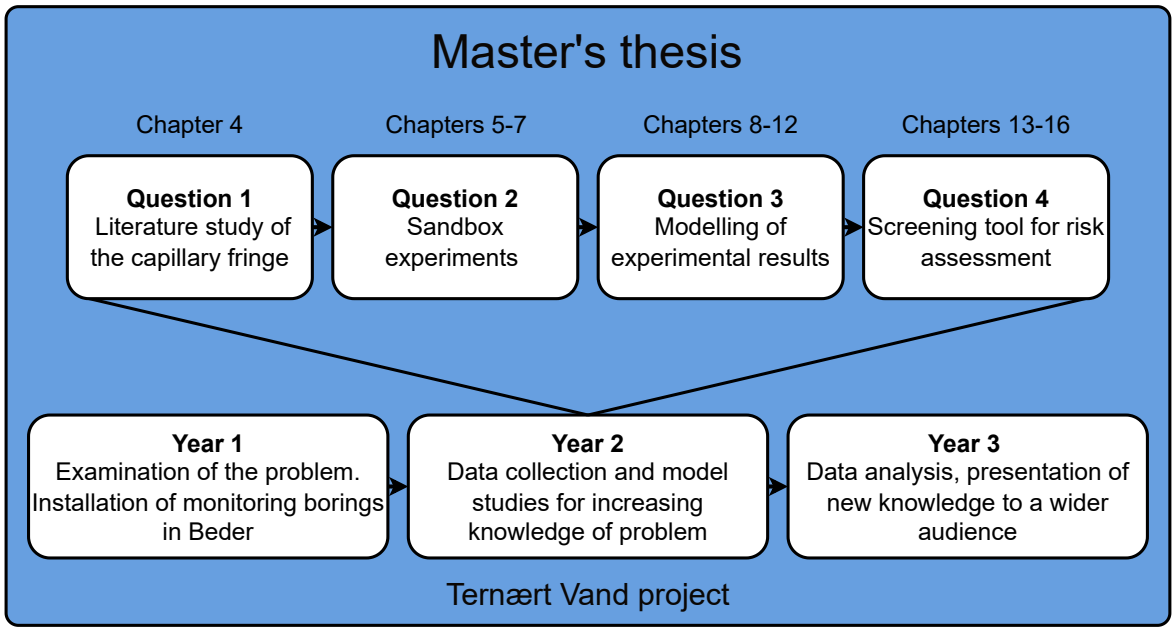

Figure 2.1: Overview of the scope of this Master's thesis within the Ternært Vand project group [2024].

3 | Previous studies of extraneous water

Studies of estimating the amounts of extraneous water have been conducted for many years across several countries and thus a wide variety of methods exist, both direct and indirect. These include time series analysis, tracer methods, mass balances and hydrogeological modelling, etc. [De Bénédettis and Bertrand-Krajewski 2005; Wittenberg and Aksoy 2010].

The method of mass balances are used by Andersen and Getreuer [2018] which compiled experiences with extraneous water from Danish municipalities. Andersen and Getreuer [2018] stated that the fraction of extraneous water in each municipality did not immediately show a correlation with neither annual precipitation, total length of pipe nor whether the catchment area consisted of separate or combined sewers. However, Andersen and Getreuer [2018] suggested that this might be explained by the large uncertainties in the estimations of extraneous water based on the mass balances for each municipality. In addition, the variations might not be quantifiable on a scale of municipalities.

Based on a catchment area scale, Thorndahl, Balling, and Larsen [2016] modelled groundwater infiltration into a sewer system by coupling a groundwater model with a sewer flow model based on measurements of flow. The coefficient of infiltration into the pipes was calibrated and the results were deemed satisfying. However, the model only incorporated interactions between saturated zone and the sewer system, why the missing dynamics of the unsaturated zone resulted in an underestimation of rapid infiltration when the system was not fully submerged in groundwater [Thorndahl, Balling, and Larsen 2016]. On a smaller scale, Guo, Yang, and Zhang [2017] used an analytical expression to model the three-dimensional groundwater infiltration into a submerged pipe with one circular leak. The expression was tested against experiments in the laboratory where the error in the modelled against measured flow lied within 10%. Thus, the model was concluded to be able to approximate inflow. However, the model in Guo, Yang, and Zhang [2017] only included a single circular leak. Contrary to this, Karpf and Krebs [2013] modelled a wide variety of leaks and shapes in MODFLOW. Here, a gaussian distribution of square leaks with widths betweeen 1-5 cm was used as well as a square pipe. The goal was to support estimates of the area of leaks per length of pipe which can be applied to entire catchments. By using Monte Carlo simulations and a sensitivity analysis, the major factors of inflow were concluded to be hydraulic conductivity of the backfill in the pipe trench as well as the thickness of the infiltration layer and area of leaks per sewer length.

Common for Thorndahl, Balling, and Larsen [2016], Guo, Yang, and Zhang [2017], and Karpf and Krebs [2013] is the exclusion of the capillary fringe in the models. This was included in Hedevang and Sørensen [2023] who made a 1D model of inflow into a pipe based on the Mean Moving Slope model. Here, infiltration only happened due to a rise in the groundwater table above the leaks in the pipe. This model was validated against data from a sandbox experiment with a buried pipe. To increase knowledge of the dynamics where millimeters of rain turns into centimeters of groundwater increase the model work by Hedevang and Sørensen [2023] was continued in this Master's thesis.

The estimation of extraneous water on a catchment scale is comprehensive in terms of data

needed and precision of the estimation. The needed data collection would in practical applications be expensive and most likely not be prioritised in a design or improvement budget. Being able to estimate areas where sewer systems either are submerged or in risk of becoming submerged could significantly reduce the needed data collection needed if e.g. the volume of extraneous water were to be estimated. This would also make the process of accounting for or potentially dealing with extraneous water much more cost-effective. Therefore, this Master's thesis developed a screening tool for identifying areas of the sewer system with a high risk of groundwater infiltration due to submersion. The screening tool was based on a model which includes increases in groundwater table due to the dynamics of the capillary fringe.

4 | Dynamics of the capillary fringe

The experiment and modelling in Hedevang and Sørensen [2023] included the dynamics of the capillary fringe. This dynamics is important when working with the hypothesis of water infiltrating into a leaky pipe due to increases in the groundwater table, as the extent of the capillary fringe affects the rise in groundwater table [Zheng, liu, and Yang 2022]. Therefore, this chapter will focus on presenting the dynamics of the capillary fringe, including effects such as air entrapment and hysteresis. Thus, the chapter answers the first question; *"Which dynamics in the soil matrix cause disproportional groundwater rise?"*.

4.1 Water movement in the capillary fringe - the transition between unsaturated and saturated zone

Water movement in soil is governed by the energy state of the water, where the water moves from a high to a lower potential. The energy state is referred to as the soil water potential, which is constituted by three main components; pressure-, solute- and gravitational energy. While solute- and gravitational potential energy is caused by osmotic and gravitational forces, respectively, the soil pressure potential is caused by adsorptive and capillary forces. These forces are caused by water molecules being attracted to the soil particles due to electrical forces, causing the water to adsorb onto the soil particles. Therefore, water contained in soil above the saturated zone is considered under negative pressure and thus removal of water from unsaturated soil requires energy or suction [Loll and Moldrup 2000].

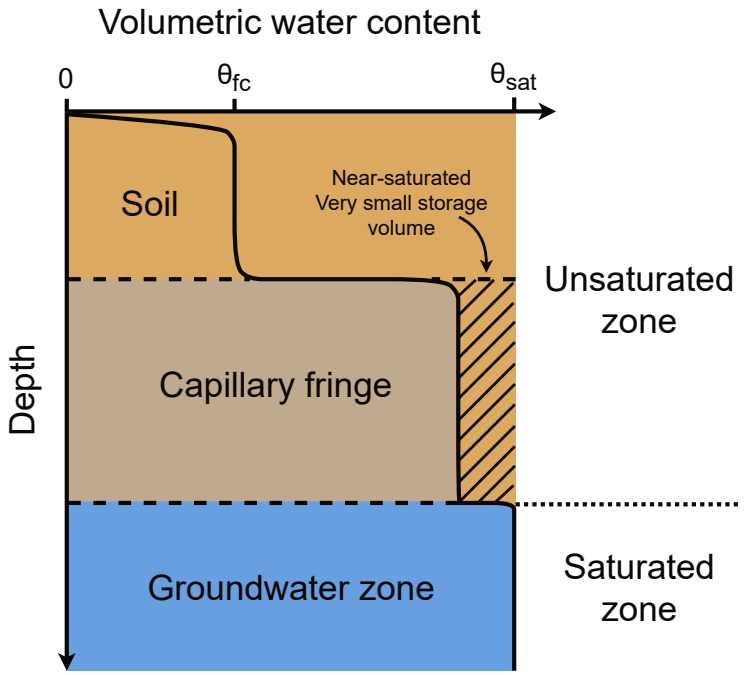

Figure 4.1: Simplified sketch of the small storage volume available in the capillary fringe. θ_{fc} = water content at field capacity, θ_{sat} = saturated water content.

The boundary between saturated and unsaturated zone is the groundwater table, where the transition between these zones is the capillary fringe, see figure 4.1. The capillary fringe is a tension saturated zone starting immediately above the groundwater table. Here, the pores are almost saturated but might contain entrapped air in 10-30% of the pore volume. Therefore, the available storage volume in the capillary fringe is very limited [Nimmo 2005; Gillham 1984]. According to Nimmo [2005] naturally saturated soil might still contain entrapped air in a significant fraction of the pore space, but still have a pressure of zero. This happens when a pore fills slower than the adjacent pores, for instance due to differences in pore size. Therefore, the term "capillary saturated" refers to a soil which is mostly water filled, but contains air in the larger pores. Here, the entrapped air might dissolve into the water, if the soil remains saturated for a longer time period [Lissard 2017]. In general, the water content of the pores immediately above the groundwater table are almost fully saturated where the water content of the pores decreases with increased distance above the groundwater level [Lissard 2017].

4.1.1 Upper boundary of the capillary fringe

The upper limit of the capillary fringe is not necessarily planar and various definitions of the boundary exists. According to Lissard [2017], some studies denote the upper boundary as the abrupt shift in the water content in the vertical direction while others define the water content at field capacity as the upper boundary. According to Miyazaki, Ibrahimi, and Nishimura [2012], the capillary fringe extends from the groundwater table at zero pressure and to a height corresponding to the suction at air entry, which is the suction where water is displaced by air. As this value depends on soil structure and texture, the extent of the capillary fringe also depends on the soil type [Miyazaki, Ibrahimi, and Nishimura 2012]. This is illustrated by the Young-Laplace equation (4.1) which calculates the height of the capillary rise [Loll and Moldrup 2000].

$$h = \frac{2 \cdot s \cdot \cos(\omega)}{r \cdot \rho \cdot g} \tag{4.1}$$

Where:

h	Height of capillary rise [m]
s	Liquid surface tension [N m^{-1}]
ω	Contact angle of air-water interface [°]
r	Capillary radius [m]
ρ	Density of water [mg m^{-3}]
g	Gravitational acceleration [N kg^{-1}]

The capillary radius from equation (4.1) is directly related to pore size [Turluck 2019]. Thus, in very coarse sand the capillary fringe extend less than a centimeter above the groundwater table while the zone in finer materials such as clay can extend several meters. This is due to the water retaining abilities of the different soils [Gillham 1984]. An example of this is seen in figure 4.2 which shows the difference between water retention for a loamy sand and a sandy loam from Hansen [1976]. Here, it is evident that the sandy loam has greater water retaining abilities as the water content is greater than for the loamy sand for all suctions. This is due to the sandy loam having a higher content of fine particles resulting in smaller pore size and a

larger surface area for water to adsorb to [Loll and Moldrup 2000].

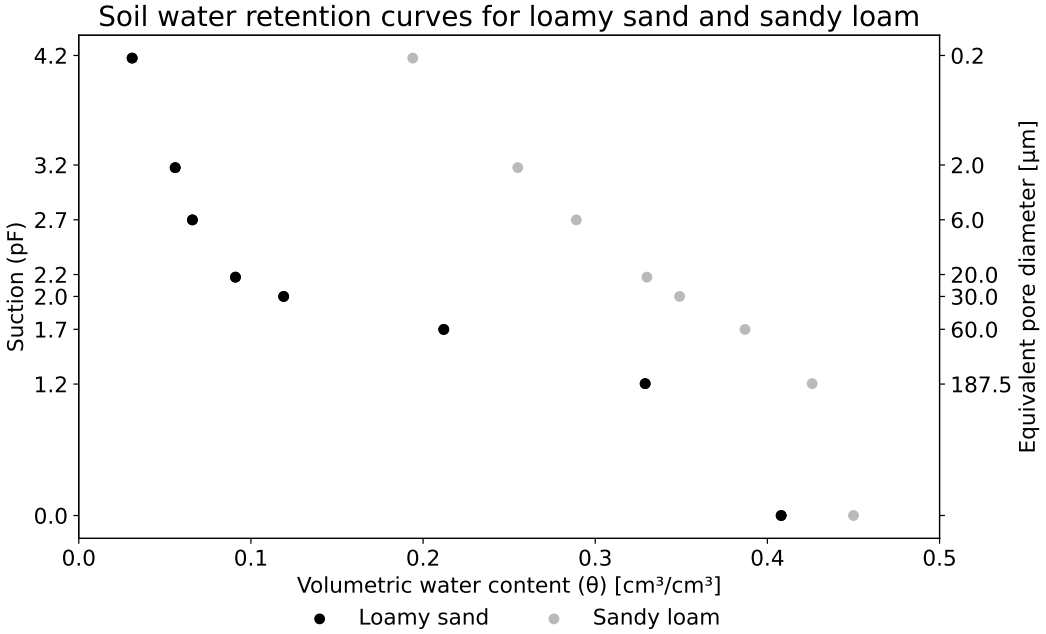

Figure 4.2: Soil water retention curve for a loamy sand with a clay fraction of 5% (Borris 40-90 cm from Hansen [1976]) and sandy loam with a clay fraction of 18.2% (Roskilde 50-80 cm from Hansen [1976]).

The capillary height in the sandy loam would be higher than in the loamy sand. Besides impacting the extent of the capillary fringe the particle size and structure of the soil also affect the velocity of the water movement [Gillham 1984].

4.1.2 Water movement in the capillary fringe

Water movement in the unsaturated zone is generally in the vertical direction due to infiltration and evaporation of water from above while there is capillary rise and recharge of groundwater in the bottom of the unsaturated zone. However, as the water movement depends on several forces, where gravity might not be the dominant one, water can move in any direction in the unsaturated zone [Pojmark 2011]. For example, Pojmark [2011] examined the water movement in the capillary fringe in a sandbox experiment with a gradient in the water level. Here, rapid horizontal movement in the capillary fringe was observed where the velocity depended on the gradient. Pojmark [2011] concluded, that the dynamics of the capillary fringe behave more similarly to the saturated zone than the unsaturated zone and thus should be modelled as part of the saturated zone. However, measurements by Mangangka [2008] indicate that the dynamics of the capillary fringe also vary from the saturated zone. Mangangka [2008] measured infiltration velocity in sand in an area with a high groundwater table using a double ring infiltrometer. Here, a change in the dynamics of the velocity was observed when the water front reached the capillary fringe and again when the water front reached the saturated zone, see figure 4.3. Here, the largest drop in velocity was observed when the water front reached the capillary fringe. Further, while the infiltration in unsaturated and saturated zone could be described with power fits ($R^2 \geq 0.830$), the infiltration in the capillary fringe was described with a linear fit ($R^2 = 0.997$). Mangangka [2008] ascribed the decrease in infiltration velocity

in the capillary fringe to the increase in water content of the soil. Mangangka [2008] concluded, that the presence of a high groundwater table of 100 cm beneath the surface greatly reduced the infiltration velocity into the soil, as infiltration velocity is dependant on soil water content.

Figure 4.3: Simplified overview of the fitted infiltration rates measured by Mangangka [2008].

4.2 Hysteresis' effect on soil water retention and extent of the capillary fringe

The water content in a soil has been observed by many studies, for instance Khaled et al. [2011], Lehmann et al. [1998], Lissard [2017], and Werner and Lockington [2003], to depend on whether the soil was undergoing a cycle of drying or wetting. This is denoted hysteresis and it is typically shown by successive cycles of wetting and drying that do not reach the saturated water content that was determined by the initial drying curve [Lissard 2017].

4.2.1 Sudden shifts in the air-water interface - the Haines Jump

One explanation of the dynamics of hysteresis is the so called "ink bottle effect" which describes how various pore shapes and sizes affect the curvature of the interface between air and water during drying and wetting, see figure 4.4. In a drying cycle, the tension will increase the curvature of the air-water interface until the limit of the degree of curvature is reached. Passing this limit will result in a sudden shift, called the Haines jump, where the interface moves lower into a narrow pore. The opposite happens during a wetting cycle, where a shift happens when the surface tension cannot withstand the decreasing curvature. Thus, the tension during a wetting cycle is determined by wider pores, while the narrow pores determine the tension during drying. The different tensions causing the Haines jump in a wetting or drying cycle results in hysteresis of the soil [Lissard 2017]. Another explanation of hysteresis is that the differences in water retention curves during wetting and drying are caused by varying pore radii and varying contact angles of the air-water interface at the liquid-solid interface [Lehmann et al. 1998; Lissard 2017].

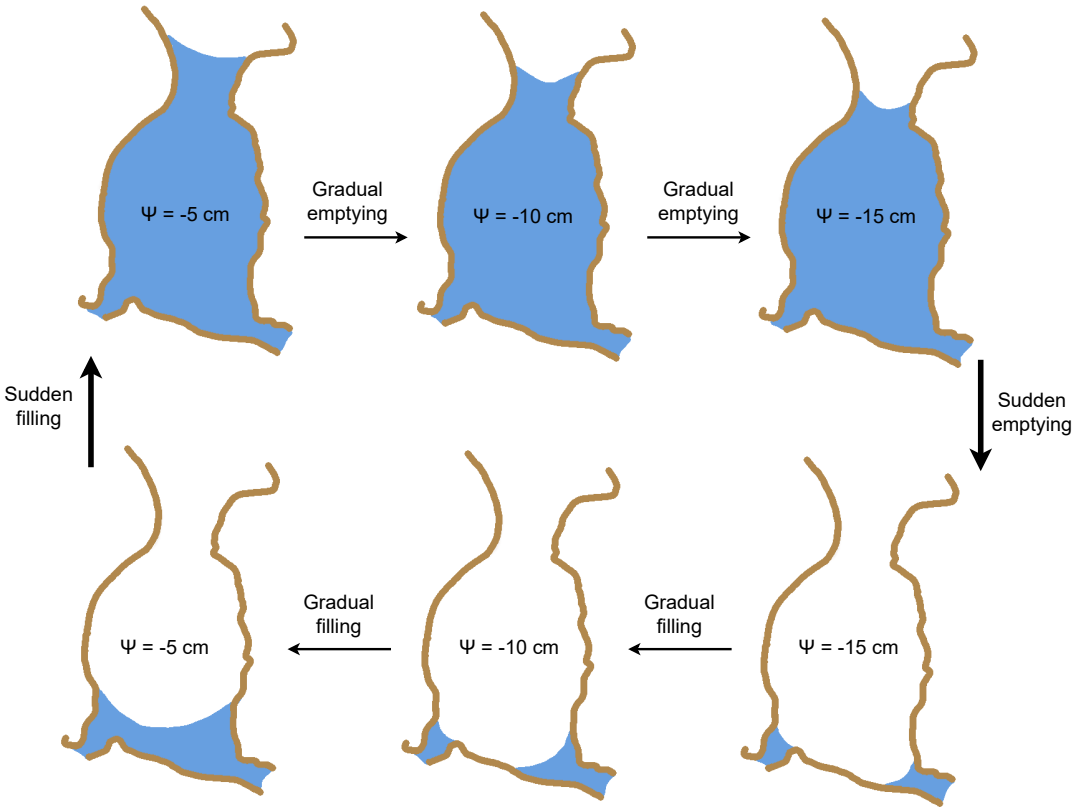

Figure 4.4: Depiction of the Haines jump in the ink bottle effect, where the curvature between the air water interface in the pores bursts and cause a sudden filling or emptying of the pore. Figure modified from Nimmo [2005]. ψ = soil water potential.

4.2.2 The air-water interface's effect on the capillary fringe thickness

The air-water interface also has an effect on the thickness of the capillary fringe due to the ink bottle effect. When the water table decreases, the upper part of the capillary fringe can remain saturated in small pores while larger pores below are drained by gravity. Thus, capillary fringes generally have a higher thickness above decreasing water tables than increasing water tables, due to the air-water interface retaining the height of the capillary fringe as long as the right pore conditions are present such as continuity of the pores [Lissard 2017].

4.3 Disproportionate rise of the groundwater table caused by dynamics in the capillary fringe

In cases where the thickness of the capillary fringe cannot fully develop, the capillary fringe becomes truncated. This often happens in shallow water tables [Zheng, liu, and Yang 2022]. However, there are several definitions of a shallow water table. While Nosetto et al. [2009] defines the shallow water table as the groundwater level being less than 1.4 m beneath the surface level, Koch et al. [2019] defines it as the uppermost water table or the groundwater or capillary fringe within plant rooting depth.

According to Gillham [1984] and Khaled et al. [2011] several studies show that shallow water

tables can lead to disproportionate increases in the groundwater table when the upper boundary of the capillary fringe extends to the ground surface. A sketch of the dynamics is shown in figure 4.5.

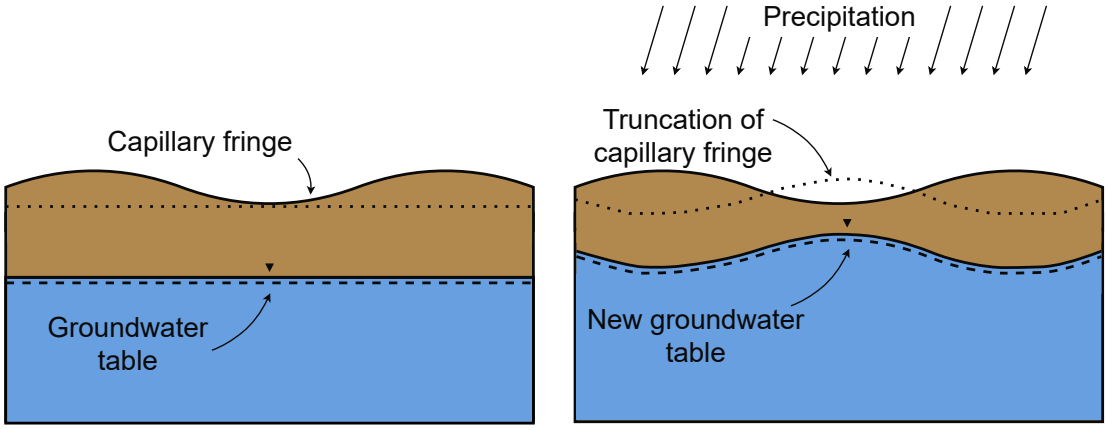

Figure 4.5: Simplified sketch of the dynamics of the capillary fringe during precipitation in a shallow groundwater aquifer. Inspired by Gillham [1984].

The disproportionate rise happens when the increase in groundwater table exceeds the amount predicted by the specific yield of the soil [Khaled et al. 2011]. Experiments by Khaled et al. [2011] with a sand (particle size of 20-300 μm with a mean of 125 μm) and a light clay (52.8/20.7/26.5 percentwise distribution of sand, silt and clay, respectively) showed more than a factor 50 in increase in groundwater table compared to the depth amount of added water for the light clay and more than a factor 100 for the sand. As seen from table 4.1 factors of 50 and 100 in increase from light clay and fine sand, respectively, are within the expected increases based on the specific yields of the soil. However, as a factor 100 increase for a fine sand requires a specific yield of 1.0% which is far from the mean value of 33%, it could be argued that a factor 100 increase is unusual for fine sand. In addition, Khaled et al. [2011] reports a rise in groundwater table of 12 cm when adding 1 mm of precipitation to the fine sand, where a 5 cm increase happened within the first 10 seconds. According to the specific yield of the sand, Khaled et al. [2011] expected that a 12 cm rise would require 36 mm of precipitation and thus the reported rise in groundwater table is highly disproportional.

Particle size	**Analyses [#]**	**Specific yield (mean) [%]**	**Factor of increase [mm/mm]**
$\leq$4.5 μm	27	1.1-17.6 (6)	90.91-5.68
4-62 μm	266	1.1-38.6 (20)	90.91-2.59
125-250 μm	287	1.0-45.9 (33)	100.00-2.18
250-500 μm	297	16.2-46.2 (32)	6.17-2.16
500-1000 μm	143	18.4-42.9 (30)	5.43-2.33

Table 4.1: Interval and mean values of specific yield based on intervals of particle sizes from Morris and Johnson [1967] along with the amount of samples per interval. The factor of increase is solely calculated based on the interval of specific yields and refers to the expected increase in groundwater table per millimeter of added rain.

Gillham [1984] also observed rapid increases in groundwater table during a field experiment in homogeneous sand. Here, Gillham [1984] observed a rise of 30 cm in groundwater table within 15 seconds by adding 3 mm of water.

The monitoring done by Ternært Vand project group [2024] shows the distance between groundwater table and surface in August is 1-3 meters, which confirms the area having a shallow groundwater table in some areas. The monitoring data from Beder as shown in figure 1.3 on page 14 also agrees with the observed dynamics of shallow groundwater tables as mentioned above. Here, an addition of 40 and 37 mm rain results in a sudden increase of 53 and 37 cm in groundwater table, respectively. For another well in the area, the same amount of precipitation resulted in increases of 45 and 42 cm, respectively. The disproportionate rise in groundwater table is hypothesised in the litterature to be explained by either the Lisse effect or the reverse Wieringermeer Effect [Khaled et al. 2011].

4.3.1 The Lisse effect

The Lisse effect explains disproportionate increases in groundwater level by entrapment and compression of air during heavy rainfall [Khaled et al. 2011]. According to Weeks [2002] it is a rare phenomenon where the surface soil is sealed during heavy rain and thus air is trapped. As the water front moves downwards, the trapped air is compressed and creates a pressure increase. This creates an instantaneous increase in the water level in the monitoring well which is much larger than the distance of the wetting front. According to Weeks [2002], this happens despite the groundwater table being largely unaffected. The subsequent recession in groundwater table lasts for several hours to a few days [Weeks 2002].

4.3.2 The reverse Wieringermeer effect

The reverse Wieringermeer effect (RWE) explains the disproportionate rise in groundwater table in cases where the capillary fringe is truncated by the surface. Here, the pores are near saturation and thus even a small amount of water would break the tension and result in a rapid increase of the water table. Subsequently, drainage of a small amount of water will also lead to a sudden decline [Miyazaki, Ibrahimi, and Nishimura 2012], which was also observed by Khaled et al. [2011] after the initial sudden increase.

4.3.3 Differences between conditions causing the Lisse and reverse Wieringermeer effect

The Lisse effect and the RWE both cause a disproportionate increase in water level but the underlying dynamics differ. According to Weeks [2002] the Lisse effect conditions cause an increase in a fully penetrating well but not in the groundwater table. Conversely, studies with the RWE shows increases in both the fully penetrating well and the groundwater table, see figure 4.6. Moreover, the Lisse effect is only triggered during heavy rain, while the RWE is triggered by both heavy and gentle rain. Lastly, the Lisse effect conditions show a slow recession of the water level during drainage lasting up to several days, while the recession under RWE conditions has an equally sharp decline as the sudden increase [Miyazaki, Ibrahimi, and Nishimura 2012].

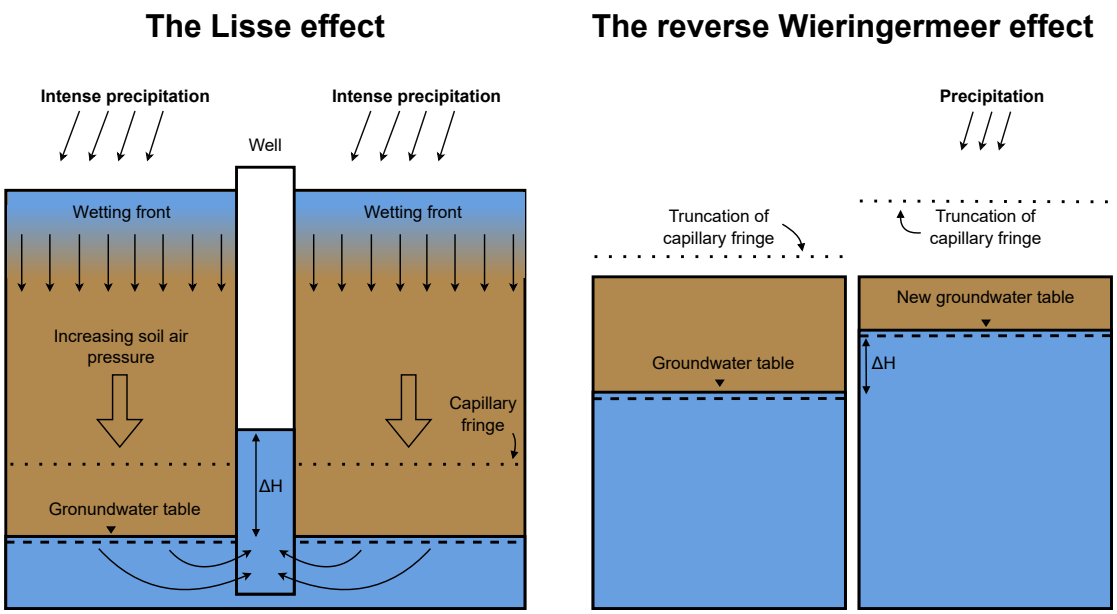

Figure 4.6: Simplified sketch of the differences in the dynamics causing the reverse Wieringermeer effect and Lisse effect. Inspired by Miyazaki, Ibrahimi, and Nishimura [2012].

Heliotis and Dewitt [1987] conducted laboratory and field studies of the Lisse effect and the RWE together with a storage effect in a peatland ecosystem. Here, the storage effect happened in 65-90% of the investigated events across 4 stations, where the storage effect was defined as the cases where the increase in water table could be predicted by the specific yield of the soil. Moreover, most hydrographs showed interactions of the effects. For instance, the Lisse effect was generally associated with either the RWE or the storage effect. Heliotis and Dewitt [1987] further noticed that for most cases the RWE only occured after an initial percolation of the precipitation to establish the soil moisture conditions that leads to the RWE. Thus, the effects were distinguished by predominant characteristics, for instance the response magnitude of the Lisse effect was generally 50-250% greater than the groundwater increase predicted by the specific yield. Further, the Lisse effect has been observed to cause an increase in groundwater table from 10-55 cm [Weeks 2002]. According to Weeks [2002] the Lisse effect has only been observed in shallow groundwater tables, for instance Heliotis and Dewitt [1987] could only reproduce the effect in the laboratory on peat core samples with depth from surface to water lower than 1 m.

4.3.4 Inclusion of hysteresis in the modelling of disproportionate rises in the groundwater table

Khaled et al. [2011] investigated the RWE on soil columns packed with sand and light clay. When modelling the recharge amount based on a wetting water content curve, the results showed poor predictions and underestimated the fluctuations in every case. However, when including the hysteresis effect the predictions were improved and very good agreements were found between the measured and modelled amount and general features of fluctuations were predicted. Moreover, Lehmann et al. [1998] investigated the fluctuating capillary fringe for different boundary conditions and fluxes in a packed column with coarse sand. Here, they observed differences in the height of the capillary fringe depending on whether they conducted

a cycle of drying or wetting of the soil. Using a water retention curve for a drying experiment showed a height of the capillary fringe of 24.5 cm, while the wetting curve showed a height of 13.6 cm. Thus, results from Khaled et al. [2011] and Lehmann et al. [1998] suggest that the water content of the packed soil at a given suction depends on the preceding wetting or drying.

4.4 Summation of the dynamics of the capillary fringe causing disproportionate groundwater increases

This part of the Master's thesis set out to answer the first question; *"Which dynamics in the soil matrix cause disproportional groundwater rise?"*

From the studies mentioned above, it becomes evident that the initial soil water content plays a major role in disproportional groundwater rise. Here, the capillary fringe reduces the available storage capacity of the soil, thus reducing the amount of water needed for increasing the groundwater table. Since the extent of the capillary fringe depends on the pore size, soils with a non uniform particle distribution and small particles typically has a greater extent of the capillary fringe and are thereby more susceptible to disproportionate groundwater rise.

The two main effects behind the disproportionate rise are the reverse Wieringermeer effect and the Lisse effect. Here, the reverse Wieringermeer effect describes situations where a small distance from the groundwater table to the surface can cause disproportionate groundwater rise due to truncation of the capillary fringe and the aforementioned small storage capacity. The disproportionate rise might also be triggered by heavy rainfall where the Lisse effect occurs. Here, air entrapment in the soil increase the soil pressure which instantaneously increase the water level in monitoring wells. These dynamics has to be taken into consideration when doing further work on the disproportionate groundwater rise.

Part II :

A study of capillary fringe induced disproportional groundwater rise and infiltration by sandbox experiments

5 Presentation and evaluation of the methods used for conducting the sandbox experiments

Part of the goal of this Master's thesis was gaining knowledge of the underlying dynamics of the disproportionate rises in groundwater table observed in the case area Beder. Therefore, this chapter presents the attempt to replicate the dynamics where millimeters of added precipitation results in centimeters of groundwater rise by using a sandbox experiment. Additionally, the hypothesis of extraneous water infiltrating due to groundwater rise from below was also tested. This was done in order to answer the second question; *"How can a sandbox experiment be used to assess the hypothesis of water infiltrating from below and how can it be used to replicate disproportional groundwater rise?"* The question is treated in chapters 5 through 7.

5.1 Experimental setup of the sandbox experiments

The sandbox experiments were conducted with the same sandbox as used by Hedevang and Sørensen [2023]. A digital sketch of the sandbox can be seen in figure 5.1.

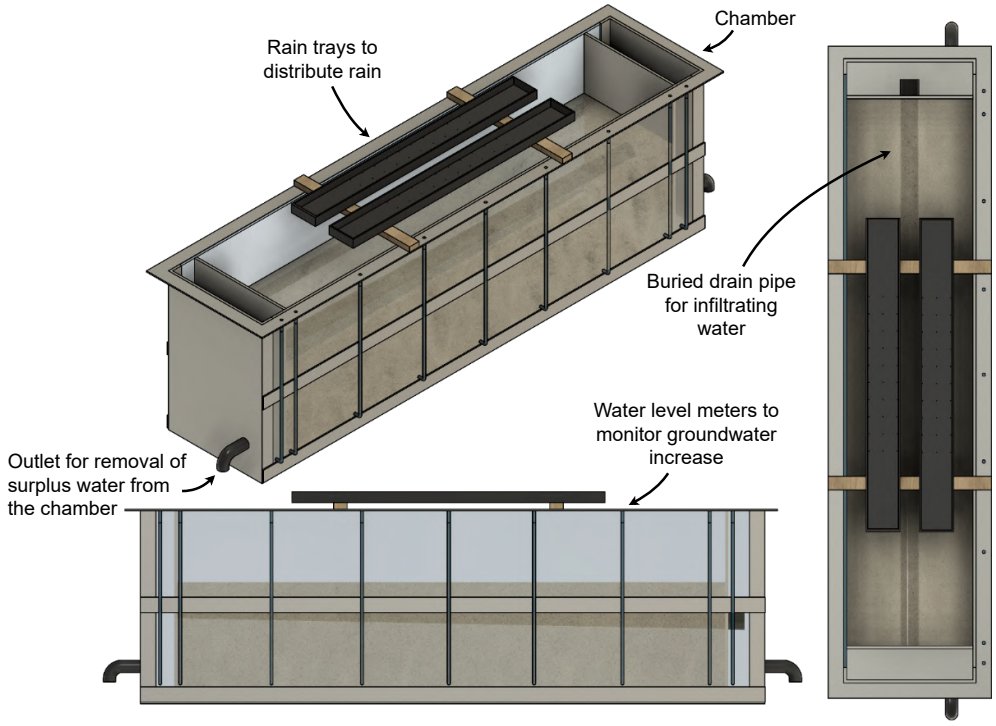

Figure 5.1: Digital sketch of the sandbox where central components of the experimental setup are highlighted. The sandbox length, width and height were approximately 180x41x63 cm, respectively.

5.1.1 Configuration and preparation of the sandbox

The experiments were conducted using a sandbox with inner length, width and height measurements of approximately 180x41x63 cm, respectively. For a complete overview of the exact measurements see appendix A. A membrane between the central part of the sandbox and the chambers on both side of the box consisted of perforated plates with a cloth covering the holes. This was done to avoid soil particles exfiltrating while allowing water to permeate to the chambers. The plates were also covered with plastic during packing of the sandbox, except the bottom 3 cm in each side to allow later emptying of the sandbox. The added plastic sheets were a modification of the procedure from [Hedevang and Sørensen 2023] in an attempt to limit the horizontal pressure gradients in the sandbox as reported by [Hedevang and Sørensen 2023].

Figure 5.2: Soil layer with a compaction of 1.5 g/cm^3 with loose soil on top.

Figure 5.3: Raked surface of the bottom layer before adding another layer.

The box was filled with approximately 290 L of sand. For soil characteristics, see section 5.1.2. At the time of packing, the gravimetric water content was around 4.5% and the soil was compacted to a bulk density of 1.5 g/cm^3. The soil was compacted in 4 layers. An example of a compacted and loose soil layer can be seen in figure 5.2. The surface between each layer was raked to ensure a homogeneous compaction, see figure 5.3. The sandbox after packing is shown in figure 5.6. A groundwater table was established by filling the two chambers on both sides of the sandbox with water until the water level remained constant over a longer duration. 7 water level meters along the length of the sandbox and 1 water level meter in each chamber measured the groundwater level. The chambers had outlet pipes at 5.4 cm above the sandbox datum (see appendix A for datum) to allow emptying of the box. Moreover, a 5 cm diameter drain pipe with slits of 0.8 mm width was installed in the middle of the sandbox

with an attempted slope of 2% to replicate a defective sewer pipe, see figures 5.4 and 5.5. The horizontal distance between the center of the slits was 0.5 cm. The slits only covered the upper half of the pipe to avoid exfiltration of water and thus the total leak area was estimated at 6% of the pipe's surface area.

Figure 5.4: Drain pipe after conducting the experiments. Slit width of 0.8 mm and horizontal distance between the center of the slits of 0.5 cm.

Figure 5.5: Placement of the drain pipe in the sandbox during packing of the sandbox.

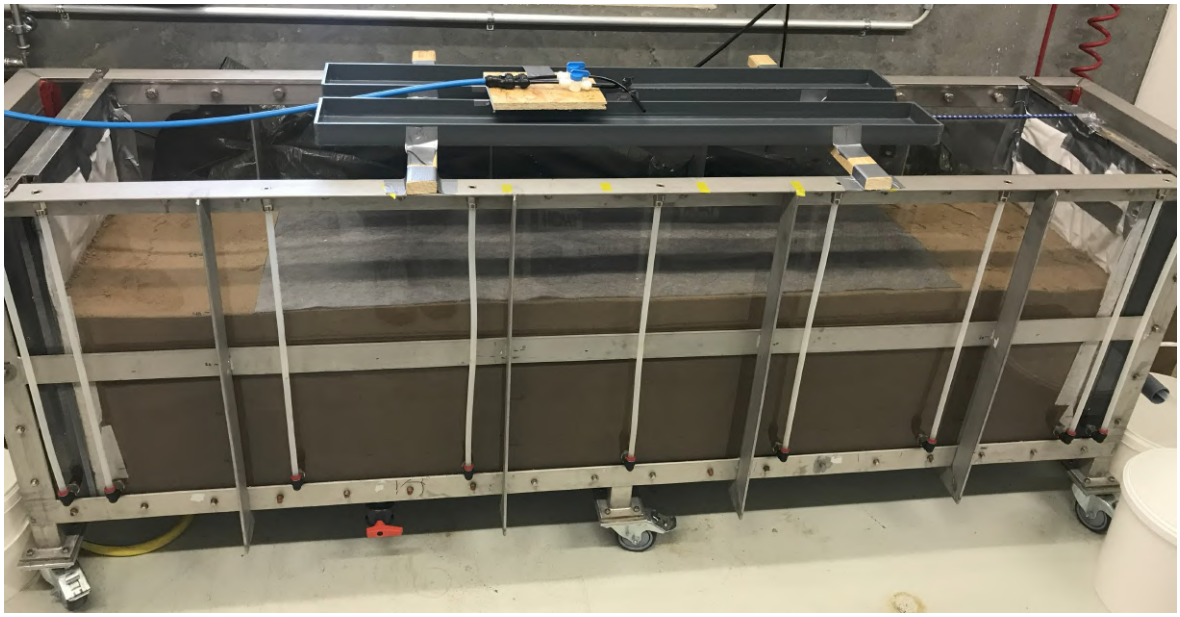

Figure 5.6: The sandbox after packing seen from the front.

5.1.2 The soil used in the sandbox experiment

The sandbox experiments were conducted with soil collected by Hedevang and Sørensen [2023] at St. Restrup Fælled 10 km west of Aalborg, Denmark. The soil was sieved through a 8 mm sieve by Hedevang and Sørensen [2023] to remove large aggregates and ensure homogeneity. Furthermore, Hedevang and Sørensen [2023] conducted a sieving analysis on 5 samples of the St. Restrup sand. The resulting soil particle distribution can be seen in figure 5.7. Here, the

sand was categorized according to ISSS standard as a coarse sand with around 55-60 % of its grains being coarse sand and the rest being fine sand or smaller [Loll and Moldrup 2000]. The clay fraction of the soil was also determined by Hedevang and Sørensen [2023] from the sieving analysis to be 0.2%. Moreover, Hedevang and Sørensen [2023] conducted an ignition loss analysis and determined the organic matter fraction at 0.57%. The hydraulic properties of the soil are further elaborated in chapter 8.

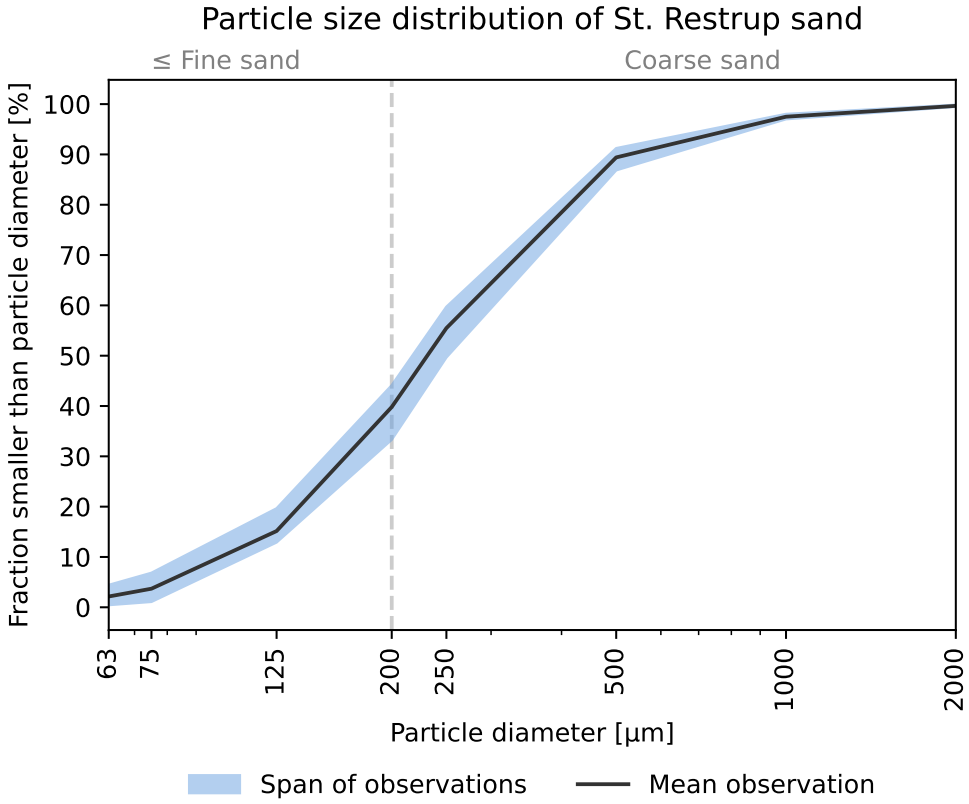

Figure 5.7: Particle size distribution curve of sand from St. Restrup Fælled. The span was made from 5 separate distribution curves dug from 2 different holes. Classification of sand according to ISSS standard.

5.1.3 Input to the sandbox - controlling the artificial precipitation

To simulate the precipitation Hedevang and Sørensen [2023] used a tray with inner dimensions of 100x10 cm and 33 holes of 1 mm diameter which covered half of the width of the tray. The exact measurements and layout of the tray is shown in appendix A. To ensure a more evenly distributed rain over the width of the sandbox another tray was manufactured with the same properties. The trays were placed in the middle of the sandbox to achieve an even distribution, see appendix A. A cloth was placed underneath to protect the surface of the sand from the impact. The rain trays and cloth during an experiment can be seen in figures 5.8 and 5.9. The configuration of the rain trays over the sandbox can be seen in figure 5.10. The water was added to the middle of each tray through two valves, one for each tray. This allowed the water flow into each tray to be regulated independently. The two valves were connected to a pipe, which was connected to the used water source. The valve contraption can be seen in figure 5.10.

Figure 5.8: Droplets on the underside of the trays.

Figure 5.9: Droplets on the cloth.

Figure 5.10: Configuration of the trays.

Three different methods were employed for controlling the artificial precipitation. A sketch of the different water inputs can be seen in figure 5.11 on the next page. In the two first experiments the valves were connected directly to a faucet with cold water. Here, an attempt was made to maintain a constant water level of 2 cm in the precipitation trays by regulating the valves and faucet continuously throughout the experiments. The intensity of the precipitation trays were tested separately from the sandbox experiment (see section 5.4) and the measured intensity was assumed to be transferable to the sandbox experiments. For the next two experiments warm water was used and a water meter was introduced on the pipe between the faucet and the valves which was an attempt to get a more accurate estimate of the added water volume. However, despite having tested the accuracy of the water meter beforehand, results from the experiments showed that the water meter underestimated the volume by up to 20 liters.

For the last experiment knowledge of the exact volume of added water was desired. Therefore, a pump and a reservoir were used to control the water input and the water level between the trays was kept at the same level. The experiment was conducted with cold water, where the water level in the pump reservoir was kept constant by adding a known amount of water into the reservoir continuously. The total volume added to the reservoir and the reservoir volume before and after the experiment were all measured. The pump setup was tested prior to implementation (see section 5.4) to make sure the output resulted in a sufficient rain intensity.

5.1.4 Output from the sandbox

During the experiments the volumes flowing out of the drain pipe and the two chambers were measured. Buckets with known volumes and water levels were placed at all three outlets with a HOBOWARE U20-001-01 Water level logger (maximum error of ± 1 cm water [Onset 2018]) in each and a logger in the room for measuring the atmosphere pressure, see figure 5.11. The

water loggers were not implemented in all buckets in every experiment. For an overview of the different uses of the water loggers between the experiments see section 5.3.2. The outflow from the left- and right chamber and drain pipe outlet were measured by subtracting the atmosphere pressure from the pressure measured by the water logger and the resulting water level was converted to a flow by creating a function of the volume of the cone shaped bucket dependant on the water height. The buckets had to be replaced several times during the experiments when full and thus the water level logger was swiftly moved to a new bucket with same initial volume as the previous. The data measured during the transition was later removed. Additionally, control measurements were taken by weighing the outflow water using a weight (maximum error ± 100 g). This mass was then converted to volume assuming a density of 1000 g/L. A sketch of the setup to measure the inflow and outflow volumes of the sandbox can be seen in figure 5.11.

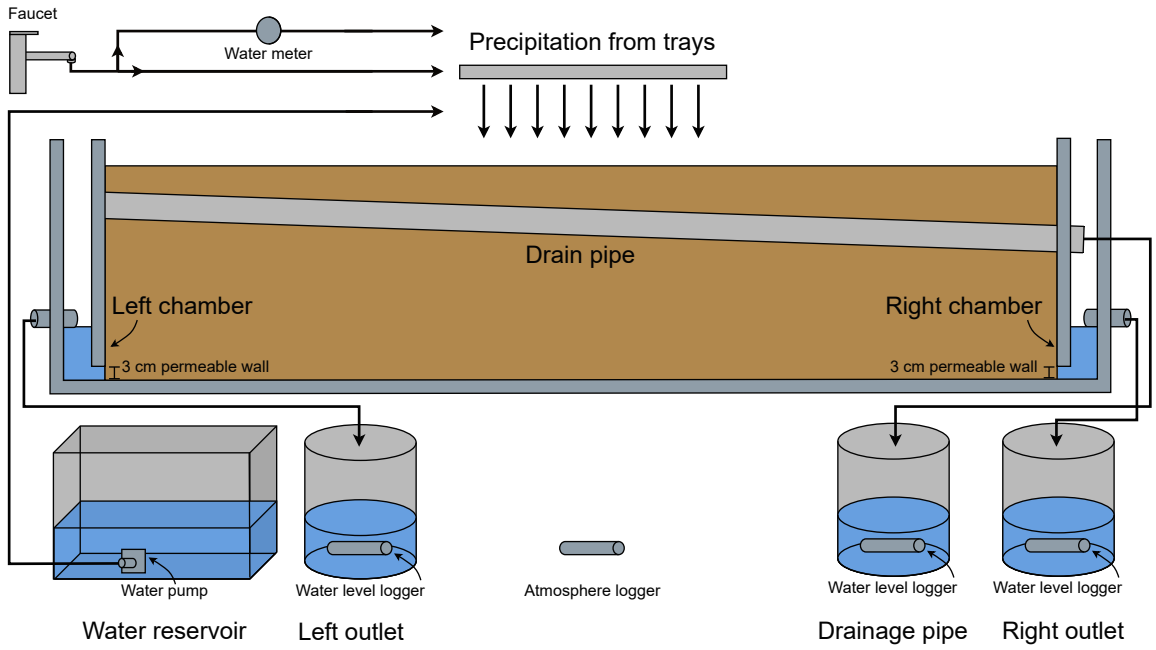

Figure 5.11: Sketch of the setup of the sandbox experiment seen from the side, including reservoirs for the precipitation and the outflow. The buckets with water loggers were not entirely cylindrical. The inflow of water originated from either the faucet, the water reservoir or the faucet with a water meter attached.

5.2 Development of hardware and software for measuring temperature in the sandbox experiments

To measure the exchange of water in the pores resulting from the precipitation conducted with warm water, temperature sensors where installed throughout the sandbox. Hedevang and Sørensen [2023] used individual commercial sensors and had to repack the sandbox in between experiments in order to gather data from their temperature sensors. To increase efficiency temperature spears were manufactured, see figure 5.12. These spears could measure the temperature in the pores surrounding the spears and track the exchange of water in the pores. The spears were 50 cm long and 6 Dallas DS18B20+ temperature sensors with a measuring uncertainty of ± 0.5 °C [Maxim Integrated 2018] were installed in a 1.6 cm diameter

pipe 3.3 cm from the bottom and every 6.6 cm. The internal circuit of the spears can be seen in figure 5.13. The insides of the pipes were cast with rubber to waterproof the temperature spears.

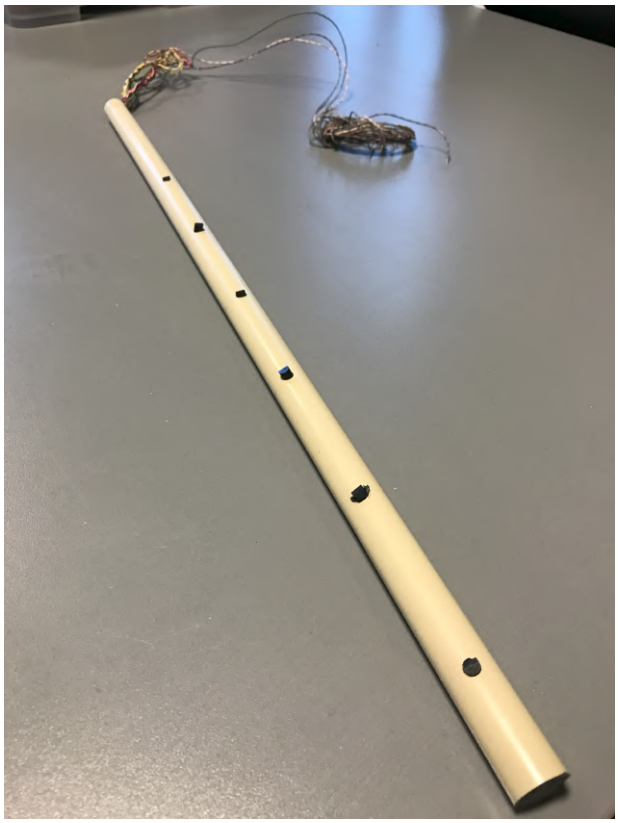

Figure 5.12: One of the manufactured temperature spears.

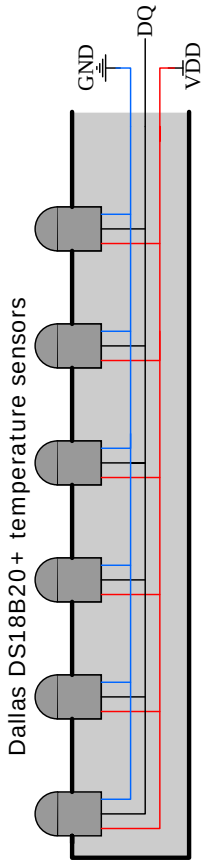

Figure 5.13: Simplified sketch of internal circuit of the temperature spears. Not to scale. GND, DQ and VDD refer to ports on an Arduino Board.

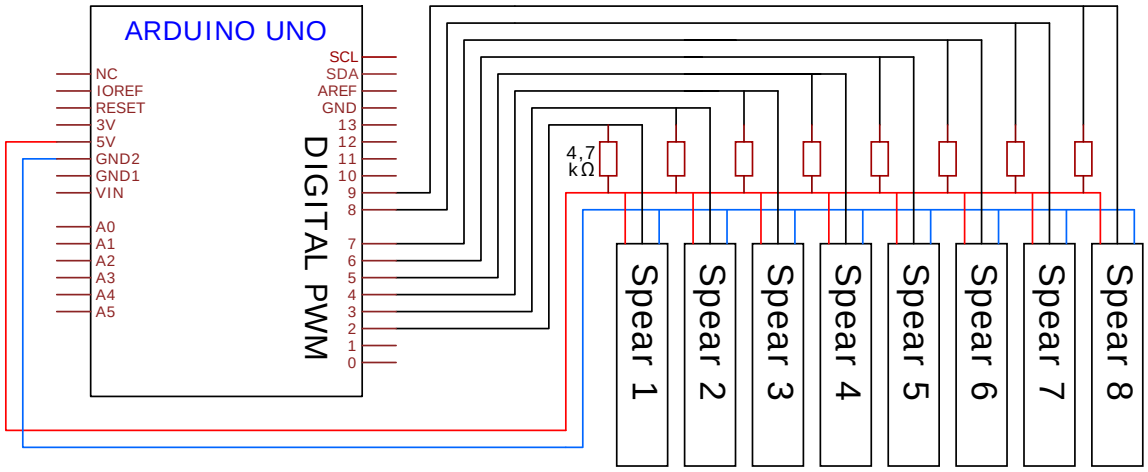

Figure 5.14: Connective circuit of the temperature spears. Not to scale.

In order to extract the data from the temperature spears an Arduino Uno board was used. The circuit connecting the sensors to the board was based on [Random Nerd Tutorials 2024] and is shown in figure 5.14.

5.2.1 Installation of the temperature spears in the sandbox

Before installing the spears in the sandbox, the soil at the spears' locations was penetrated with thin metal rods of increasing size with pointy ends. Next, the spears were inserted in the holes with the sensors pointing away from the drain pipe and lastly turned to face the drain pipe to ensure soil contact. The placement of the spears and spear labels can be seen in figures 5.15 and 5.16.

Figure 5.15: The placement of the temperature spears in the sandbox before the spears were connected. Seen from above.

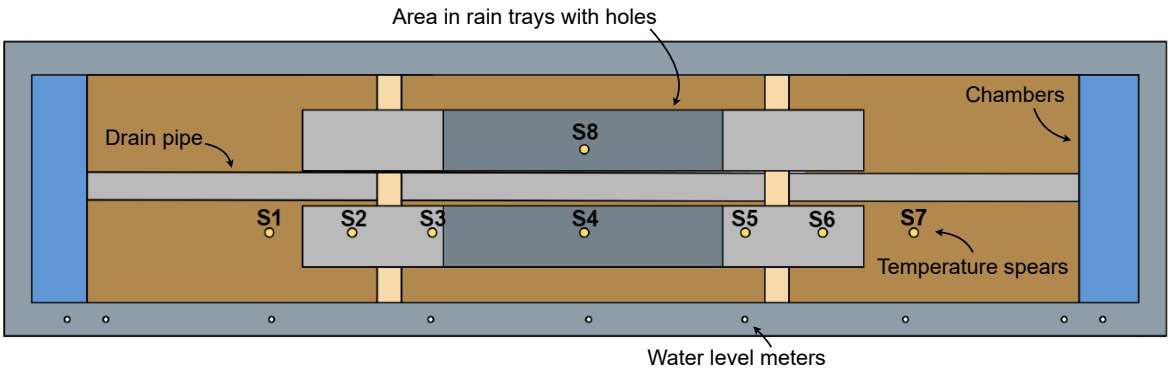

Figure 5.16: The placement of the temperature spears and their corresponding labels in relation to the rain trays and drain pipe. Sandbox seen from above. S1 = spear 1 etc.

Five spears, S1, S3, S4, S5 and S7, were placed according to the level meters, see figure 5.16. S2 and S6 were placed between the outer level meters to ensure a high data resolution to capture horizontal movement. Lastly, a control spear, S8, was placed behind S4 to investigate whether the water dynamics differed across the sandbox. The initial purpose of the temperature spears was to measure the water front of the precipitation. However, due to dynamics such as the heat of the water being transferred to the soil the temperature spears measured the exchange

of water in the pores instead of the water front.

5.2.2 Temperature spear software

In addition to manufacturing the temperature spears, software for reading the data was also produced. Here the program named "ThermoSpear" was created in the programming language python. A screenshot of the ThermoSpear software appears in figure 5.17. The program displayed live data from the Arduino in a table and plot, to evaluate the changes in temperature in the sandbox during the execution of the experiments.

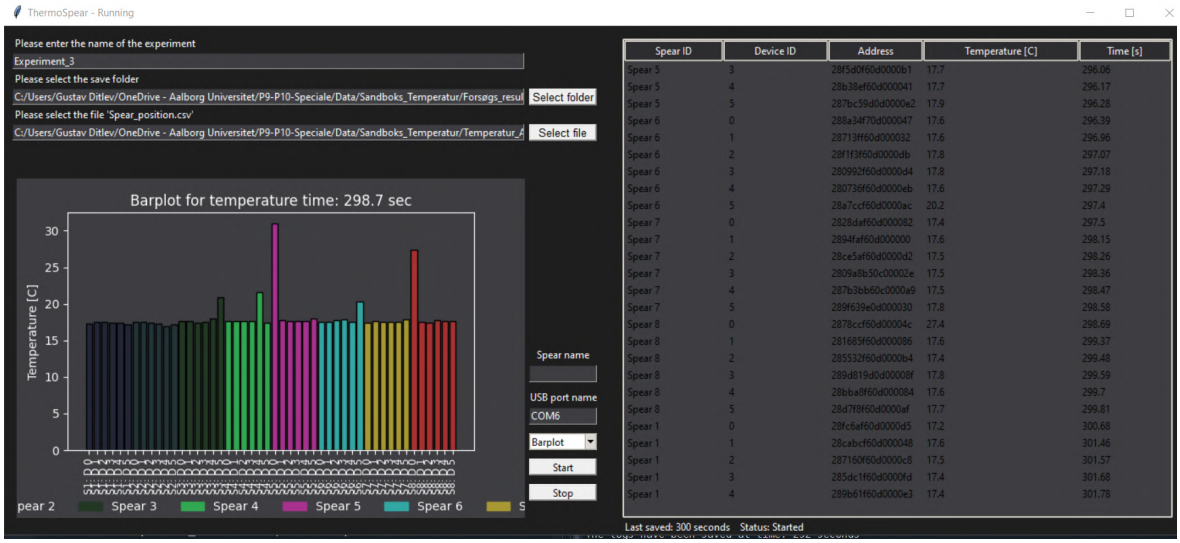

Figure 5.17: Screenshot of the software ThermoSpear for displaying live data from the temperature spears.

5.3 Execution of the sandbox experiments - overview of the differences in equipment, initial conditions and methodology

The experiments were conducted over a period of multiple months, during which iterative improvements were made to the methodology and boundaries, resulting in better boundary control and data gathering but also differences in initial conditions. In total five experiments were conducted. In between the experiments the sandbox was covered with a tarp to avoid evaporation. A timeline of the experiments with their designated labels can be seen in figure 5.18.

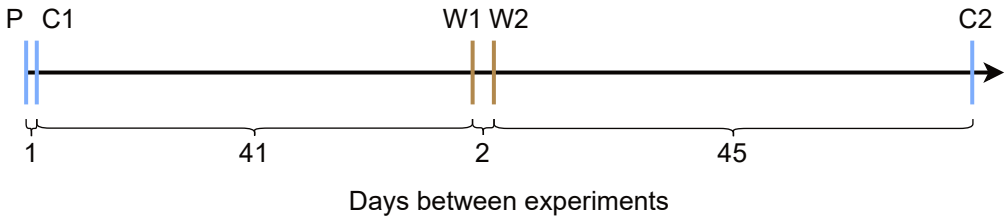

Figure 5.18: Timeline of the experiment order and amount of days between the experiments. Blue lines are cold water experiments while brown lines are warm water experiments. P = Pilot experiment, W1 = Warm experiment 1, C1 = Cold experiment 1, etc.

Here, experiment P (pilot experiment), C1 (Cold experiment 1) and C2 (Cold experiment 2) were conducted with cold water (approximately 9°C) and experiment W1 (Warm experiment 1) and W2 (Warm experiment 2) with warm water (approximately 44°C). The spears were installed between experiment C1 and W1. The final experiment C2 was conducted with cold water since a cold water experiments with complete control over the boundaries was needed for model calibration, see chapter 9 and 10.

5.3.1 Initial and boundary conditions of the sandbox experiments

The initial conditions differed for each experiment, which affected the dynamics observed in the sandbox. Here, mainly the water content of the sandbox and the initial groundwater level varied between experiments. Before adding precipitation, the groundwater level was noted in all level meters and loose soil samples were taken in the surface soil of the sandbox by brushing the particles into a test tube. The loose soil samples were immediately analysed for gravimetric water content on a Mettler Toledo HE73 Moisture Analyzer. The gravimetric water content was converted to volumetric water content by multiplying with the bulk density in the sandbox of 1.5 g/L.

Experiment	**Date**	**Left side [cm^3 H_2O/ cm^3 soil]**	**Right side [cm^3 H_2O/ cm^3 soil]**	**Water level [cm]**	**Dry days before [#]**
P	06/12/2023	0.111*	0.112*	5.4	-
C1	07/12/2023	0.192	0.191	5.7**	1
W1	17/01/2024	0.137	0.129	2.1**	41
W2	19/01/2024	0.135	0.209	4.5	2
C2	04/03/2024	0.096	0.162	5.0**	45

Table 5.1: Initial conditions of the experiments. Water content samples were taken in the top soil of the sandbox right before initiating the experiments near each chamber of the sandbox. P = Pilot experiment, C1 = Cold experiment 1, W1 = Warm experiment 1, etc. * Measured the day before the experiment. ** Calculated using the average level of every water level meter.

Experiment P was wetted from the bottom and the capillary fringe was established by tension. The wetting spanned the duration of 4 days before the groundwater table reached 5.4 cm corresponding to the level of the left and right outlets. Experiment C1 was conducted one day after experiment P. The groundwater table had not yet decreased to the initial water level of 5.4 cm. Nonetheless, since both the left and right outlet pipes were dry, the sandbox was assumed to be finished draining. Measurements of the water content from the top soil indicates that the sandbox overall water content was higher in experiment C1 than experiment P, see table 5.1. 41 days passed between experiment C1 and W1 and therefore the groundwater table had decreased to an average level of 2.05 cm. The experiment was conducted without adding any water before start in order to investigate the dynamics of drier soil. This was an attempt to replicate experiment P as it was expected that the soil was not completely wetted before experiment P.

Experiment W2 had almost the same initial conditions as experiment C1. The experiment was conducted 2 days after experiment W1 and therefore had an initial water content similar

to that of C1. Moreover, measurements and visual inspection both showed that the water content in the top soil differed, with the left side being drier than the right side, see table 5.1. Experiment C2 was conducted 45 days after experiment W2 and the sand was therefore dry. To establish a groundwater table the sand was wetted, similarly to experiment P, until an average water level of 5 cm was reached. This process only spanned a couple of hours, suggesting that the sandbox still contained more water than before experiment P. After conducting all the experiments, the capillary fringe was once again established and the volumetric water content was analyzed throughout the soil column, see section 5.5.1.

5.3.2 Methodology for conducting the sandbox experiments

The five sandbox experiments were essentially conducted by turning on the water source and continuously measuring the increase in groundwater table as observed in the water level meters. The differences in measuring equipment between the experiments are shown in figure 5.19.

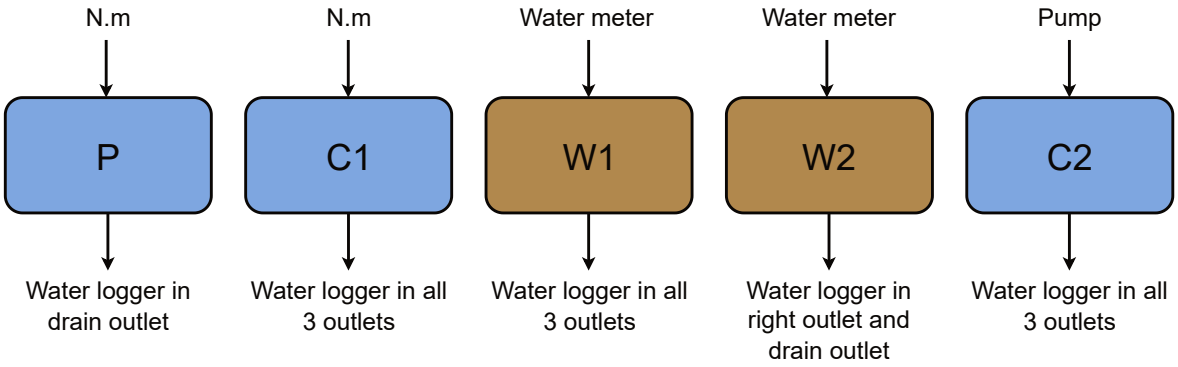

Figure 5.19: Overview of the equipment used for measuring water inputs and outputs in the different experiments. Blue boxes are cold water experiments while brown boxes are warm water experiments. N.m = Not measured, P = Pilot experiment, C1 = Cold experiment 1, W1 = Warm experiment 1, etc.

After turning on the precipitation, the height of water in the water level meters were noted on the side of the sandbox with a marker at appropriate intervals depending on how rapidly the groundwater rose. The precipitation was turned off when the groundwater level stopped increasing in most of the water level meters. Then, the decrease of the groundwater table was marked for all experiments except experiment P. The decrease was measured until a groundwater level of approximately 5.4 cm was reached. The total volumes added in each experiment is presented in table 5.2.

Experiment:	**P**	**C1**	**W1**	**W2**	**C2**
Rain volume [L]	N.m	39*	65*	57*	59.6
Duration of rain [min]	60	57	61	46	76
Rain flow [L/min]	N.m	0.68	1.1	1.2	0.79

Table 5.2: Overview of parameters of the added rain during the experiments. N.m = not measured, P = Pilot experiment, C1 = Cold experiment 1, W1 = Warm experiment 1, etc., *Calculated from outflow volumes.

5.4 Evaluation of the equipment used to simulate precipitation

Due to differences in the equipment used for measuring the precipitation in the sandbox experiments, several experiments were conducted with the rain trays to evaluate the flow out of the trays under the different conditions.

5.4.1 Evaluation of how evenly the trays distributed the water

To evaluate how evenly the precipitation trays distributed the water a separate collection container under each tray was installed. It was also ensured that the trays were level. Moreover, each tray was connected using the same valve system as in the sandbox experiment which was connected to a water meter. The experiment was conducted 3 times on the side of the sandbox to limit the bends in the pipes. For experiment setup see figure 5.20.

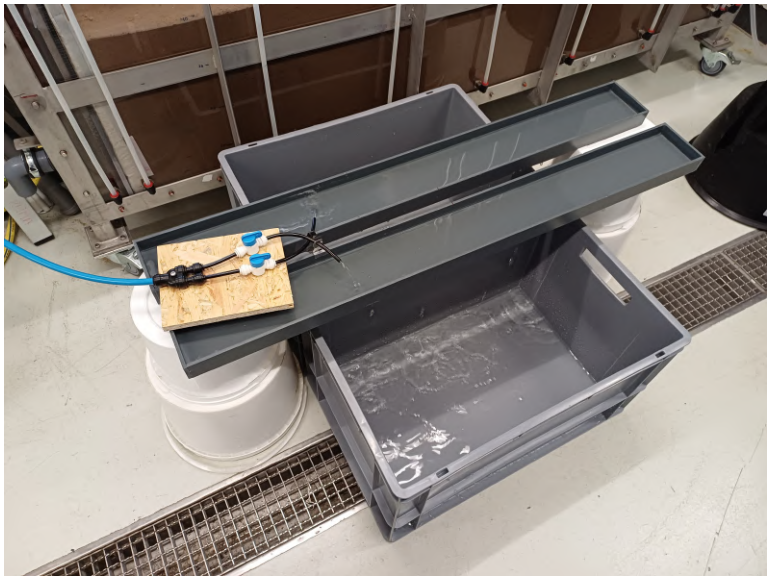

Figure 5.20: The setup for evaluating how evenly the rain trays distributed the water.

The 3 experiments were conducted by filling the two trays to the same water level and turning on the faucet. The experiments lasted 10 min each where a constant water level in the trays were maintained. After turning off the faucet, water from each container was weighed and converted into a volume by assuming a water density of 1000 g/L. The results appear in table 5.3. Even though the flow varied between the trays, the trays were deemed sufficient for the purpose.

Experiment	**A**	**B**	**C**	**Mean ± SD**
Flow of tray 1 [mL/min]	349.9	400.7	302.1	350.9 ± 49.3
Flow of tray 2 [mL/min]	325.1	380.7	391.9	365.9 ± 35.8
Tray 2's share of the total volume [%]	48.2	48.7	56.5	51.1 ± 4.6

Table 5.3: Result of the rain tray experiment with mean and standard deviation (SD). The experiments lasted 10 min each.

5.4.2 Evaluation of warm water flow through the precipitation trays compared to cold water flow

In experiment W1 and W2 a much greater rain intensity was added to the sandbox than previously which formed a pool on the top of the sandbox despite that the rain setup had not been altered. Thus, an experiment was conducted to evaluate whether the water temperature impacted the flow through the rain trays due to a change in the water viscosity. This was hypothesized as the water viscosity is halved when the temperature increases from 10 °C to 40 °C [Brorsen and Larsen 2009, p. 186]. The experiments were conducted by filling the two trays with water and measuring the amount of water precipitated after 3 minutes for both cold and warm water, see table 5.4.

Experiment	**Cold**	**Warm**
Water temperature [°C]	10	50
Precipitated volume of tray 1 [mL/min]	348.3	448.3
Precipitated volume of tray 2 [mL/min]	330.0	548.3

Table 5.4: Result of the experiments with rain trays with different temperatures. Both experiments were conducted over 3 minutes. Only the difference between cold and warm water for each tray should be compared and not the flow between the trays due to slight variations between the setup of tray 1 and 2.

As shown in table 5.4 it became apparent that the temperature had a considerate impact on the amount of precipitation each tray delivered. This was also concluded based on a visual evaluation during the experiment. Therefore, the final experiment, C2, was conducted with cold water.

5.4.3 Evaluation of precipitation intensity with the pump setup

In experiment C2 a pump was used in order to know the exact amount of water added as precipitation during the experiment. Before using the pump, the rain intensity resulting from the pump setup was tested. The rain intensities used in experiment W1 and W2 proved too high as pools of water formed on the surface of the sandbox. Therefore, a similar intensity to the ones in experiment P and C1 was desired. The only method for controlling the pump output was the height from the pump to the rain trays. Thus, the output from the pump was tested for multiple heights by regulating the height of the reservoir until a precipitation intensity close to the intensity in experiment C1 was achieved, see table 5.2 on page 39. Then, the pump was run until the water level in the tray stabilised in order to determine the initial water level for the experiment in the trays.

5.5 Excavation and analysis of the sandbox after the experiments

After finalizing all experiments the sandbox was excavated to confirm the placement of the drain pipe and to measure the volumetric water content throughout the capillary fringe.

5.5.1 Determination of volumetric water content throughout the capillary fringe of the sandbox

In the week up to the excavation of the sandbox both chambers were filled continuously with water to ensure the capillary fringe was established. After one week, the initial groundwater level was still not even in all level meters with a variation of about 0.7 cm. Loose soil samples were taken at the surface and every 5 cm by digging into the soil and ensuring all loose soil was removed. The samples were taken from the soil right behind level meter L2, L4 and L6 to compare the water content with the level meters, see figure 5.21.

Figure 5.21: Excavation of soil behind level meter 6 (L6) to measure volumetric water content in the capillary fringe.

The loose soil samples were stored in tight plastic bags until analyzed, where all samples were analyzed for gravimetric water content on a Mettler Toledo HE73 Moisture Analyzer within 6 hours.

5.5.2 Measurement of actual placement of the drain pipe during excavation of the sandbox

After taking soil samples for volumetric water content the soil between the drain pipe and the water level meters were dug out to measure the placement of the drain pipe, see figure 5.22.

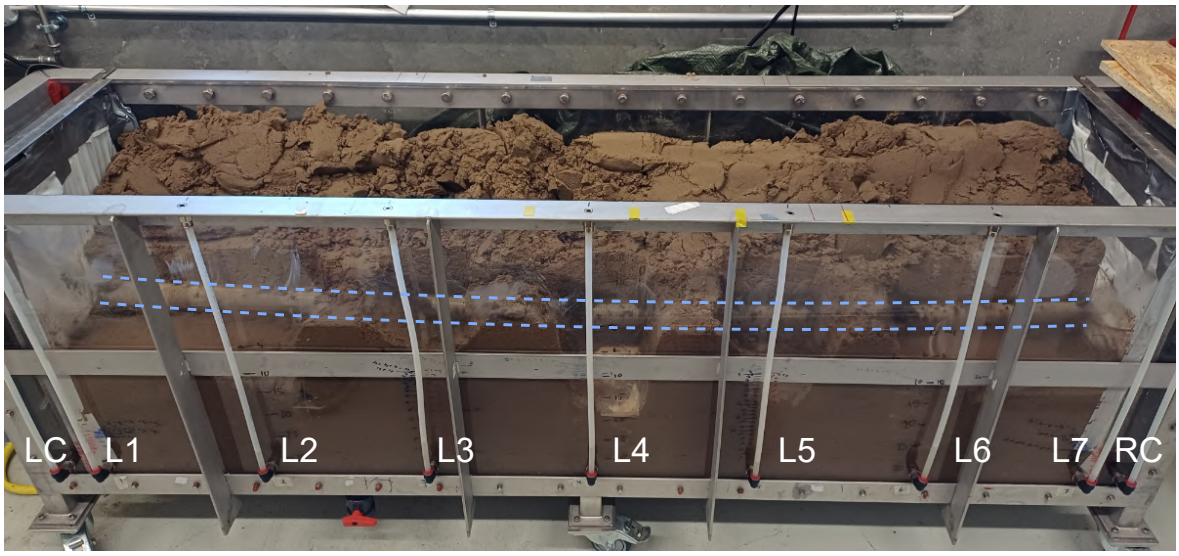

Figure 5.22: Excavation of soil between drain pipe and water level meters to measure location of the drain pipe, marked with the blue dotted lines. The soil above the pipe was not excavated. LC = Left chamber, RC = Right chamber, L1 = Level meter 1, etc.

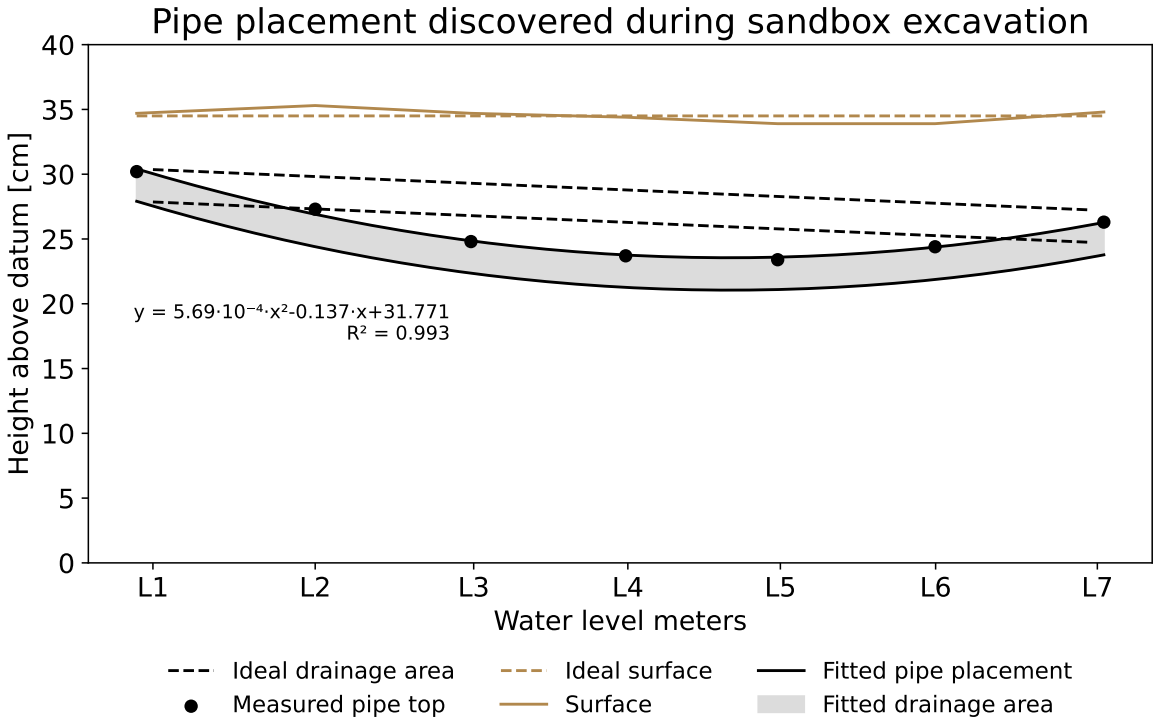

Figure 5.23: Actual placement of the pipe and surface of the sandbox compared to ideal placements. The drainage area refers to the top half of the pipe with slits. The pipe top was measured at the location of the water level meters. L1 = Level meter 1, etc.

During the execution of the experiments it was assumed that the pipe was buried with a 2% slope. However, excavation of the sandbox showed a curvature in the pipe where the lowest point was at L5, see figure 5.23. Furthermore, figure 5.23 shows that the pipe was placed approximately 5 centimeters lower at L4 than initially assumed.

5.5.3 Estimating the stored volume inside the drain pipe

Due to the curvature of the drain pipe, there was a risk of storage of water inside the pipe, which would not be included in the outflow data. This volume was estimated numerically as partial filled cylinders using a horizontal discretization of 1 mm. The volume was estimated to be 0.93 L, see figure 5.24.

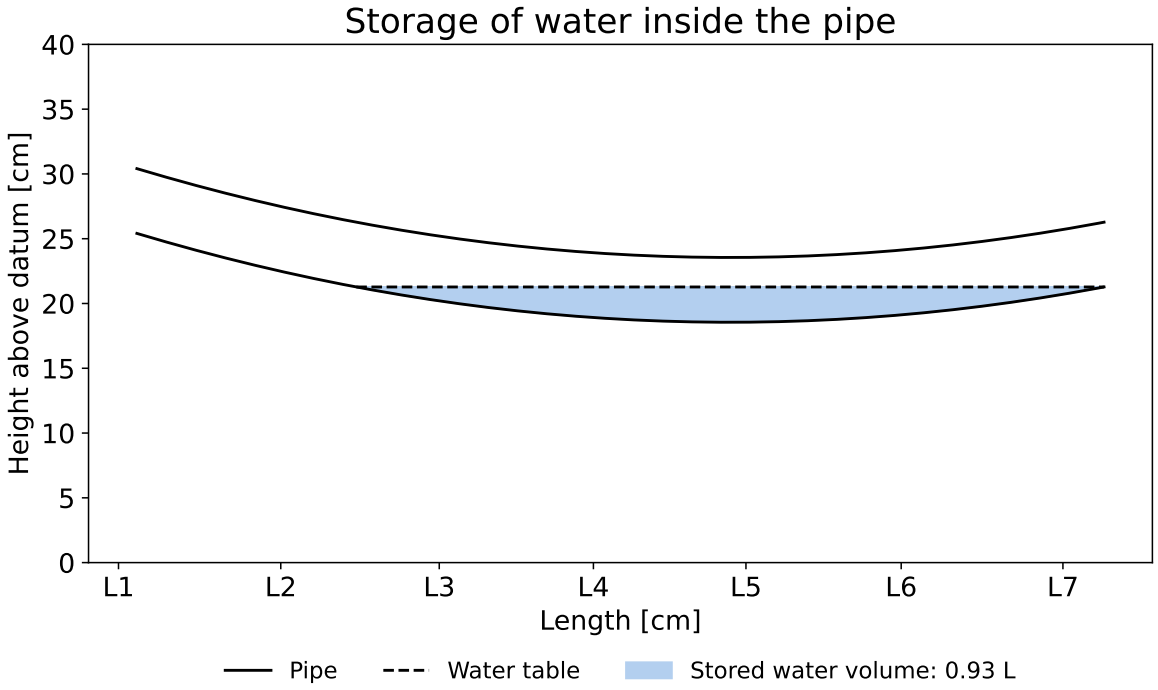

Figure 5.24: Estimation of storage of water inside the drain pipe.

6 Results from the sandbox experiments

Five sandbox experiments were conducted with the purpose of analyzing if the groundwater rise observed in Beder of millimeters of rain resulting in centimeters of groundwater rise could be replicated in a controlled environment. Furthermore, the hypothesis of water only infiltrating from below was also assessed. In this chapter the results of the experiments are presented. Here, the reader should notice that all figures of measured water level shows the initial water level above datum and thus the groundwater level does not start at 0 cm. Here, datum was the lowest measurable point on the outside of the sandbox, see appendix A. Furthermore, the 8 temperature spears and 9 water level meters are referred to by their designated labels. For labels and locations in the sandbox see figure 6.1.

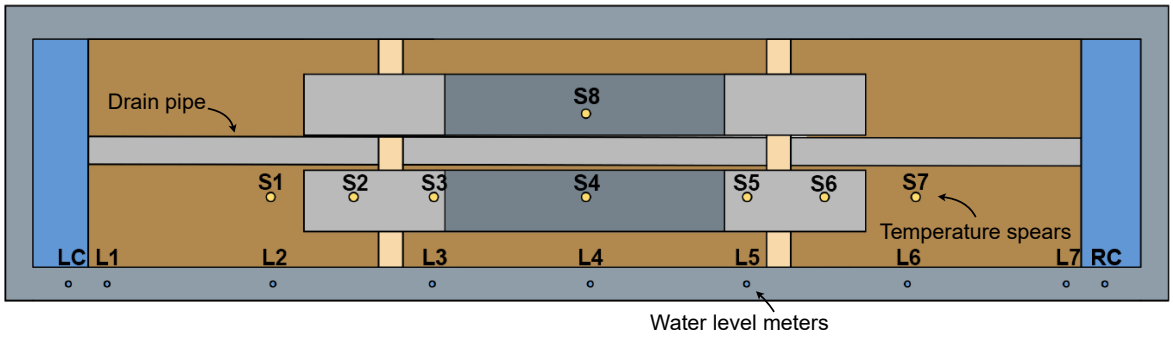

Figure 6.1: The placement of the temperature spears and water level meters and their corresponding labels in relation to the rain trays and drain pipe. Sandbox seen from above. S1 = Spear 1, LC = Left chamber, RC = Right chamber, L1 = Level meter 1, etc.

6.1 Measurements of the groundwater rise and descend in the sandbox experiments

During each experiment, the placement of the groundwater table was registered using the water level meters, see figure 6.1 for placement. Figure 6.2 shows the placement of the groundwater table plotted against time relative to the drainage area, defined as the upper half of the pipe which is the area of the pipe where the slits were present and drainage expected to occur. From this figure it can be observed that only 4 water level meters, L3, L4, L5 and L6, ever reach the drainage area in any of the experiments. Moreover, it appears that the groundwater table in the experiments with wetter initial conditions (experiment C1 and W2) rose faster than the experiments with drier initial conditions (experiment P, W1 and C2). For initial conditions see table 5.1 on page 38.

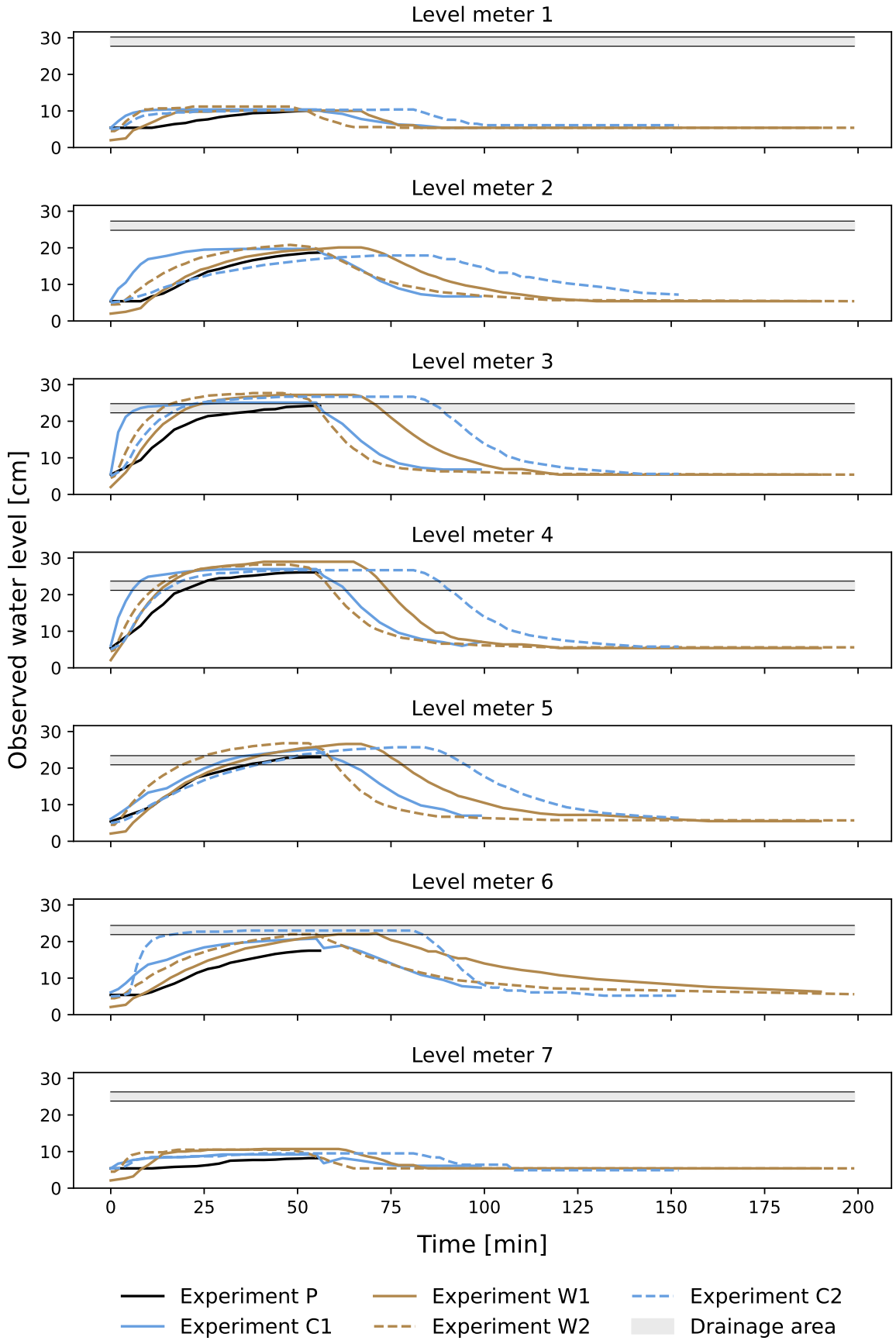

Figure 6.2: The water level observed in level meters 1 through 7 during the experiments. P = Pilot experiment, C1 = Cold experiment 1, W1 = Warm experiment 1, etc.

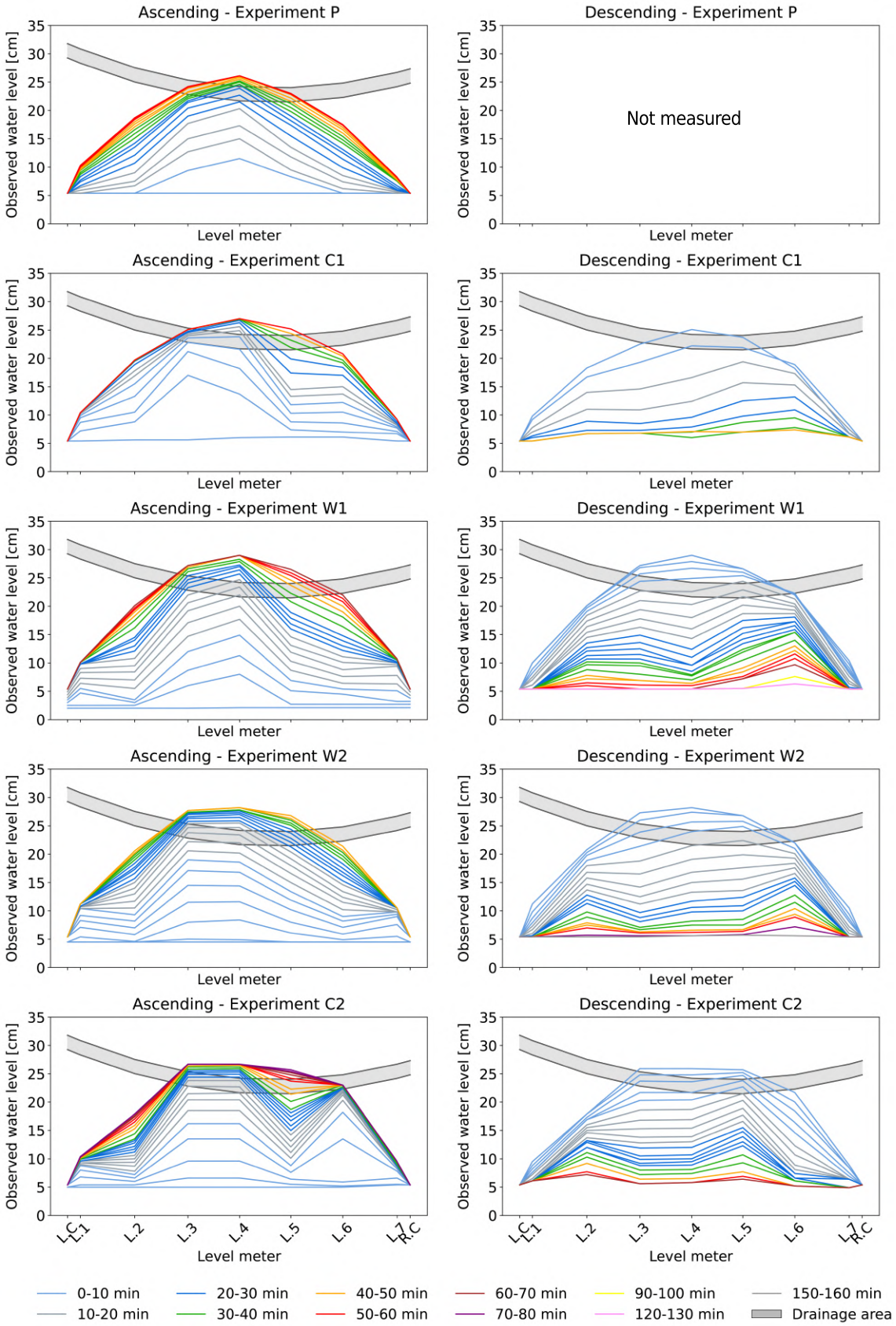

Figure 6.3: Shape of the groundwater table over time, created by linear interpolation between measurement points. The color intervals change for every new 10 minutes, i.e. a measurement at 10 min is grey instead of blue. Notice that the later measurements in the descending plots were measured in intervals greater than 10 minutes. For placement of water level meters, see figure 6.1. P = Pilot experiment, C1 = Cold experiment 1, W1 = Warm experiment 1, etc.

From figure 6.3 it can be observed that the shape of the groundwater right before turning off the rain and the maximum extent were similar across all experiments. Moreover, the figure shows that the groundwater rose faster in the left side compared to the right. When comparing the rise in groundwater table with the descend it is noticed that the descend is almost as fast as the rise. The figure is based on an assumption of a linear water table between measuring points, which is most likely a wrong assumption.

6.1.1 Measurement of the groundwater table's rise and descend relative to the drain pipe

To validate if the hypothesis of extraneous water only occurring when local increases in the groundwater table reaches the drainage area, the rise in groundwater table and the time before observing drainage was compared, see figures 6.4 through 6.8. The figures include the water level meters that measured the groundwater table closest to the drainage area at the time of observed drainage. The comparison shows that the measured groundwater level reached the drainage area before the time of observed drainage in experiment P and C1. However, in experiments W1, W2 and C2, the groundwater table was measured below the drainage area at the time of observed drainage.

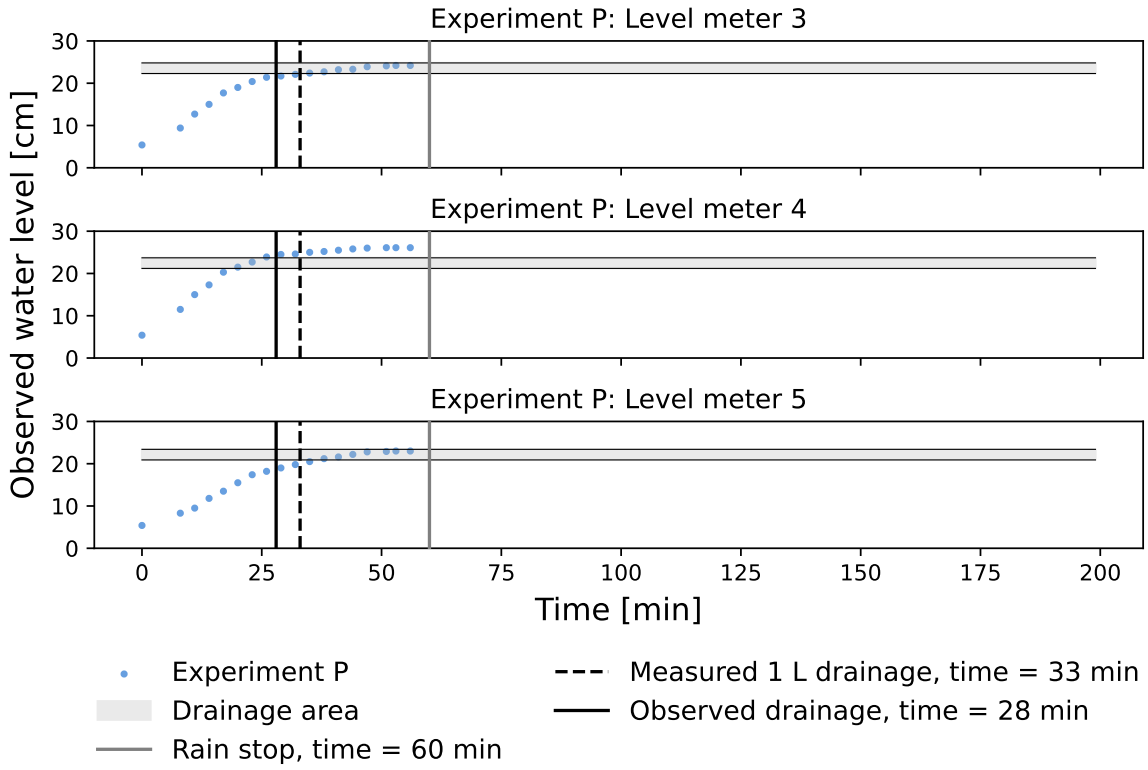

Figure 6.4: Comparison of the level of the groundwater to the time of observed drainage along with time of 1 liter drainage and rain stop in the pilot experiment (P).

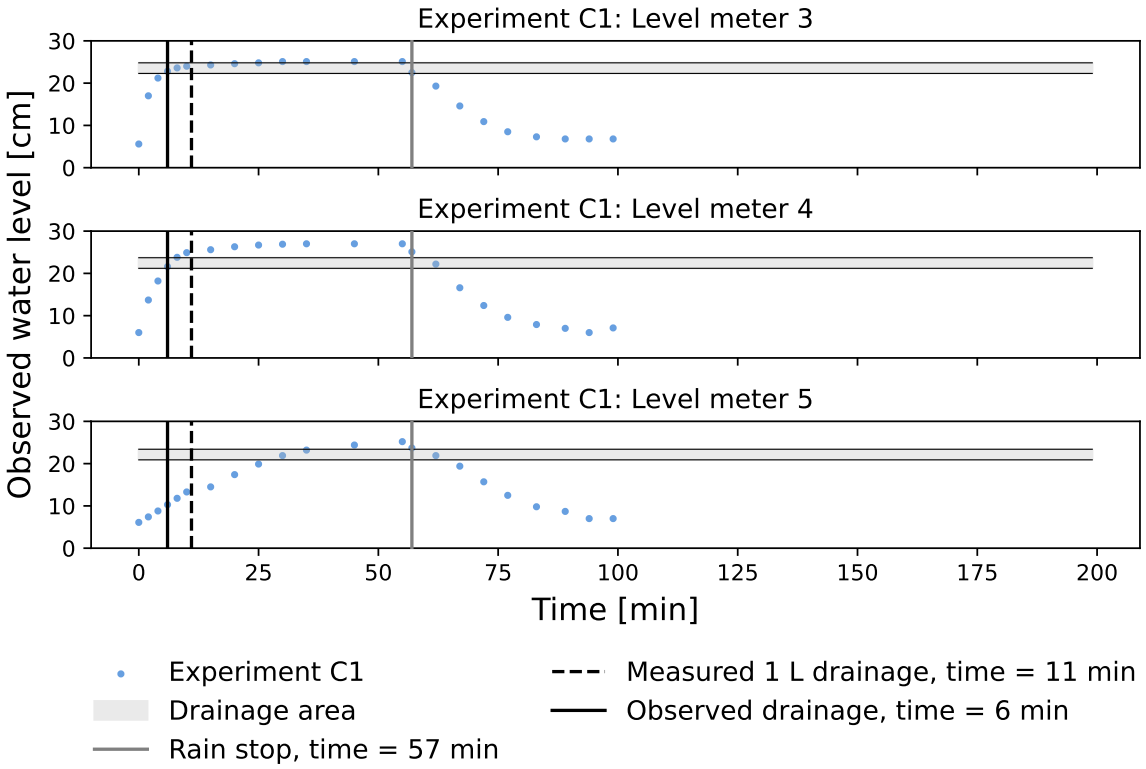

Figure 6.5: Comparison of the level of the groundwater to the time of observed drainage along with time of 1 liter drainage and rain stop in Cold experiment 1 (C1).

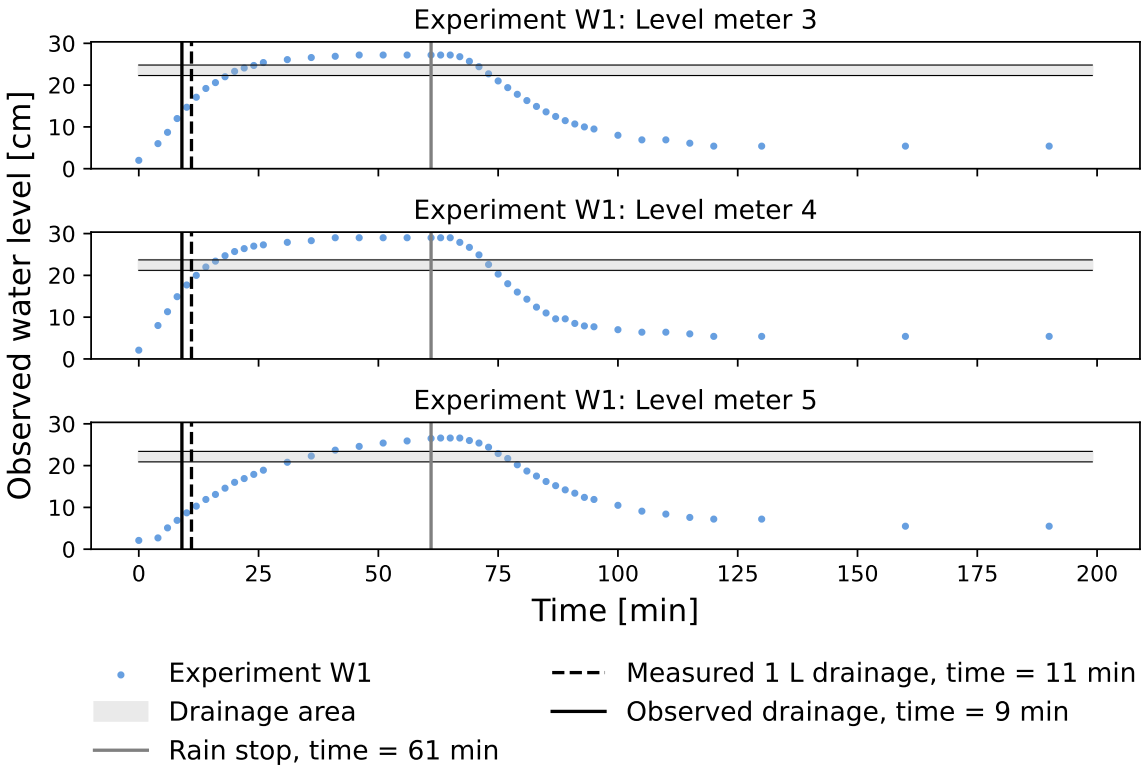

Figure 6.6: Comparison of the level of the groundwater to the time of observed drainage along with time of 1 liter drainage and rain stop in Warm experiment 1 (W1).

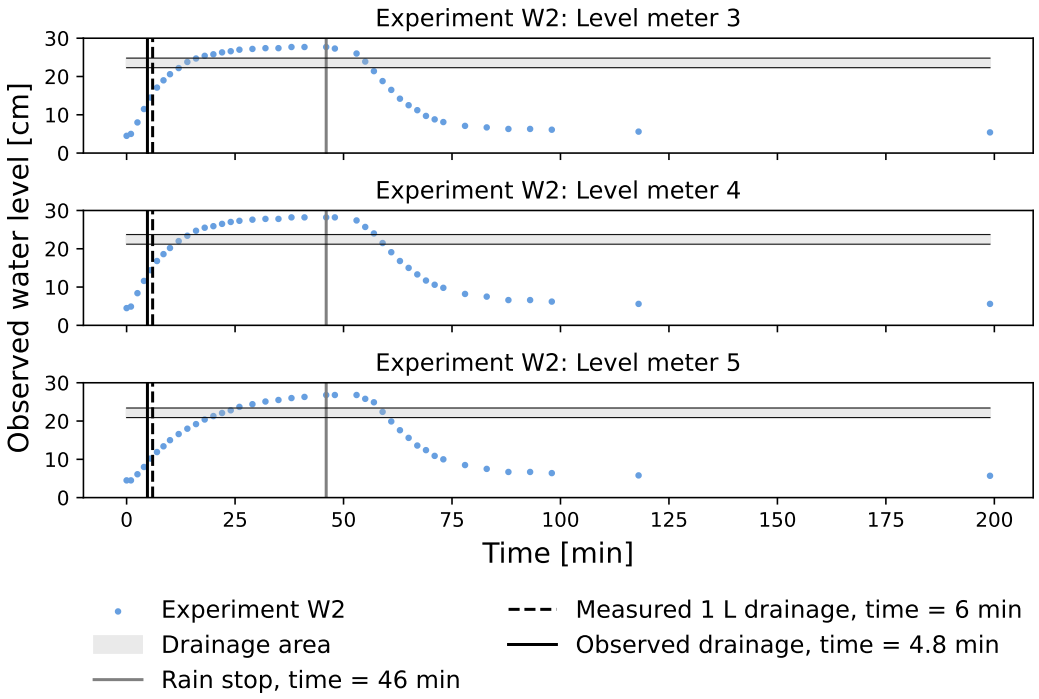

Figure 6.7: Comparison of the level of the groundwater to the time of observed drainage along with time of 1 liter drainage and rain stop in Warm experiment 2 (W2).

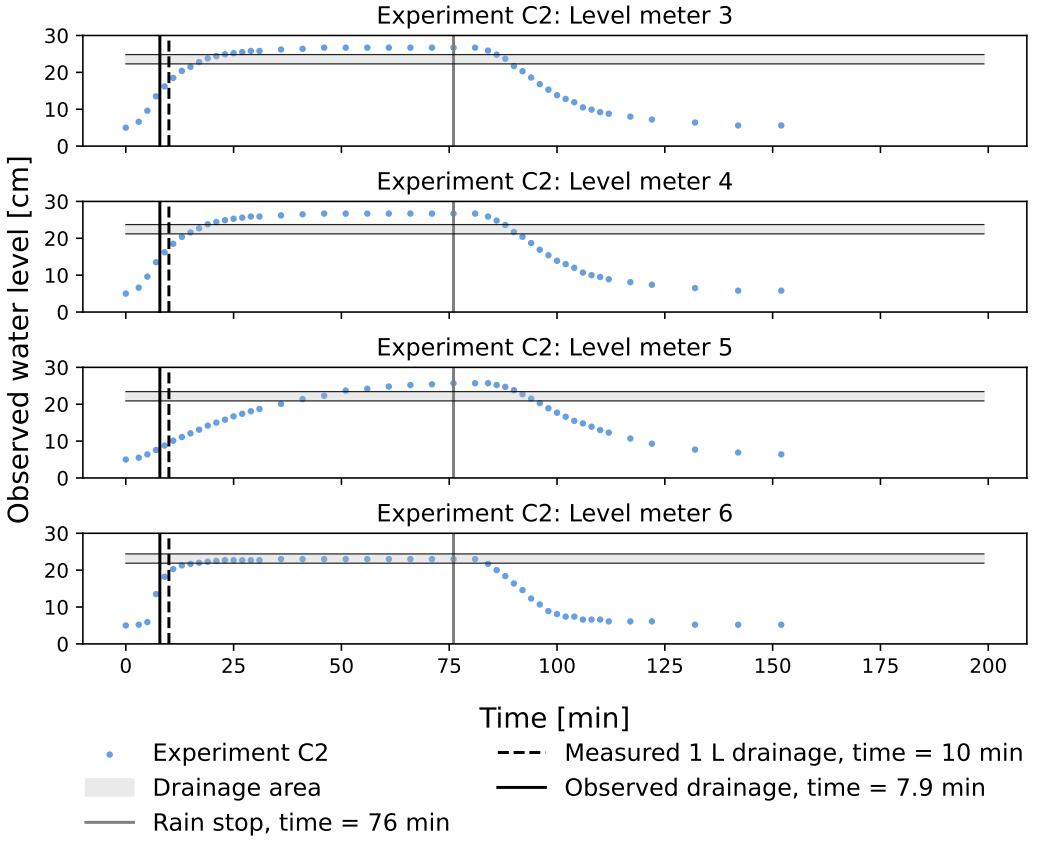

Figure 6.8: Comparison of the level of the groundwater to the time of observed drainage along with time of 1 liter drainage and rain stop in Cold experiment 2 (C2).

The minimum distances from the measured groundwater table to the drainage area at the time of observed drainage is shown in table 6.1. Here, the experiment in which the groundwater table was the farthest from the drainage area at observed drainage was experiment W2 with a distance of 11.09 cm. Moreover, in experiment P and C1, the groundwater table rose at least 1.6 cm above the drainage area before drainage was observed. The minimum distances indicate a shift in dynamics between experiment C1 and W1.

Experiment	**P**	**C1**	**W1**	**W2**	**C2**
Minimum distance [cm]	-3.3	-1.6	4.9	11.09	10.52

Table 6.1: Minimum distance from groundwater level to drainage area at time of infiltration across the experiments. Distances were calculated by linear interpolation between measurements assuming constant velocity if no measurement was taken at time of infiltration.

6.2 Groundwater rise compared to rain depth

In order to compare the groundwater rise in the sandbox with the rain added, the area the rain was distributed over was estimated. Here, figure 6.9 shows the minimum and maximum area the rain was expected to be distributed over.

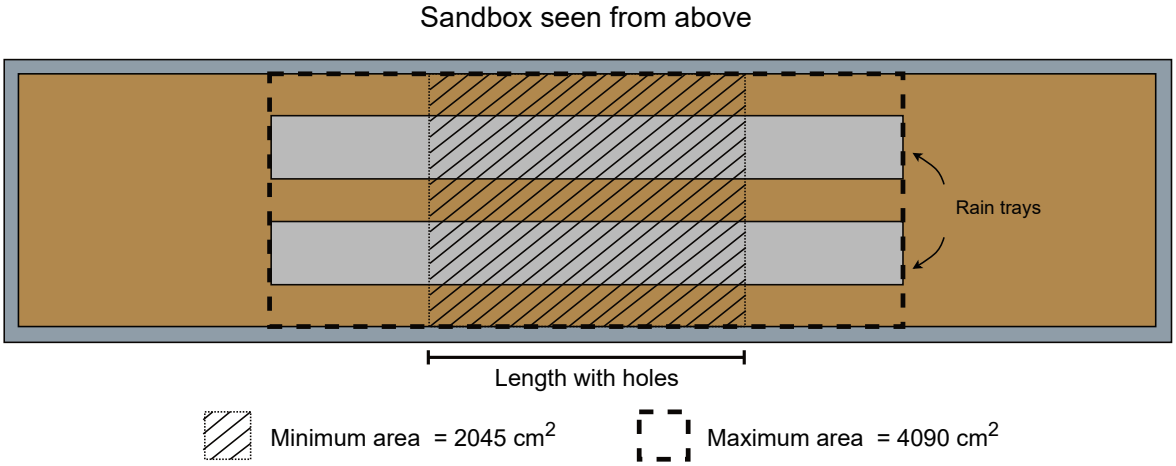

Figure 6.9: Visualization of the areas used to calculate rain intensities. The minimum area covers the width of the rain trays with holes. The maximum area covers the entire width of the rain trays.

The groundwater rise was evaluated for L4 due to this level meter being the least affected by horizontal movement of the water. Then, for every measurement of the groundwater table in L4 the expected amount of added rain was calculated based on the rain intensity and time since experiment start, resulting in figure 6.10 Here, the interval of observed increase is based on rain depth calculated from the minimum and maximum area the rain was expected to be distributed over, see figure 6.9. Moreover, the expected increase was calculated from a specific yield of 0.254, corresponding to the effective porosity of the St. Restrup sand. As seen in the figure all intervals of observed increase lie around the expected increase except in experiment C1 where both the maximum and minimum observed increase is above the expected. Moreover, the increase in groundwater table stagnates around 20-25 cm corresponding to the height where drainage through the pipe starts.

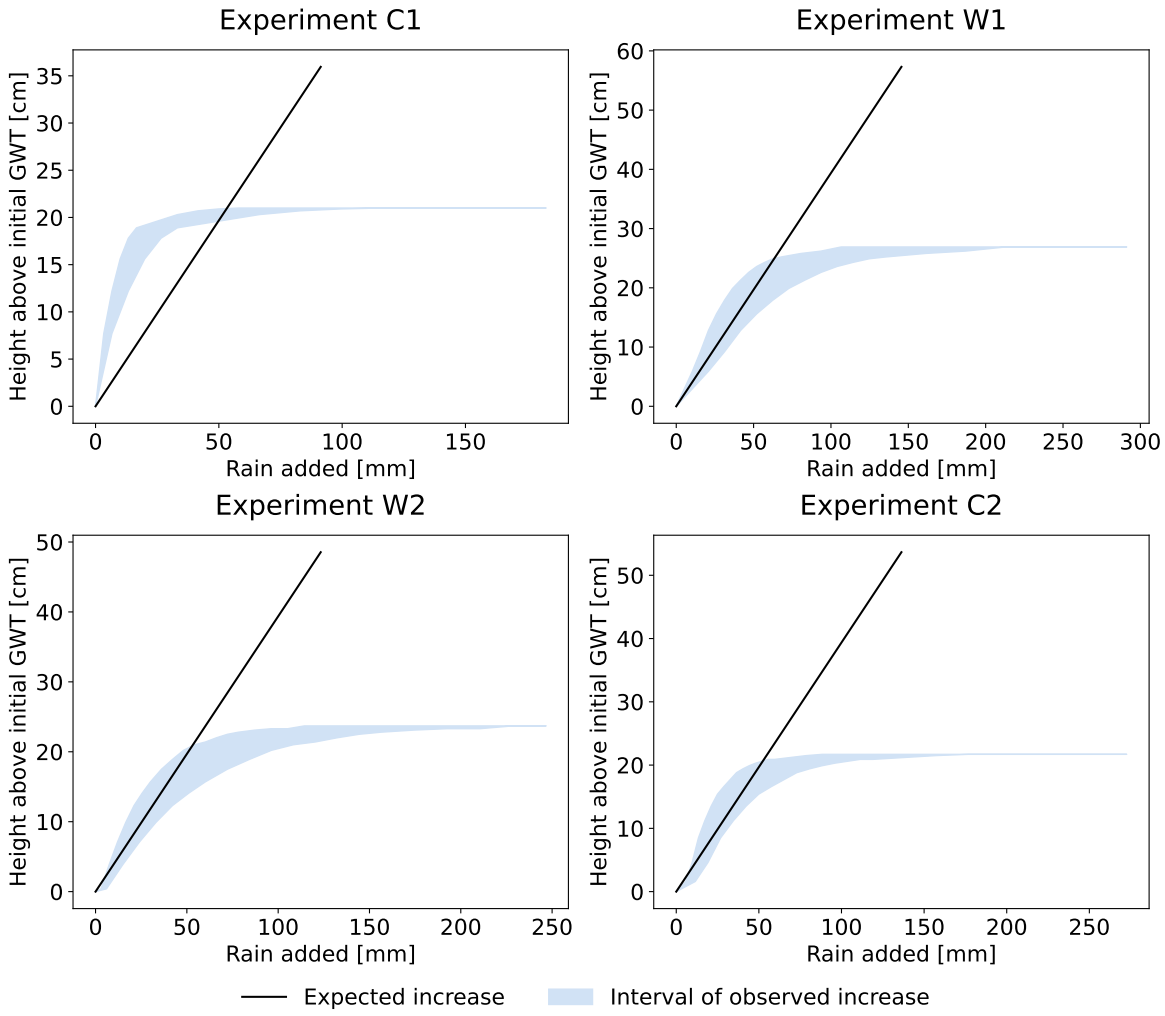

Figure 6.10: Interval of observed increase in groundwater table (GWT) at level meter 4 compared to the estimated amount of water added. Interval is based on rain depths calculated from average rain intensities and distributed over an area of 2045-4090 cm^2, see figure 6.9. Expected increase is calculated from a specific yield of 0.254, corresponding to the effective porosity of the soil.

6.3 Measurements of outflows from the chambers and drain pipe

During the experiments the water which did not contribute to an increase in the groundwater table was measured. Here, figures 6.11 through 6.15 show the measurements of outflow from the chambers and drain pipe. From these figures it can be observed that drainage occurred within approximately 5 minutes of the groundwater reaching the drainage area. This is with the exception of experiment P, where the groundwater table reached the drainage area 10 minutes before drainage was measured. Furthermore, it can be observed that the drain pipe contributed with approximately 50% of the total outflow and that the right chamber had a tendency to drain more water than the left. This tendency increased through out the experiments. Lastly, experiments W1 and W2, which were conducted with warm water, shows the drain pipe started draining before the chambers.

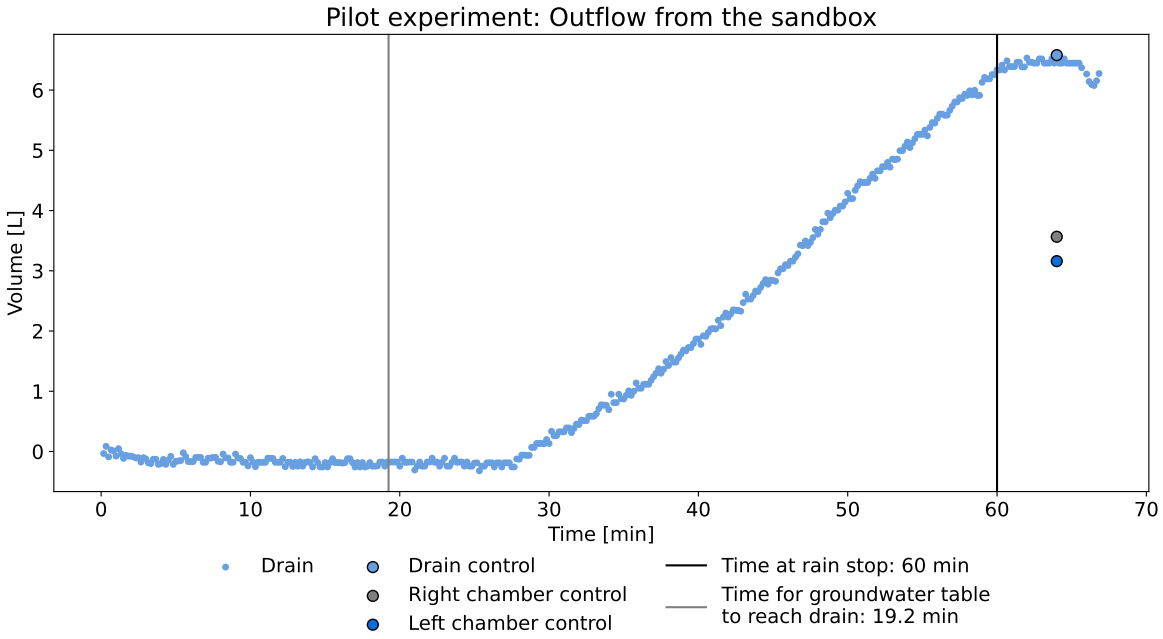

Figure 6.11: Cumulative outflow volume from the sandbox in the pilot experiment compared with the time for the groundwater to reach the drain pipe and the time at rain stop. Water level loggers for measuring the right and left outflows were not yet implemented.

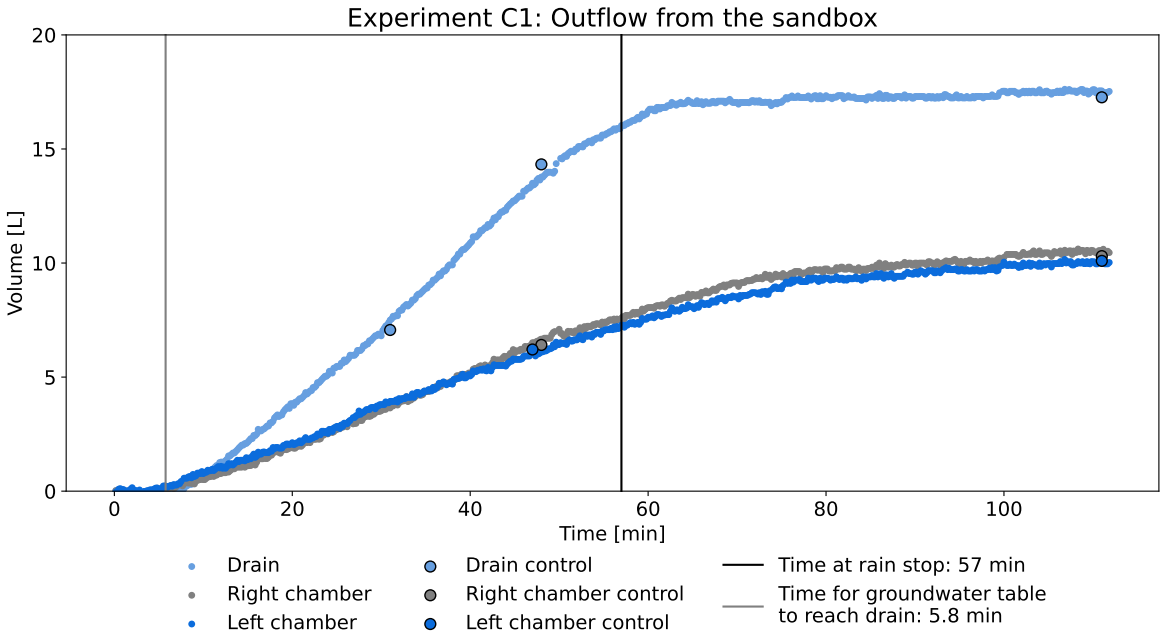

Figure 6.12: Cumulative outflow volumes from the sandbox in Cold experiment 1 (C1) compared with the time for the groundwater to reach the drain pipe and the time at rain stop.

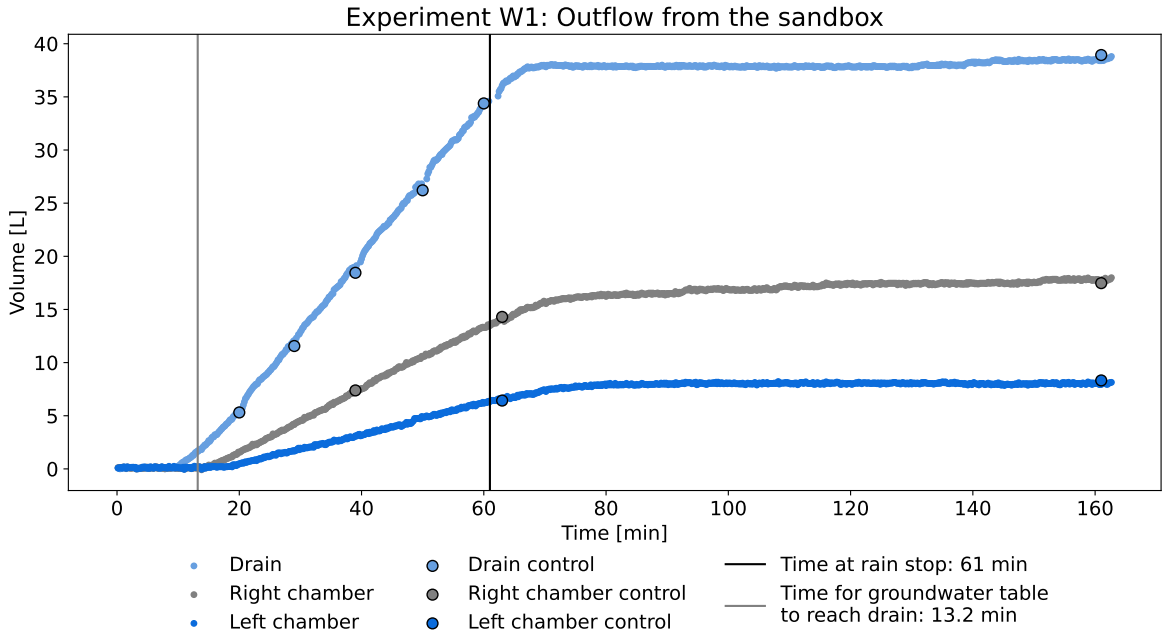

Figure 6.13: Cumulative outflow volumes from the sandbox in Warm experiment 1 (W1) compared with the time for the groundwater to reach the drain pipe and the time at rain stop.

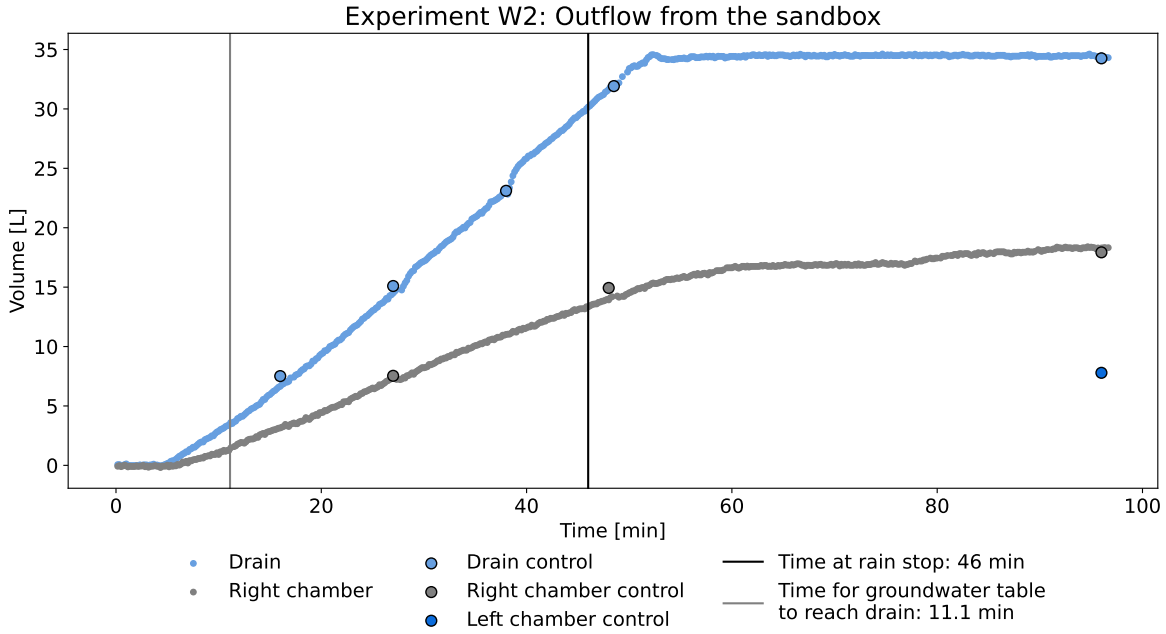

Figure 6.14: Cumulative outflow volumes from the sandbox in Warm experiment 2 (W2) compared with the time for the groundwater to reach the drain pipe and the time at rain stop. The water level logger of the left chamber failed.

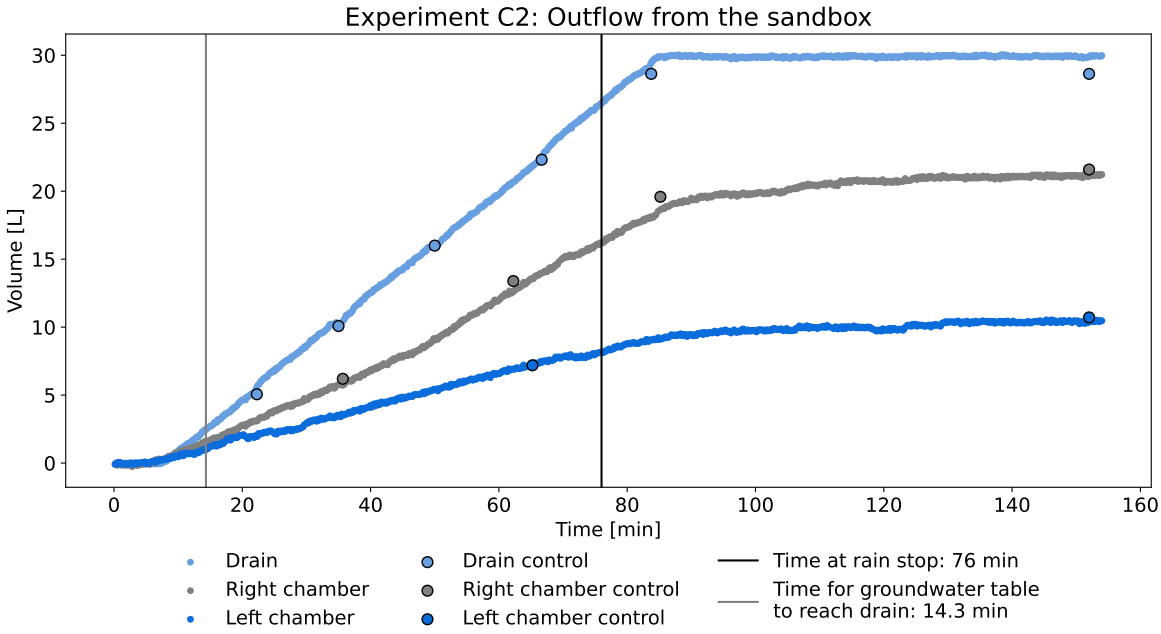

Figure 6.15: Cumulative outflow volumes from the sandbox in Cold experiment 2 (C2) compared with the time for the groundwater to reach the drain pipe and the time at rain stop.

6.4 Measurements of the water temperature in experiment W1 and W2 using the temperature spears

During experiment W1 and W2 the temperature spears described in section 5.2 on page 34 were deployed. Figure 6.16 compares the measured temperatures for each spear with their symmetrical counterpart. From the figure it can be observed that the largest increase in temperature was measured in the sensors closest to the surface. The change in temperature dwindled the deeper the sensors were placed, with the deepest sensors almost measuring no temperature change. Moreover, it can be observed that the spears on the right side of the sandbox generally show an increase in the temperature before the spears in the left side. This indicates that the water flow is greater to the right side of the sandbox. The measurements of spear 4 and spear 8 show an almost equal distribution of the water from the rain trays.

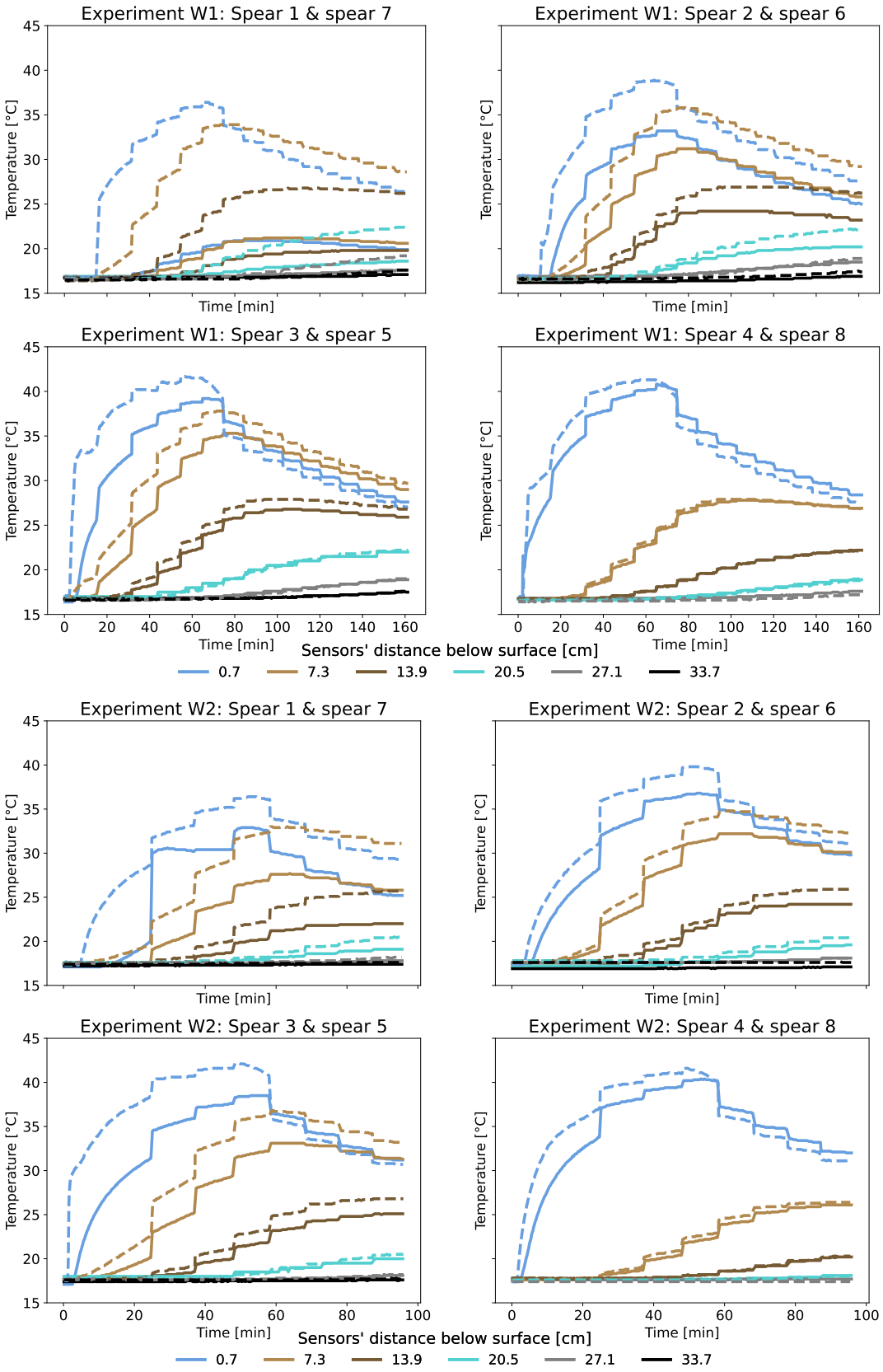

Figure 6.16: Temperature spear data measured in Warm experiment 1 (W1) and 2 (W2). The spears are plotted with their symmetrical counterpart with the exception of spear 4 and 8, see figure 6.1 on page 45 for placement of the spears. The spears placed in the right side of the sandbox (spear 5-7) and the control spear (spear 8) is plotted with dashed lines.

6.5 Measurements of the soil water content through out the sandbox - an indication of the capillary fringe

The results of the measurements of soil water content when excavating the sandbox after the experiments can be seen in figure 6.17. Here, the measurements show the water content in the sandbox being relatively homogeneous. Moreover, the figure shows 4 measurements taken from the top soil after the sandbox had dried for 30 and 42 days. Here, it can be observed that the water content in the surface was greater due the wetting of the sandbox from below before the excavation.

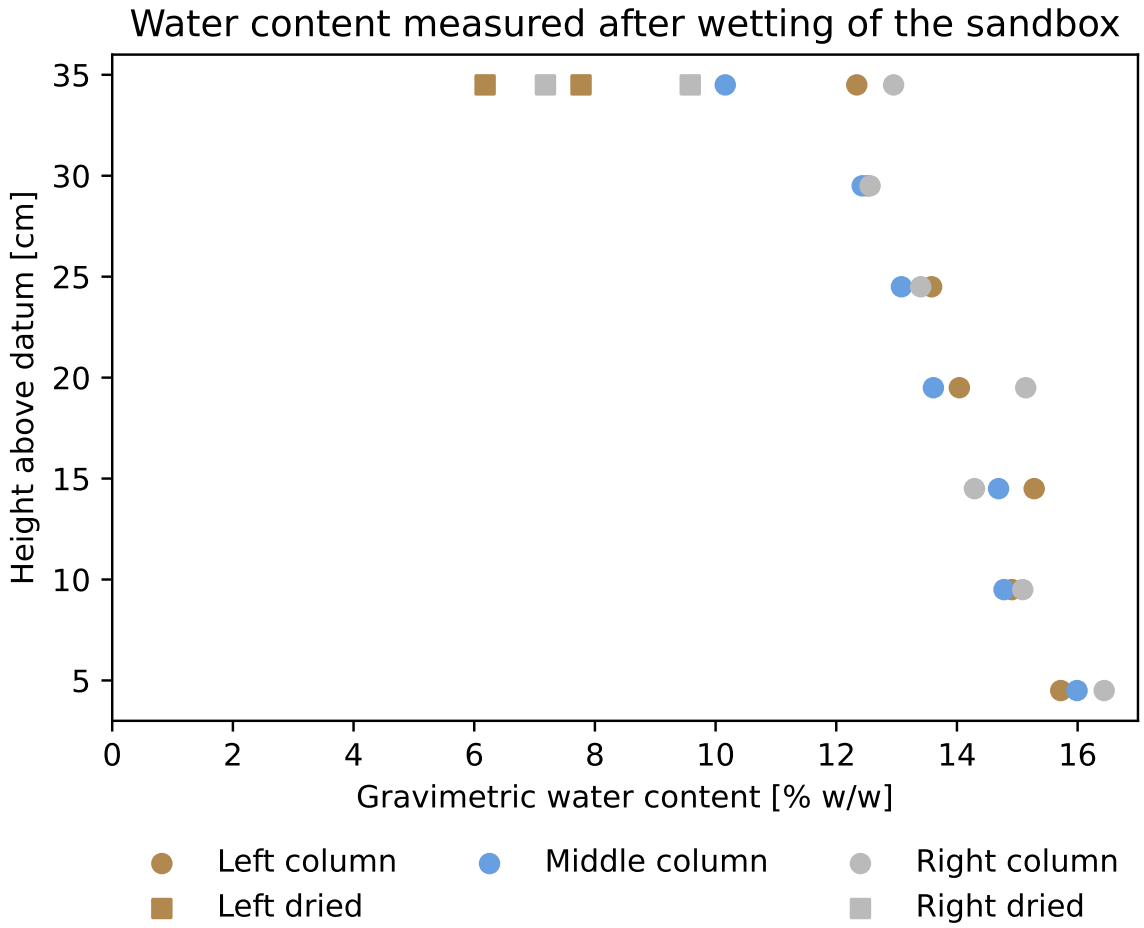

Figure 6.17: Water content sampled in three columns behind level meter 2 (left column), level meter 4 (middle column) and level meter 6 (right column). "Dried" refers to samples which were taken after the sandbox had dried for 30 and 42 days.

6.6 Noteworthy observations during the sandbox experiments

During the experiments observations were made of the sandbox, which might help explain some of the dynamics presented above. This section will present the most noteworthy of the observations.

6.6.1 Fractures appearing in the right side of the sandbox between the experiments

One of the noteworthy observations was the fractures appearing in the right side of the sandbox between the experiments. When the sandbox dried after experiment C1 a fracture appeared in the right side of the sandbox which was not visible before experiment P, see figures 6.18 and 6.19. This fracture disappeared during the experiments when water was added, but reappeared when the sandbox dried.

Figure 6.18: The right side of the sandbox before the pilot experiment seen from above. The corners had dried out.

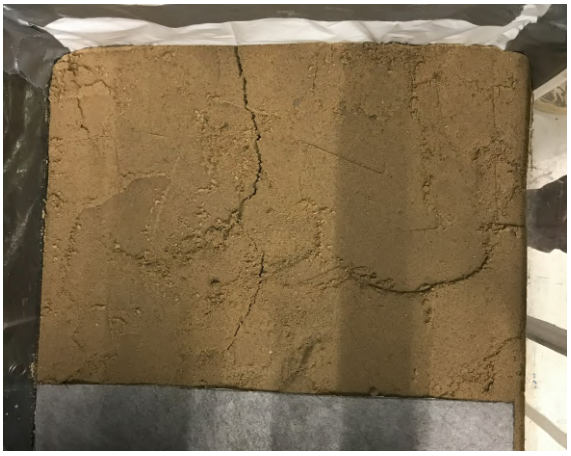

Figure 6.19: Fracture in the right side of the sandbox after Cold experiment 1 seen from above.

6.6.2 Reservoirs forming on the surface of the sandbox during experiments

Besides the fractures in the right side of the sandbox, there was also visible water on the surface of the soil during experiment W1, W2 and C2. During experiment W1 a small puddle of water formed in the right side, while a reservoir of several centimeters formed on the right side of the sandbox during experiment W2 and C2, see figures 6.20 and 6.21.

Figure 6.20: The right side of the sandbox during Warm experiment 2 seen from above. The entire surface is flooded in the right side.

Figure 6.21: The right side of the sandbox during Warm experiment 2 seen from the front. The entire surface is flooded in the right side.

Although a reservoir formed on the right side surface of the sandbox, the left side showed no signs of water added in all three experiments. When the rain was stopped the extent of the reservoir started from the left side of the cloth beneath the rain trays and ended at the right side of the sandbox. Moreover, the flow from the faucet needed to sustain a constant water level in the rain trays was visibly greater during both warm experiments compared to the previous cold experiments.

When the sandbox had dried after experiment W2 the soil beneath the reservoir had settled in the corner, as shown in figure 6.22. Here, marks from the water level of the reservoir also appears along with the fracture in the soil.

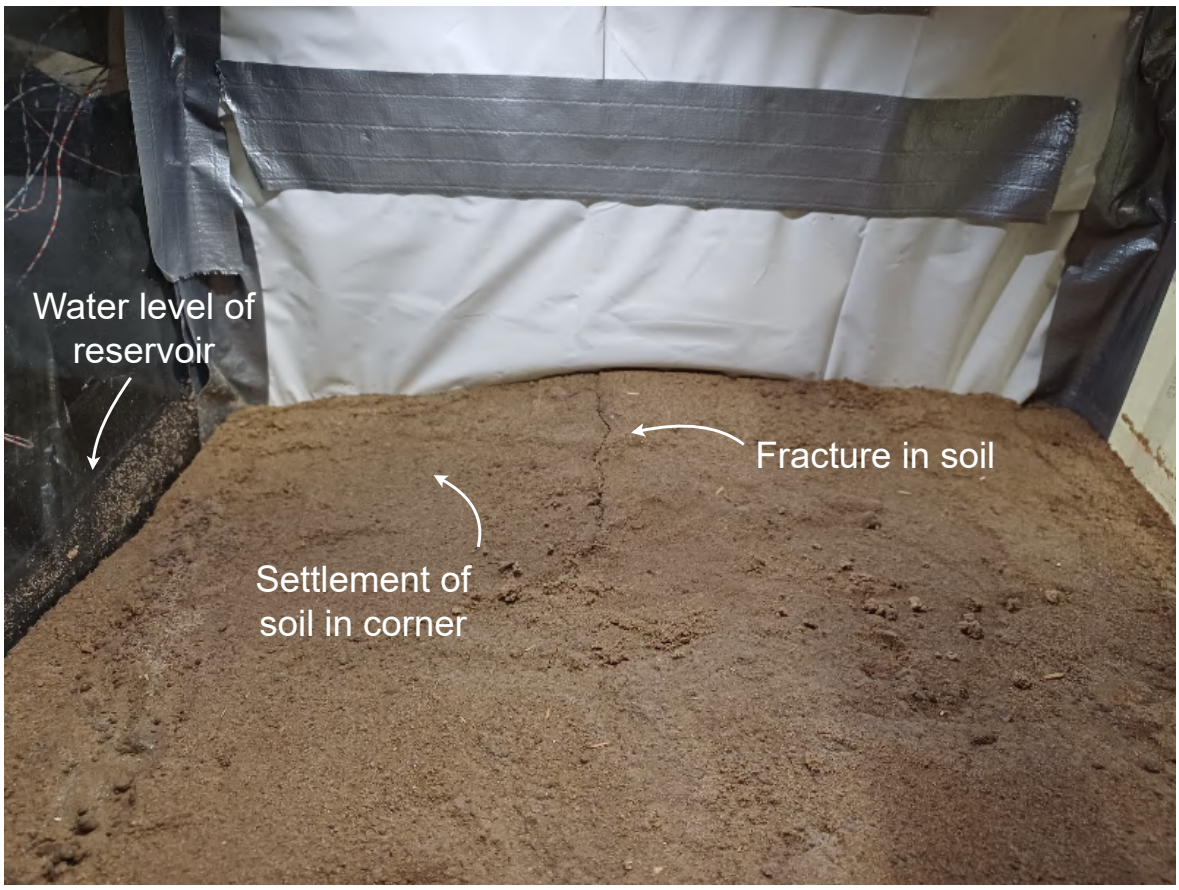

Figure 6.22: The right side of the sandbox after 2 weeks of drying after Warm experiment 2. The corner at the back settled between experiments and produced a fracture when dry.

6.6.3 Air bubbles and the formation of a macropore during experiment W2

Experiment W2 was the experiment with the largest extent of the reservoir on the surface. During this experiment, air bubbles were also observed in the middle of the sandbox at the surface, see figure 6.23. Additionally, a macropore formed beneath the surface around the bubbles. This pore collapsed shortly after the sandbox started draining.

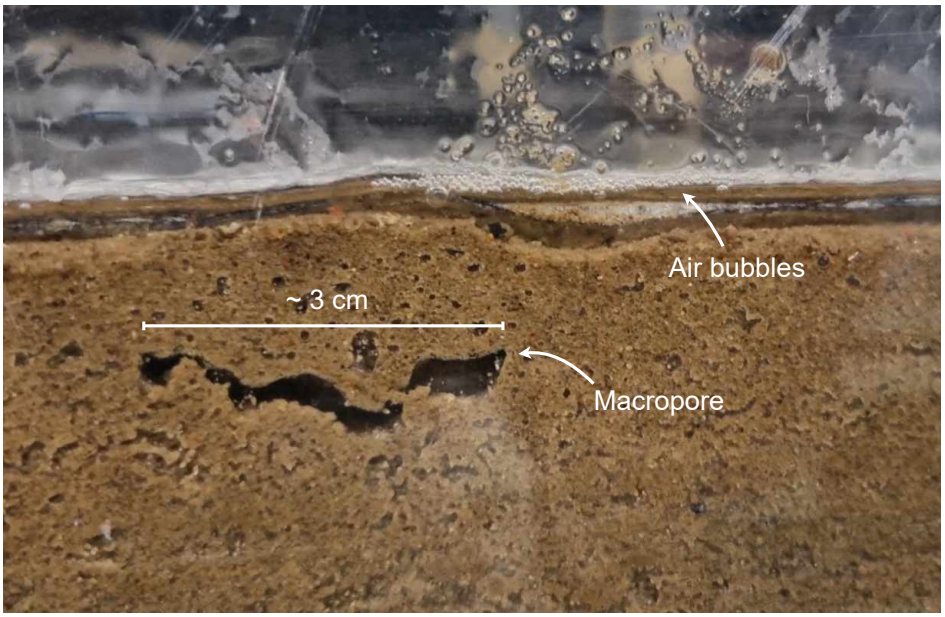

Figure 6.23: Bubbles and macropore forming in the middle of the sandbox during Warm experiment 2.

6.6.4 Discrepancies of measurements from the water level meters

In experiment C2, L5 measured a groundwater table several centimeters lower than the surrounding water level meters, see figure 6.24.

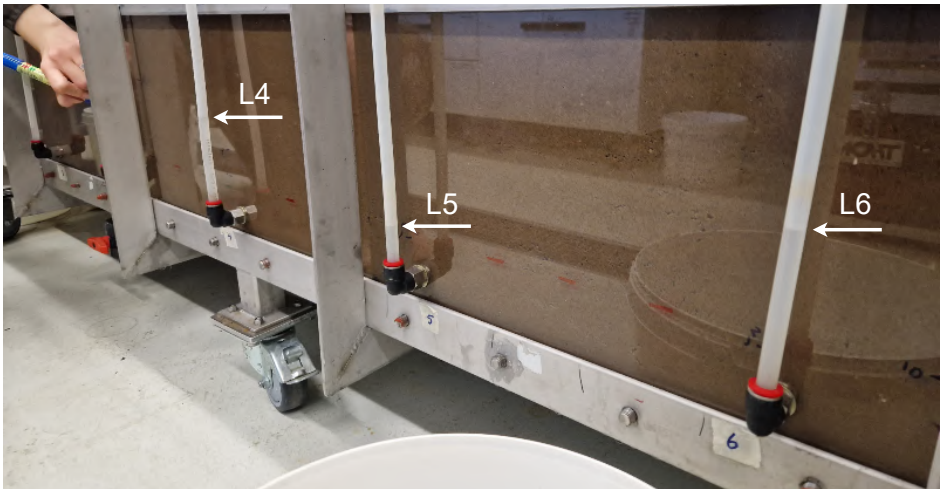

Figure 6.24: Example of L5 measuring lower water levels than the surrounding water level meters in Cold experiment 2. Water levels indicated by the tip of the arrows.

The water levels also underestimated the groundwater table during the excavation of the sandbox, where a water table formed behind L4. By comparing the water level meter to the water table it seems that it underestimated the water table level with 0.7 cm, see figure 6.25. The same tendency was observed in several level meters.

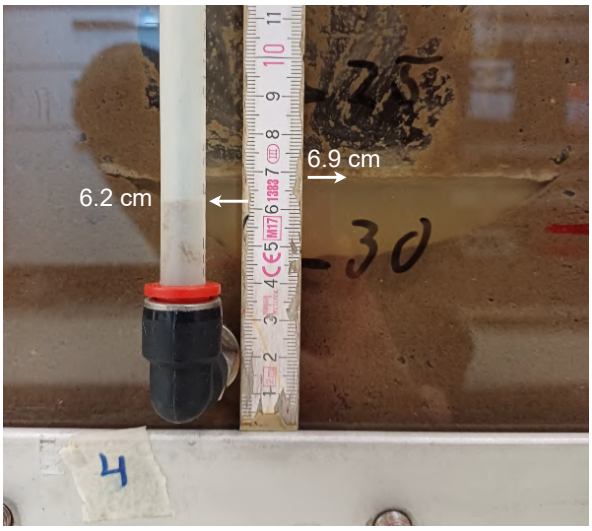

Figure 6.25: Discrepancy between water table visible from the sandbox and the measured water table in level meter 4. Water levels indicated by the tip of the arrows.

6.6.5 Soil particles in the water collected from the drain pipe

The buckets collecting the water from the drain pipe during the experiment clearly showed, that the water contained soil particles due to the yellow tint of the water, see figure 6.26. The water had a yellow tint in all the experiments.

Figure 6.26: Yellow tint of the collected water from the drain pipe during Warm experiment 1.

The observations presented above might help explain some of the dynamics observed during the sandbox experiments, for instance why the water infiltrated before the groundwater table reached the drainage area according to the level meters. This will be discussed in the next chapter.

7 | Discussion of the results from the sandbox experiments

The dynamics of the sandbox experiment presented in chapter 6 are discussed in this chapter. Here, the focus will be on answering the second question: *"How can a sandbox experiment be used to assess the hypothesis of water infiltrating from below and how can it be used to replicate disproportional groundwater rise?"*

7.1 Assessment of the increase, descend and extent of the groundwater table

It was evident from the experiment results that the velocity of the rise of the groundwater table depended on the soil water capacity and the initial water content. For instance, the experiment with the slowest groundwater increase was experiment P, since it did not retain any water from prior experiments. Moreover, experiment C1 was conducted the day after experiment P, hence the sandbox still retained water from the last experiment. This resulted in the soil water storage capacity being lower and the soil therefore reaching saturation more quickly. The dependence on soil water content was further supported by the descend velocity being similar across all experiments, with an average velocity of 1.23 ± 0.09 cm/min. This can be attributed to the pores being saturated at the time of rain stop and thus the descends across all the experiments started with the same initial water content.

Besides the decrease velocity being similar, the maximum extent of the groundwater was also similar across all experiments, despite being conducted with varying rain intensities. This might be explained by the extent of the groundwater table nearing an equilibrium between the added rain and the removed water from the drain and the horizontal movements. However, none of the experiments reached equilibrium, as evident from the continual increases in groundwater table. The experiment closest to reaching equilibrium was experiment C2, which is apparent from the ascending dynamics, as the maximum extent of the groundwater table around L4 did not increase substantially for at least 30 min. It can be theorised, that the small differences in rain intensity did not alter the shape of the maximum extent of the groundwater significantly, due to the increased horizontal distribution caused by larger gradients. Here, a wider distribution of the water increases the area in contact with the drain pipe and thus limits the vertical extent of the groundwater.

7.2 Evaluation of the hypothesis of water infiltrating from below and formation of a secondary groundwater table

As observed from the outflows during the experiments, the drain pipe constituted 41-59% of the total outflow volumes across all experiments. This is a large fraction, considering the hypothesis of water only infiltrating due to groundwater rising from beneath. Moreover, approximately 930 mL of water can be assumed stored inside the pipe due to the bend of the pipe. This storage is evident from the outflow volumes measured in experiment P, where the

groundwater reached the drain almost 10 minutes before drainage was observed. Moreover, since the minimum distances to the drainage area at time of infiltration were negative for both experiment P and C1, it is evident that there was storage of water inside the pipe, since the observed drainage was delayed. Still, this large fraction of water drained by the pipe questions the hypothesis of water only infiltrating from below. Especially since drainage by the pipe was observed before drainage from the chamber outlets in both experiment W1 and W2. This is further supported by the observed drainage in both experiment W1, W2 and C2 before any of the level meters showed a groundwater table reaching the drain pipe.

In experiments W1, W2 and C2 the minimum distance to the drain pipe from the groundwater table across the level meters at the time of infiltration was 4.9, 11.09 and 10.52 cm, respectively. One explanation supporting the hypothesis might be, that the level meters did not show the maximum height of the groundwater table and thus the infiltration happened between two of the level meters. This could be further supported by the observation during the excavation of the sandbox where the level meters did not accurately show the height of the groundwater. However, the error of the level meters was less than 1 cm, and thus the explanation would require a steep local peak between the level meters for all three experiments in order to reach the drainage area. Therefore, it seems more likely that the infiltration was caused by a formation of a secondary water table around the drain pipe due to water movement in preferential pathways, if the hypothesis of water infiltrating from below should remain.

7.2.1 Water movement in preferential pathways causing the formation of a secondary groundwater table around the drain pipe

A secondary water table formed in the right side of the sandbox during experiments W1, W2 and C2 as water was observed on the surface of the sandbox. Whether this secondary water table extended down to the drain pipe is uncertain, but might be supported by the velocities of the water due to the warm water and the fracture in the right side of the sandbox.

According to Phillips [2021], water selects the path of least resistance, resulting in preferential flow paths. These flow paths are typically associated with fractures. The theory of water moving in preferential pathways is supported by the changing dynamics between experiment C1 and W1, as the fracture in the right side of the sandbox occurred for the first time after experiment C1. Where the left and right outlet contributed with the same outflow volumes for experiment P and C1, the rest of the experiments showed a surplus of 9-10 liters in the right outlet volume compared to the left. This might be explained by faster water movement in the fracture in the right side of the sandbox which is further supported by the data from the temperature spears showing the flow of the surface water during experiment W1 and W2 favoring the right side. Therefore, it seems reasonable to assume there was an increased water flow in the right side of the sandbox during experiment W1, W2 and C2 due to preferential pathways. This increased flow to the right side of the sandbox also caused ponding of water, which increased the load on the soil. As observed after experiment W2, the corner at the back of the right side of the sandbox had settled substantially, which might be an effect caused by the ponding water.

The reservoirs forming on the surface of the right side of the sandbox might have worsened the conditions of the right side due to the existing fracture and thus enhanced the water movement in the preferential pathways. For instance, during experiment C2, which was the

last experiment, a rapid groundwater rise was observed in the right side of the sandbox where the fracture was located and water infiltrated before the groundwater table reached the pipe. From the level meter data it can be assumed that the initial infiltration happened at L6, which was located near the fracture, as this was the level meter with the groundwater level closest to the drainage area at the time of infiltration. Therefore, it could be theorised that the secondary water table extended from the surface to the drain pipe during experiment C2 due to the fast velocity of water in preferential pathways. This increased velocity of the water might have affected the pore pressure around the drain pipe. As the movement of water from an area is limited by the slowest velocity, the mass balance would result in storage of water in the pores, due to a higher velocity of water entering the pores than exiting the pores. This could have been further enhanced in the experiments with the warm water due to an interface between the warm rain (44 °C) and cold pore water (17 °C), as the warm water has a higher velocity.

In addition to possible storage of water in the pores, observations made during experiment W2 also showed air bubbles in the ponded water on the surface and the formation of a macropore in the center of the sandbox. This indicates that some of the same dynamics of the Lisse effect occurred, where air is compressed during intense rain. This is further supported by the collapse of the macropore at the end of the experiment, as it was likely composed of compressed air, which decompressed when the surface was no longer sealed by water. Therefore, due to the velocity of the water, it could be theorised that the larger pores filled slower than the small pores, thus entrapping and compressing air and saturating the pores around the drain pipe, thus creating a secondary water table which would allow infiltration.

To summarize the answer to the first part of the question; the results from the sandbox experiments showed infiltration into the pipe before the groundwater in the level meters reached the pipe in three out of five experiments. Therefore, the hypothesis of water only infiltrating from below due to an increase in groundwater table cannot be unequivocally confirmed. However, the hypothesis cannot be rejected either, as observations from the experiments indicate the formation of a secondary water table around the pipe, which would confirm the hypothesis, though it cannot be validated with the current observations.

7.3 Assessment of whether the observed groundwater rise in the sandbox was disproportionate

This section answers the second part of the question which revolves around replicating disproportional rise in the sandbox experiments. Disproportionate rise in groundwater table is often observed in shallow groundwater tables due to either the Lisse effect or the reverse Wieringermeer effect, as reported by Novakowski and Gillham [1988], Khaled et al. [2011], and Zheng, liu, and Yang [2022] among others. Here, the RWE is associated with a truncated capillary fringe.

Whether the capillary fringe was truncated in the sandbox was assessed by using the Young-Laplace equation (see equation 4.1 in section 4.1.1 on page 20) where the capillary radius was assumed to be 15% of the D_{50} particle diameter [ESSG-AAU 2022]. Here, the theoretical capillary rise was estimated at 42 cm, which would result in the capillary fringe being truncated in the sandbox as the height of the soil above the groundwater table in the sandbox was

around 30 cm. To further support this, measurements of volumetric water content in the sandbox during the excavation were conducted. However, the sampling method resulted in only the water content in the small pores being measured, as the large pores collapsed during sampling. As a consequence the measured water content was not the actual water content of the soil matrix and thus the extent of the capillary fringe could not be accurately determined based on the measurements. Nonetheless, the measurements showed an increase in volumetric water content in the surface of the sandbox during wetting, which implies capillary action in the surface of the sandbox and thus the capillary fringe might have been truncated. However, whether the capillary fringe was truncated might be questioned by comparing the volumetric water content with measurements conducted by Novakowski and Gillham [1988]. Here, Novakowski and Gillham [1988] measured the volumetric water content to a depth of almost 70 cm from the surface in a swampy area with medium to fine grained sand and shallow groundwater table. A decrease in water content when nearing the surface was observed similar to what was observed in the sandbox. However, this was for a location where the capillary fringe was not truncated. Furthermore, according to Novakowski and Gillham [1988] a truncated capillary fringe is characterised by the surface soil being saturated, which was not the case in the sandbox.

The effect of a truncated capillary fringe was observed in Novakowski and Gillham [1988] where the response when applying simulated rainfall was measured. The experiment was conducted on a location with and without a truncated capillary fringe, resulting in a increase of 25 mm/mm and 6.7 mm/mm, respectively. Moreover, Khaled et al. [2011] measured increases of 50 mm/mm and 100 mm/mm for a light clay and sand, respectively, caused by the reverse Wieringermeer effect. For comparison, the increase observed in the sandbox across the experiments based on a maximum and minimum rain depth varied from 3 mm/mm to 17.3 mm/mm. This is a much smaller response than observed in Khaled et al. [2011] and around the response measured by Novakowski and Gillham [1988] for both a capillary fringe with and without truncation. However, due to the experimental setup of the sandbox, some of the water did not contribute to an increase in groundwater table but instead moved horizontally. This was due to both the water being added only in the center of the sandbox and the open boundaries at the chambers. Therefore, the increase in groundwater compared to rain cannot be directly compared to Novakowski and Gillham [1988] and Khaled et al. [2011] where the rain was added over the entire area. Moreover, the question of whether a disproportionate rise was observed in the sandbox greatly depends on the area the rain infiltrated over and thus the rain depth, which makes the exact value of the expected increase difficult to determine. This might also help explain the differences in increase measured in the sandbox experiment and by Khaled et al. [2011] who conducted the experiment in a 50 cm soil column with a diameter of 7.5 cm and thus limited horizontal flow. As a consequence a disproportional rise in groundwater table might not be easily measured in the sandbox due to the experiment setup and boundaries.

Despite the uncertainty of the groundwater rise due to the experimental setup, a comparison with specific yield does imply that a disproportionate rise occurred due to the reverse Wieringermeer effect. This was observed for experiment C1 for both the minimum and maximum area used for calculating rain depth. Moreover, as the increase for experiment W1, W2 and C2 lied within the expected increase based on specific yield, it could be argued that the increase would have been disproportionate if all the water added had contributed to an increase instead of allowing outflow from the chambers and drain pipe. This exemplifies that the

expected increase cannot be calculated from the specific yield alone due to the aforementioned removal of water and the horizontal movements.

7.4 Evaluation of the homogeneity of the sandbox

In addition to giving an indication of the capillary fringe, the measurements of volumetric water content in the sandbox during the excavation implied a high degree of homogeneity of the water content through out the sandbox. This is in contrast to the measurements of the top soil taken before each experiment. Due to the rise patterns observed in the experiments it can be deduced that the sandbox was not entirely homogeneous. However, based on the measurements done during the excavation it was evaluated that the sandbox was sufficiently homogeneous to be modelled as such.

7.5 Summation of the sandbox experiment

This part of the Master's thesis set out to answer the second question; *"How can a sandbox experiment be used to assess the hypothesis of water infiltrating from below and how can it be used to replicate disproportional groundwater rise?"*

The hypothesis of water infiltrating from below was assessed by comparing water level meter data to pipe outflow data. However, the hypothesis could neither be confirmed nor rejected definitively by the sandbox experiments since outflow was observed prior to groundwater reaching the drainage area in three out of five experiments. Moreover, due to the open boundaries and horizontal flows the setup of the sandbox was not advantageous for measuring a disproportional groundwater rise. Here, limiting the horizontal flow would result in a larger fraction of water contributing to groundwater rise and thus remove one of the main uncertainties in the measurement of disproportional groundwater rise. Another improvement would be applying rain over the entirety of the sandbox to decrease the uncertainty of the rain depth. Still, experiment C1 showed a disproportionate rise despite the experiment setup, which might be caused by the larger initial water content in the pores creating the conditions for the reverse Wieringermeer effect. This illustrates the importance of including the effect of the capillary fringe in groundwater models as the capillary fringe alters the available storage in the pores.

Though the sandbox experiment lacked improvements for analysing disproportional groundwater rise or to asses the hypothesis, its data was useful for calibrating a numerical model of water flow and groundwater rise in unsaturated soil. The numerical model is explained in the following part of the Master's thesis.

Part III :

Investigating disproportional groundwater rise and infiltration through numerical modelling of sandbox experiments

8 | Hydraulic properties of the soil used for the sandbox experiments and numerical models

In order to model the dynamics of the groundwater as presented in chapter 6 and 7 the St. Restrup sand used in the sandbox was analyzed. Here, the hydraulic properties were determined in order to implement them in the models. This was done in order to answer the third question; *"Utilizing experimental results, how can a 1D and 2D numerical model of water flow and groundwater rise in unsaturated soil be employed to model the dynamics of the sandbox experiments?"*. The question is investigated in chapters 8 through 12.

The numerical models presented in chapter 9 and 10 requires four soil parameters in order to run. The parameters and their method of determination is presented in table 8.1.

Soil parameter		**Determined from**
Sat. vol. water content (θ_{sat})	[cm^3 H_2O/cm^3 soil]	Total porosity of intact sample
Campbell b (b)	[-]	Sorptivity, water content at given suctions
Air entry suction (ψ_e)	[cm H_2O]	Soil column experiment
Sat. hydraulic conductivity (K_{sat})	[cm/min]	Darcy experiment

Table 8.1: Soil parameters needed for the Mean Moving Slope (MMS) model and which methods they were determined with.

The soil parameters shown in table 8.1 were all calculated by Hedevang and Sørensen [2023] based on experiments they conducted. However, some of the values for the soil parameters were recalculated in this Master's thesis as presented in this chapter where it is relevant.

8.1 Determination of water content at different soil water potentials

The soil water retention curve of the soil used in the sandbox experiments was determined with a combination of recalculated values and values directly adopted from Hedevang and Sørensen [2023], namely the values at pF 6, 4.2 and 0. The water content at pF 4.2 (wilting point) was 0.0180 cm^3 H_2O/cm^3 soil and was calculated by Hedevang and Sørensen [2023] based on the fraction of clay from the sieving analysis and organic matter content from ignition loss. Furthermore, Hedevang and Sørensen [2023] also measured the water content at pF 6 (air dry) to be 0.00283 cm^3 H_2O/cm^3 soil, while the soil water content at pF 2 (field capacity) was determined from a suction box experiment. The suction box experiment was conducted by Hedevang and Sørensen [2023] on wetted intact samples at intervals from 105-794 cm H_2O suction (pF 2.02-2.90). Here, the values from Hedevang and Sørensen [2023] seemed low compared to the expected values for a coarse sand. Thus, water content at pF 2 was recalculated based on values measured by student from Aalborg university attending the course

EHC-AAU [2023], see figure 8.1.

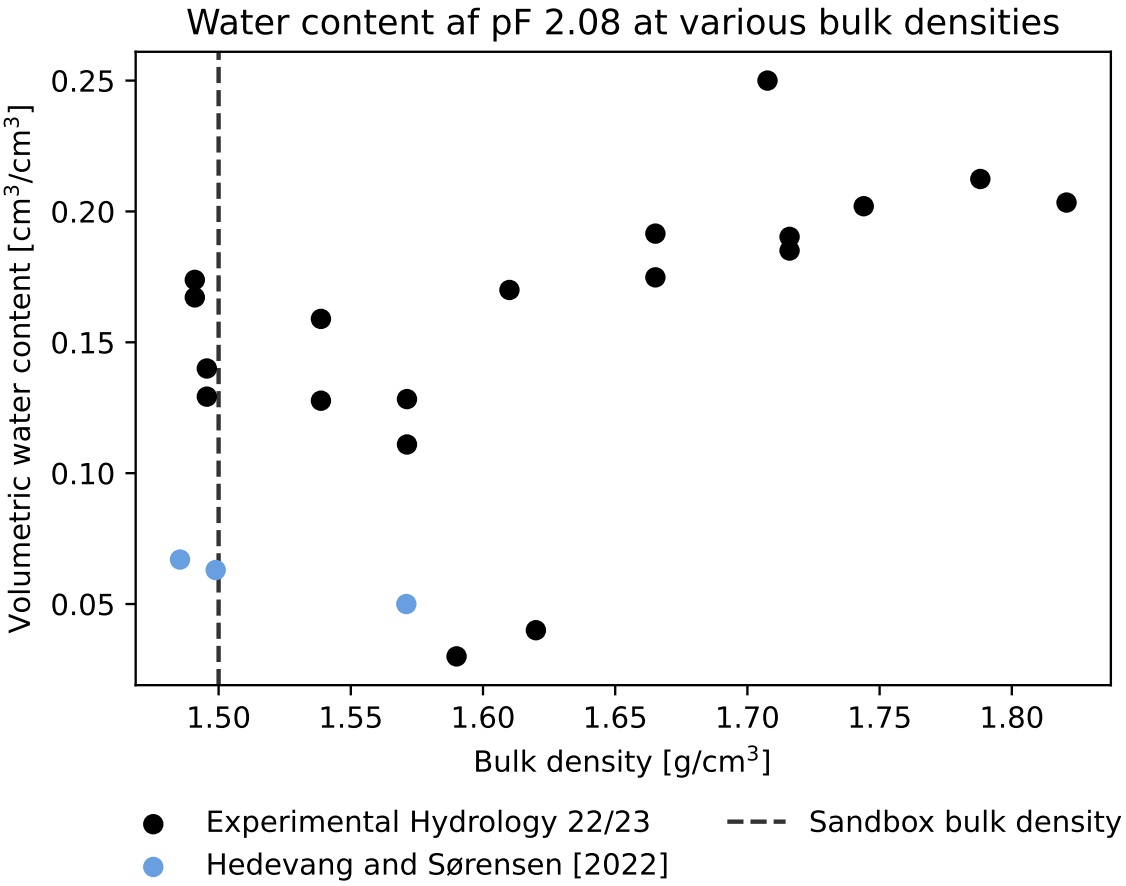

Figure 8.1: Data of water content at -119 cm suction (pF 2.08) gathered from suction box experiments conducted by student from Aalborg university attending the course EHC-AAU [2023] from 2022 and 2023 compared with data from Hedevang and Sørensen [2023].

From figure 8.1 the data from Hedevang and Sørensen [2023] seems like outliers, even though two measurements from EHC-AAU [2023] measured similar values. Nonetheless, the water content around pF 2 from Hedevang and Sørensen [2023] was discarded and instead a mean of the four values around a bulk density of 1.50 g/cm^3 was used. Thus, the water content at pF 2.08 used to fit the water retention curve was 0.1526 cm^3 H_2O/cm^3 soil.

Lastly, Hedevang and Sørensen [2023] determined the air entry suction at -2.19 cm H_2O. However, this value resulted in negligible velocities of water at low volumetric water contents in the MMS-model. Therefore, a new value of -16 cm H_2O was chosen based on capillary rise column experiments from Hedevang and Sørensen [2023], as the air entry suction can be assumed equivalent to the height of the capillary fringe in some soils [Pojmark 2011]. This also corresponds better with the average value for sand of 12.1 $\pm$ 14.3 from Loll and Moldrup [2000]. An overview of the values used in the soil water retention curve is shown in table 8.2.

pF	**Water content** [cm^3 H_2O/cm^3 **soil]**	**Based on**
6.9	0	-
6	0.00283	Air dried sample
4.2	0.0180	Organic matter and clay fraction
2.08	0.153	Suction box
1.20	0.434	Soil column experiment
0	0.434	Total porosity of intact sample

Table 8.2: Volumetric water content at given suctions and sources of the data. The volumetric water content at pF 6, 4.2 and 0 was directly adopted from Hedevang and Sørensen [2023] while the values at pF 2.08 and 1.20 were recalculated.

Based on the volumetric water contents presented above, the soil water retention curve was fitted with the Campbell model in equation (8.1), which was used used from air entry suction to pF 4.2. Linear relationships were assumed between the points from pF 4.2-6.9 [Loll and Moldrup 2000].

$$\theta = \theta_{sat} \cdot \left(\frac{\psi_e}{\psi}\right)^{\frac{1}{b}} \tag{8.1}$$

Where:

θ	Volumetric water content [cm^3 H_2O/cm^3 soil]
θ_s	Volumetric water content at saturation [cm^3 H_2O/cm^3 soil]
ψ_e	Suction at air entry [cm H_2O]
ψ	Suction [cm H_2O]
b	Campbell b [-]

In order to use equation (8.1) a Campbell b value based on experimental data was found.

8.2 Determination of Campbell b based on experimental data

The sorptivity of the St. Restrup sand was found in order to calculate a Campbell b value, where sorptivity can be determined from horizontal infiltration due to capillary forces, see equation (8.2) [Minasny and Cook 2011].

$$S = \frac{I_{acc}}{\sqrt{t}} \tag{8.2}$$

Where:

S	Sorptivity [$cm/\sqrt{min}$]
I_{acc}	Accumulated infiltration [cm]
t	Time [min]

Based on equation (8.2) the accumulated infiltration was estimated from a timelapse of the capillary rise taken in a corner during initial wetting of the sandbox. Here, the distance traveled

by the water front was found by converting the horizontal infiltration distance measured in the video to the real distance in the sandbox. This was done by finding the scale betweeen the distances. Then, the distance in each frame was converted to a real distance and the time elapsed converted to real time, as each frame in the video corresponded to 6 seconds. A schematic of how the distances were measured is shown in figures 8.2 and 8.3.

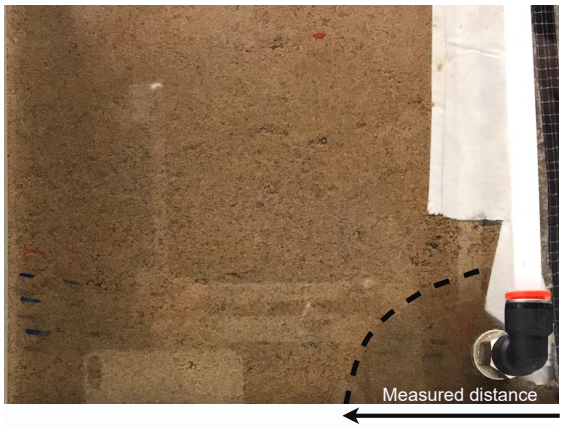

Figure 8.2: Sketch of how the infiltration distance was measured.

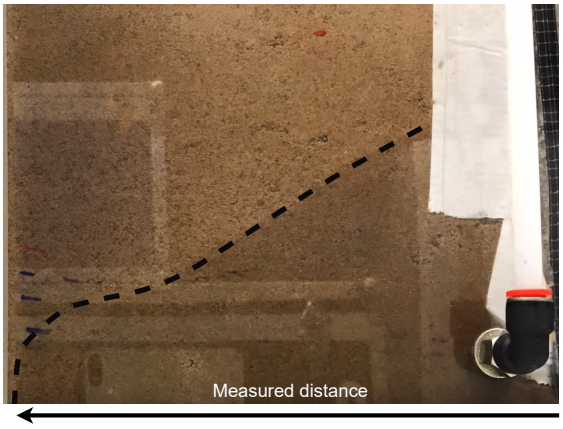

Figure 8.3: Sketch of how the infiltration distance was measured.

The infiltration distance was measured at 14 frames in the timelapse, where the infiltrated distance was easily converted to real distance based on distinguishable features in the frame. Then, the infiltration distance was converted to accumulated infiltration with equations (8.3) and (8.4). Here, the initial volumetric water content during packing of the sandbox of approximately 0.068 cm^3 H_2O/cm^3 soil was used.

$$I_{acc} = I \cdot \phi_{initial} \tag{8.3}$$

$$\phi_{initial} = \theta_{sat} - \theta_{initial} \tag{8.4}$$

Where:

I	Infiltration distance from timelapse [cm]
ϕ_{initial}	Initial air content [cm^3 H_2O/cm^3 soil]
θ_{initial}	Initial volumetric water content [cm^3 H_2O/cm^3 soil]

The calculated infiltration distances were plotted in figure 8.4, where the sorptivity is the slope of 6.733 $cm/\sqrt{min}$.

Campbell b was then determined from the sorptivity by using the following equation (8.5) from Petkov [2021]:

$$b = \frac{5.12}{\sqrt{S}} \tag{8.5}$$

This resulted in a Campbell b of 1.97.

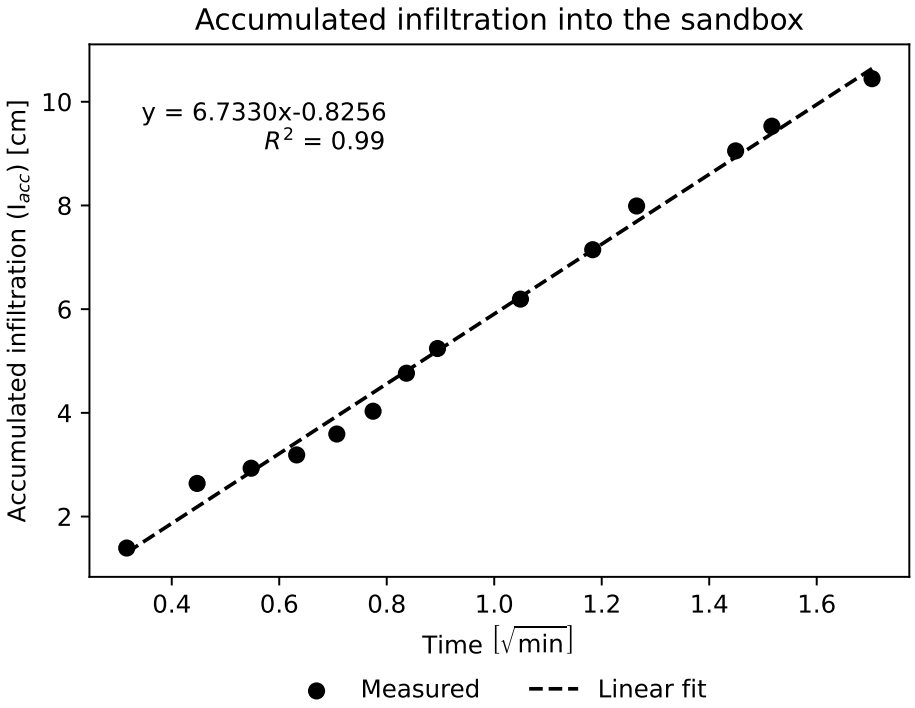

Figure 8.4: Linear fit of the accumulated infiltration into the corner of the sandbox based on the 14 frames of the timelapse. The slope corresponds to the sorptivity of the soil.

According to Loll and Moldrup [2000] the Campbell b value can also be found as the numerical value of the slope when plotting the suction against the logarithmic to the volumetric water content as seen in figure 8.5. Here, the values from table 8.2 for pF 1.2, 2.08 and 4.2 are used.

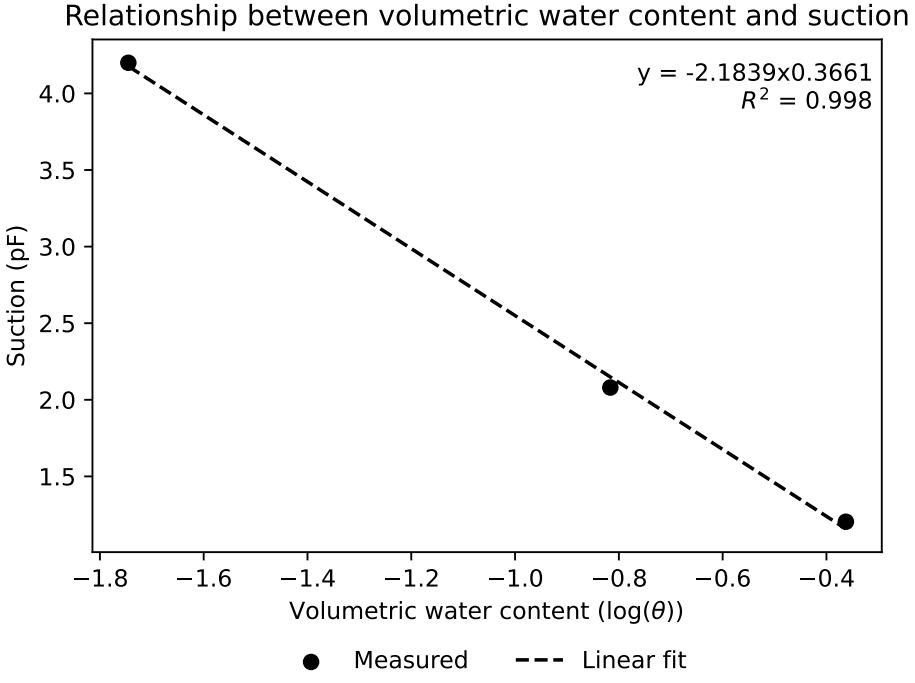

Figure 8.5: Determination of Campbell b as the numerical value of the slope of the suction against the logarithmic volumetric water content (θ).

As seen in figure 8.5 the Campbell b value based on the measured data is determined to be 2.18 with an R^2 value of 0.998.

The calculated Campbell b values of 1.97 and 2.18 are both close to the value of 2.28 as used by Hedevang and Sørensen [2023] who fitted the soil water retention curve using the Van Genuchten model as described in Loll and Moldrup [2000]. These values were used as guidelines when the soil water retention curve was fitted with equation (8.1), which was applied in the interval between air entry suction and pF 4.2. Here, Campbell b was varied until an agreeable fit was found with the known volumetric water content at different suctions. This resulted in a Campbell b of 2.1. The resulting soil water retention curve can be seen in figure 8.6. The corresponding water content at pF 2 based on the Campbell curve was 0.181 cm^3 H_2O/cm^3 soil.

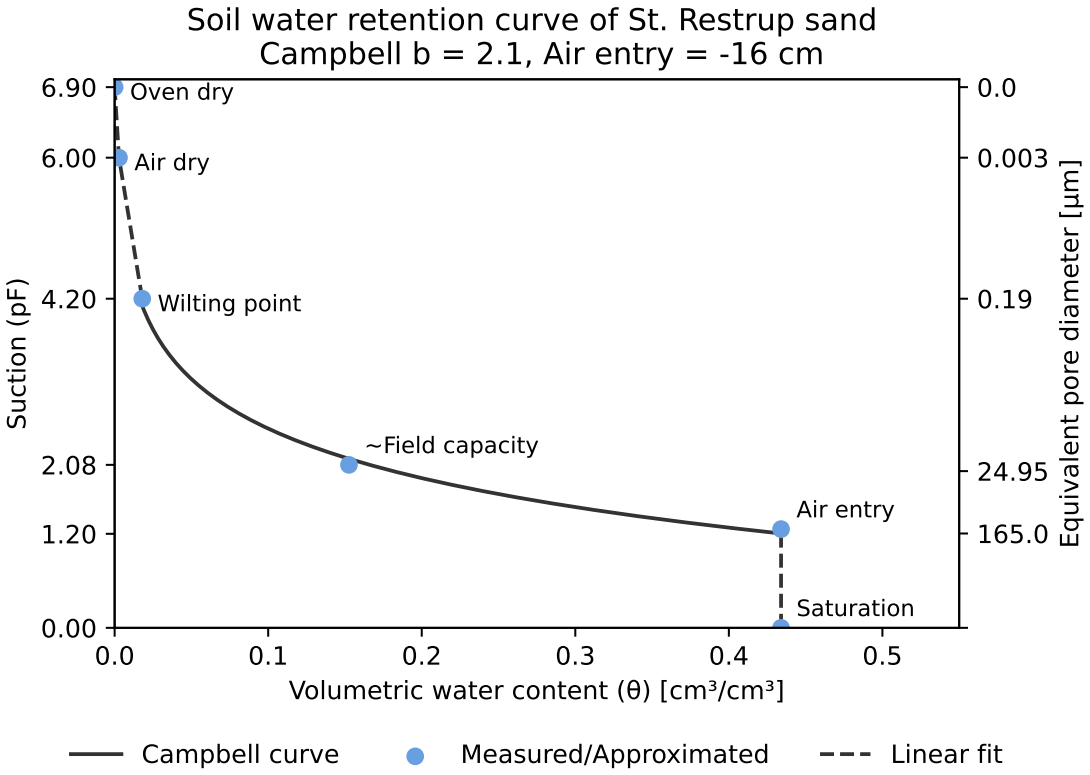

Figure 8.6: Soil water retention curve of sand from St. Restrup Fælled. Campbell curve is fitted to data points which are based on measured soil properties.

According to Clapp and Hornberger [1978] the average Campbell b value for sand is 4.05 ± 1.78, which agrees well with the found Campbell b. A comparison of the St. Restrup sand with 1446 soils categorized within 11 different textures from Clapp and Hornberger [1978] is shown in figure 8.7. Here, sorptivities for the St. Restrup sand are calculated for the Campbell b values of 2.28, 2.18 and 2.1 using equation (8.5).

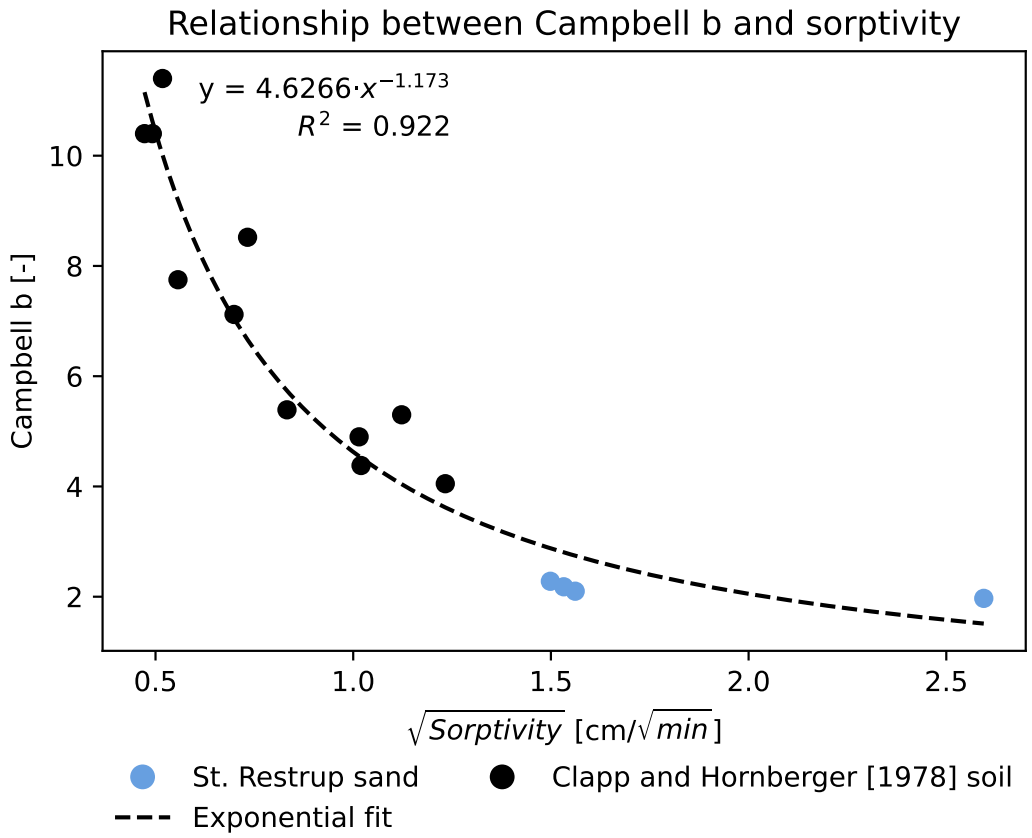

Figure 8.7: Comparison of sorptivity and Campbell b for the St. Restrup sand with average values for 11 differently textured soils from Clapp and Hornberger [1978].

Figure 8.7 shows that the estimated Campbell b and sorptivity agrees well with representative values of the different soil types. Moreover, typical values of Campbell b for a coarse textured sandy soil lie in the range 1-5 [Loll and Moldrup 2000]. As the St. Restrup sand used was classified as a coarse sand (ISSS standard) a Campbell b of 2.1 was used in the initial calibration of the MMS-model as this yielded reasonable results through the testing of the model. Furthermore, this Campbell b value was used for creating the hydraulic conductivity curves for different soil water potentials and volumetric water contents.

8.3 Hydraulic conductivity dependant on soil water potential and volumetric water content

Campbell curves between the hydraulic conductivity at different volumetric water contents and soil water potentials were found using the Campbell b from the soil water retention curve in combination with equations 8.6 and 8.7 [Loll and Moldrup 2000].

$$K(\theta) = K_{sat} \cdot \left(\frac{\theta}{\theta_{sat}}\right)^{2b+3} \qquad (8.6)$$

$$K(\psi) = K_{sat} \cdot \left(\frac{\psi_e}{\psi}\right)^{2+3/b} \qquad (8.7)$$

Where:

K	Hydraulic conductivity [cm/min]

Equations (8.6) and (8.7) were used to produce figures 8.8 and 8.9, which should be considered approximations of the real hydraulic conductivity at different water contents and soil water potentials. The parameters used in the equations are summarized in table 8.3 on page 77. From figure 8.8 it is seen, that the hydraulic conductivity decreases more rapidly after the volumetric water content moves below field capacity at 0.18 cm^3 H_2O/cm^3 soil. This is expected as lowering the volumetric water content decreases the connectedness of the soil pores, making the path of water more tortuous and increasing the friction. Therefore, the hydraulic conductivity is greatest at saturation [Nimmo 2005]. The hydraulic conductivity at saturation for the St. Restrup sand is 0.33 cm/min and was determined by Darcy experiments conducted on intact samples by Hedevang and Sørensen [2023].

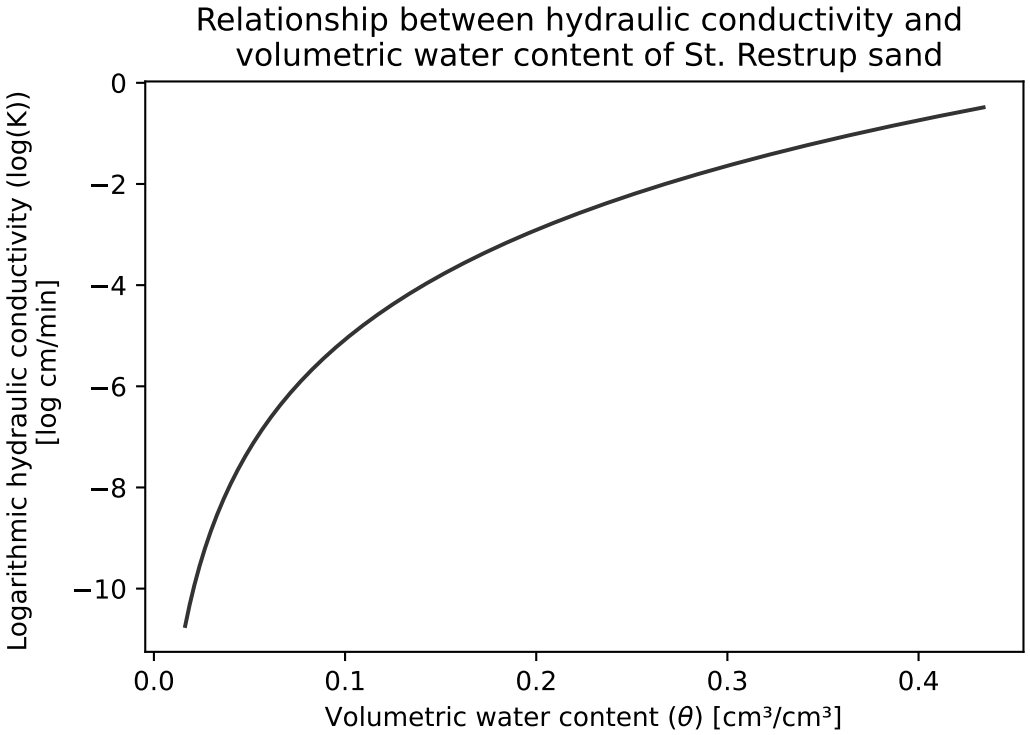

Figure 8.8: Relationship between hydraulic conductivity and volumetric water content for the St. Restrup sand. Based on equation (8.6).

The water content in the pores is influenced by the matric pressure, why the hydraulic conductivity is also affected by soil pressure through its effect on water content [Nimmo 2005], see figure 8.9. In addition, hydraulic conductivity is affected by temperature due to changes in viscosity, along with biological or chemical activity in the soil [Nimmo 2005].

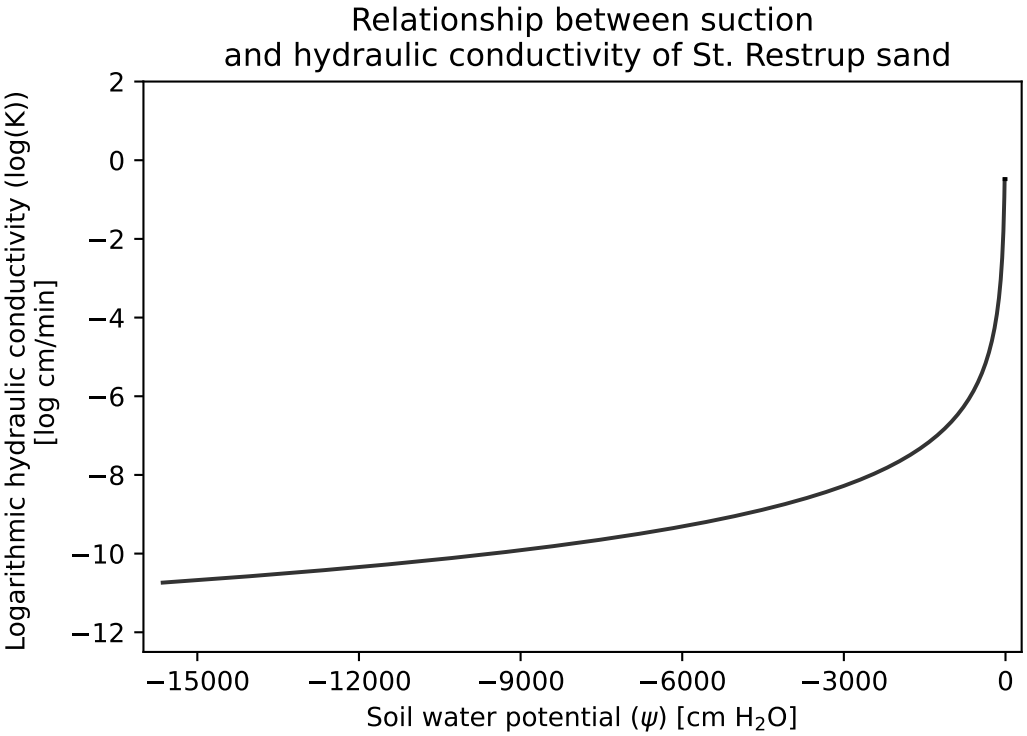

Figure 8.9: Relationship between suction and hydraulic conductivity of the St. Restrup sand. Based on equation (8.7).

8.4 Infiltration velocity due to capillary absorption

Though the saturated hydraulic conductivity is an expression of the maximum conductivity of the soil, the velocity of the water can far exceed the hydraulic conductivity due to pressure gradients. This is the case when water infiltrates into an initially dry soil where large pressure gradients occur [Guymon 1994]. The infiltration velocity into the soil during wetting of the sandbox was found with equation (8.8) from Petkov [2021]:

$$V = \frac{S \cdot \sqrt{t} - I_{acc}}{t} \tag{8.8}$$

Where:

V | Infiltration velocity [cm/min]

Here, calculation of the accumulated infiltration and sorptivity was repeated with the same method as described in section 8.2, except that the infiltrated distance was based on infiltration in a 45° angle instead and measured from 13 new frames from the timelapse.

According to Petkov [2021] the transmissivity can be assumed equal to the saturated hydraulic conductivity over longer timesframes. As shown in figure 8.10 the infiltration velocity almost reached the saturated hydraulic conductivity at 0.33 cm/min.

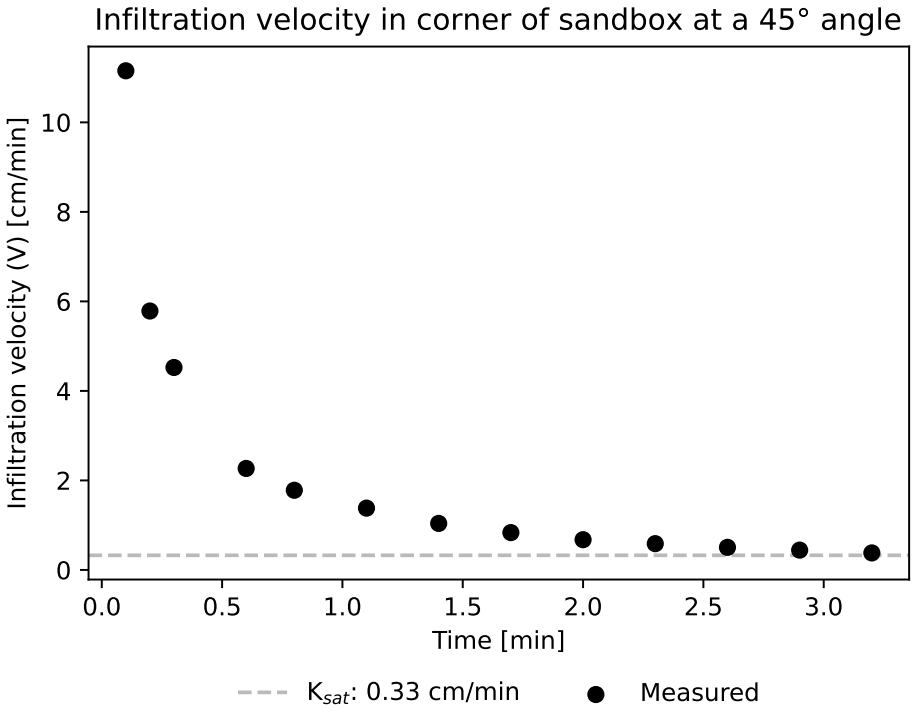

Figure 8.10: Velocity of infiltration in a 45° angle into the corner of the sandbox based on the 13 frames from the timelapse. K_{sat} = saturated hydraulic conductivity.

Figure 8.10 corresponds well to the expected decrease in velocity due to a decreased suction gradient as the soil was wetted [Guymon 1994]. It was expected that the infiltration velocity would stagnate at the saturated hydraulic conductivity, however the video only covered a small corner of the sandbox where a steady infiltration was not fully established. Moreover, the decrease in infiltration velocity is much greater than observed by Mangangka [2008] for a sandy soil (21% coarse sand, 57% medium sand, 18% fine sand, 4% silt and clay), where a decrease in velocity in the unsaturated zone from 3 cm/min to 1.67 cm/min took 40 min.

The measured infiltration velocity was not directly implemented into the numerical model, however comparisons were made between the dynamics of the sandbox and the model, see section 9.3.2 on page 86.

8.5 Summary of initial soil properties used in the numerical 1D model

Based on the analyses above, the following soil properties were used as initial values when calibrating the 1D model.

θ_{sat} [cm^3 H_2O/cm^3 **soil**]	**b [-]**	ψ_{e} **[cm** $\mathbf{H_2O}$**]**	$\mathbf{K}_{\text{sat}}$ **[cm/min]**
0.434	2.1	-16	0.327

Table 8.3: Initial parameters used in numerical model. Saturated volumetric water content (θ_{sat}) and saturated hydraulic conductivity (K_{sat}) were derived from [Hedevang and Sørensen 2023]. ψ_{e} = air entry suction, b = Campbell b.

9 | One dimensional numerical model of water flow and groundwater rise in unsaturated soil

In order to model the dynamics of the groundwater observed in the experiments in chapter 5 both a 1D and 2D numerical model were made. The main part of the 1D model was based on Moldrup, Rolsten, and Hansen [1989] and is a 1D vertical numerical model of water flow and groundwater rise in unsaturated soil. The 1D model was only used to model the vertical flow and could therefore only partly model the dynamics of the experiment in chapter 5 and served as the base for the screening tool described in chapter 13. In this chapter the vertical 1D model is derived and explained. The model domain for the 1D model in comparison to the 2D model can be seen in figure 9.1. Here, the two model domains can be seen compared to the sandbox experiment.

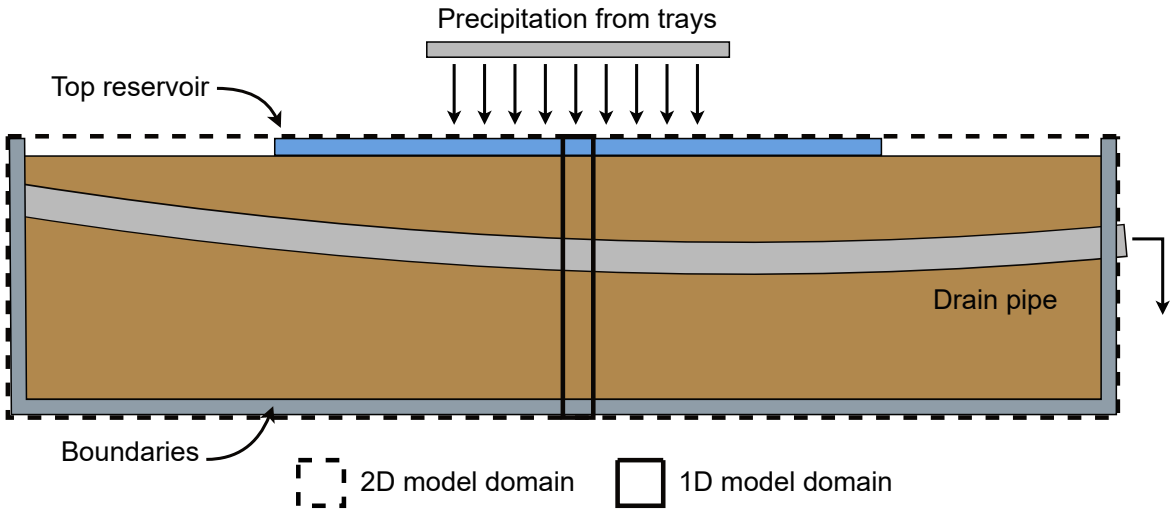

Figure 9.1: 1D and 2D model domains with different domain components shown.

9.1 Governing equations of the 1D numerical model for unsaturated soil - the MMS-model

The engine behind the 1D model used is the Mean Moving Slope (MMS) model [Moldrup, Rolsten, and Hansen 1989]. The directions and corresponding notion used for the model can be seen in figure 9.2.

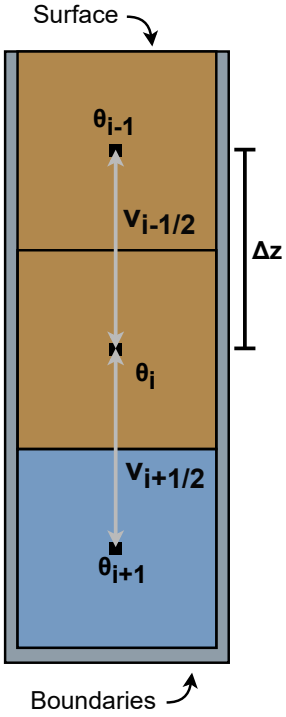

Figure 9.2: 1D finite difference grid at point i. θ = volumetric water content, v = Darcy flux, Δz = vertical discretization.

The MMS-model is a numerical model of unsaturated water flow and is a rapid alternative to e.g. using the Richards equation. It is based on the equation of continuity in equation (9.1) and the Darcy flow equation for unsaturated soil in equation (9.2). [Moldrup, Rolsten, and Hansen 1989], [Loll and Moldrup 2000]

$$\frac{\delta v}{\delta z} = -\frac{\delta \theta}{\delta t} \tag{9.1}$$

$$v = K(\psi)\frac{\delta H}{\delta z} \tag{9.2}$$

Where:

v	Darcy flux (positive downward) [cm/min]
z	Discretization in the z direction, see figure 9.2 [cm]
θ	Volumetric water content [cm^3 H_2O/cm^3 soil]
t	Discretization in time [min]
K	Hydraulic conductivity [cm/min]
ψ	Pressure potential [cm H_2O]
H	Total soil-water potential [cm H_2O]

In the MMS-model the volumetric water content is calculated numerically in each timestep using the explicit finite-difference approximation of the continuity equation shown in equation (9.3) [Moldrup, Rolsten, and Hansen 1989].

$$\theta_i^{t+1} = \theta_i^t - \left(v_{i+1/2}^t - v_{i-1/2}^t\right) \cdot \frac{\Delta t}{\Delta z} \tag{9.3}$$

The Darcy flux terms in equation (9.3) were determined according to Moldrup, Rolsten, and Hansen [1989]. Here, the vertical Darcy flux between consecutive cells was calculated using equation (9.4). This equation was derived by Richter [1980] and pivots around an analysis of the hydraulic conductivity and can account for the different hydraulic conductivities between consecutive cells when calculating the Darcy flux between the cells. Here, the $K - \psi$ curve is approximated to a number of exponential approximations, each valid in separate ψ intervals [Moldrup, Rolsten, and Hansen 1989].

$$v_{i+1/2} = -\frac{K_N e^{\alpha_N \psi_{i+1}} - K_N e^{\alpha_N \psi_i}}{e^{\alpha_N \Delta z} - 1} + K_N e^{\alpha_N \psi_i} \tag{9.4}$$

Where:

K_N	Average K between consecutive nodes calculated using equation (9.5) [cm/min]
α_N	Average α between consecutive nodes calculated using equation (9.6) [-]

Equation (9.5) and (9.6) show how the average hydraulic conductivity and α coefficient between consecutive vertical nodepoints were calculated [Loll and Moldrup 2000].

$$K_N = \frac{K_{L,i} + K_{L,i+1}}{2} \tag{9.5}$$

$$\alpha_N = \frac{\alpha_{L,i} + \alpha_{L,i+1}}{2} \tag{9.6}$$

Where:

$K_{L,i}$	Local approximation of the K curve around the soil-water potential at node i [cm/min]
$\alpha_{L,i}$	The slope of the hydraulic conductivity curve in a semi-log plot at the soil-water potential at node i [-]

The values for α and K for local approximation of the $K - \psi$ curve around the soil-water potential in cell i, denoted ψ_i, were calculated using equation (9.7) and (9.8): Here, the model from Campbell [1974] was used to calculate the α coefficient [Loll and Moldrup 2000].

$$K_{L,i} = K(\psi_i) e^{-\alpha_{L,i} \psi_i} \tag{9.7}$$

$$\alpha_{L,i} = \frac{2 + 3/b_i}{-\psi_i} \tag{9.8}$$

Where:

b_i	Campbell b for soil type at node i [-]
$K(\psi_i)$	Hydraulic conductivity at ψ_i [cm/min]

When using the MMS-model equation (9.3) through (9.8) were applied on all model cells and cell boundaries in the reverse order compared to the sequence they are presented in. An overview of the interdependency and sequence of the used equations can be seen in figure 9.3. The sequence of equations yields a volumetric water content in every cell in each timestep. In the next timestep, the volumetric water content needs to be converted to a soil water potential in order to be used in the equations. The conversion is done at the start of each timestep using equation (9.9). Based on this new soil water potential, the hydraulic conductivity used

for equation (9.7) is calculated using equation (9.10) [Loll and Moldrup 2000] and thus the cycle of calculations repeats through all timesteps.

$$\psi_i = \psi_{e,i} \cdot \left(\frac{\theta_i}{\theta_{sat,i}} \right)^{-b_i} \quad (9.9) \qquad K(\psi_i) = K_{sat,i} \cdot \left(\frac{\psi_{e,i}}{\psi_i} \right)^{2+3/b_i} \quad (9.10)$$

Where:

$\psi_{e,i}$	Suction at air entry at node i [cm H_2O]
$\theta_{sat,i}$	Saturated volumetric water content at node i [cm^3 H_2O/cm^3 soil]
$K_{sat,i}$	Saturated hydraulic conductivity at node i [cm/min]

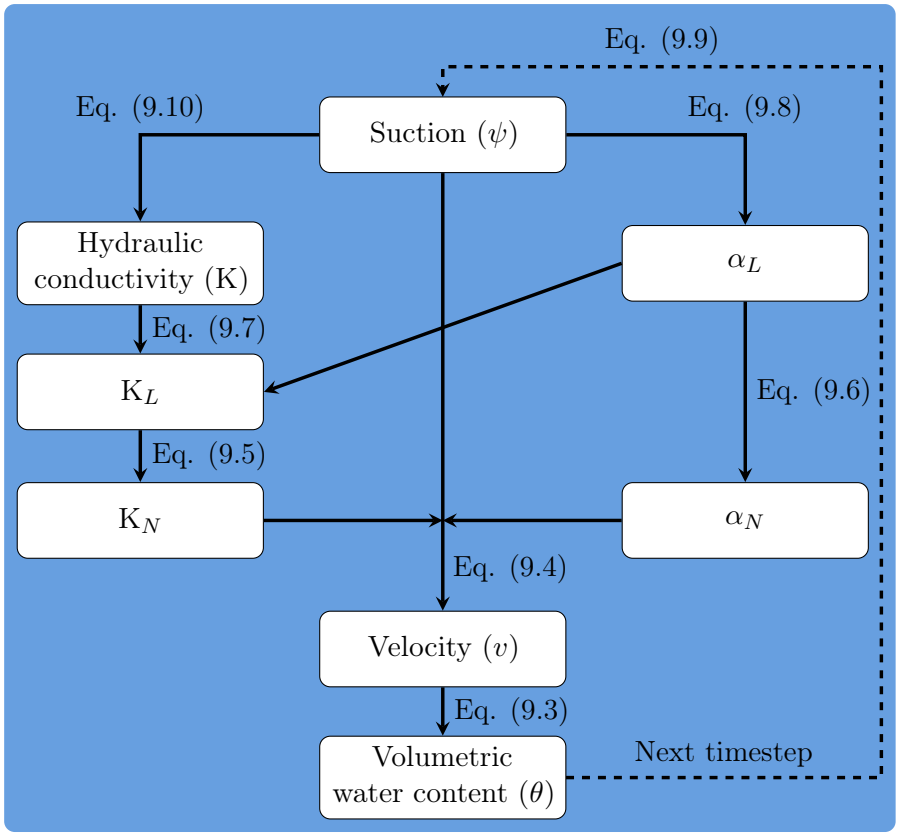

Figure 9.3: Interdependency of the parameters and their sequence of calculation in the MMS-model.

9.2 1D model stability criterion and model instabilities

In the utilization of numerical models, the consideration of model instability is imperative, along with an examination of its underlying causes. When using the MMS-model both a spacial and temporal resolution was selected. If either the temporal resolution was too large or the spacial resolution too small compared to the other, the model was susceptible to numerical oscillations. These oscillations can cause the model values to spiral creating unrealistic values for e.g the volumetric water content and the model will eventually become unstable. Another instability observed was cells becoming supersaturated. This was a product of how the Darcy flux is calculated using equation (9.4). Here, the last term of the equation will always yield

a Darcy flux even if two cells have the same volumetric water content. This results in the bottom cell of the model becoming supersaturated due to the limited Darcy flux out of the cell caused by the lower boundary.

9.2.1 MMS-model criterion for avoiding numerical oscillations

Moldrup, Rolsten, and Hansen [1989] suggest different criteria for avoiding numerical oscillations in the MMS-model. These are based on previous work and tested for the MMS-model by Moldrup, Rolsten, and Hansen [1989]. The criterion used in this Master's thesis is shown in equation (9.11).

$$\frac{dK}{d\theta} \cdot \frac{e^{\alpha_N \cdot \Delta z} + 1}{e^{\alpha_N \cdot \Delta z} - 1} \cdot \frac{\Delta t}{\Delta z} < 1 \tag{9.11}$$

Equation (9.11) can be used to check whether there were numerical oscillations for each cell in each time step. This was not done for every run of the 1D model. It was however done for one of the first model runs. Here, values of the temporal resolution relative to the required spatial resolution for avoiding numerical oscillations were calculated. These values were used for the model resolution for all other model runs of the sandbox experiments as the stability criterion was not implemented for every model run. This was due to the calculation speed of the model being sufficiently rapid. However, the stability criterion was implemented in the 1D model of screening tool, see chapter 13. Thus, the stability criterion was used to continuously calculate the maximum allowable timestep length between all cells of the model. Here, 95% of the smallest maximum allowable timestep length between two cells was used as the timestep length.

9.2.2 Accounting for instabilities caused by supersaturated cells

To fix the instabilities caused by a cell becoming supersaturated a module counteracting supersaturated cells was implemented into the model. If a supersaturated cell is present at the end of a timestep the module moves the excess water to the cell above, which might make that cell supersaturated. Thus, the module repeats the process until there are no more supersaturated cells. If the top cell is supersaturated the water is moved up into the top reservoir. The reasoning behind this module is that the water ending up in the supersaturated cell in reality would not have been able to flow into that cell, therefore moving the water up counteracts the excess flow and thereby creates a more realistic distribution of the water.

9.3 Setup and conditions of the 1D numerical model for unsaturated soil and model additions

The equations constituting the 1D model was programmed in the computer programming language Python. The model was programmed as the explicit solution shown in equation (9.3) using the associate equations as explained above. Here, the MMS-model served as the engine behind the calculations of volumetric water content, as modules were implemented to calculate pipe inflow and counteract supersaturation. The numerical model was effectively programmed as a column vector where the value in each row was the volumetric water content

of the soil in that specific cell, see figure 9.2. Before running the model its domain was built. Here, the dz and timesteps length were chosen and the desired soil parameters inputted. Then the volumetric water content was calculated in each timestep based on the Darcy flux between the individual cells and boundaries throughout the column, see figure 9.4. The finished model could run with multiple soil types and/or compaction levels throughout the model column.

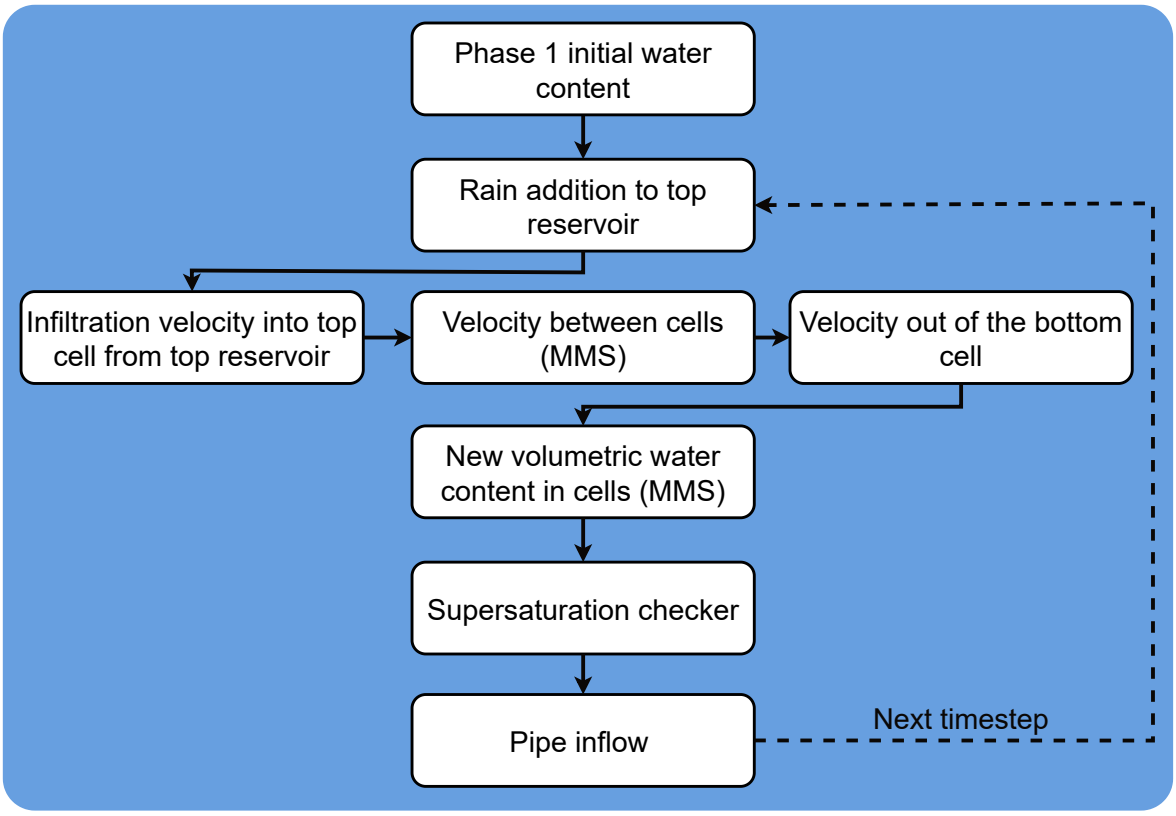

Figure 9.4: Conceptual sketch of the calculation order of the 1D numerical model. For explanation of phase 1, see section 9.3.1.

9.3.1 Initial conditions and lower boundary

The model was run in two phases, where phase 1 was run to calculate the initial conditions i.e. the volumetric water content in the capillary fringe. In phase 1, the model was run with a time resolution between 1/500 min and 1/1000 min, which is a very fine time resolution and was run with an open lower boundary. Here, the Darcy flux over the lower boundary into the bottom cell was modelled as if there was a saturated cell below the bottom cell. This allowed water both to flow in or out of the model domain. The initial water content in all cells was set at water content at field capacity. However, this value only determined the simulation time for phase 1 since water could both enter and leave the model during phase 1. Thus, phase 1 of the model either removed or added water until the capillary fringe reached equilibrium. This was defined when the change in volumetric water content between consecutive time steps in the same cell was lower than 10^{-6} cm^3 H_2O/cm^3 soil in all cells. A criterion of 0 change can never be met due to numerical oscillations in the model. The result of phase 1 was the volumetric water content in the final timestep which was saved and used as the initial conditions for phase 2. Figure 9.5 shows the differences between phase 1 and phase 2.

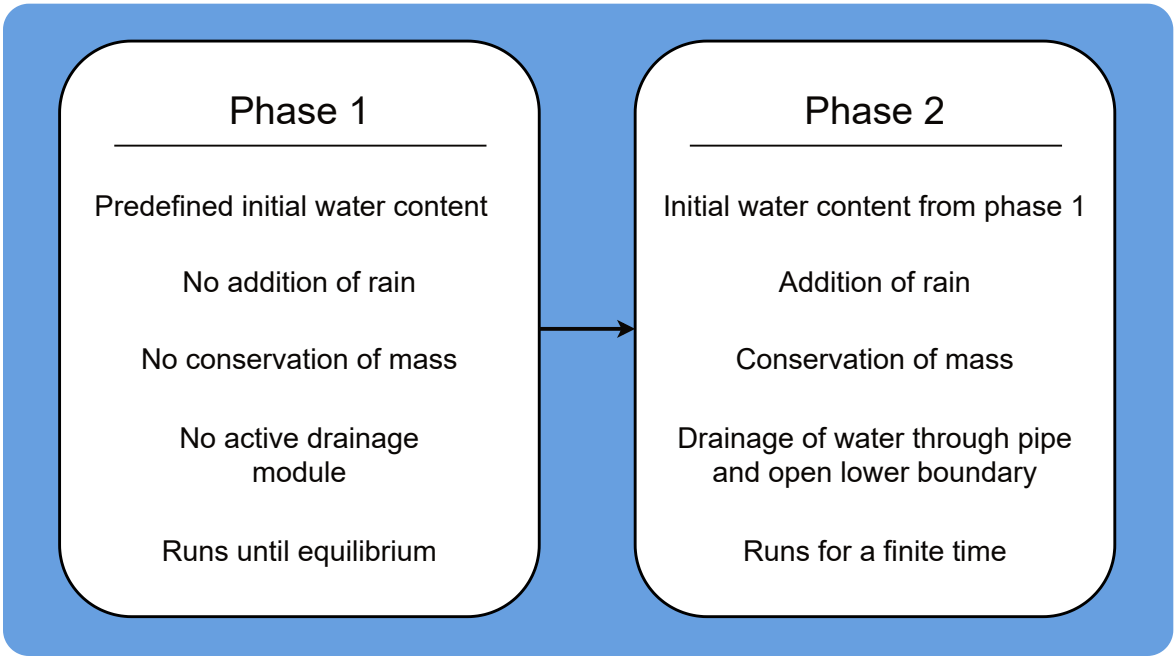

Figure 9.5: Overview of the differences in calculation between phase 1 and phase 2 of the model.

For phase 2 a constant Darcy flux over the lower boundary was applied if the bottom cell of the model was saturated. In the experiments there was only flow out of the left and right chambers when the water level rose above the initial water level, why the constant Darcy flux was only applied when the bottom cell was saturated. The constant Darcy flux was applied to simulate the effect of the left and right outlets in the sandbox experiment. In the experiments the water ran out of the outlets on either side due to the bottom 3 cm of each side being permeable. However, the 1D model only covered a single column of the sandbox which in it self only accounted for the part of the sandbox experiments that was above the initial water table. Therefore, the bottom cell of the model was equivalent to the cell above the initial water table from the experiment. This is illustrated in figure 9.6. The constant Darcy flux applied at the boundary was calculated using equation (9.12)

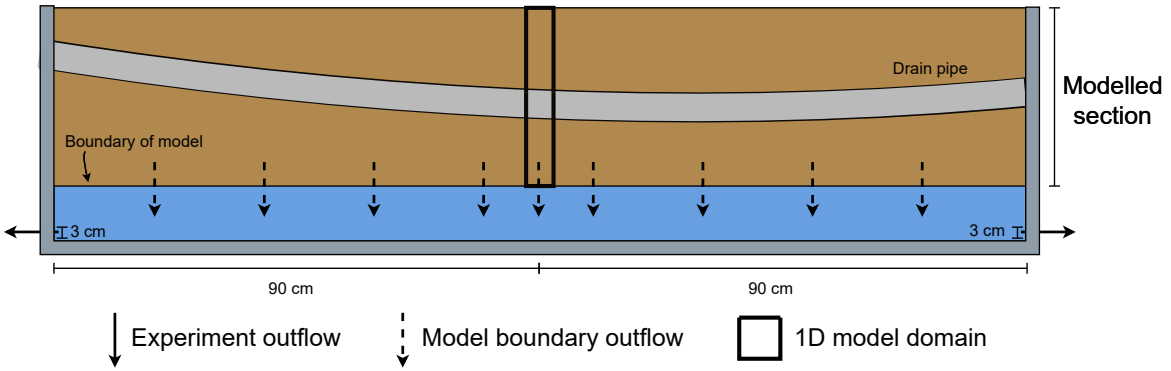

Figure 9.6: Sketch of the lower boundary with the model domain compared to the sandbox experiment.

$$v_{lb} = k_{eq} \cdot \frac{3\,\text{cm}}{90\,\text{cm}} \tag{9.12}$$

Where:

v_{lb}	Scaled constant Darcy flux applied at the lower boundary [cm/min]
k_{eq}	Equivalent conductivity through the membrane [cm/min]

The Darcy flux in equation 9.12 is equal to the equivalent conductivity through one membrane scaled to the length of half the central part of the sandbox (90 cm), see figure 10.2. The equivalent conductivity through the membranes between the sandbox and the chambers was calculated based on the measured data from the experiments. The equivalent conductivity was calculated using equation (9.13) which was derived from Darcy's law. A schematic representation of the parameters in equation (9.13) can be seen in figure 9.7.

$$k_{eq} = \frac{Q \cdot \Delta x}{A \cdot \Delta h} \tag{9.13}$$

Where:

Q	Flow through the membrane [cm^3/min]
A	Cross sectional area of the membrane [cm^2]
Δx	Length of the gradient, see figure 9.7 [cm]
Δh	Difference in water table over the membrane, see figure 9.7 [cm]

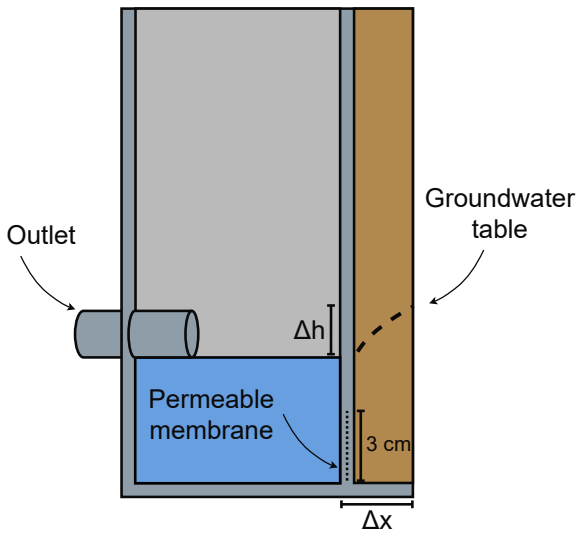

Figure 9.7: Schematic of the parameters for calculating the conductivity through the permeable membrane dividing the chamber from the sandbox. The figure shows the left chamber of the sandbox. Δh = difference in water table over the membrane, Δx =length of the gradient.

The flow through the membrane was assumed equal to the measured flow out of each chamber. Thus, equivalent conductivities were not calculated for the pilot experiment, where the water level loggers were not implemented yet, nor for the left side of experiment W2, where the water level logger failed. The used cross sectional area of the membrane was the area of the

lower 3 cm (width 40.5 cm) of permeable membrane shown in figure 9.7. The equivalent conductivities were calculated for multiple data points from the experiment. The result can be seen in appendix B.

9.3.2 Upper boundary condition - rain and infiltration into the top soil

The upper boundary was modelled using an artificial reservoir placed above the top cell, denoted the top reservoir. The rain volume in each timestep was added to the top reservoir at the start of a timestep. Then, the Darcy flux equivalent to the infiltration velocity from the reservoir into the top cell was calculated using equation (9.14). [Guymon 1994]

$$v = -K(\psi)\frac{\delta H}{\delta z} \tag{9.14}$$

The total soil-water potential (δH) in equation (9.14) was calculated using equation (9.15), where δz was set to $\delta z = dz$ and the hydraulic conductivity was set to $K(\psi) = K_{L,0}$. Thereby, the local approximation of the hydraulic conductivity around the soil-water potential at the top cell below the reservoir was used.

$$\delta H = \psi_e - \psi_0 \tag{9.15}$$

Where:

ψ_0	Suction at the top cell of the model [cm H_2O]

In most cases the flux into the top cell calculated using equation (9.14) yielded a larger inflow volume to the top cell than the volume stored in the reservoir. To account for this, the Darcy flux required for emptying the reservoir was also calculated each timestep based on the water content in the reservoir using continuity. Then, the smallest of the two fluxes was used to calculate the flux into the top cell and thus the removal of water from the top reservoir. This resulted in all the rain added in a timestep ending up in the top cell. For the cases where the flux calculated using equation (9.14) was not sufficient to empty the reservoir the residual volume was carried over to the next time step. This would only happen either if the rain intensity was high compared to the hydraulic conductivity of the soil, if the model was filled with water or initially when the top cell was dry and the hydraulic conductivity low.

The infiltration into the model was tested for a 2 m soil column in order to demonstrate the functionality of equation 9.14. Here, the model was run with two different infiltration conditions. The model was run with the same rain as when running the sandbox experiment (0.194 cm/min, see section 11.1) and an infinitely filled top reservoir. Running the model with rain demonstrates how the model infiltration functions when modeling the sandbox experiments, while running the model with an infinite top reservoir result in the maximum theoretical infiltration into the model. The result can be seen in figure 9.8. The theoretical maximum infiltration into the model was also compared to the measured infiltration into the corner of the sandbox described in section 8.4. This was done in order to validate the model infiltration and the result can be seen in figure 9.9.

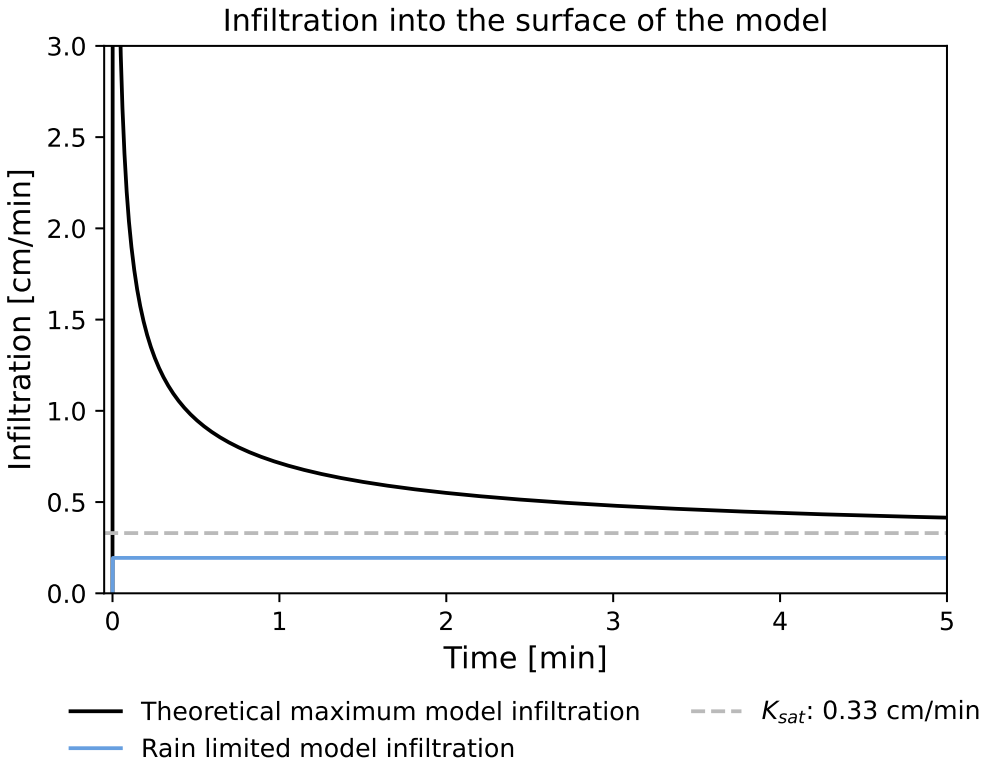

Figure 9.8: Comparison of the two different tests of the infiltration calculation in equation 9.14. K_{sat} = saturated hydraulic conductivity.

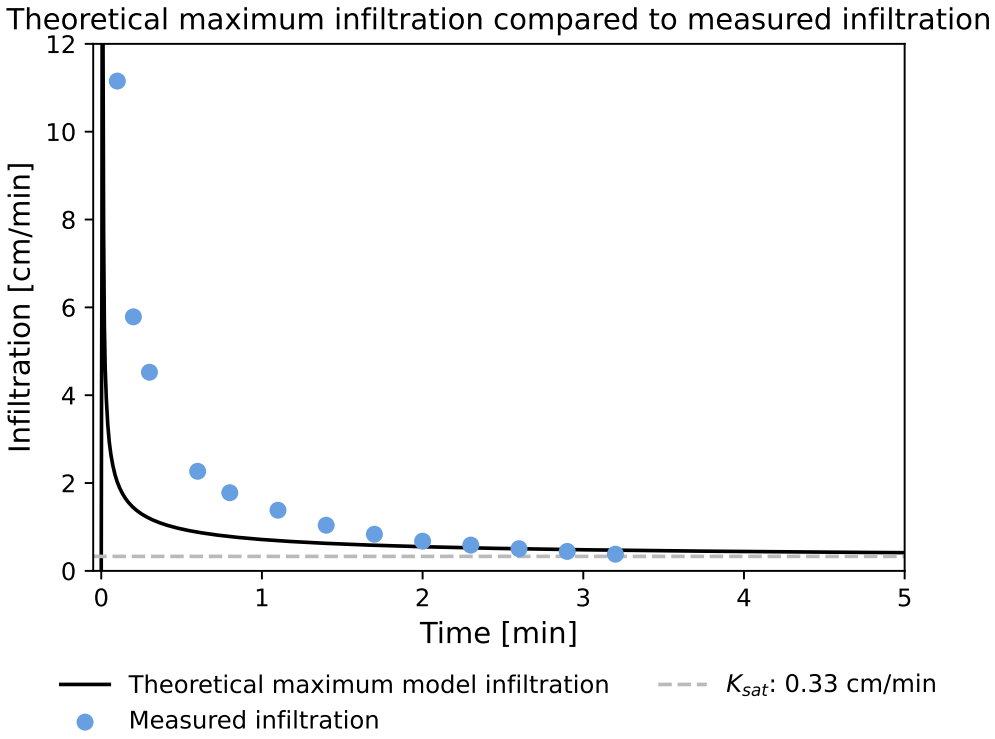

Figure 9.9: Comparison of the maximum theoretical infiltration with the measured infiltration. The measured infiltration is sideways, see section 8.4. K_{sat} = saturated hydraulic conductivity.

Looking at figure 9.8 it can be seen that the rain is controlling the infiltration into the model since the rain limited infiltration almost instantly becomes equal to the rain intensity. As long as the rain intensity is lower than the maximum infiltration velocity, the rain will control the infiltration since the soil can absorb more water than the rain adds in the model. If the rain intensity is larger than the maximum infiltration velocity the limiting factor will be a combination of the rain and the soil. The simulation done with an infinite top reservoir follows typical infiltration models, since the infiltration velocity is high initially and then becomes asymptotic with the saturated hydraulic conductivity [Guymon 1994]. Looking at figure 9.9 it can bee seen that the theoretical maximum infiltration decreases faster than the measured data. Here, the dynamics fit quite well despite the measured infiltration being in a different direction relative to gravity. This supports the uses of the infiltration module in the model.

When the infiltrating water front reaches the modelled capillary fringe, the infiltration dynamics do not change to a linear infiltration velocity as observed by Mangangka [2008]. Instead, the infiltration velocity nears the saturated hydraulic conductivity until the model domain eventually fills all cells and the infiltration becomes zero. For all uses of the 1D model in this part of the Master's thesis the rain will be controlling the infiltration rate since all used rain intensities are lower than the maximum infiltration velocity of the soil. This effectively results in infiltration being applied as a constant when the 1D model was used to model the sandbox experiments. However, when used in the screening tool the infiltration varied and the rain was not necessarily the controlling factor.

9.3.3 Incorporation of the drain pipe into the 1D model domain

To model the experiments presented in chapter 5 the flow into the drain pipe was incorporated into the model structure. Since the pipe inflow is not part of the model governing equations, it could not be directly incorporated into the model continuity through the equations. It was therefore incorporated as an attached module to the main equations. Here, the flow into the pipe was calculated at the end of each time step. The resulting drained amount was then removed from the model by subtracting it from the topmost saturated cell and thereby artificially reducing the water table. The flow into the pipe was only calculated if at least one of the cells surrounding the top half of the pipe was saturated as this was the area with the leakages in the pipe. Here, the volume drained by the drain pipe was calculated in each timestep using equation (9.16). The equation is an empirical equation based on sandbox experiment data and the approach done by Hedevang and Sørensen [2023].

$$V_{infiltration} = A_R \cdot L_p \cdot P_{dc} \tag{9.16}$$

Where:

$V_{infiltration}$	Infiltration volume into the drain pipe [cm^3]
A_R	Reduction factor accounting the percentage of the pipe holes covered by the water table [-]
L_p	Length of pipe in the model domain [cm]
P_{dc}	Empirical drainage coefficient for the pipe [cm^3/min/cm]

The reduction factor A_R was introduced to account for a water level that only partially covers the holes in the pipe. It was calculated using equation (9.17) [Hedevang and Sørensen 2023]. The equation calculates the percentage of the pipe holes submerged under the water table using angular circle geometry. An example of the values of the reduction factor can be seen in figure 9.10.

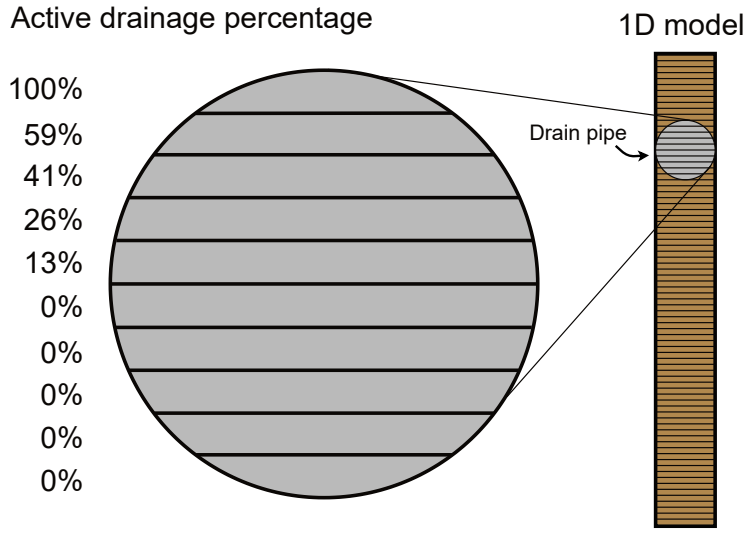

Figure 9.10: Conceptual sketch of the placement of the pipe in the 1D domain and the percentage of the total area of leakages covered by water in each saturated cell. The reduction factor A_R was based on the amount of cells that were submerged in the model for each timestep. Inspired by Hedevang and Sørensen [2023].

$$A_R = \frac{arccos(1 - (2 \cdot y \cdot d^{-1})) - 90°}{90°} \quad \text{for} \quad \frac{d}{2} \leq y \leq d \qquad \text{and} \qquad A_R = 1 \quad \text{for} \quad y > d \tag{9.17}$$

Where:

d	Diameter of the pipe [cm]
y	Distance from the water table to bottom of the pipe [cm]

The length of pipe in the model domain was set to 1 cm for the 1D model. The empirical drainage coefficient for the pipe was calculated using the experiment data. Essentially, the coefficient equates to the flow into the pipe per cm pipe. It was calculated from a combination of the measured water level and pipe outflow data, see section 6.3, using equation 9.18.

$$P_{dc} = \frac{Q_{pipe}}{L_p} \tag{9.18}$$

Where:

Q_{pipe}	Measured flow out of the drain pipe [cm^3/min]

The flow out of the drain pipe Q_{pipe}, was determined from the water level loggers' data and was calculated from the interval where multiple water level meters showed groundwater within

the pipe drainage area. Here, the length of submerged pipe was difficult to determine due to the low resolution of water level meter data with a horizontal accuracy of about 25-30 cm. This becomes evident when looking at figure 6.3 on page 47 which shows that the top of the groundwater table only reached substantially above the pipe drainage area in 3 out of 5 experiments. The L_p can only be calculated when the groundwater in 2 or more level meters are above the drainage area of the pipe. During the experiments there were at max four level meters with groundwater above the pipe drainage area at a time. In cases where the groundwater was above the pipe in two or three level meters the L_p can be calculated from the distance between the two outer level meters and the angle of the pipe. The key values used in the calculation and the resulting P_{dc} can be seen in table 9.1.

Experiment:	**P**	**C1**	**W1**	**W2**	**C2**
Flow AVG when 2 level meters above PDA [cm^3/min]	-	305	698	693	-
Flow AVG when 3 level meters above PDA [cm^3/min]	223	324	692	812	-
Flow AVG when 4 level meters above PDA [cm^3/min]	-	-	-	-	399
Distance level meter 3-4 [cm]	23.3	23.3	23.3	23.3	23.3
Distance level meter 3-5 [cm]	56.7	56.7	56.7	56.7	56.7
Distance level meter 3-6 [cm]	80.1	80.1	80.1	80.1	80.1
Drainage coefficients 2 level meters [cm^3/min/cm]	-	13.1	29.9	29.7	-
Drainage coefficients 3 level meters [cm^3/min/cm]	3.9	5.7	12.2	14.3	-
Drainage coefficients 4 level meters [cm^3/min/cm]	-	-	-	-	5.0

Table 9.1: Key values from the calculation of the empirical drainage coefficient for the pipe. PDA = pipe drainage area, AVG = average, "-" = not calculable due to the number of consecutive level meters over the PDA

The P_{dc} calculated using equation (9.18) is between 4-30 cm^3/min/cm. The large interval was partly a product of the poor horizontal resolution of the water level meters. The used distance for the length of pipe above the pipe drainage area varied more than the two values used here and the real values were most likely larger. The interval was suspected to be too large compared to the real P_{dc} since the used values of L_p was suspected to be too low. Therefore, a low value of the calculated interval for the P_{dc} was used initially when calibrating the model, see section 9.4.2.

9.4 Evaluation of phase 1 initial conditions and calibration and validation of the 1D numerical model

Before calibrating the 1D model, the modelled capillary rise in phase 1 of the model was analysed compared to measured data.

9.4.1 Comparison of modelled phase 1 results with measured capillary rise

The initial conditions of phase 2 of the 1D model, created by phase 1 is important for replicating the dynamics observed in the sandbox. Therefore, to investigate whether the phase 1 results were representative of the soil, they were compared to data from capillary rise experiments conducted by Hedevang and Sørensen [2023].

Hedevang and Sørensen [2023] conducted two column experiments with the St. Restrup sand with two columns in each experiment. Here, the columns were wetted from below and the subsequent capillary rise was measured as the visible wetting front. The soil in column experiment 1 was not compacted by a predefined degree and thus Hedevang and Sørensen [2023] repeated the procedure with column experiment 2, where a compaction of 1.5 g/cm^3 was ensured. The initial water content of the soil in the columns were input as initial conditions in the 1D model during phase 1 and the model was run with a compaction of 1.5 g/cm^3 for both experiments. The rise in the model was defined as when the volumetric water content increased with 0.05 cm^3 H_2O/cm^3 soil compared to the initial value in the cell. The corresponding rise in the model for each experiment was plotted against the result from Hedevang and Sørensen [2023], see chapter 11.

9.4.2 Fitting the soil and model parameters in the 1D model to measured data - calibration and validation of the 1D model

After analysing the phase 1 results the calibration of the model was initiated. Here, multiple calibration parameters were considered and over numerous iterations tweaked until an acceptable result was achieved. The calibration process is illustrated in figure 9.11.

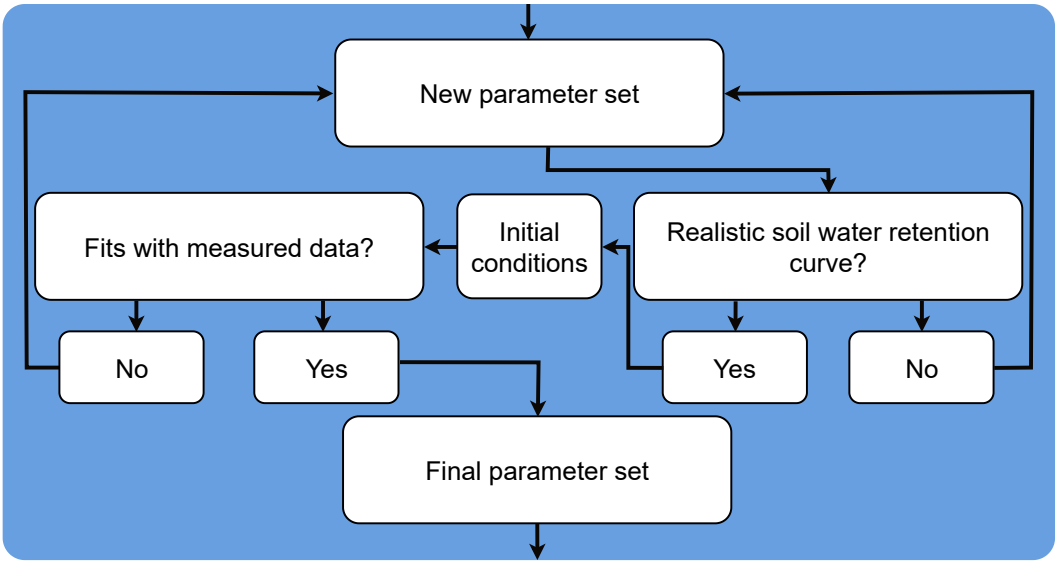

Figure 9.11: Calibration process of the soil parameters used in the 1D model. The calibrated parameters were Campbell b, air entry suction and saturated hydraulic conductivity.

The calibration parameters were as follows; the air entry suction, Campbell b, saturated hydraulic conductivity, pipe drain coefficient and the equivalent conductivities through the membranes. The initial values used in the calibration of the soil parameters were the estimated values explained in chapter 8 and the initial values used for the pipe drain coefficient and the equivalent conductivity through the membranes were based on the values calculated from the experimental data. The calibration was run with the rain intensity, rain duration and initial distance to surface from experiment C2. This experiment was selected since it was the only experiment where the boundary conditions and input was exactly known. For the validation experiment C1 was selected. This was chosen since it was the experiment with the highest data resolution of the two remaining experiments with cold water. The two experiments with

warm water were not used in the calibration or validation since the warm water impacted the flow dynamics of the sandbox due to the lower viscosity of the water.

When the model was validated against experiment C1 all the calibration, initial, input and model parameters were the same as for the calibration with the exception of the rain intensity and the equivalent conductivities through the membranes. The rain was scaled to fit with experiment C1 and the equivalent conductivity was scaled according to the measured calculated values, see appendix B. The equivalent conductivity was scaled with a factor of 0.86 in the validation compared to the calibration which corresponds to the scaling between the calculated mean values of the equivalent conductivities from experiment C1 and C2, see appendix B. This was done since the equivalent conductivity seemed to have increased due to the deterioration of the sandbox and it was also depending on the rain intensity. Since C1 had a lower rain intensity than C2 its membrane conductivity should be lower.

During the calibration, a new soil water retention curve for each new parameter set of Campbell b and air entry suction was created to ensure realistic soil parameters. Likewise, the initial Campbell b of 2.1 already seemed low compared to theoretical values (see section 8.2 on page 70) and thus was not lowered substantially during the calibration. As a result, parameters sets were tested with a Campbell b varying between 1.5-3.5 while the air entry suction was altered between -5 to -30 cm. When fitting the soil water retention curve, a numerically higher air entry generally resulted in a lower Campbell b. Thus, due to the water movement in the MMS-model being very sensitive to numerically low air entry suctions, a numerically high air entry and its subsequent theoretically low Campbell b was prioritized.

The final calibrated values for the 1D model and model parameters used to run the model can be seen in section 11.1. The calibrated parameters were found by comparing the rise in groundwater table from the 1D model with the water level meters L4 and L5 (see figure 6.1 on page 45 for placement in the sandbox). This was done by plotting the modelled and measured groundwater table against each other. In addition, the model run with the measured soil parameters is also shown in the plot in order to show the effect of calibrating the soil parameters. L4 and L5 were chosen for the comparison as the precipitation was applied directly over L4 and thus it was the level meter which was expected to be least impacted by horizontal movements of water. Moreover, L5 was included as this showed the slowest increase of the two water level meters adjacent to L4. This way, the comparison with measured data was an attempt to fit the modelled increase between L4 and L5. In addition to comparing the rise in groundwater table the outflow from the model was also compared to the measured outflow. Based on both comparisons the accuracy of the calibration and validation was manually evaluated. No specific calibration criterion was used and the quality of the calibration and validation was therefore entirely subjective. The comparison with the subjective best fit is shown in chapter 11.

10 | Two dimensional numerical model of water flow and groundwater rise in unsaturated soil

In the experiments in chapter 5 both vertical and horizontal flow was observed. Therefore a 2D model was developed to model both dimensions. In chapter 9 the 1D and 2D domains can be seen relative to each other. In this chapter the 2D model is derived and explained and the uses of the model are shown. The 2D numerical model of water flow and groundwater rise in unsaturated soil was based on Guymon [1994], where a finite differences approximation of the flow equation in 2D is presented. For the 1D model the Mean Moving Slope (MMS) model from Moldrup, Rolsten, and Hansen [1989] was solely used. The used 2D model in this project was derived by integrating the Mean Moving Slope (MMS) into the Guymon [1994] model. Here the continuity and numerical solution from the Guymon [1994] model was used with the Darcy flux calculated by the MMS-model.

10.1 Governing equations of the 2D numerical model for unsaturated soil

The directions and corresponding notion used for the 2D model can be seen in figure 10.1.

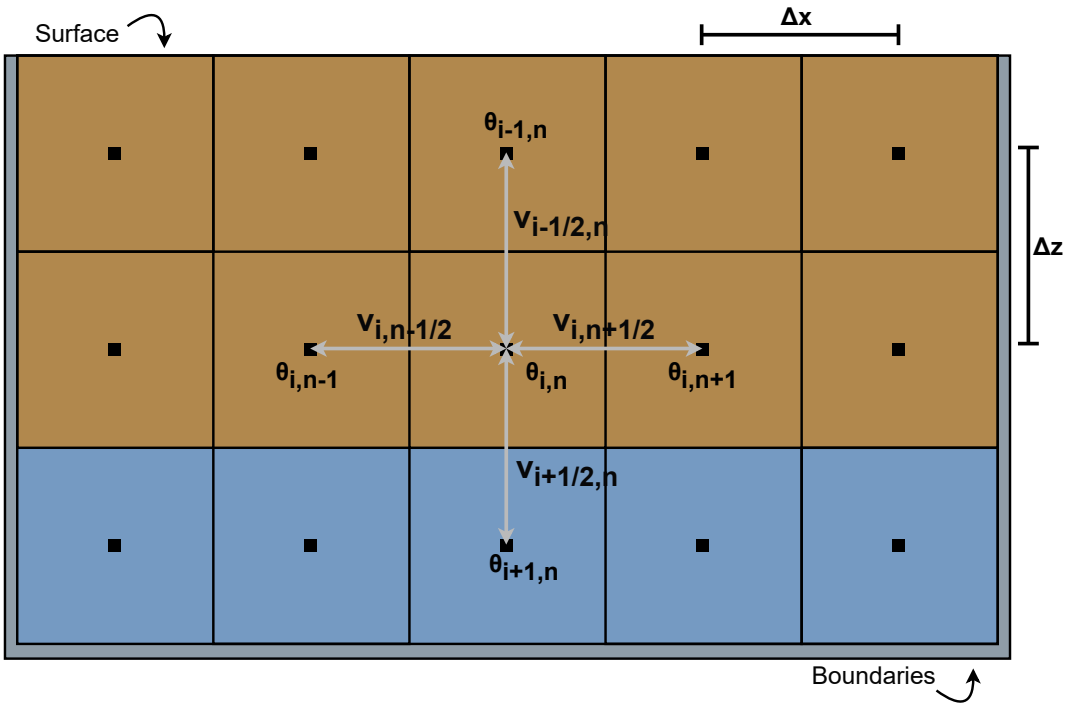

Figure 10.1: Simplified sketch of two-dimensional finite difference grid at point i,n. θ = volumetric water content, v = Darcy flux, Δz = vertical discretization, Δx = horizontal discretization.

According to Guymon [1994] equation (10.1) is a simple finite difference approximation of the flow equations. Here, a 2D vertical slice model with no sources or sinks is considered (positive downwards).

$$-\frac{\delta\theta}{\delta t} = \frac{\delta}{\delta x}\left[K(\psi)\frac{\delta H}{\delta x}\right] + \frac{\delta}{\delta z}\left[K(\psi)\frac{\delta H}{\delta z}\right] \tag{10.1}$$

Where:

x	Discretization in the x direction, see figure 10.1 [cm]
K	Hydraulic conductivity [cm/min]
ψ	Pressure potential [cm H_2O]
H	Total soil-water potential [cm H_2O]
z	Discretization in the z direction, see figure 10.1 [cm]
θ	Volumetric water content [cm^3 H_2O/cm^3 soil]
t	Discretization in time [min]

Given equation (10.2) equation (10.1) can be rewritten as equation (10.3). [Moldrup, Rolsten, and Hansen 1989]

$$v_x(\psi) = K(\psi)\frac{\delta H}{\delta x} \qquad \text{and} \qquad v_z(\psi) = K(\psi)\frac{\delta H}{\delta z} \tag{10.2}$$

Where:

v	Darcy flux (positive downward) [cm/min]

$$-\frac{\delta\theta}{\delta t} = \frac{\delta v_x(\psi)}{\delta x} + \frac{\delta v_z(\psi)}{\delta z} \tag{10.3}$$

The partial differential terms in equation (10.3) was approximated using a finite difference approximation. For the x direction the Darcy flux was approximated at the midpoint between each node as shown in equation (10.4) for the x direction. The approximation was the same in the z direction just with the appropriate annotation. [Guymon 1994; Moldrup, Rolsten, and Hansen 1989]

$$v_x(\psi)|^t_{i,n-1/2} \sim v^t_{i,n-1/2} \qquad \text{and} \qquad v_x(\psi)|^t_{i,n+1/2} \sim v^t_{i,n+1/2} \tag{10.4}$$

The Darcy flux between the nodes was determined using a hydraulic conductivity as some average over the Δx interval. The partial differential terms on the left side of equation (10.3) was approximated as shown in equation (10.5). The time derivative in equation (10.3) was approximated between time steps as shown in equation (10.6) [Guymon 1994]

$$\frac{\delta v_x(\psi)}{\delta x} \sim \frac{v^t_{i,n+1/2} - v^t_{i,n-1/2}}{\Delta x} \qquad \text{and} \qquad \frac{\delta v_z(\psi)}{\delta z} \sim \frac{v^t_{i+1/2,n} - v^t_{i-1/2,n}}{\Delta z} \tag{10.5}$$

$$\frac{\delta\theta}{\delta t} \sim \frac{\theta^{t+1}_{i,n} - \theta^t_{i,n}}{\Delta t} \tag{10.6}$$

Finally, the calculation of volumetric water content in each cell based on vertical and horizontal fluxes was achieved by combining equation (10.3), (10.5) and (10.6) yielding equation (10.7).

$$\theta_{i,n}^{t+1} = \theta_{i,n}^{t} - \left(\frac{v_{i,n+1/2}^{t} - v_{i,n-1/2}^{t}}{\Delta x} + \frac{v_{i+1/2,n}^{t} - v_{i-1/2,n}^{t}}{\Delta z} \right) \cdot \Delta t \tag{10.7}$$

10.1.1 Integration of the MMS-model into the 2D model and calculation of the Darcy flux

The Darcy flux terms in equation (10.7) were determined using the Mean Moving Slope model (MMS-model). This model pivots around an analysis of the hydraulic conductivity and can account for the different hydraulic conductivities between consecutive cell when calculating the Darcy flux between the cells. This is further explained in chapter 9. [Moldrup, Rolsten, and Hansen 1989; Loll and Moldrup 2000]

Moldrup, Rolsten, and Hansen [1989] determined the Darcy flux between cells for vertical flow only. The vertical flux is shown in equation (10.8). This is the same equation used in the 1D model, see equation (9.4) on page 80. A similar derivation to what Moldrup, Rolsten, and Hansen [1989] presented for the vertical flow was done for the horizontal flow resulting in equation (10.9). The derivation is shown in appendix C on page 164.

$$v_{i+1/2,n} \downarrow \quad = -\frac{K_N e^{\alpha_N \psi_{i+1,n}} - K_N e^{\alpha_N \psi_{i,n}}}{e^{\alpha_N \Delta z} - 1} + K_N e^{\alpha_N \psi_{i,n}} \tag{10.8}$$

$$v_{i,n+1/2} \rightarrow \quad = -\frac{K_N e^{\alpha_N \psi_{i,n+1}} - K_N e^{\alpha_N \psi_{i,n}}}{\alpha_N \Delta x} \tag{10.9}$$

Where:

K_N	Average K between consecutive nodes [cm/min]
α_N	Average α between consecutive nodes [-]

The average hydraulic conductivity and α coefficient between consecutive vertical and horizontal nodepoints were calculated using the same method as the 1D model. All other equations of the MMS-model were used in the same way and order as for the 1D model for both horizontal and vertical Darcy fluxes through the model domain. All the used equation are explained in section 9.1 on page 78.

10.2 2D model stability and limitations

The 2D model as it was set up in this project had several limitations. A limitation was the requirement of horizontal homogeneity in the soil. This reduced the model's usability since it reduced the real world scenarios that can be modelled. Another limitation was that all rain must infiltrate into the model cell it was added to and therefore water could not run on the surface. This could result in the rain being more concentrated than observed during the sandbox experiments. This was however partly countered by applying the rain over a wider

length of the sandbox compared to the width of the area with holes in the rain trays. Further, the 2D model was also subject to cells becoming supersaturated just as in the 1D model, see section 9.2.2. This was resolved using the same method as for the 1D model in each column in the 2D model. This means that the excess water from supersaturated cells was moved upwards in their respective columns.

It is possible to make the model more complex in order to eliminate the above mentioned limitations. However, increasing the complexity also reduces the overall model stability, which can lead to excessive simulation time due to the required fine resolution needed to run it. However, none of the current model limitations had a significant effect on the desired use of the model in this project.

10.2.1 Evaluation of a stability criterion

Knowing whether a model simulation is stable before running it is quite advantageous and can be a useful tool to reduce overall time spent on a simulation. Guymon [1994] suggests the stability criterion shown in equation (10.10) for the simple finite difference approximation of the flow equations in equation (10.1). However, by incorporating the MMS-model into the 2D model suggested by Guymon [1994] the combined model is less stable than the individual models. This criterion was tested by running different time and spatial resolutions. The result was that even if the combined 2D model fulfilled the stability criterion given in equation (10.10) the model was not necessarily stable. However, if they were not met they quickly became unstable. No other stability criterion was derived for the combined model and therefore a trial an error approach was employed instead when determining the needed model resolution.

$$\frac{\Delta t \cdot K(\psi)}{\frac{\Delta\theta}{\Delta\psi} \cdot \Delta x^2} \leq \frac{1}{2} \qquad \text{and} \qquad \frac{\Delta t \cdot K(\psi)}{\frac{\Delta\theta}{\Delta\psi} \cdot \Delta z^2} \leq \frac{1}{2} \tag{10.10}$$

10.3 Setup and conditions of the 2D numerical model for unsaturated soil

In order to run the 2D model it was programmed in the computer programming language Python. The model was programmed as the explicit solution shown in equation (10.7) to the governing differential equation (10.1). Due to the nature of the 2D model it effectively functioned as a matrix where each model cell was an element within the matrix. Before running the model its domain was built. Here, the dz, dx and timesteps length were chosen and the desired soil parameters inputted. The model can run with multiple soil types and/or compaction levels as long as the soil parameters only vary vertically same as for the 1D model.

A sketch of the model's different boundaries placement relative to each other can be seen in figure 10.2. An advantage of the 2D model when compared to the 1D model is that the model can both model horizontal water movement and account for the horizontal heterogeneity of the model domain. Looking at figure 10.2 it can be seen how the model domain necessitates the use of the 2D model since the drain pipe was sloped and the rain only covered part of the model.

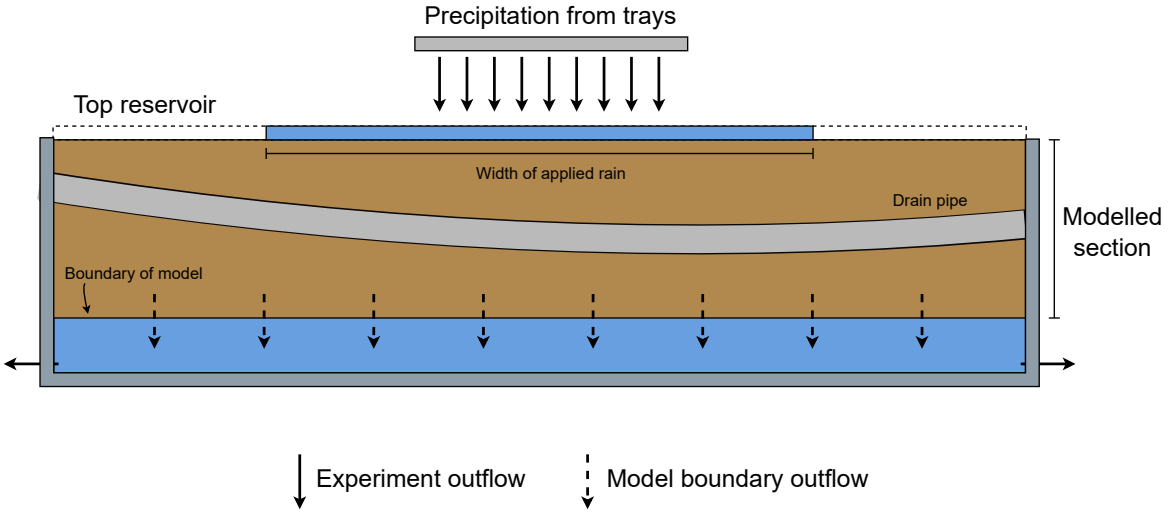

Figure 10.2: Sketch of the relative placement of the model domains' boundaries.

10.3.1 Initial conditions and lower boundary

The 2D model was run in the same two phases as the 1D model and the lower boundary was modelled the same way in each column of the 2D model as was done in the single column of the 1D model, see section 9.3.1. During phase 1 there is horizontal homogeneity as the pipe and rain does not affect the capillary rise. Therefore, the 1D model could be used to run phase 1 by inputting the 1D result into each column in 2D, thereby creating a phase 1 result for the 2D model. This reduced the simulation time since the 1D model was considerably faster.

10.3.2 Upper and side boundary

The upper boundary was modelled above the top cell of the sandbox by adding a row of cells constituting the top reservoir. Here, the model was programmed so the rain was added to the top reservoir cells. This enables the rain to be distributed over the desired amount of cells and does not necessarily have to cover the entire width of the model domain. Each interaction between reservoir cell and top cell was modelled the same way as the 1D model using the same equations, see section 9.3.2 on page 86. Furthermore, there was no flow between the reservoirs and the water therefore could not run on the surface in the model. The boundary on the left and right side of the model were set up as a no flow boundary and the Darcy flux here was set to zero along the boundary. Each column under the rain functioned the same way as the 1D model, see figure 10.3. Here, the infiltration quickly becomes equal to the rain intensity.

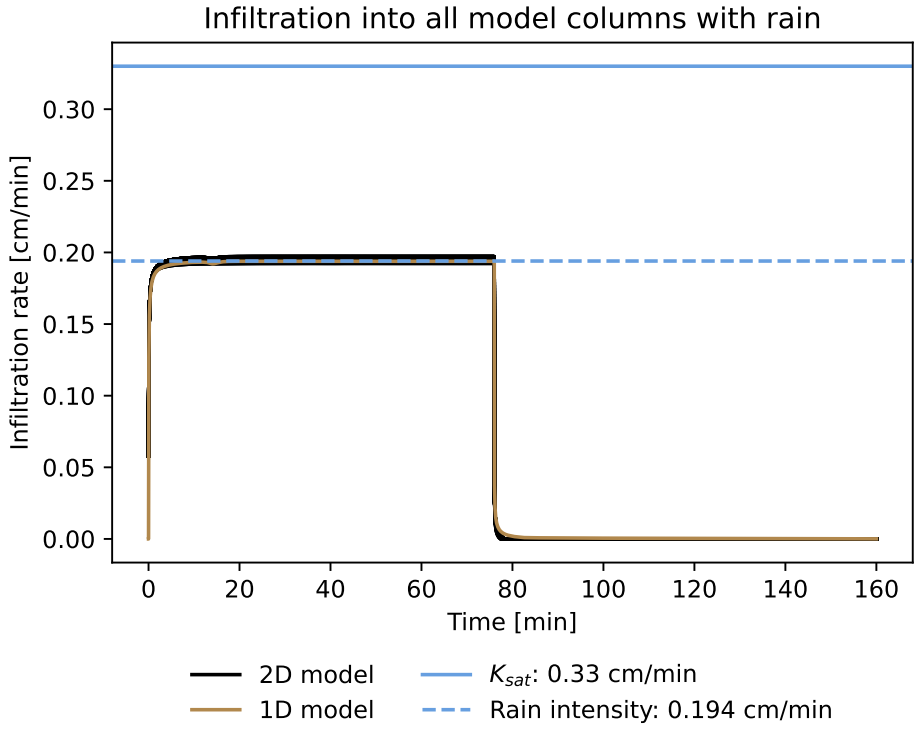

Figure 10.3: The infiltration from the model calibration, see section 10.4 for both the 1D and 2D model. Here, the central 50 columns from the 2D model subjected to rain are all plotted. K_{sat} = saturated hydraulic conductivity.

10.3.3 Incorporation of the drain pipe into the 2D model domain

To model the experiment explained in chapter 5 the flow into the drain pipe was incorporated into the model structure. Since the model domain was modelled as a horizontally aligned grid and the pipe was implemented with a curvature it did not fit perfectly into the model grid. Here, the best fit of the drain cells (cell covering the top half of the pipe in the model) was made and the quality of the fit depended on the domain resolution. How the pipe was fitted into the 2D model domain used to calibrate and validate the model can be seen in figure 10.4.

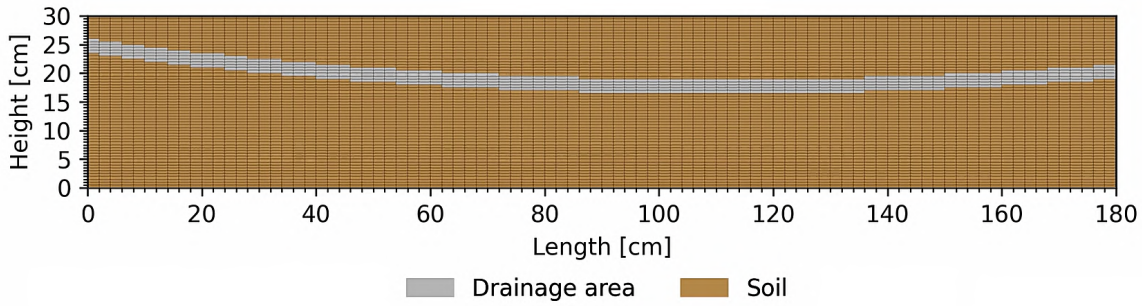

Figure 10.4: The placement of the pipe in the 2D model domain.

The infiltration into the drain pipe in each column of the model domain was calculated using the same method and equations as the 1D model, see section 9.3.3. The pipe was considered

to have a sufficient capacity to remove the water and the internal flow in the pipe was not modelled. Therefore, water flowing into the pipe was immediately removed in the model.

10.4 Calibration and validation of the 2D numerical model for unsaturated soil

The main use of the 2D model in this Master's thesis was modelling the sandbox experiment. For this the model was calibrated against experiment C2 and validated against experiment C1 in the same way as for the 1D model, see section 9.4.2. The process and method of the validation and calibration was also the same as for the 1D model with the exception that all seven level meters were considered instead of only considering level meter L4 and L5. This was done since the 2D model can model the entire length of the sandbox experiment in contrast to the 1D model only modelling a single column. The result of the calibration and validation of the 2D model can be found in chapter 11.

11 | Results from the numerical models of water flow and groundwater rise in unsaturated soil

This chapter presents the results of calibration and validation of the 1D and 2D models (explained in chapters 9 and 10) along with the results of the analyses conducted using the models. Lastly, a comparison between the 1D and 2D model is presented. The reader should notice that all figures of water level that is either modelled or measured from the sandbox experiment shows the initial water level above datum and thus the groundwater level does not start at 0 cm. Here, datum was the lowest measurable point on the outside of the sandbox, see appendix A.

11.1 Input parameters used for running the 1D and 2D model

Prior to model execution all input parameters must be selected including the model domain parameters, boundary values and soil parameters. The chosen values influence the model's behavior and output where some of the values have a greater influence than others. The model parameters used when running 1D model, except for the soil parameters, can be seen in table 11.1. Here it can also be seen which values were used to produce which results.

Model parameter	**Column experiment**	**Calibration**	**Validation**
Experiment [-]	[-]	C2	C1
Model domain height* [cm]	35	30	29
Vertical discretization (dz) [cm]	0.25	0.5	0.5
Temporal discretization (dt) [min]	1/1000	1/1000	1/1000
Simulated time [min]	45-60	160	160
Rain intensity** [cm/min]	[-]	0.194	0.168
Rain Duration [min]	[-]	76	57
Pipe drainage coefficient*** [cm^3/min/cm]	[-]	0.164	0.164
Equivalent membrane conductivity [cm^3/min/cm]	[-]	0.996	0.858
Used for result in figure	11.3 and 11.4	11.5, 11.7 and 11.14	11.6 and 11.8

Table 11.1: Parameters used for 1D model of the column experiment, calibration and validation. *Equivalent to the height from the initial groundwater table to the surface soil in the sandbox. **Equivalent rain intensity over 1 cm^2. Scaled by using the maximum area from figure 6.9. ***Scaled from the full depth of the sandbox of 41 cm to only 1 cm^2. The equivalent pipe drainage coefficient for the entire sandbox is 6.6 which fits well with the calculated interval of values as seen in table 9.1.

The model parameters used when running the 2D model can be seen in table 11.2.

Model parameter	**Calibration**	**Validation**
Experiment [-]	C2	C1
Model domain height [cm]	30	29
Model domain length [cm]	180	180
Vertical discretization (dz) [cm]	0.5	0.5
Horizontal discretization (dx) [cm]	0.5	0.5
Model length [cm]	180	180
Temporal discretization (dt) [min]	1/1600	1/1600
Simulated time [min]	180	180
Rain intensity [cm^3/min]	785	679
Rain Duration [min]	76	57
Rain length* [cm]	100	100
Pipe drainage coefficient [cm^3/min/cm]	6.55	6.55
Equivalent membrane conductivity [cm/min]	0.996	0.858
Used for result in figures	11.9, 11.11, 11.12 and 11.14	11.10, 11.11 and 11.13

Table 11.2: Parameters used for the 2D model in the validation and calibration. *Length of the applied rain, 100 cm is equivalent to the central 100 cm of the total 180 cm model domain length.

The soil parameters used for both model can be seen in table 11.3. The soil parameters are the same in both the 1D and 2D models. The soil water retention curve, K-θ curve and K-ψ curve for the calibrated soil parameters can be seen in section 13.2.3

Soil parameter	**Initial**	**Calibrated**
Sat. vol. water content (θ_{sat}) [cm^3 H_2O/cm^3 soil]	0.434	0.434
Campbell b (b) [-]	2.1	2.0
Air entry suction (ψ_e) [cm H_2O]	-16	-23
Sat. hydraulic conductivity (K_{sat}) [cm/min]	0.33	0.33
Used for result in figures [-]	11.1, 11.3, 11.4 and 11.9	11.1 - 11.14

Table 11.3: Initial and calibrated soil parameters used for the 1D and 2D model.

11.2 Phase 1 result used for all model results and comparison to measured data

The phase 1 result from the 1D model is shown in figure 11.1. The shown phase 1 result for the calibrated soil parameters is used as the initial condition for all shown phase 2 results. It is evident from the figure that the modelled capillary fringe is truncated for both sets of soil parameters as the volumetric water content exceeds the water content at field capacity in the top of the modelled sandbox at approximately 34 cm. Moreover, due to the suction being linear, it is evident that the water content in phase 1 had reached equilibrium. In order to evaluate whether the initial conditions were correctly determined, the phase 1 results from the 1D model were compared to measured data from the column experiments conducted by Hedevang and Sørensen [2023] and to measurements of water content in the sandbox sampled during excavation of the sandbox. Figure 11.2 shows the modelled volumetric water content compared to what was measured throughout the sandbox during the excavation. Here, the data

was normalized due to the collapse of large pores during sampling. The normalization used the gravimetric water content measured near the datum of the sandbox as the normalization factor assuming that specific measurement to be fully saturated. The figure shows that the modelled water content generally lies within the measured range of water content when the nomalized data is considered.

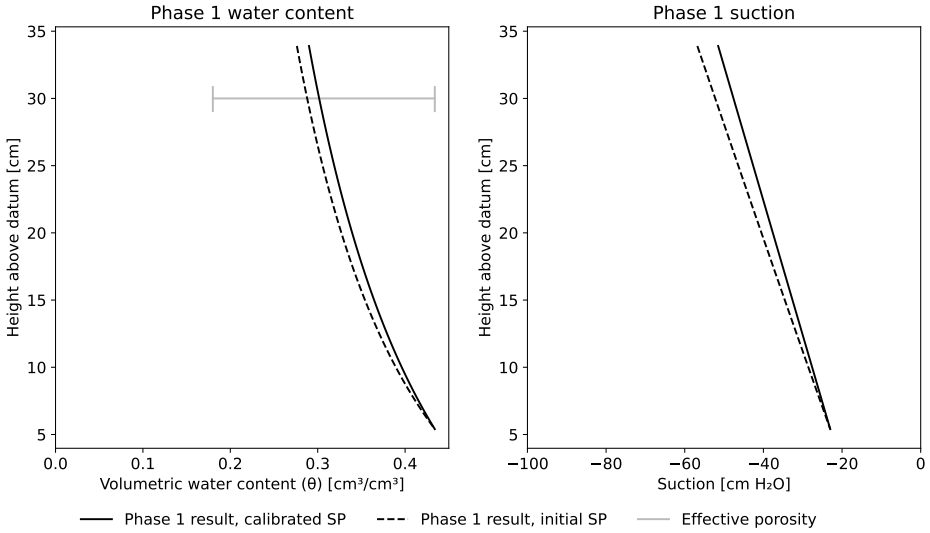

Figure 11.1: Phase 1 modelled water content and suction in the sandbox for both the initial and calibrated soil parameters compared to the effective porosity. SP = soil parameter.

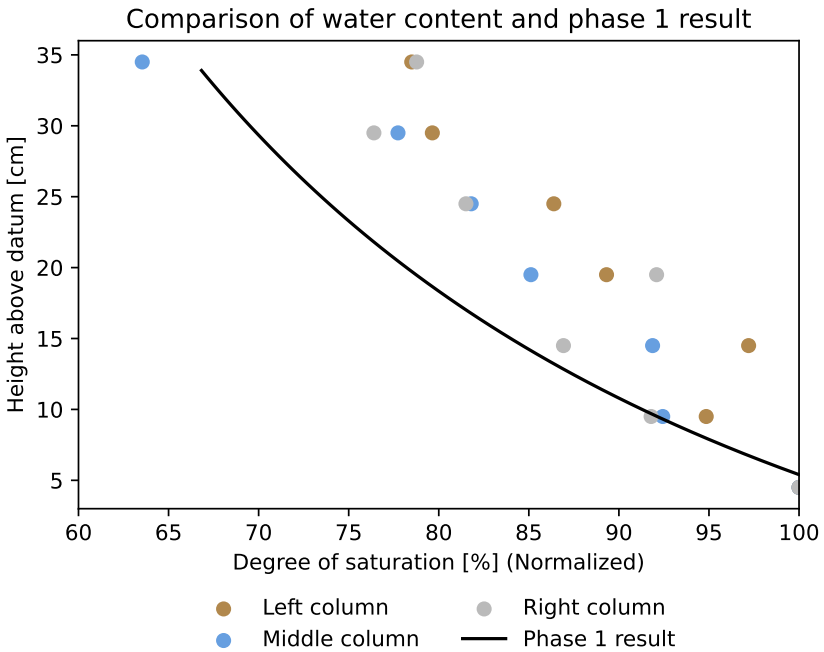

Figure 11.2: Phase 1 modelled water content compared to the measured water content during the excavation of the sandbox. The measured gravimetric water content was normalised using the measured water content near datum of the sandbox as the normalization factor assuming saturation. The modelled water content was normalised based on the water content at saturation.

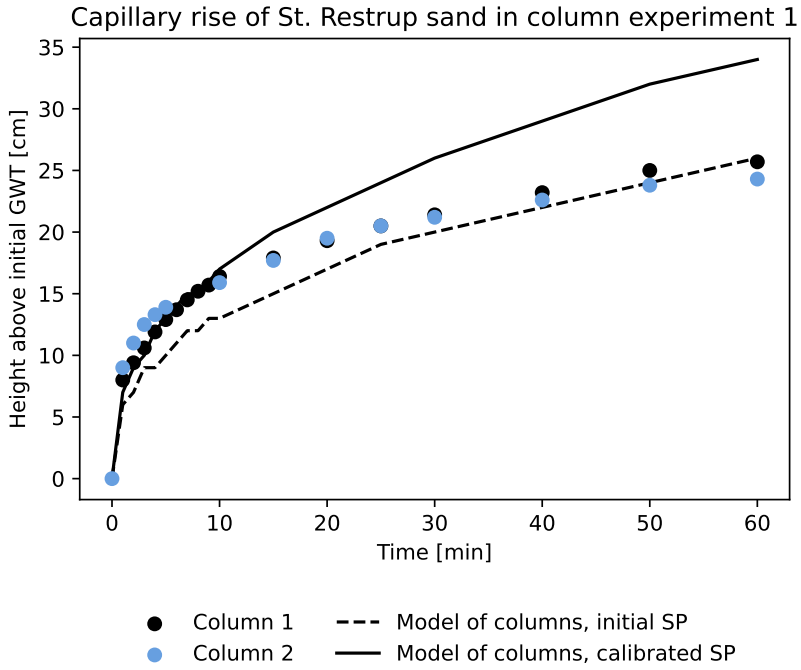

Figure 11.3: Capillary rise modelled with the 1D model compared to the column experiments. The model was run with an initial gravimetric water content of 4%. SP = soil parameters, GWT = groundwater table.

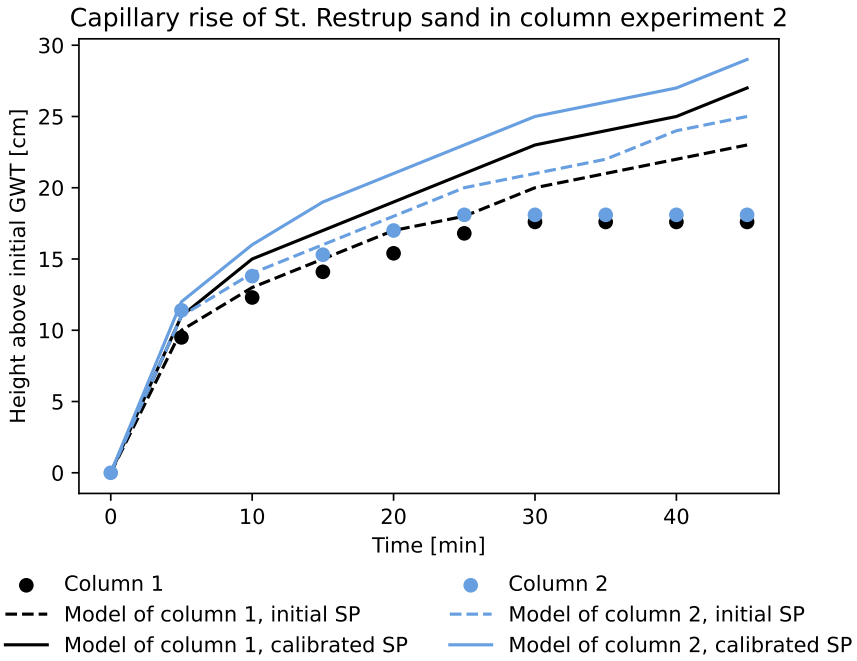

Figure 11.4: Capillary rise modelled with the 1D model compared to the column experiments. The model was run with an initial gravimetric water content of 3.56% in column 1 and 6.41% in column 2. SP = soil parameters, GWT = groundwater table.

Figures 11.3 and 11.4 show the comparison between the phase 1 result of the 1D model and the column experiments. As evident from the figures, the calculations from phase 1 with

calibrated soil parameters show a greater height above initial groundwater table for both column experiment 1 and 2. The model of column experiment 1 with the initial soil parameters is closest to the observed groundwater increase.

11.3 The 1D model calibration and validation

The calibration and validation of the models were quantified by comparing the measured and modelled water level along with the outflow volumes. Here, the measured and modelled water levels for the calibration and validation of the 1D model are shown in figures 11.5 and 11.6. It is evident from the figures that the model is able to replicate the groundwater dynamics observed in the experiments. The validation result shows a slight delay in both the increase and decrease compared to the calibration result. Moreover, the velocity of the groundwater rise decreases when nearing the drainage area in the sandbox experiments which is not replicated with neither the calibration nor validation result.

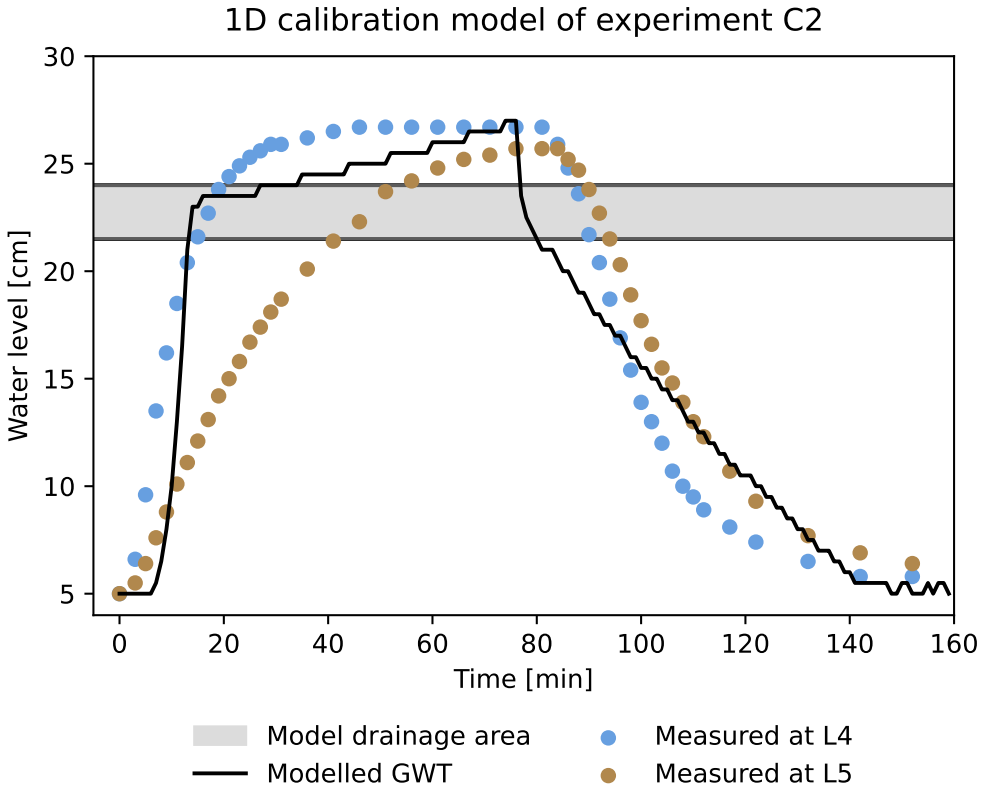

Figure 11.5: Result of level meters from the 1D model calibration. GWT = groundwater table, L4 = level meter 4, L5 = level meter 5. For location of level meters, see figure 6.1 on page 45.

The outflow volumes from the calibration and validation are seen in figures 11.7 and 11.8. The figures show that the 1D model does not accurately estimate neither the outflow dynamics nor the distribution of the outflow volumes from both the drain pipe and the chamber outlets. This applies to both the calibration and validation result.

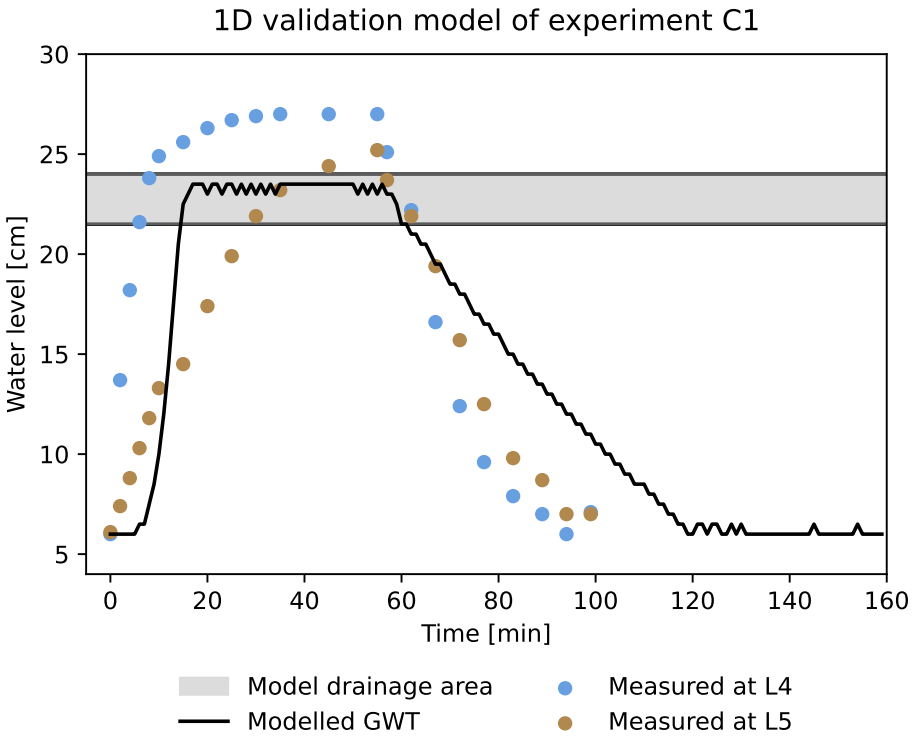

Figure 11.6: Result of level meters from the 1D model validation. GWT = groundwater table, L4 = level meter 4, L5 = level meter 5. For location of level meters, see figure 6.1 on page 45.

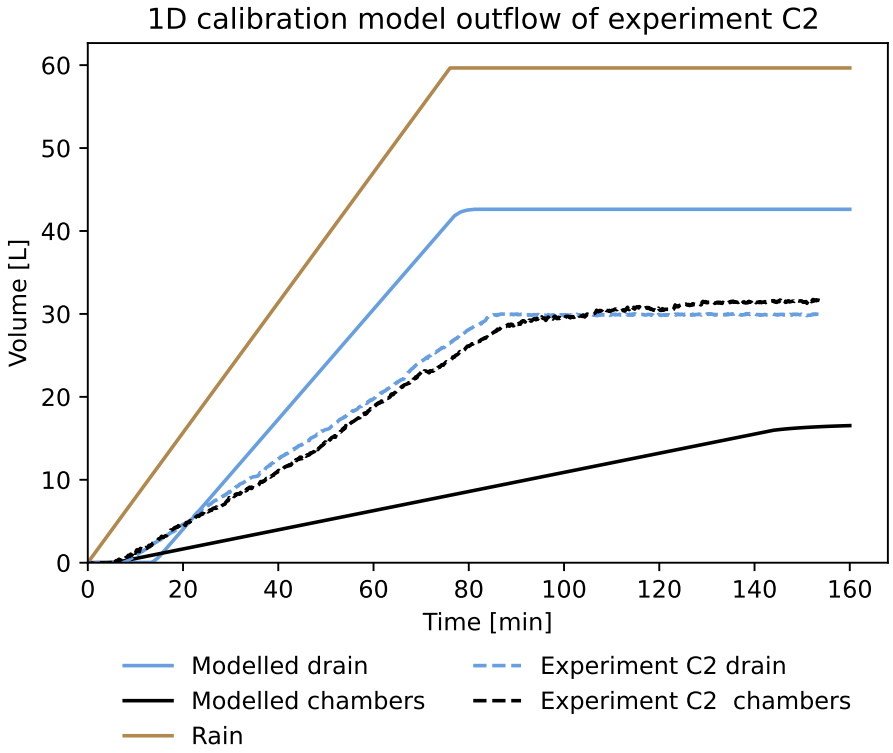

Figure 11.7: Calibration result of the in- and outputs from the 1D model calibration. The model was run for 160 min to allow the model to fully drain.

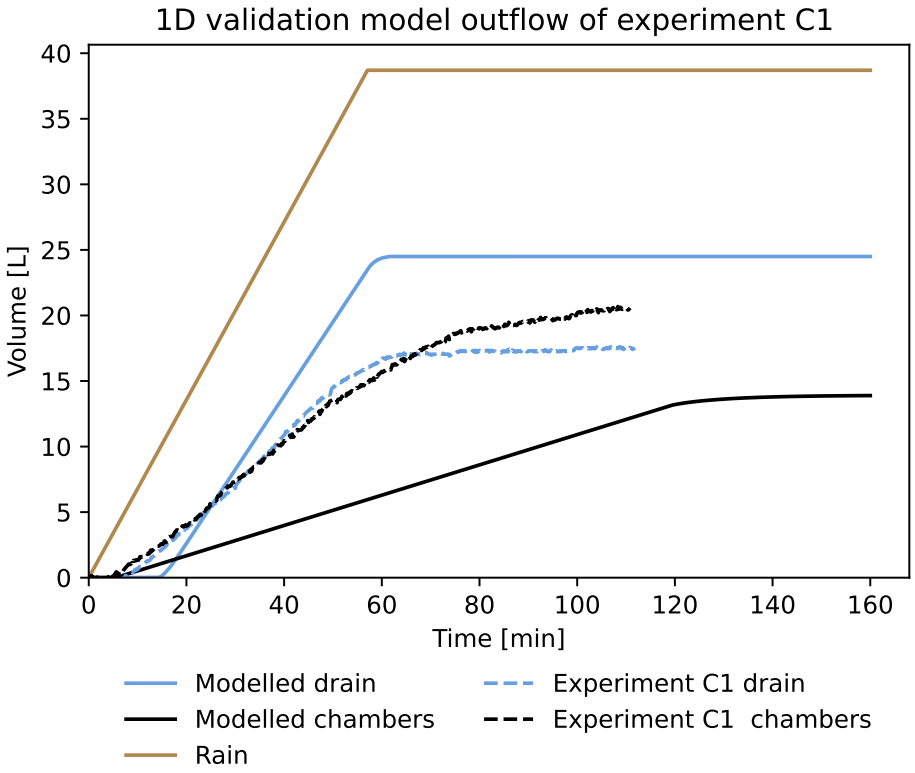

Figure 11.8: Result of the in- and outputs from the 1D model validation. The model was run for 160 min to allow the model to fully drain.

11.4 The 2D model calibration and validation

The 2D model was an attempt to replicate the dynamics caused by horizontal flow which the 1D model could not represent. The calibration and validation were also quantified by the water level and outflow volumes same as for the 1D model.

The calibration of the 2D model based on the water level along with a model run with the initial soil parameters is shown in figure 11.9. As evident from the figure the model follows the dynamics of the groundwater table closely above the pipe in L2 through L4 and generally reaches the same water level as measured in the experiment, except in L6. Moreover, the model run with the initial soil parameters show that the calibration of the soil parameters primarily altered how fast the groundwater table responded to the rain. In addition, it is evident that the modelled water level has a quick initial drop as soon as the rain stops while the measured doesn't.

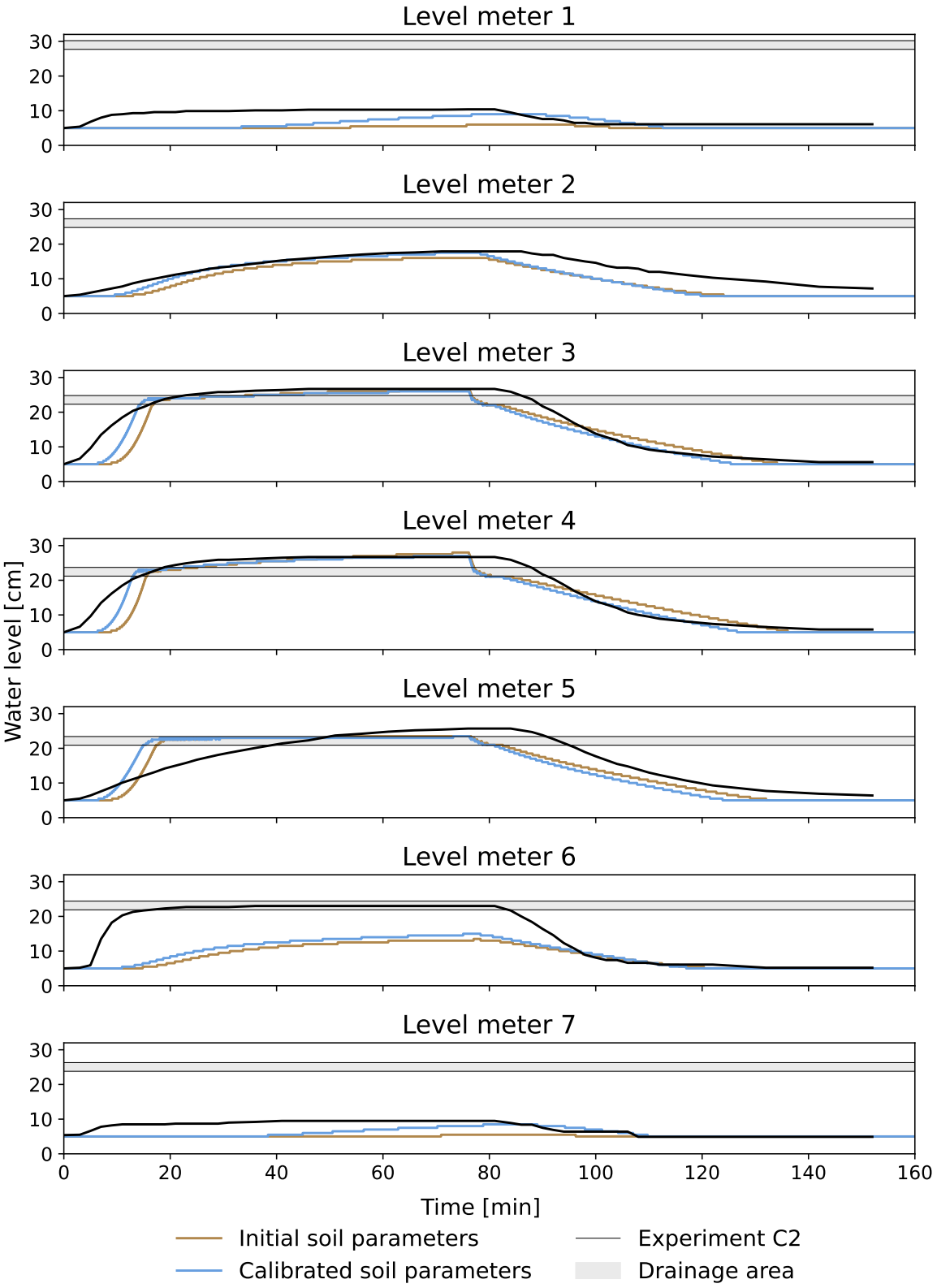

Figure 11.9: Result of level meters from the 2D model calibration. For location of level meters, see figure 6.1 on page 45. C2 = Cold experiment 2.

The measured and modelled water level for the validated 2D model is presented in figure 11.10. In general, the model predicts the total water level, though it does not follow the water table as closely as in the calibration.

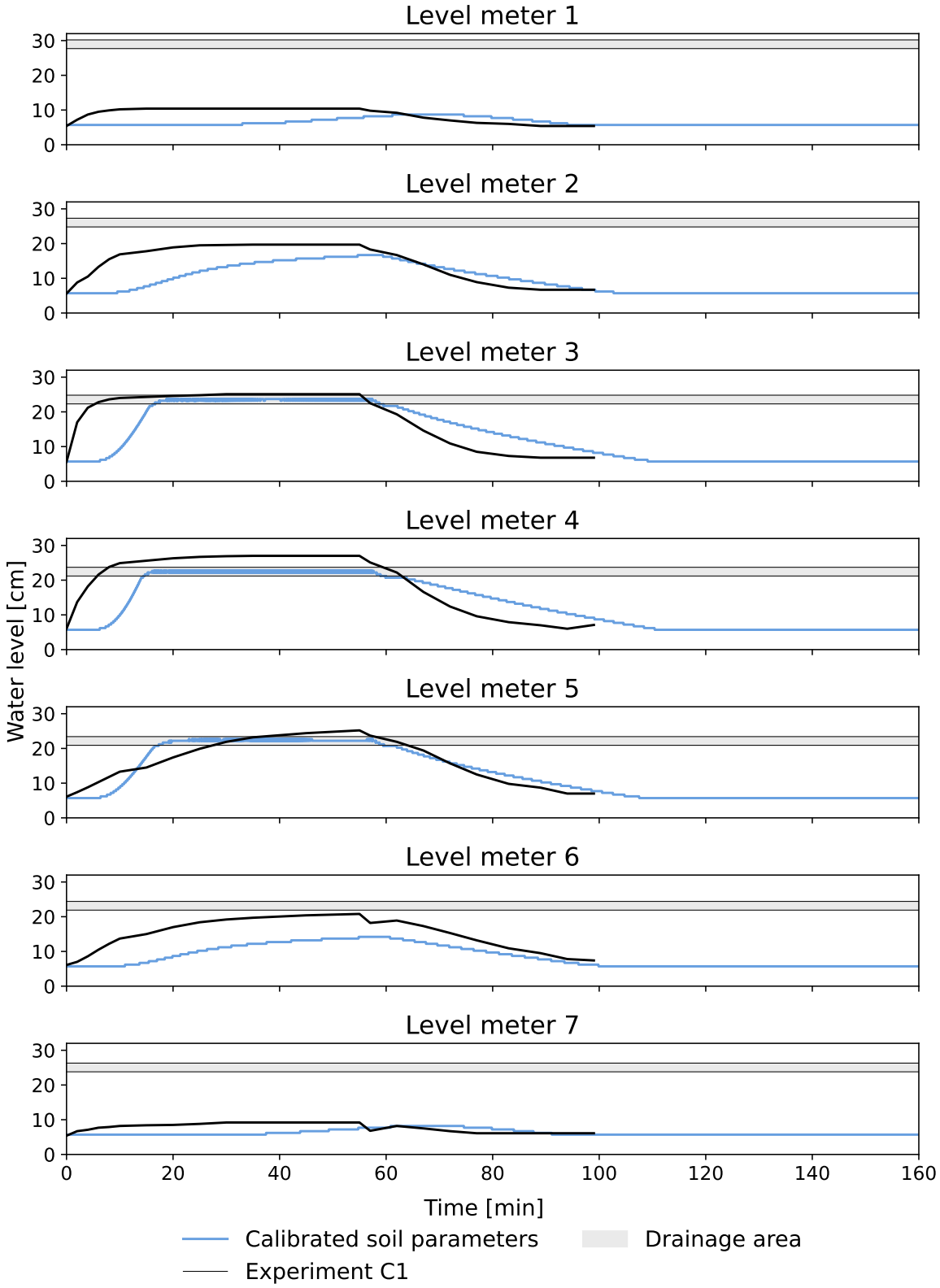

Figure 11.10: Result of level meters from the 2D model validation. For location of level meters, see figure 6.1 on page 45. C2 = Cold experiment 2.

The modelled water levels throughout the sandbox is shown in figure 11.11 for the calibrated and validated model. Here, it is seen that the increase of the water level in the center of the sandbox happens rapidly while the horizontal distribution of the water is much slower. Moreover, the initial decrease of water below the drain pipe is also fast, where the decrease slows down after reaching below the drain pipe. The effect of the drainage by the pipe is also evident from the extent of the groundwater, as the water reaches above the drainage area in the calibrated model, but is fully drained in the validated model.

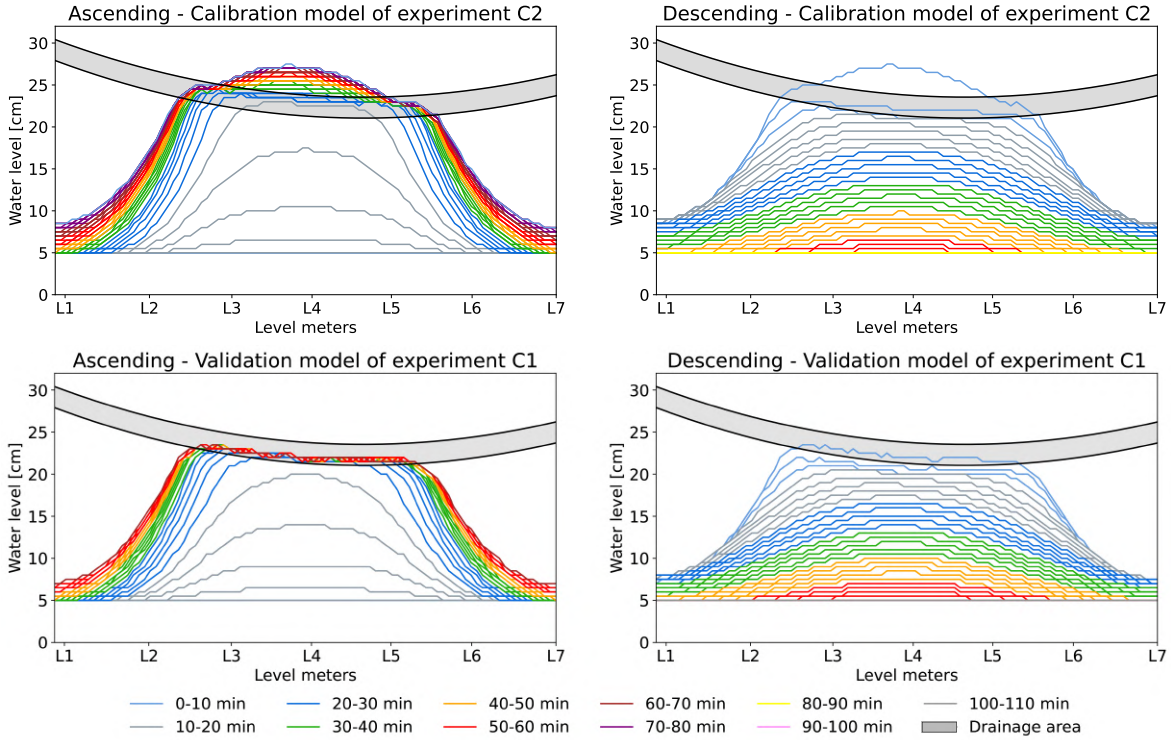

Figure 11.11: Shape of the groundwater table over time from the 2D model. The color intervals change for every new 10 minutes, i.e. a measurement at 10 min is grey instead of blue. For placement of water level meters, see figure 6.1 on page 45. C1 = Cold experiment 1, etc.

The outflow volumes were also compared for the calibration and validation as seen in figures 11.12 and 11.13. In general, the dynamics of the outflow is not replicated with the 2D model, where the outflow from the chambers is too slow while the drainage by the pipe is too fast. However, the total volumes removed by each are close to the measured volumes in the calibration model and accurately replicated in the validation model.

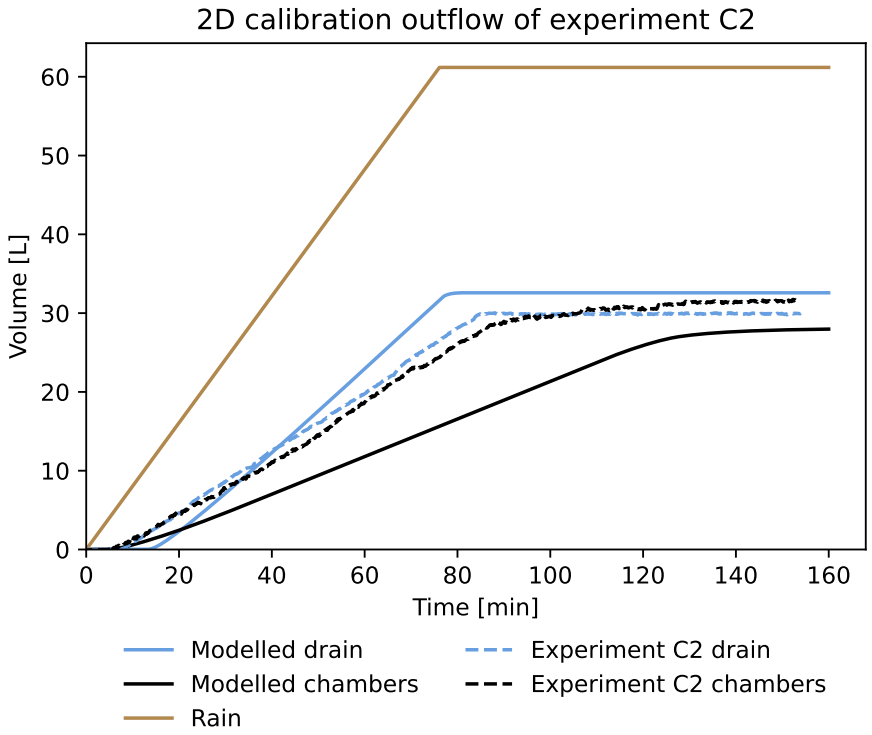

Figure 11.12: Result of the in- and outputs from the 2D model calibration. The model was run for 160 min to allow the model to fully drain. C2 = Cold experiment 2.

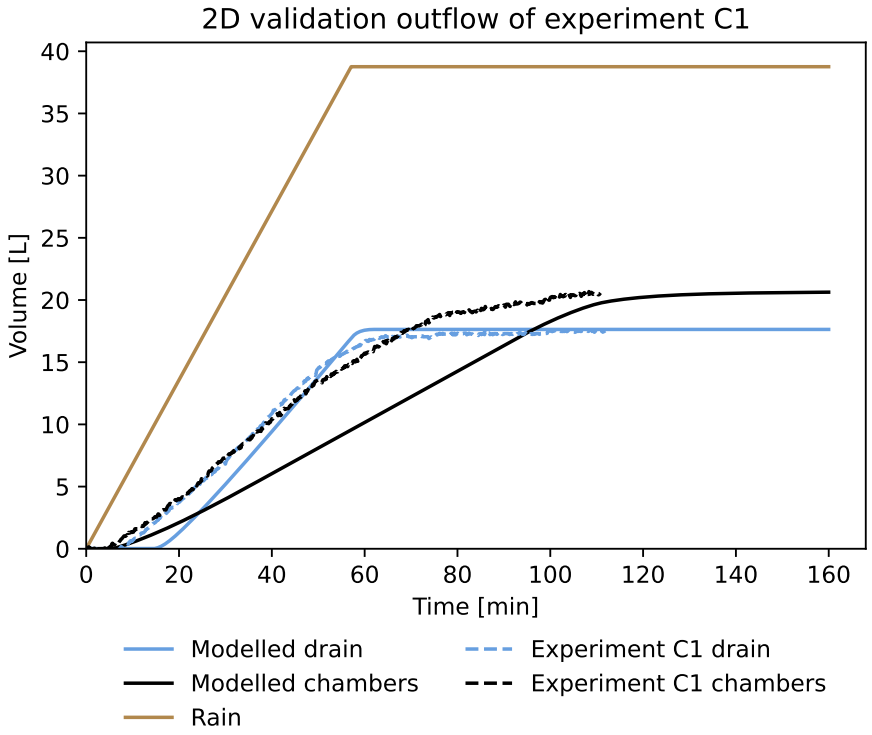

Figure 11.13: Result of the in- and outputs from the 2D model validation. The model was run for 160 min to allow the model to fully drain. C1 = Cold experiment 1.

11.5 Comparison of the result from the 1D and 2D model calibrations

As presented above, neither the 1D nor 2D model were able to replicate the velocity of the increase in groundwater level, which was the purpose of the 2D model. Therefore, in order to see the effect of using a 2D model compared to a 1D on the modelled groundwater table the results of the two calibrations are compared in figure 11.14. Here, the groundwater table is from the center column of the 2D model. It is seen, that the expansion to a 2D model altered the increase above the drain pipe as well as the descend of groundwater table, but did not have any effect on the increase in groundwater table before reaching the drain pipe.

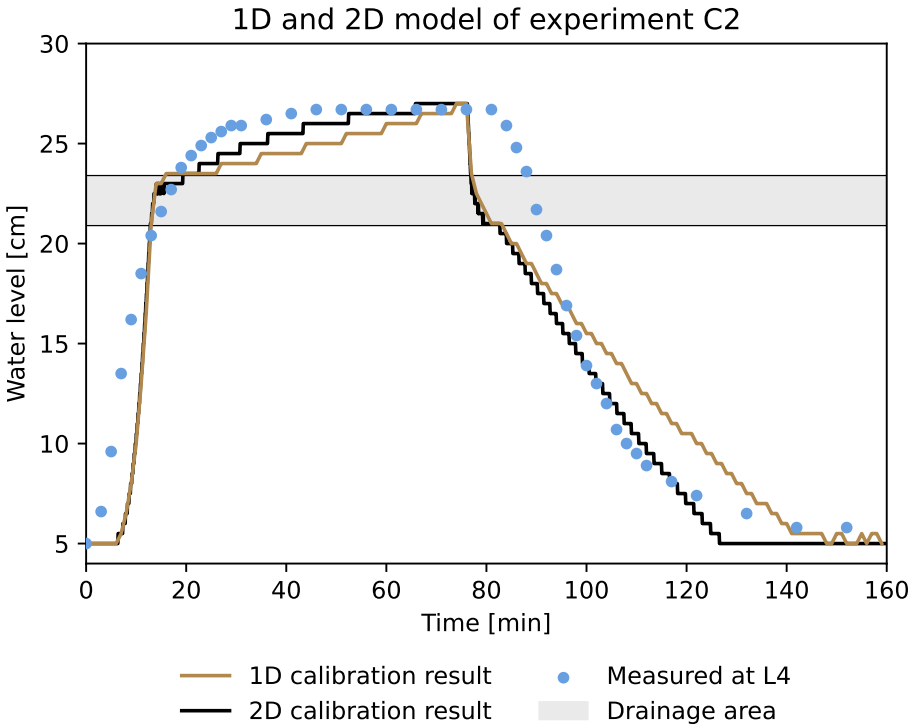

Figure 11.14: Comparison of the 1D and 2D model calibration results. C2 = Cold experiment 2, L4 = level meter 4. For location of level meters, see figure 6.1 on page 45.

When considering the modelled groundwater rise and dynamics it is important to consider the underlying causes which can aid in explaining the result of the simulation. The result of using the 1D and 2D numerical models of water flow and groundwater rise in unsaturated soil are therefore discussed in the following chapter.

12 | Discussion of the results from the numerical models of water flow and groundwater rise in unsaturated soil

In this chapter the 1D and 2D numerical models of water flow and groundwater rise in unsaturated soil presented in chapter 9 and 10 and the result hereof presented in chapter 11 are discussed. Here, the focus will be on answering the third question: *"Utilizing experimental results, how can a 1D and 2D numerical model of water flow and groundwater rise in unsaturated soil be employed to model the dynamics of the sandbox experiments?"*

12.1 Differences in using initial and calibrated soil parameters in the numerical model

The effect of calibrating the soil parameters compared to using the initial parameters estimated from measurements was shown in the phase 1 result, the capillary rise experiment and in the 2D model of the sandbox experiment. For the phase 1 result the calibrated soil parameters resulted in a slightly higher volumetric water content compared to initial soil parameters. This is to be expected since the calibrated soil parameters has a numerically larger air entry with only a minimal difference in Campbell b, resulting in better retainment of water. This ability to retain water can also be seen in the result of the comparison with the capillary rise experiment. Here, the calibrated soil parameters result in a faster and larger increase in the volumetric water content compared to the initial soil parameters. The minimal difference between the two phase 1 results is also reflected in the soil water retention curves for the two sets of soil parameters.

For the phase 2 result the calibration of the soil parameters affected the time between addition of rain and the increase of the observed groundwater rise, but only slightly altered the velocity of the groundwater rise. It had no effect on the maximum groundwater level reached. Since neither of the soil parameter sets could replicate the velocity of the increase but still reached the same water level, the calibration of soil parameters did not significantly change the outcome of the model. Consequently, this indicates that as long as the soil parameters are sufficiently measured, they can be used and the model still shows good results without calibration. This is due to the main difference between the initial and calibrated soil parameters being the increase in groundwater table which happened faster with the calibrated soil parameters due to a larger water content of phase 1.

12.2 Representativeness of the initial conditions determined by phase 1 of the model

In order to model groundwater table rise it is paramount to correctly model the extent of the capillary fringe in phase 1 as a wrong estimation affects the velocity and extent of the groundwater rise.

The comparison of phase 1 with the collumn experiments showed better agreement between the measured rise and modelled rise when using the initial soil parameters. However, the calibrated soil parameters still followed the general dynamics of the capillary rise and their fit with the measured capillary rise was deemed sufficient. Especially when considering that a major difference between the column experiment and the modelled capillary rise was the column experiment being dependant on visible change in the soil water content, which likely did not coincide with the criterion set in the model of an increase of 0.05 cm^3 H_2O/cm^3 soil. Therefore, the criterion used in the model was not necessarily representative of the experiment. This was observed since changing the criterion for both the initial and measured soil parameters achieved better fits with the measured capillary rise. However, this could easily result in an over fitting of the data, why a small criterion of 0.05 cm^3 H_2O/cm^3 soil was chosen.

The phase 1 results were further compared to the water profile taken in a column in the sandbox during excavation. Here, the phase 1 results showed a good agreement with the measurements, though the water content in the top soil lied in the low range of the measured water contents. However, since the sandbox was not wetted as extensively before the experiments as before the excavation, the top soil at the time of the experiments must have been more affected by air drying which further supports the phase 1 results being representative of the capillary fringe of the sandbox.

12.3 Evaluation of the calibration and validation of the model along with the most sensitive parameters in the calibration

After evaluation of the phase 1 results, the model was calibrated and validated. Based on the calibration and validation results from both the 1D and 2D model it is evident, that the curvature of the groundwater increase in both models did not predict the measured curvature in any of the experiments. This curvature could not be replicated in any of the calibration attempts. In general, the changing dynamics between the experiment and the dynamics caused by the fracture in the right side of the sandbox made it difficult to calibrate and validate the model. For instance, one calibration result very accurately predicted the total outflow volumes over time, while its extent of the groundwater was nowhere near the measured extent. Thus, the final calibration was an attempt to both reach a good agreement between outflow volumes and extent of the groundwater table.

When calibrating the models it was found that the main controlling parameters were the pipe drainage coefficient and the equivalent membrane conductivity. Especially the pipe drainage coefficient was decisive for the extent of the groundwater table, and thus was calibrated in the 1D model by changing the decimals. The sensitivity of the pipe drainage coefficient resulted in the groundwater table not reaching above the drainage area in the validation in contrast to the calibration since the same value was used in both. This was a consequence of the

inflow into the pipe being heavily simplified in the 1D model. The simplification was initially thought to be partly responsible for the lacking decrease in velocity of the groundwater table right before reaching the drainage area in the model compared to what was observed in the experiments. Moreover, the lacking decrease was also initially theorised to be caused by horizontal movements in the sandbox experiments that distributed the water and decreased the velocity of the rise, which was the reasoning behind the expansion of the 1D model to a 2D model.

12.4 Ability of the 1D and 2D models to predict disproportionate groundwater increase and outflow volumes from the experiments

As shown in the comparison between the 1D and 2D model, the increase of groundwater before reaching the drainage area was almost identical in the 1D model and the center column of the 2D model and thus the expansion to a 2D model did not alter the dynamics considerably as initially expected. This is due to the center column of the 2D model behaving like a 1D scenario due to limited horizontal movement. Still, the 2D model enabled a prediction of the total water level along the length of the sandbox, although it also lacked behind in the initial increase of the groundwater like in the 1D model. The small discrepancies between the measured water level compared to the modelled was assumed to be caused by the inhomogeneity of the sandbox which was not included in the 2D model, for instance as evident from the sudden increase in water level in L6 during experiment C2 where the dynamics differed considerably compared to the rest of the experiments. Still, both models proved their ability to model the capillary fringe and the resulting disproportionate increase caused by the reverse Wieringermeer effect as observed in the experiments. Additionally, the decrease in water level was also accurately modelled in both 1D and 2D, though there was a slight delay in some of the experiments due to the formation of a top reservoir in the sandbox which did not occur in the model.

12.4.1 Potential improvement of prediction of groundwater increase by inclusion of hysteresis

The 1D and 2D models were able to replicate groundwater rise and decrease without including the effect of hysteresis. Here, hysteresis was not included due to a lack of a wetting curve of the soil. According to Khaled et al. [2011] hysteresis is important to include when modelling dynamics caused by the reverse Wieringermeer effect. Moreover, Lehmann et al. [1998] and Khaled et al. [2011] both showed model results with better agreement with measured results when including the effect of hysteresis in their models. Despite not having included hysteresis, the modelling results from this Master's thesis showed a good agreement between measured and modelled water level. However, as the model was run based on data from a drying curve, a better fit during increase in water table might have been achieved with a wetting curve. For instance, Khaled et al. [2011] showed a better fit with modelled increase in water table dependant on the amount of rain added when using the soil moisture profile from a wetting curve than from a drying curve. Therefore, the small delay before increasing the water table observed in the model compared to measured might have been avoided if a soil moisture profile from a wetting curve was used instead.

12.4.2 Differences in prediction of outflow volumes in the 1D and 2D model

As for predicting the outflow volumes, the removal by the drain pipe was far overestimated in the 1D model. This is due to the 1D model only taking into account removal from the drain pipe and the bottom, why surplus water from a saturated cell cannot move horizontally like in the 2D model. Therefore, these dynamics were far greater replicated with the 2D model where the total volumes and the distribution between the outflow from the chambers compared to the drain pipe was more accurate due to the horizontal distribution of the water. This also enlightens the advantage of applying a 2D model for modelling the experiment.

12.5 Summation of the 1D and 2D numerical models of water flow and groundwater rise in unsaturated soil

This part of the Master's thesis set out to answer the third question; *"Utilizing experimental results, how can a 1D and 2D numerical model of water flow and groundwater rise in unsaturated soil be employed to model the dynamics of the sandbox experiments?"*

The modelling of the experimental results showed that both the 1D and 2D model are able to model the disproportionate groundwater rise observed during the sandbox experiments. Here, the advantage of the 2D model is its ability to predict the water level along the entire length of the sandbox and not just in the center. As the groundwater increase further away from the center of the sandbox is more affected by horizontal movements, this cannot be replicated with the 1D model and requires a 2D model. Moreover, the outflow volumes further supported the need of a 2D model if the purpose of the model would be quantifying the volume drained by the pipe, as the 1D model did not accurately replicate the experiments with neither total volumes nor the velocity of the removal. However, the disadvantage of the 2D model is the more complex model domain which requires more knowledge of the modelled area while also increasing simulation time considerably.

In short, the 1D model is sufficient for modelling the disproportionate increase in groundwater table right beneath the applied rain, while the 2D model is required if the volume drained by the pipe has to be quantified or if the increase of groundwater outside the area of applied rain has to be modelled. As the screening tool for risk assessment of rain induced groundwater infiltration was centered around quantifying the groundwater increase beneath the applied rain the 1D model was deemed sufficient for the purpose. The screening tool is further elaborated in chapter 13.

Part IV :

Development of a groundwater infiltration screening tool and application of the tool in Beder

13 | Setup and input to the screening tool for risk assessment of groundwater infiltration into the sewer system in the case area Beder

A screening tool was developed for risk assessment of rain induced groundwater infiltration into leaky sewer systems based on the 1D numerical model of groundwater rise and flow into unsaturated soil presented in chapter 9. Here, the risk of groundwater infiltration was based on the sewer system either already being submerged or potentially becoming submerged. This chapter presents the setup, functionality and input data to the screening tool in order to answer the fourth question; "*How can the risk of groundwater infiltration into the sewer system in Beder be assessed by integrating the 1D model into a screening tool?*" The question is treated in chapters 13 through 16.

13.1 Purpose and functionality of the screening tool

Figure 13.1 illustrates the principles of the calculation and outputs of the screening tool along with the necessary inputs.

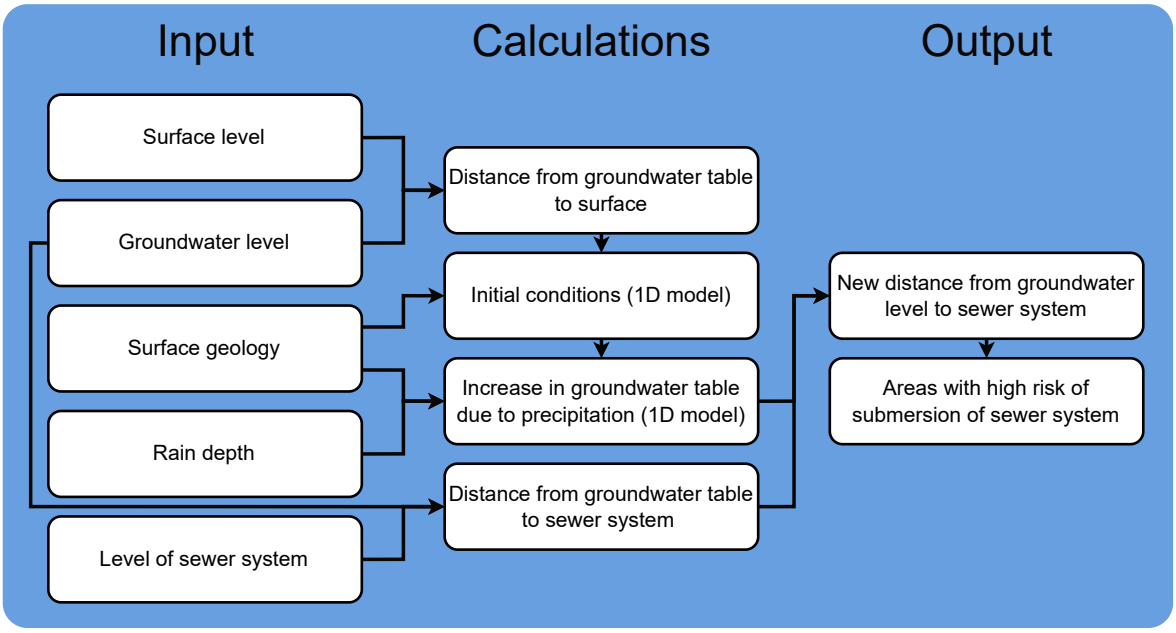

Figure 13.1: Concept of the input, calculations and output of the screening tool.

The purpose of the screening tool was to make a risk assessment of rain induced groundwater infiltration into leaky sewer systems based on a rain input defined by the user. The screening tool works by dividing the investigated area into a grid where the 1D model is applied onto

every grid cell to calculate the increase in groundwater table based on the rain depth. Thus, the calculation in each grid cell is independent of the other grid cells. Based on the level of the sewer system and the groundwater increase resulting from a rain event, the screening tool divides the area into three risk categories; "high risk", "medium risk" and "low risk" of groundwater infiltration. Here, the results from the risk assessment could be used for prioritizing what parts of the sewer system should be renovated first based on a specific return period of the rain. Furthermore, the results could be used to assess which parts of the sewer system would become submerged during a climate projected precipitation.

13.1.1 Implemented differences in the 1D model in the screening tool and model stop criteria

The 1D model served as the engine of the screening tool, however some changes were made compared to when the 1D model was used to model the sandbox experiment. Firstly, the drainage through the open lower boundary and the drainage from the pipe were removed from the 1D model. These were removed due to the desire of calculating the increase in groundwater table solely based on the capacity of the capillary fringe and thus without drainage. Moreover, the drainage through the open lower boundary in the 1D model of the experiments was a calibration parameter, which would have created an uncertainty of which drainage to allow for the different soil types in the screening tool.

Secondly, the scale of the sandbox model was a 39 cm column, which necessitated a fine vertical discretization, why 0.5 cm was used. However, as the screening tool was intended to model columns of several meters, the vertical dicretization was changed to 10 cm. This was justified since the most precise accuracy class for Danish pipes is 25 cm [Styrelsen for dataforsyning og infrastruktur 2023]. This results in the uncertainty of the pipe placement being larger than the vertical discretization. Therefore, the uncertainty of the risk assessment would be at least 25 cm nonetheless. This change in vertical discretization greatly improved simulation time as the amount of required cells for each 1D model in each grid cell was reduced by at least a factor 20. To further increase the efficiency of the model the variable time steps explained in section 9.2.1 was implemented in the screening tool. This resulted in the modelling of clay being much faster than sand due to the much larger allowable time steps for soil with a lower hydraulic conductivity, see equation (9.11) on page 82.

The screening tool was run as a steady state model where only the rise in groundwater table was desired. Here, the time it takes the groundwater table to reach a steady state was not considered. When running the 1D model with the screening tool the following three stop criteria were used. When applied, the stop criteria result in the MMS-model in the specific grid cell stopping and the last calculation being saved as the result.

1. Maximum change in the volumetric water content in all column cells between two consecutive time steps is less than 10^{-7} for 100 consecutive time steps.
2. Model has reached maximum user defined simulation time of 100000 minutes
3. Grid cell has achieved the high risk category

The first break criteria is equivalent to the model having achieved a steady state and the groundwater table having achieved its maximum height. The second criteria was implemented as a fail safe in order to avoid the calculations getting stuck on a grid cell if the steady state

criteria was unachievable. In order to make the screening tool more efficient the third break criteria was also implemented. In the case where the high risk criteria has been achieved no further calculations are necessary, as the result would not change.

13.1.2 Quantification of the risk categories

The three risk categories of the risk assessment "high risk", "medium risk" and "low risk" were represented with the colors red, yellow and green, respectively. The principle behind the quantification of the risk is shown in figure 13.2.

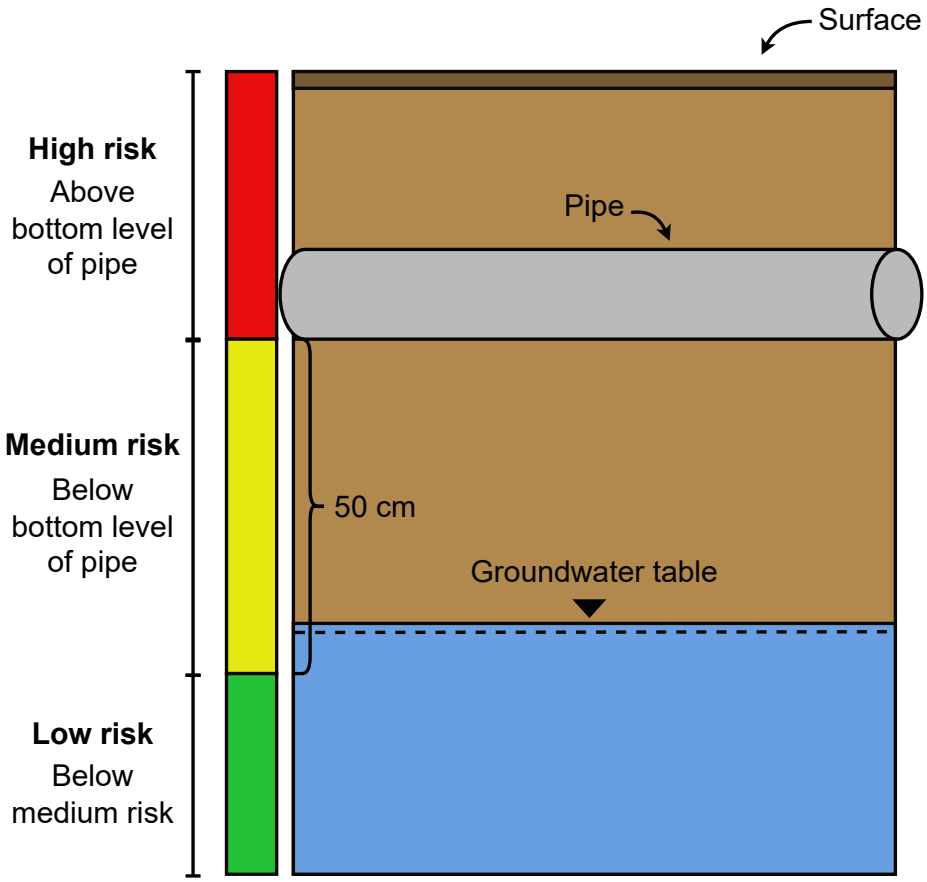

Figure 13.2: Conceptual sketch of how the risk categories were quantified. The groundwater table in this example would yield a medium risk.

Figure 13.2 shows that the high risk category extends from the surface to the bottom of the pipe, as groundwater needs to be above the pipe in order to infiltrate according to the hypothesis of water only infiltrating from below. The medium risk starts at the bottom level of the pipe and extends 50 cm beneath it. This threshold comprises the uncertainty of both the location of the pipe along with the uncertainty in the rise of the groundwater table. For instance, the rise of the groundwater table is computed with 10 cm discretization and thus a certain margin of error must be accounted for in the medium risk zone. As the groundwater rise in the screening tool does not incorporate drainage, it was perceived as the maximum rise, which is why the high risk zone does not start beneath the bottom level of the pipe.

13.1.3 Assumptions of the screening tool

In order to make the screening tool accessible some general simplifications and assumptions were made. Firstly, the screening tool does not include drainage due to either vertical or horizontal movement of the water. Therefore, all water added in a cell will either contribute to groundwater rise or increase the water content in the capillary fringe. Secondly, the screening tool assumes a drainage coefficient of 0 and thus all added rain is assumed to infiltrate into the soil. This results in a larger amount of water contributing to groundwater rise than what would be observed in reality, as much of the water would be removed by rain water pipes. Further improvement of the screening tool could implement a drainage coefficient in the area and thereby account for the water volume removed by storm water pipes. Thirdly, the screening tool assumes that the geology from surface to groundwater is described by the surface geology in that point, which is a notable simplification. Here, the uncertainty of this assumption increases as the modelled distance increases, especially in areas with varying geologies. However, this simplification enables the model in any area of Denmark where the surface geology is mapped instead of requiring extensive data sampling of bore profiles. Therefore, the simplification eases the task of gathering the input data for the screening tool.

13.2 Input data to the screening tool and introduction to the case area Beder

As shown from figure 13.1, the required inputs for the screening tool are knowledge of the analyzed area's surface level, groundwater level, surface geology and level of the sewer system. The case area used for developing the screening tool was the city of Beder due to the focus of Ternært Vand project group [2024] being centered around Beder. Despite this, data gathered by Ternært Vand project group [2024] showed strong correlation between rainfall and amount of water pumped in the sewer system. Combined with a high groundwater table, this indicates that the extraneous water in the sewer system originates from groundwater infiltration.

In order to monitor the groundwater Ternært Vand project group [2024] established 7 monitoring borings in Beder and monitored the groundwater levels starting from august 2023. At the time of writing the monitoring was still active. The location of the borings along with the wastewater sewer system are shown in figure 13.3. The rain water pipes were not included in the calculations as these do no contribute water to the wastewater treatment plants. Therefore, they are outside the scope of the problem with extraneous water handled in this Master's thesis.

Bore profiles from the monitoring borings showed the geology consisting mainly of sand and clay. Moreover, as shown in figure 13.4 the surface geology in Beder and the surrounding area predominantly consists of clay with some areas of sand and gravel. A comparison of the surface geology with the surface level in figure 13.5 shows the sand generally being located in the lowest area of Beder. Moreover, the surface level around Beder generally lies around 30-55 m (DVR90). The difference in surface level occurs over small distances and thus the landscape of Beder is hilly.

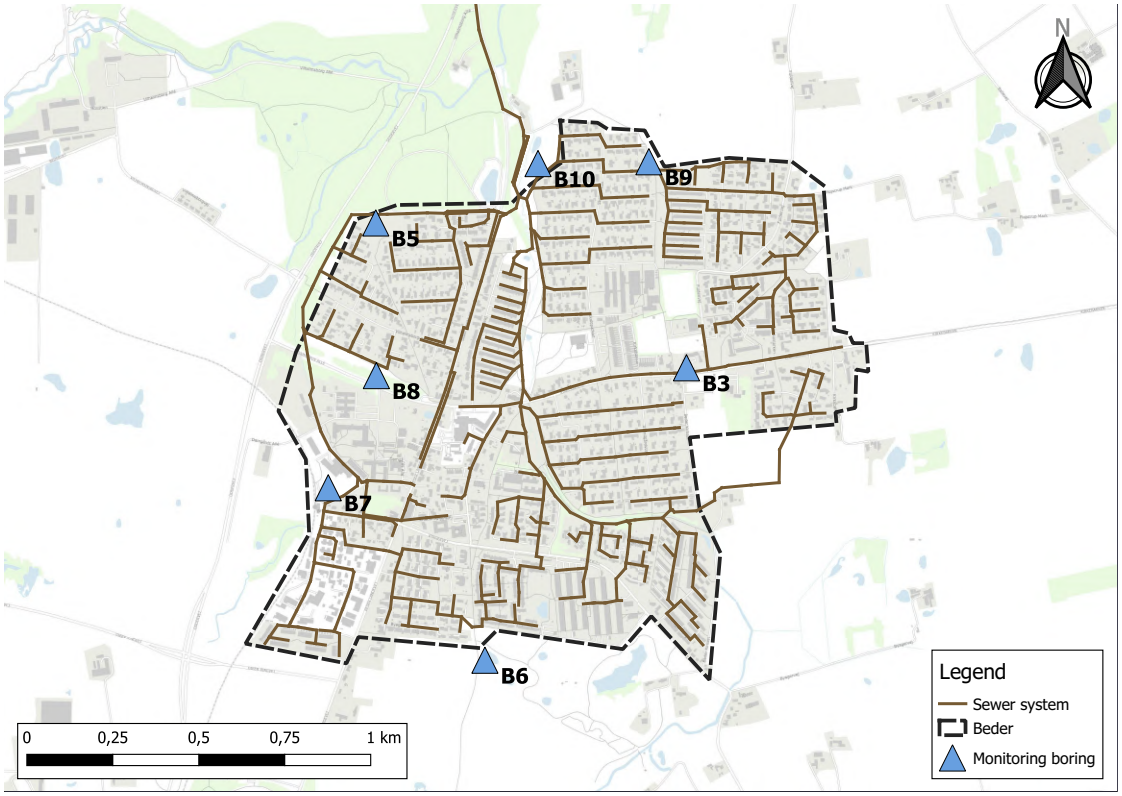

Figure 13.3: Wastewater sewer system and location of the 7 monitoring borings established by Ternært Vand project group [2024] in Beder.

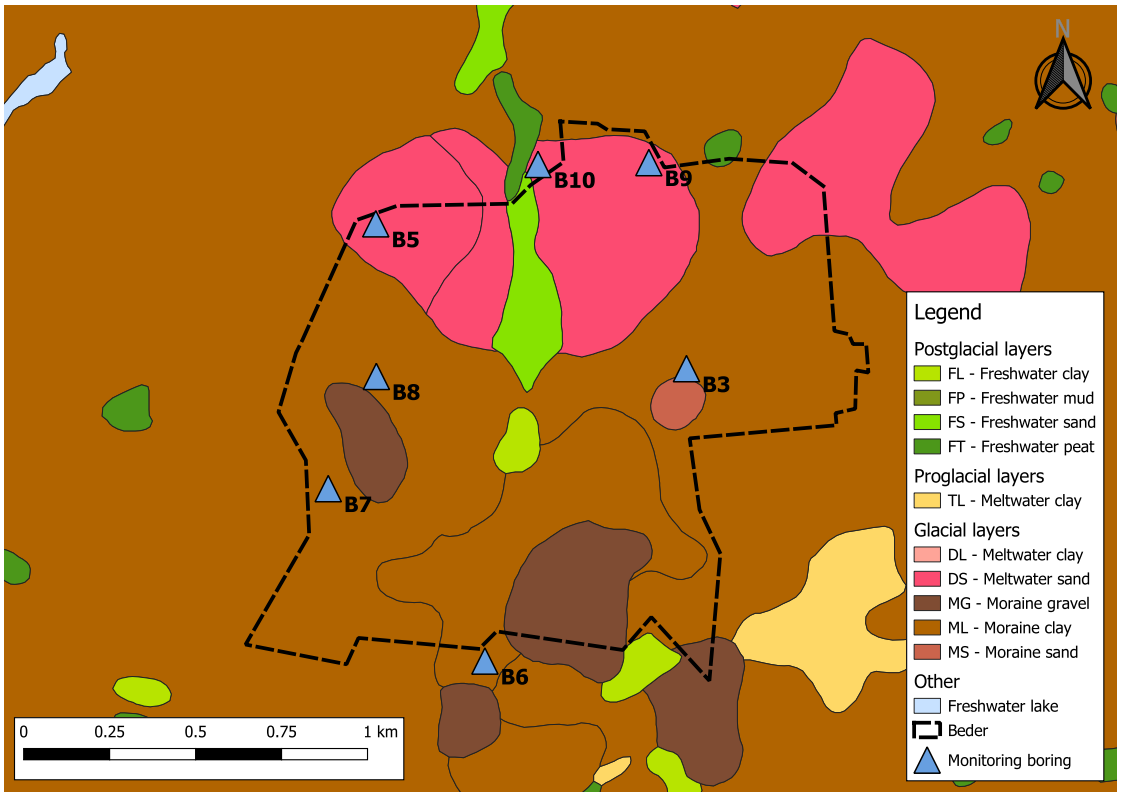

Figure 13.4: Surface geology in the city of Beder. Measured approximately 1 m below surface [GEUS 2024].

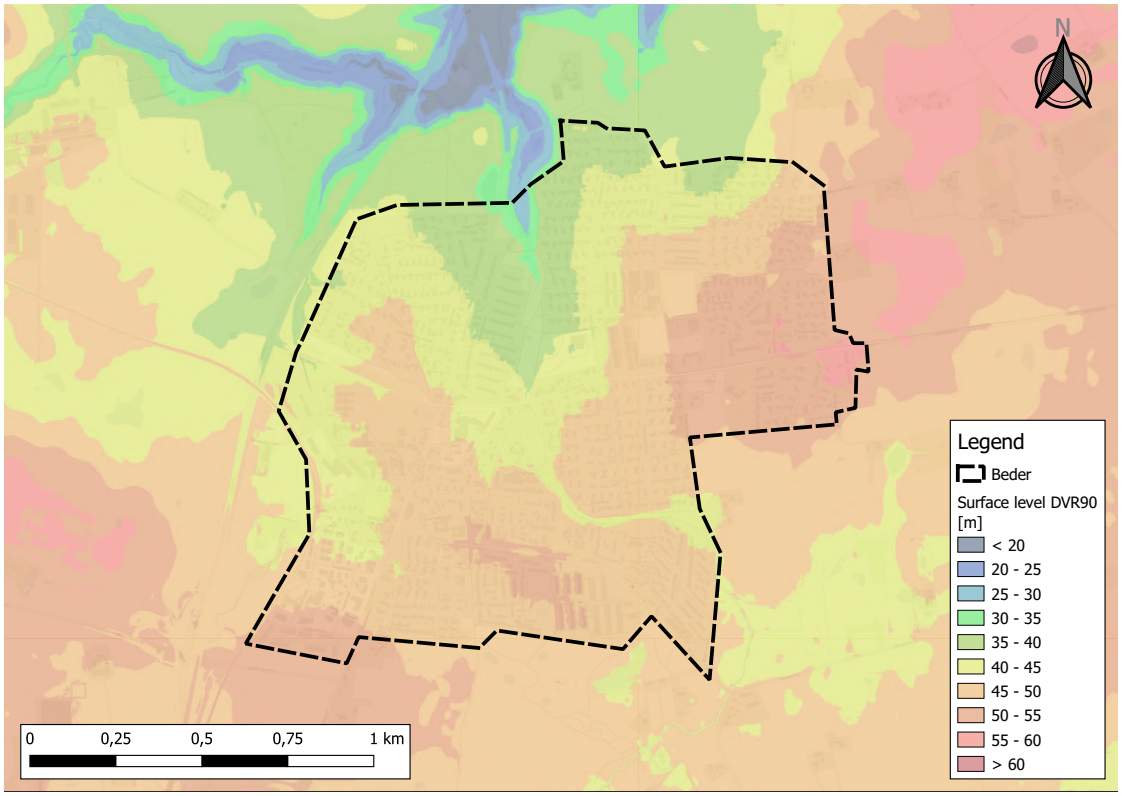

Figure 13.5: Surface level of the area around Beder in DVR90. Data from Dataforsyningen [2024a].

13.2.1 Groundwater table used for the Beder area

The last needed input for the screening tool was the groundwater level in Beder. Here, data from the HIP (Hydrological Information and Forecasting System) model was used. The HIP model has been calibrated and validated against data from approximately 300 streamflow stations, thousands of observation wells and thousands of lakes. The calibration of the model gave special attention to data for near surface groundwater to achieve the best possible accuracy for it [Henriksen et al. 2020].

For the screening tool the winter groundwater from the high-resolution machine learning version describing the depth to near-surface groundwater based on historical periods (DK-model HIP10m ML) was used [Henriksen et al. 2020]. Here, the groundwater table is the statistically frequent winter groundwater table. The used groundwater table is shown in figure 13.6 along with the 7 monitoring borings by Ternært Vand project group [2024]. From the figure it can be seen that the winter means (October - March) in the monitoring borings differ in varying degrees from the HIP data.

The mean of the difference of the distance below surface for the groundwater table for both the calculated winter mean for the 7 monitoring borings in Beder and the frequent winter value from the HIP model is 1.33 m and the standard deviation is 1.17 m. Considering the mean and standard deviation there is in general a large difference between the HIP data when compared to the measured value in the monitoring borings. This is expected since the HIP model is a national model and therefore the accuracy on a local scale can be limited and can vary between areas. The area south of Aarhus where Beder is located is one of the least

accurate regions of the model due to its high content of moraine clay and varying topography [Dataforsyningen 2024b]. Additionally, the mean error per well in the majority of the country is between ± 2m for the near-surface groundwater [Henriksen et al. 2020].

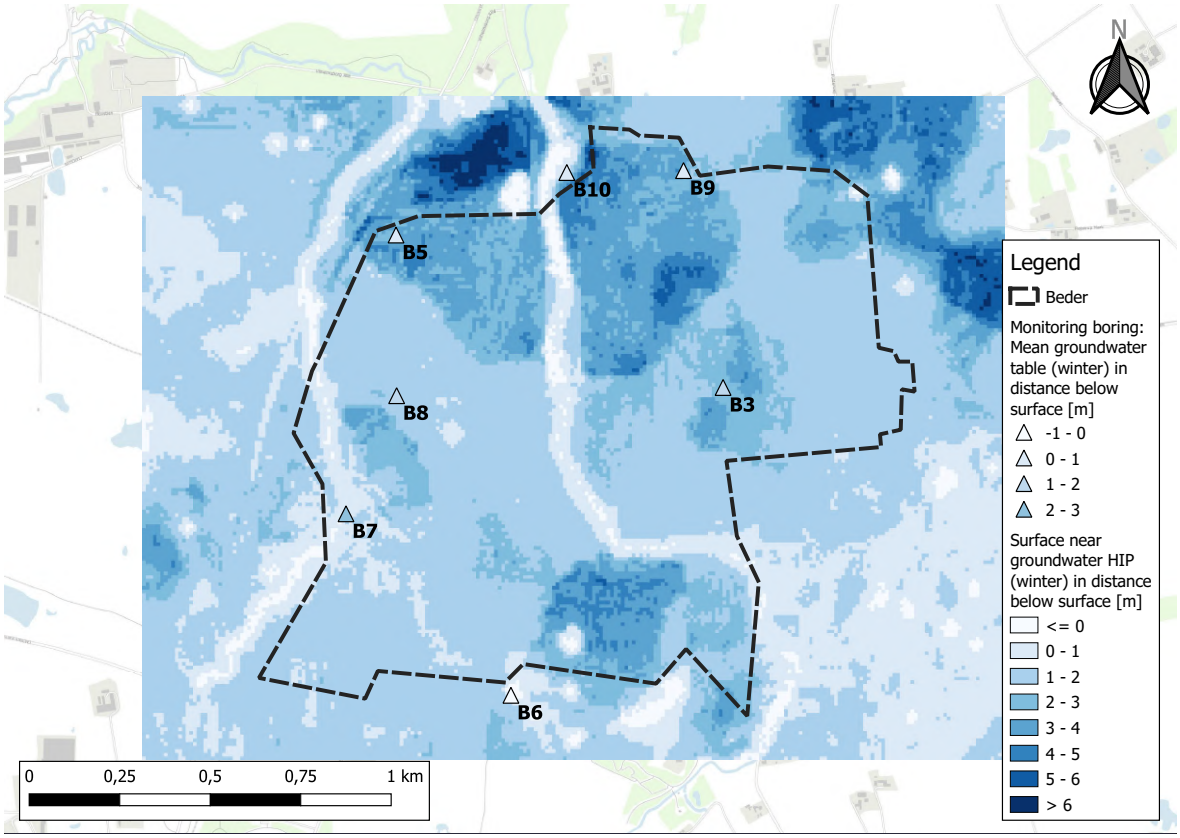

Figure 13.6: Frequent winter groundwater table from the HIP model. Data from Dataforsyningen [2024b]

The groundwater level in Beder as shown in figure 13.6 was not expected to accurately represent the groundwater level due to the inaccuracy of the available data. However, as the screening tool was developed as a "proof of concept" the uncertainty of the groundwater level was accepted.

13.2.2 Simplification of the geology in Beder and initial soil properties

In contrast to the groundwater table being extracted from the HIP data, the geology was not inputted directly into the model. In order to replicate the changing dynamics depending on the geology as observed in Beder, the surface geologies within the boundary of Beder (see figure 13.4) were simplified into four soil types, see table 13.1.

Surface geology	**Simplified soil type**
Freshwater peat (FT)	Clay
Freshwater clay (FL)	Clay
Moraine clay (ML)	Sandy clay loam
Moraine sand (MS)	Loamy sand
Meltwater sand (DS)	Sand
Freshwater sand (FS)	Sand
Moraine gravel (MG)	Sand

Table 13.1: Simplification of the soils from figure 13.4 into different geologies. The sand is based on the St. Restrup sand, while the rest are derived from average values of soils from Clapp and Hornberger [1978].

The soil properties of the St. Restrup sand was used for the sand, while clay, loamy sand and sandy clay loam were based on average values from Clapp and Hornberger [1978] sampled from 30-140 soils. Here, peat was modelled as clay as this was the soil type in Clapp and Hornberger [1978] with the most similar retention capabilities to peat even though the peat would have a higher saturated hydraulic conductivity compared to clay [Miljøstyrelsen 2004]. However, since the screening tool was run as a steady state model the difference in conductivity would not affect the resulting groundwater increase as the retention curve would be the dominant factor. This simplification was also deemed sufficient as the modelled area with peat was minimal. Furthermore, the clay from Clapp and Hornberger [1978] was also used to model freshwater clay as it is a fairly standard clay [Andersen, Anthonsen, and Jakobsen 2023].

Moraine clay was classified as sandy clay loam since both soil types are non uniform and both contain clay, silt and sand. According to Andersen, Anthonsen, and Jakobsen [2023] moraine clay contains at least 12% clay. As the sandy clay loam from Clapp and Hornberger [1978] has a mean clay fraction of 28 % this fits within the possible values for moraine clay. Moreover, the hydraulic capabilities of both soils vary from deposit to deposit and largely depend on the composition and history of the soil. Therefore, due to the varying uniformity and hydraulic capabilities of both moraine clay and sandy clay loam it was deemed that sandy clay loam was the soil type from Clapp and Hornberger [1978] which best represented moraine clay [Andersen, Anthonsen, and Jakobsen 2023; Clapp and Hornberger 1978].

Like moraine clay the moraine sand is also a non uniform soil type. Using the same argument as for moraine clay a less uniform soil type from Clapp and Hornberger [1978] was used to model moraine sand, namely loamy sand. Loamy sand is the least uniform soil type from [Clapp and Hornberger 1978] where sand is the dominant soil fraction as it is for a moraine sand [Andersen, Anthonsen, and Jakobsen 2023].

Both the meltwater and freshwater sands from Beder were simplified to the St. Restrup sand. This was due to meltwater and freshwater sand both being fairly uniform sands where especially meltwater sand tends to be coarse [Sørensen 2019]. This fits well with the measured particle size distribution of the St. Restrup sand. Furthermore, the moraine gravel was also simplified to the St. Restrup sand. This is despite of e.g the uniformity of the two soils differing with the moraine gravel being non uniform [Sørensen 2019]. However, of the considered soil types it was evaluated that the St. Restrup sand was the best soil for modelling the moraine gravel.

A spatial overview of the simplified surface geologies from table 13.1 is shown in figure 13.7 along with the monitoring borings.

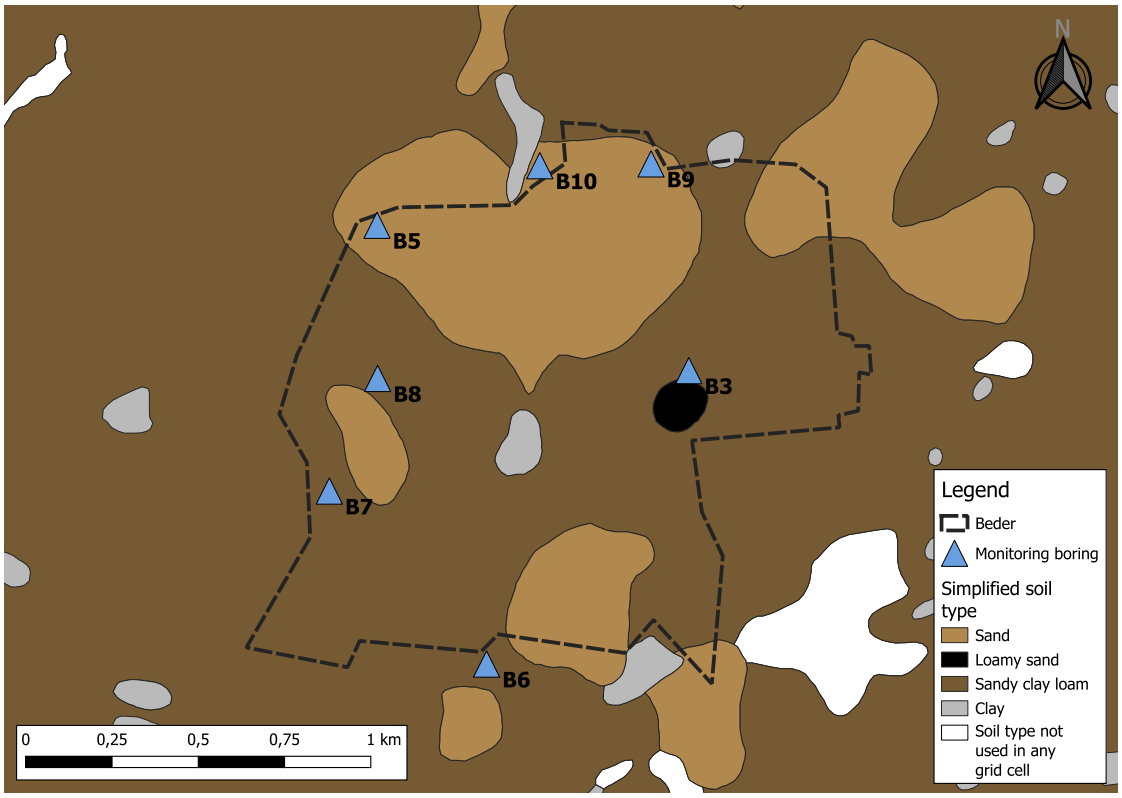

Figure 13.7: Simplification of surface geology in the city of Beder to simplified soil types.

Due to the soil being based on average values of a large number of soil samples, a combination of all properties, e.g. organic matter content, air entry suction, Campbell b and saturated water content, did not necessarily yield realistic soils. In order to ensure that the properties of the soil made physical sense, soil parameters were fitted by ensuring a realistic soil water retention curve and hydraulic conductivity curves. The initial values used for fittings the soils are presented in table 13.2.

Soil type	θ_{sat} **[cm^3/cm^3]**	**b [-]**	ψ_{e} **[cm H_2O]**	$\mathbf{K}_{\text{sat}}$ **[cm/min]**	**Source**
Clay	0.482	11.40	-40.5	0.0077	Clapp and Hornberger [1978]
Sandy clay loam	0.420	7.12	-29.9	0.038	Clapp and Hornberger [1978]
Loamy sand	0.410	4.38	-9.0	0.94	Clapp and Hornberger [1978]
Sand	0.434	2.0	-23.0	0.33	St. Restrup sand

Table 13.2: Initial soil properties before fitting the values. θ_{sat} = saturated volumetric water content, b = Campbell b, ψ_{e} = air entry suction, K_{sat} = saturated hydraulic conductivity.

13.2.3 Fitting the soil properties for the simplified soil types

The soil properties for the soils were derived by fitting the soil water retention curve using the Campbell model from air entry to pF 4.2 as described in section 8.1. As Clapp and Hornberger [1978] did not contain an average water content for the soils at pF 4.2, they were instead calculated using equation (13.1) from Hansen [1976].

$$W = 0.38 \cdot CF + 0.76 \cdot OM + 0.38 \tag{13.1}$$

Where:

W	Gravimetric water content of water at pF 4.2 [%]
CF	Clay fraction [%]
OM	Organic matter fraction [%]

In order to convert the gravimetric water content to volumetric water content equation (13.2) was used, which assumes a water density of 1 g/cm^3 [Jury and Horton 2004].

$$\theta_{wp} = \frac{W}{100} \cdot \rho_b \tag{13.2}$$

Where:

θ_{wp}	Volumetric water content at pF 4.2 [cm^3 H_2O/cm^3 soil]
ρ_b	Bulk density [g/cm^3]

The bulk density of the soil was calculated based on equation (13.3) from Loll and Moldrup [2000]:

$$\rho_b = -(-1 + \phi) \cdot \rho_s \tag{13.3}$$

Where:

ϕ	Total porosity [cm^3 air/cm^3 soil]
ρ_s	Density of particles [g/cm^3]

The density of particles was assumed to be 2.65 g/cm^3 [Loll and Moldrup 2000] and the total porosity was assumed equal to the water content at saturation. The used water content at saturation was the same as presented in table 13.2. The calculated bulk density was used to calculate water content at wilting point (θ_{wp}). A summary of the values for the different soils are shown in table 13.3.

Soil	θ_{wp} **[cm^3/cm^3]**	ρ_s **[g/cm^3]**	**CF [%]**	**OM [%]**
Clay	0.37	1.37	60	4.50
Sandy clay loam	0.20	1.54	28	2.50
Loamy sand	0.071	1.56	6	2.50
Sand	0.013	1.50	0.2	0.57

Table 13.3: Overview of the values used for calculating water content at wilting point and the resulting water content for the different soil types. The clay and organic matter fractions for the sand were measured by Hedevang and Sørensen [2023]. For all other soils the clay fractions were derived from Clapp and Hornberger [1978] while organic matter fractions were derived from Magdoff and van Es [2021]. θ_{wp} = Water content at pF 4.2, ρ_s = bulk density, CF = clay fraction, OM = organic matter fraction.

The water contents at pF 4.2 for each soil were then used for fitting the soil water retention curve between air entry suction to pF 4.2. The used air entry suctions were the averages from

Clapp and Hornberger [1978] for each soil except for the sand. In order to fit the Campbell curve between the two points, the Campbell b value was changed from the average from Clapp and Hornberger [1978] by iterating until an agreeable eye fit was reached. The final values for each soil are summarized in table 13.4. Note that the only change from table 13.2 is the Campbell b values for clay and sandy clay loam.

Soil type	θ_{sat} **[cm^3/cm^3]**	**b [-]**	ψ_{e} **[cm H_2O]**	K_{sat} **[cm/min]**
Clay	0.482	21.0	-40.5	0.0077
Sandy clay loam	0.420	8.12	-29.9	0.038
Loamy sand	0.410	4.38	-9.0	0.94
Sand	0.434	2.0	-23.0	0.33

Table 13.4: Final soil properties for the soils used for modelling the surface geology in Beder. θ_{sat} = saturated volumetric water content, b = Campbell b, ψ_{e} = air entry suction, K_{sat} = saturated hydraulic conductivity.

The most significant change made from the average values from [Clapp and Hornberger 1978] in table 13.2 to the used values in table 13.4 is the Campbell b for clay that was changed from 11.4 to 21, which is still within the expected range of a clay [Loll and Moldrup 2000]. The resulting soil water retention curves are shown in figure 13.8.

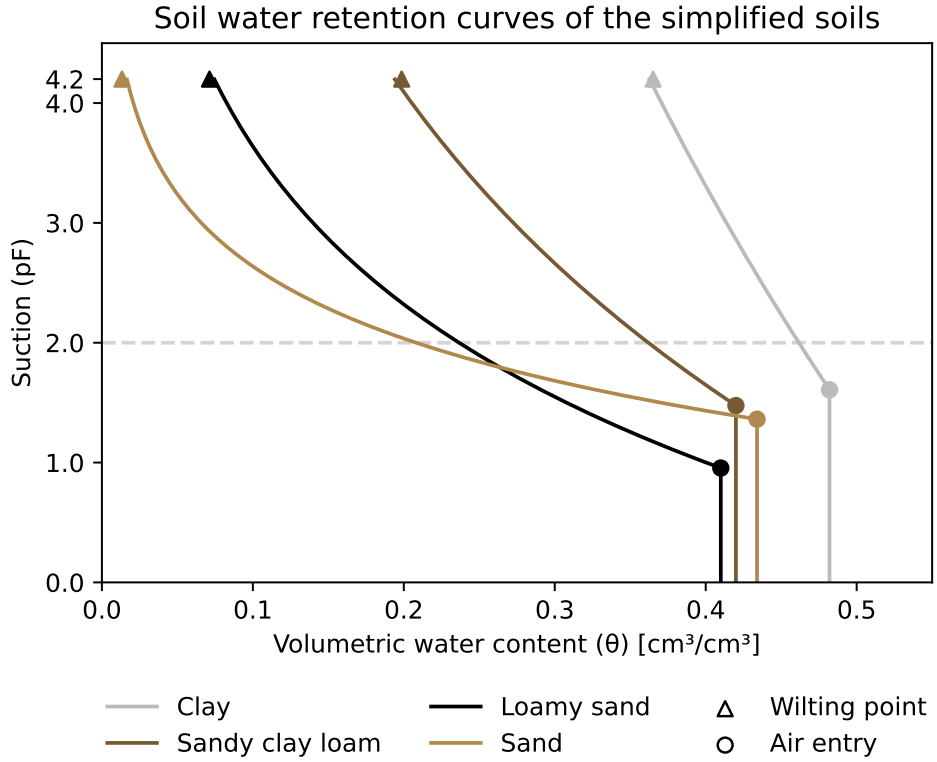

Figure 13.8: Soil water retention curves for the simplified soil types. Based on equation (8.1) on page 70 from air entry suction to pF 4.2.

The soil water retention curves show that in general the higher the clay content of the soil the greater the soil retention capabilities are at a given suction. This is e.g reflected by the Campbell b and air entry suctions of clay and sand. For instance, the air entry suction of

-40.5 cm and -23 cm for the clay and sand, respectively, shows clay requiring almost twice the suction to release water from the largest pore. Moreover, the Campbell b of clay at 21 is more than a factor 10 larger than the value for sand at 2, which also reflects that the sand has a more uniform pore size distribution and thus will release much more water by a slight increase in suction compared to the clay. At low pF values the loamy sand retains less water than the sand at a given suction. This is a result of the numerically lower air entry value of the loamy sand compared to the sand. However, due to the larger Campbell b value of the loamy sand, it has better retention capabilities at higher pF values.

The change in hydraulic conductivity compared to suction and volumetric water content is shown in figures 13.9 and 13.10. Considering the $K - \theta$ curve in figure 13.9 it can be seen that soils with finer textures has a lower hydraulic conductivity at the same volumetric water content than those with coarser texture. This is to be expected since the hydraulic conductivity highly depends on the soil structure where soils with a more coarse texture and more uniform soil distribution has larger pores with higher connectivity [Loll and Moldrup 2000]. In contrary, soils with higher clay content have pores that can retain more water at a specific suction. As a result, the hydraulic conductivity of clay can surpass that of sandy soils within a certain range of suction. This dynamics appear in the $K - \psi$ curves in figure 13.10. Additionally, the $K - \psi$ curves within the range of pF 0-2 is illustrated in figure 13.11. Here, it appears that within -100 cm H_2O the hydraulic conductivity for sandy clay loam exceeds the hydraulic conductivity for both sand and loamy sand which both have a significant higher saturated hydraulic conductivity.

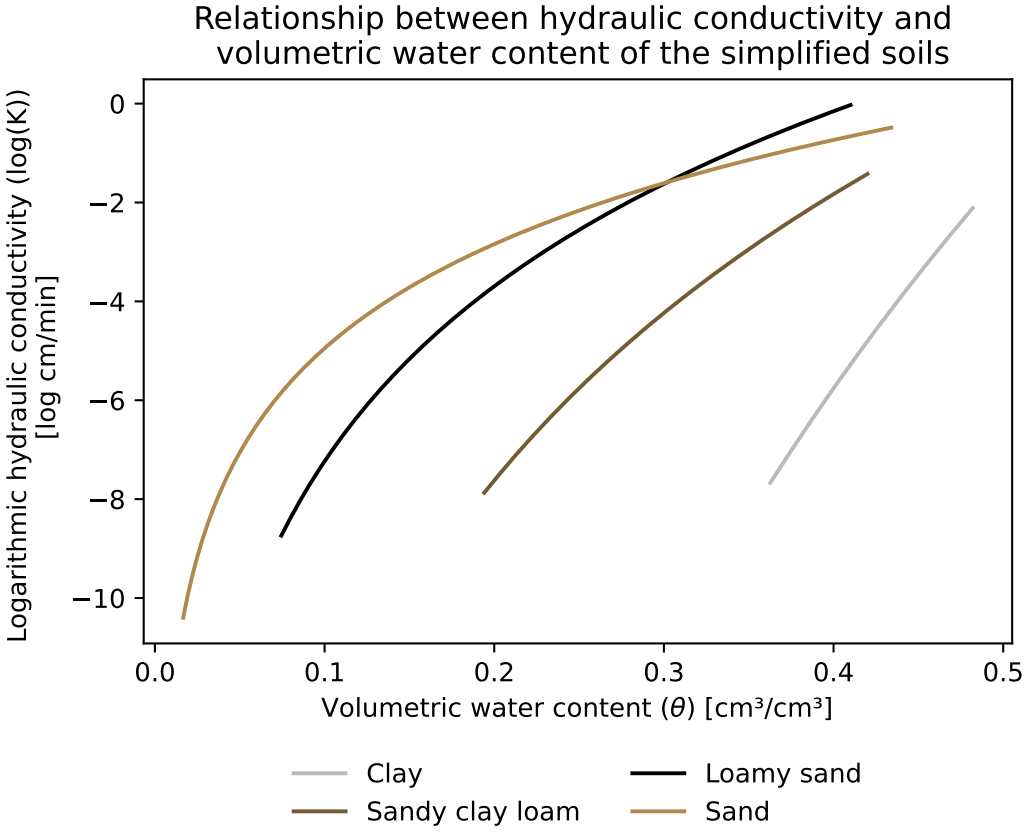

Figure 13.9: Relationship between hydraulic conductivity and volumetric water content for the simplified soils. Based on equation (8.6) on page 74 from air entry suction to pF 4.2.

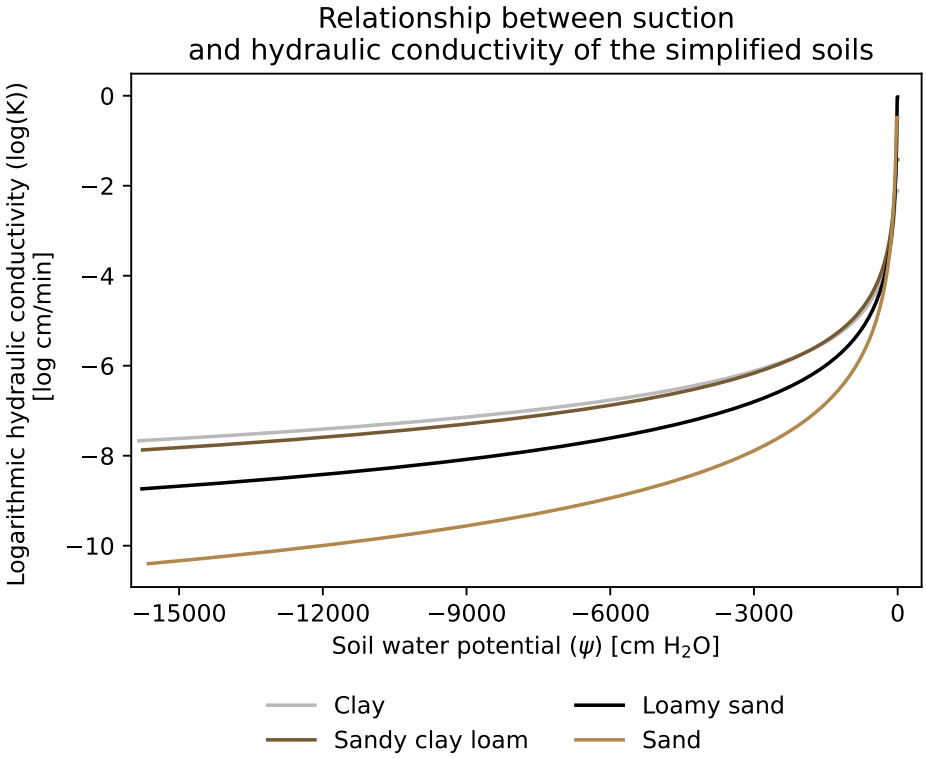

Figure 13.10: Relationship between suction and hydraulic conductivity for the simplified soils. Based on equation (8.7) on page 74 from air entry suction to pF 4.2.

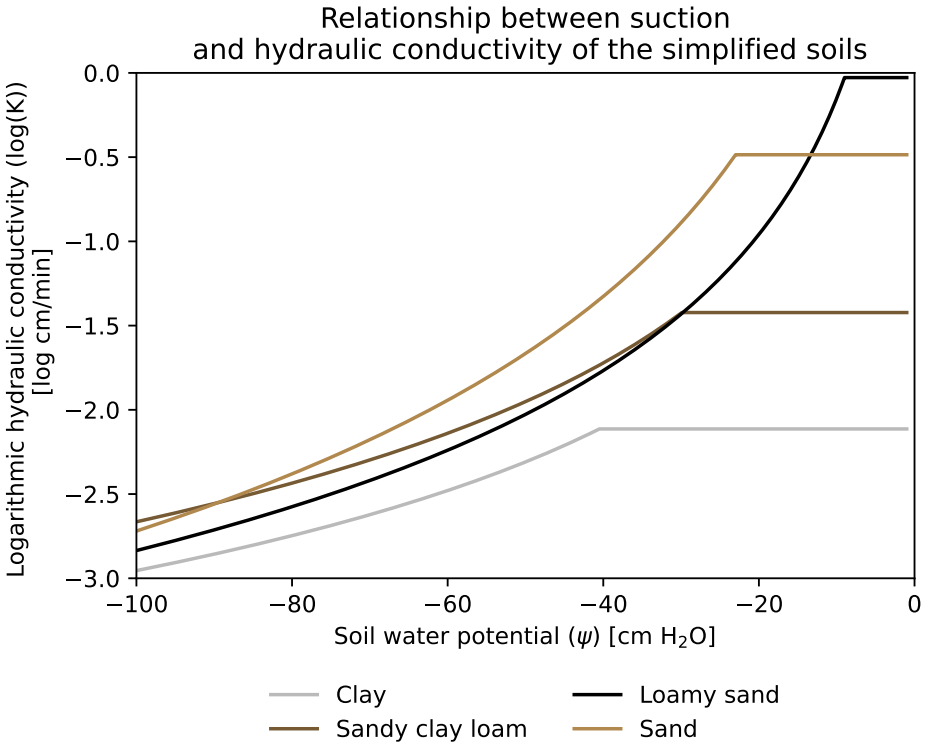

Figure 13.11: Relationship between suction and hydraulic conductivity for the simplified soils. Based on equation (8.7) on page 74 from air entry suction to pF 2.

After evaluating the three curves for water retention, suction and hydraulic conductivity the simplified soils were deemed realistic and could thus be inserted into the screening tool.

13.3 Creating the screening tool domain and applying the model inputs

The aforementioned input data was implemented into the screening tool in a 25x25 m grid where the grid cells only covered the sewer system of Beder. As the input data had a finer spatial discretization than 25x25 m, a representative value of the area had to be chosen for each grid cell. Here, the values were assigned by using the following principles:

- Sewer level: Lowest sewer level within grid cell
- Geology: Most dominant surface geology within grid cell based on area
- Surface level: Average surface level within grid cell
- Groundwater level: Average groundwater level within grid cell

The resulting grids containing the inputs can be seen in figures 13.12 through 13.15

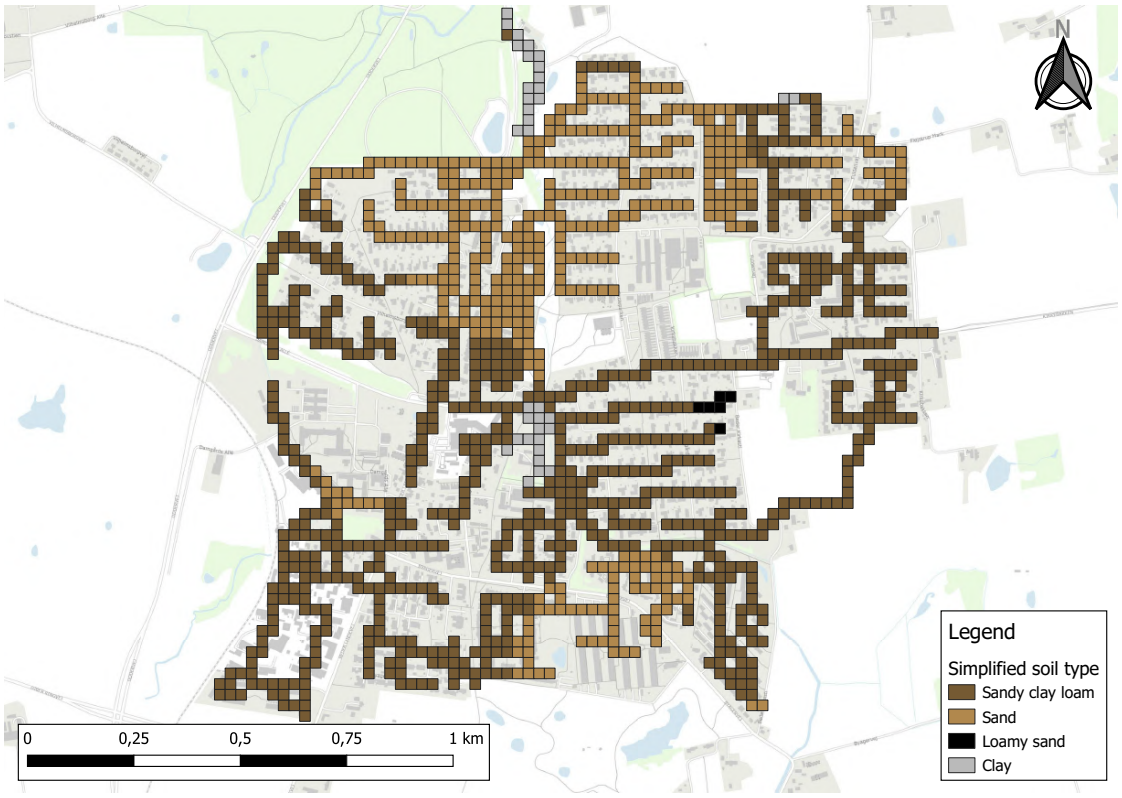

Figure 13.12: Distribution of the simplified soil types in the modelled area of Beder in a 25x25 m grid.

From figure 13.12 it becomes evident that the predominant simplified soil types in the area of Beder are the sandy clay loam and sand, where only small parts are simplified to clay and loamy sand. The geology grid closely resembles figure 13.7 as expected.

The geology is also reflected by the groundwater level as shown in figure 13.13. Here, the greatest distance to the groundwater table generally lies in the sandy areas, where the groundwater table in the grid cells modelled as sandy clay loam generally lies a few meters from the surface.

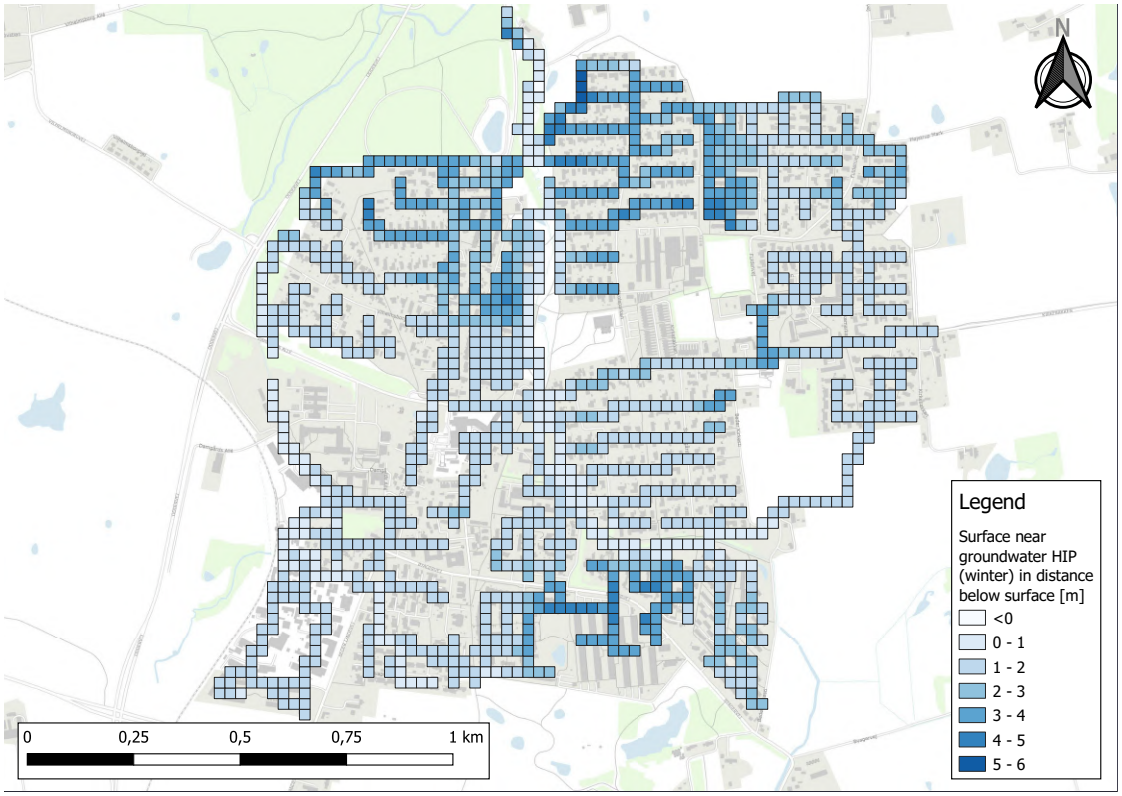

Figure 13.13: Distance from groundwater table to the surface in the modelled area of Beder in a 25x25 m grid.

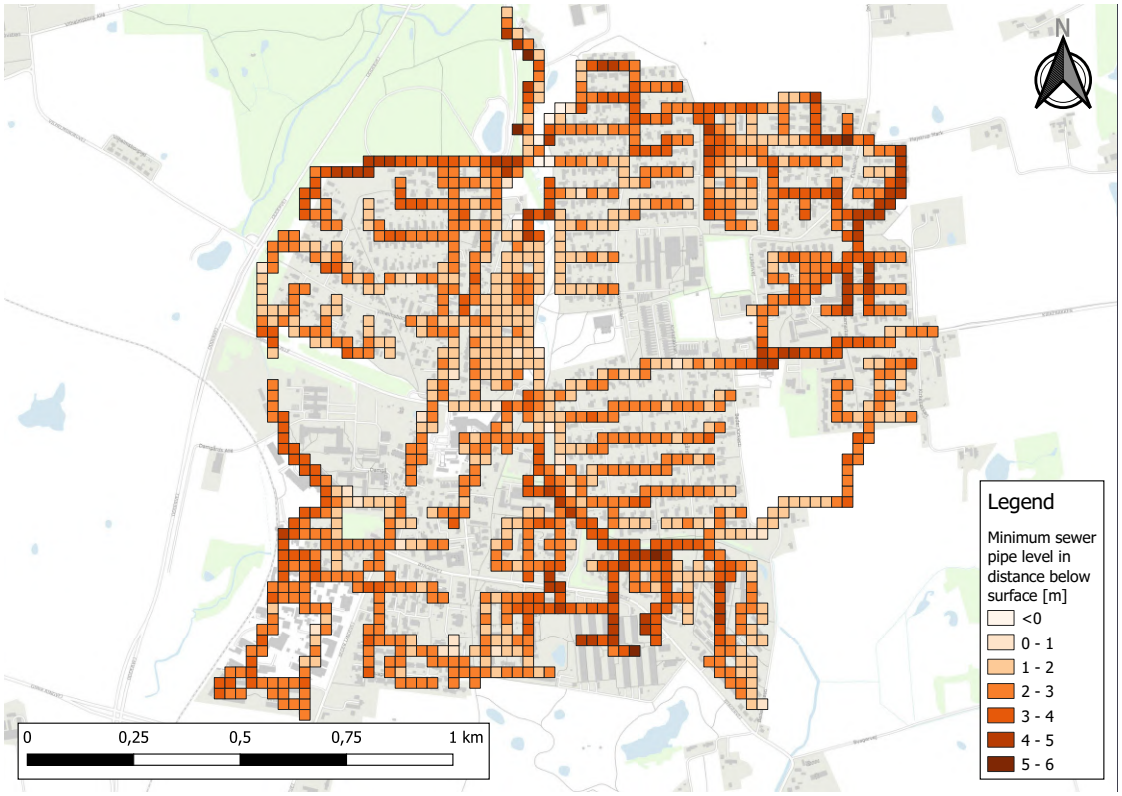

Figure 13.14: Distance from the sewer system to the surface in the modelled area of Beder in a 25x25 m grid.

Figure 13.14 shows the distance from the surface to the lowest lying pipe in the grid cell. Generally, many of the lowest points are within 3 meters from the surface.

The surface near groundwater table results in the groundwater being close to the pipes and exceeding the bottom level of the pipes in many grid cells as shown in figure 13.15. Here, the cells with a distance ≤ 0 shows the pipe level already being submerged before adding rain.

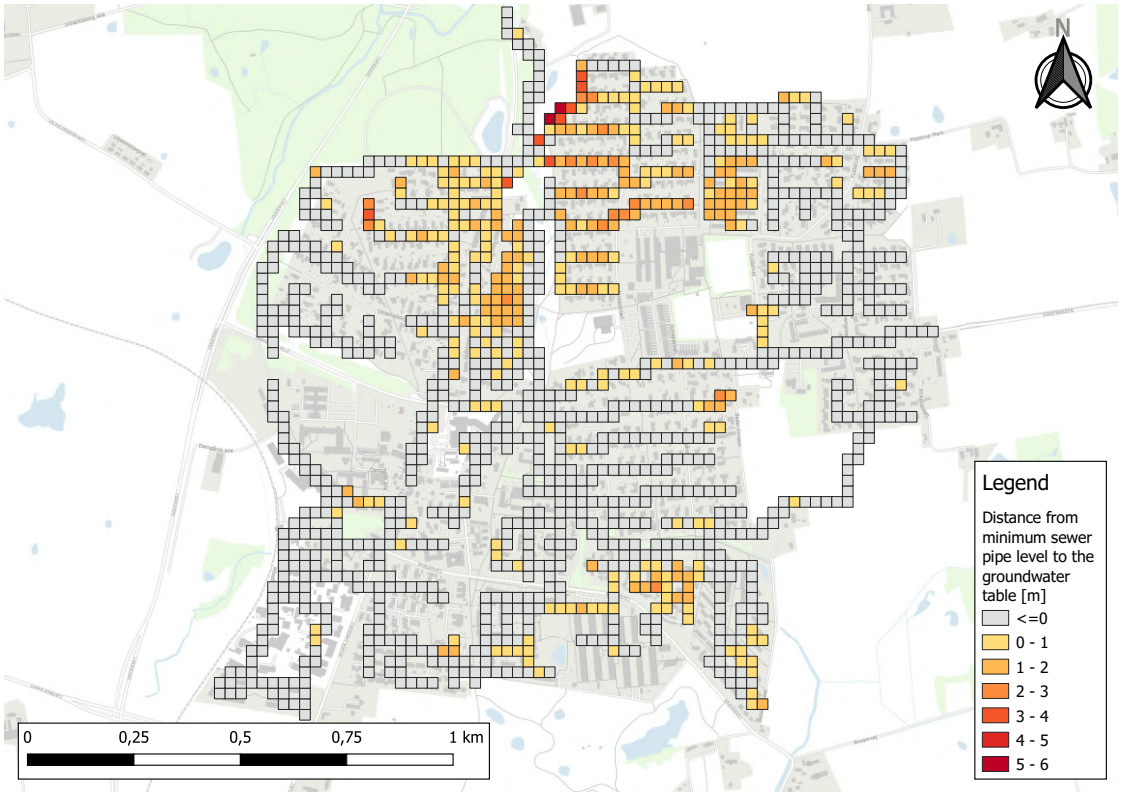

Figure 13.15: Distance from the groundwater table to the sewer system in the modelled area of Beder in a 25x25 m grid.

13.3.1 Simplifications of the screening tool domain to reduce simulation time

In order to save simulation time the grid cells that were already submerged were omitted from the calculations, as the resulting high risk classification was known beforehand. In addition, due to many large distances to the groundwater in sand, which was a soil type with a high simulation time, a criterion was made for omitting calculations where it was known beforehand that the grid cell would be classified as low risk. Here, the groundwater rise for a 150 mm rain added in a 100 cm column yielded a groundwater rise of 60 cm. Therefore, grid cells containing sand where the distance from the pipe bottom level to the groundwater table was ≥ 110 cm were classified as low risk and excluded from the model run. This was done since an increasing distance to the surface yields lower increases in groundwater table and therefore for all realistic uses of the screening tool the sand would always be classified as low risk when the distance from the pipe bottom level to the groundwater table is 110 cm or more. For the rest of the grid cells the modified 1D model was applied. An overview of the omitted grid cells and grid cells that were classified as low risk before applying the model can be seen in figure 13.16.

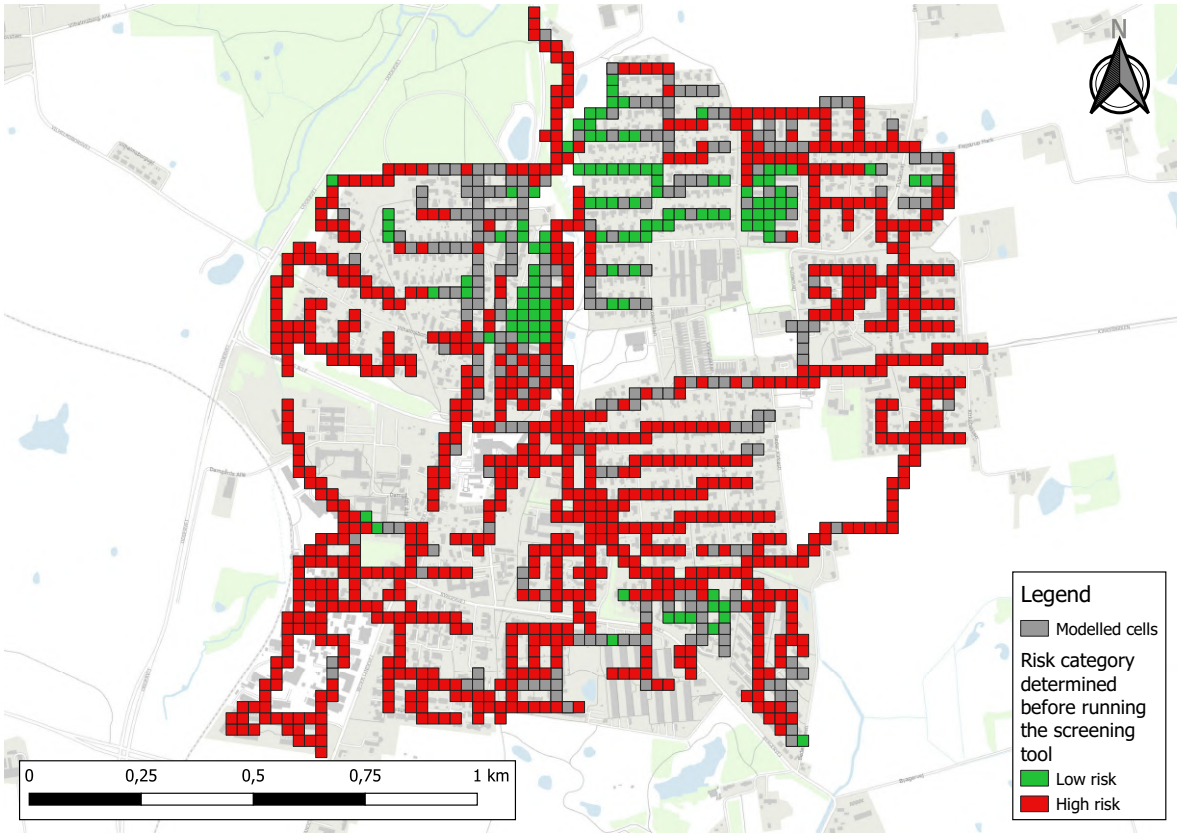

Figure 13.16: Overview of the modelled grid cells and which grid cells were classified as low- and high risk before running the screening tool. High risk grid cells were omitted from the calculations.

Another method of reducing the simulation time was to pre-calculate the initial conditions for all soil types. This was done by calculating phase 1 of the 1D model for the largest distance to the groundwater table. As shown in figure 13.13 the greatest distance from the surface level to groundwater table was 7.9 m for the HIP data. However, another groundwater table was initially used with a maximum distance of 15.83 m. Therefore, initial conditions were calculated for all 4 simplified soil types for 15.9 m columns and then initial conditions for every grid cell were sampled from the bottom. For instance, an initial distance from groundwater to the surface level of 2.5 m in a grid cell would sample the bottom 2.5 m from the 15.9 m column. This pre-calculation of the initial conditions reduced overall simulation time when running the screening tool.

13.4 Running the screening tool

When running the screening tool a user-defined rain depth is applied in all grid cells. The resulting groundwater increase from the 1D model after a steady state is achieved is compared to the bottom level of the pipe and classified according to the aforementioned risk categories. This results in a "traffic light" map for the model grid which divides the area into low, medium and high risk of groundwater infiltration due to rain. This map can be produced for every desired rain depth, but due to the simplification of calculations mentioned in section 13.3.1 the maximum rain depth is 150 mm. In this Master's thesis the screening tool was run with

rain depths of 15 mm, 20 mm, 30 mm and 40 mm as these rain depths were observed in Beder during the monitoring of the groundwater. The result of the model runs can be seen in chapter 15. In order to evaluate whether the results of the screening tool could accurately represent the dynamics observed in Beder, an evaluation of the groundwater rise of the simplified soils were compared to measured data from Beder. This is further elaborated in chapter 14.

14 | Analysis of the ability of the chosen simplified soils to replicate the dynamics observed in Beder

As the 1D model had previously only been used to run a sandy soil, an evaluation of its ability to compute a groundwater rise for other soil types was conducted. This was further compared to measurements from Beder in order to evaluate whether the observed dynamics in Beder could be replicated. Here, the boring B6 from Beder was used due its rapid response to groundwater combined with its near surface groundwater table which enabled faster simulation time [Ternært Vand project group 2024]. Figure 14.1 shows a time series of the groundwater where a 40 mm rain event results in a rapid increase in the groundwater of 53 cm.

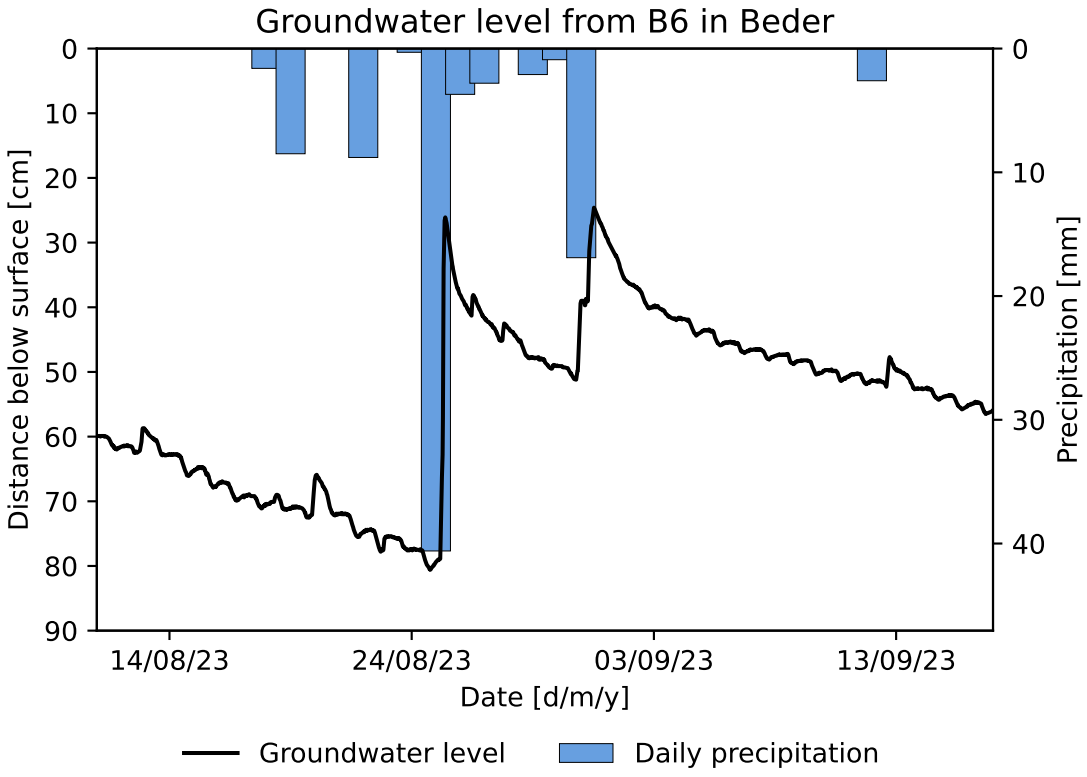

Figure 14.1: Precipitation and concurrent rise in groundwater table at monitoring boring B6 in Beder. The geology in the boring consists of clay. Data from Ternært Vand project group [2024].

An attempt was made to replicate the rise observed in figure 14.1 with the 1D model of the screening tool. Here, all simplified soils were run through phase 1 and phase 2 of the 1D model to compare the output of the different soils.

14.1 Phase 1 simulation of the capillary fringe of the simplified soils

Phase 1 of the 1D model was run for all four simplified soils to create the initial conditions for phase 2. The soil parameters used for the soils were presented in table 13.4 on page 127. In order to compare the first rapid rise in B6 a 80 cm column was used in phase 1, as this was the initial distance from groundwater table to the surface before the rain event. The vertical discretization was 10 cm as in the screening tool and phase 1 was run until reaching equilibrium. The phase 1 result of the modelled capillary fringe is shown in figure 14.2.

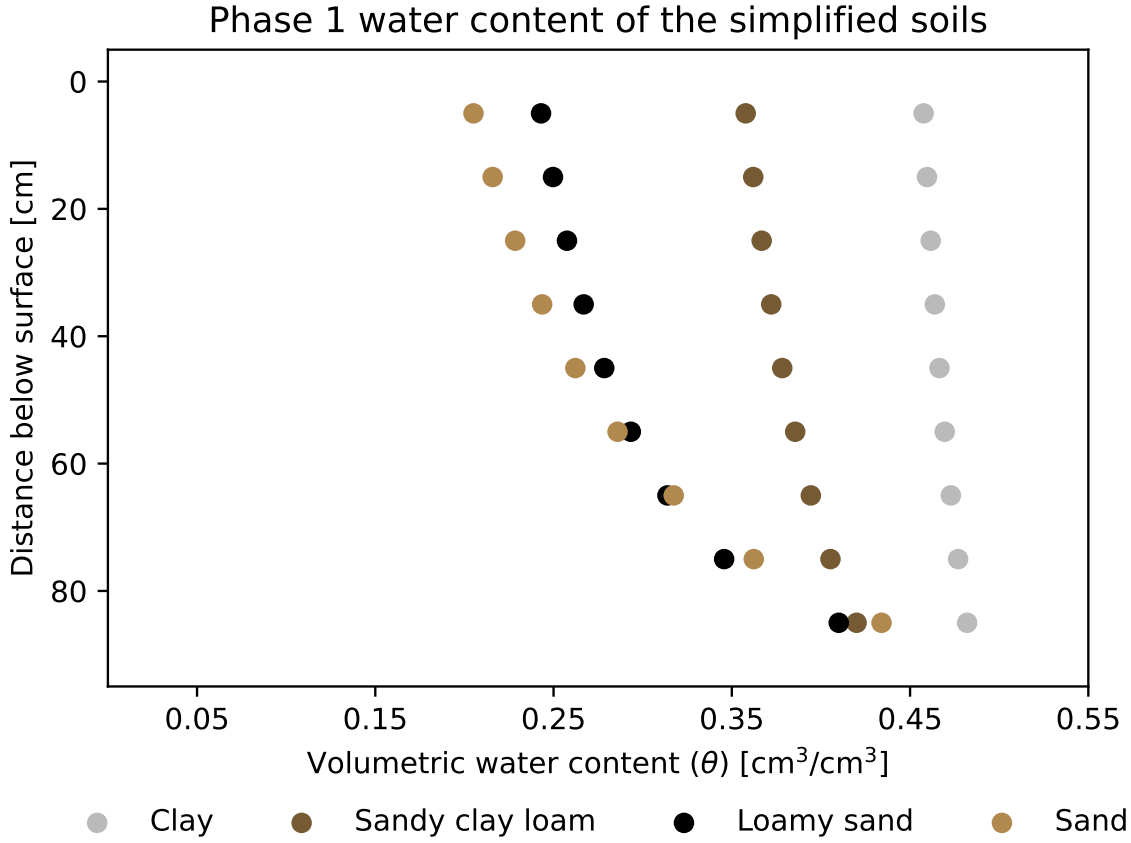

Figure 14.2: Result from phase 1 simulation of the capillary fringe for the simplified soils. As the vertical discretization is 10 cm, the values are plotted in the middle of the range, i.e. the water content from 0-10 cm is plotted at 5 cm below surface.

Soil type	**Top cell saturation [%]**
Clay	95
Sandy clay loam	85
Loamy sand	59
Sand	47

Table 14.1: Water content in the top cell expressed as percentage of saturation compared to the saturated volumetric water content.

As evident from figure 14.2 the water content in the surface soil during phase 1 contains more water the higher the clay fraction and Campbell b is, corresponding with the soil water retention curves presented in figure 13.8. After phase 1, the surface soil contains a larger

water content for the clay soil than the sand contains at full saturation. The water content of the loamy sand lies close to the sand, but partly due to the higher Campbell b, the water is more retained at the same suction, and thus the loamy sand has a higher water content. The curvature of the water content of the sandy clay loam is similar to the clay, but starts at a lower water content and decreases more than the clay. From table 14.1 it is also evident, that the clay is almost saturated even at the top most cell at 95% of saturation, while the sand is only at 47% saturation in the top cell and thus the sand has a much larger storage capacity throughout the soil column. Overall, the phase 1 simulation was capable of modelling the expected difference of the capillary fringe between the simplified soils.

14.2 Phase 2 simulation of the groundwater increase of the simplified soils

The phase 1 results were used as initial conditions of phase 2. The measured increase at B6 was 53 cm at 40 mm of rain and an initial distance of 80 cm from the surface to the groundwater. As the surface soil at the location of B6 was simplified to sandy clay loam (shown in figure 13.7 on page 125), this soil was expected to have the closest result to the measurement from B6 of all the simplified soils. However, adding 40 mm of rain resulted in the groundwater rising the 80 cm to the surface for a sandy clay loam. Instead, the rain depth which came closest to the increase of 53 was 30 mm, see figure 14.3.

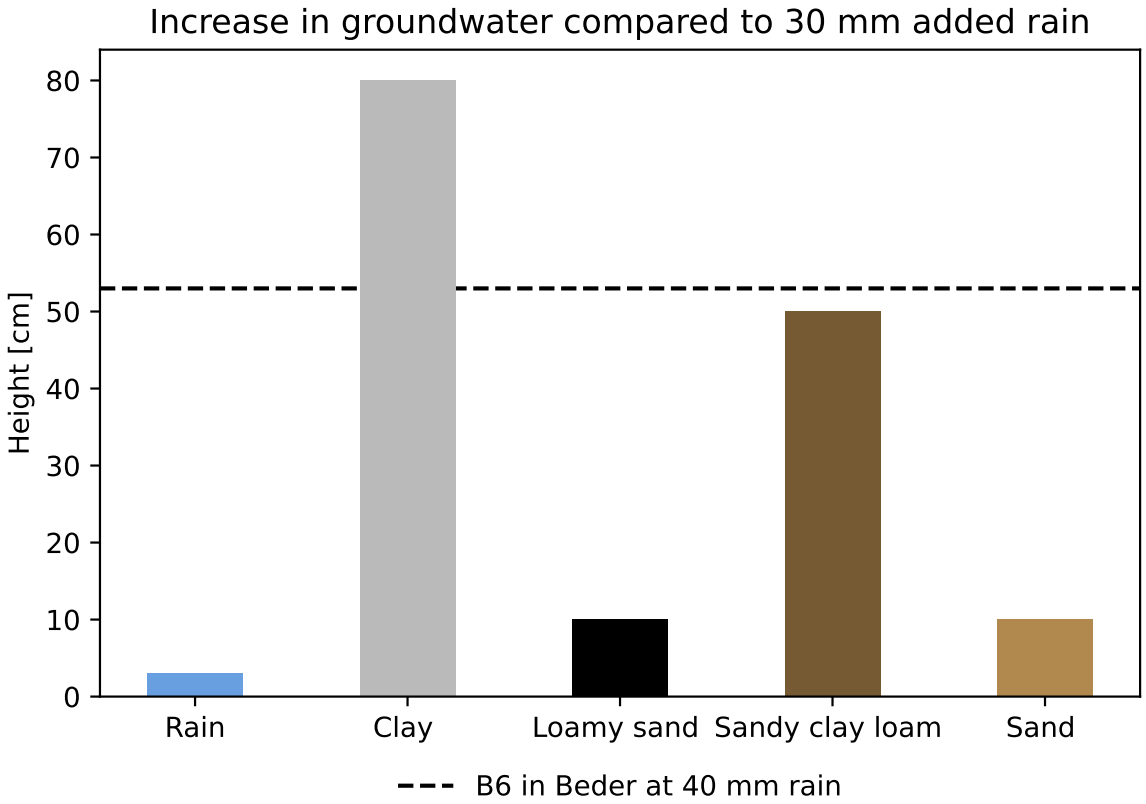

Figure 14.3: Resulting increase in groundwater table for the simplified soils based on an input of 30 mm rain compared to the measured increase in monitoring boring B6 at 40 mm rain. The initial distance to the surface was 80 cm.

From figure 14.3 it becomes evident, that the 1D model overestimates the rise compared to observed in Beder, as the closest fit was found when adding 30 mm of rain instead of 40 mm. Here, the difference in storage capacity from the phase 1 simulation is also obvious. Where the groundwater in the clay rises to the surface, the sand only rises 10 cm. This is due to the water content being much closer to saturation in the clay than the sand. The loamy sand also shows an increase of 10 cm like the sand. Here, a smaller vertical discretization than 10 cm might show differences between the sand and loamy sand.

Due to the 1D model being run as a steady state model in the screening tool, the groundwater rise after a specific duration was not deduced. However, for illustration of how the different soils work in the model, the simulated durations are shown in figure 14.4.

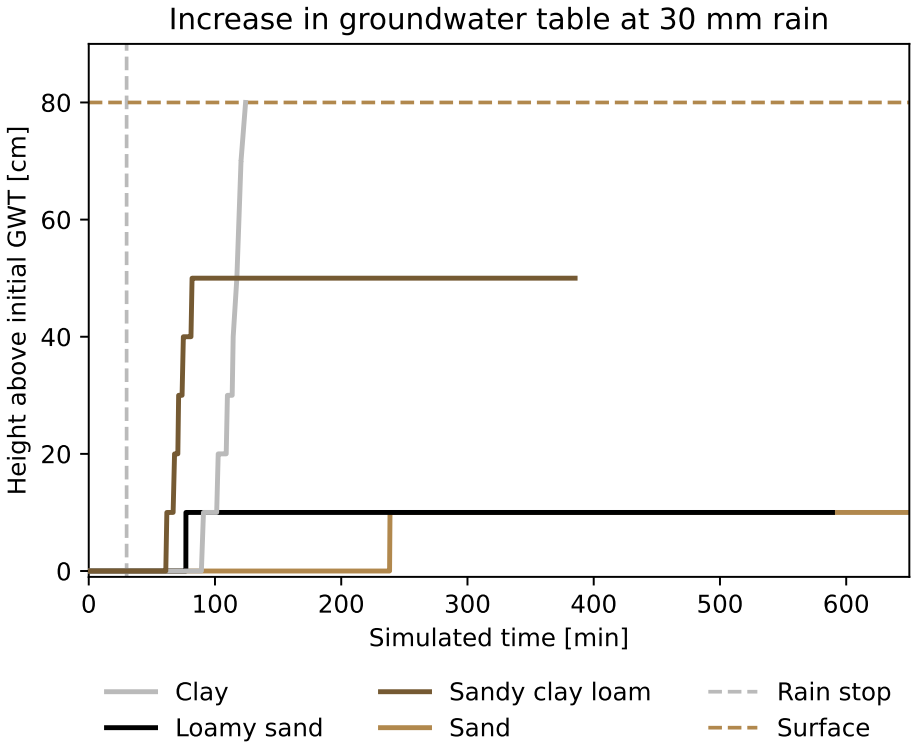

Figure 14.4: Increase in groundwater above the initial groundwater table over time. The 30 mm rain was applied for a duration of 30 min. The simulated time of the different soils varies as the simulations were run until one of the stop criteria mentioned in section 13.1.1 on page 118 was reached.

Figure 14.4 shows the difference in response time between the simplified soils for a 30 mm rain. The rain was added over a duration of 30 min, though this duration only affects how fast the response is and the total simulation time, but does not affect the final increase in groundwater. Generally, the sandy clay loam responds the fastest. This is due to the high initial water content from phase 1. The response is faster than the clay which has an initial higher water content and also higher degree of saturation in the top most cell at 95% for the clay and 85% for the sandy clay loam. However, the saturated hydraulic conductivity is more than a factor 5 greater for the sandy clay loam, which enables the water to travel faster. The sand has the slowest response, despite having a saturated hydraulic conductivity a factor 8 higher than sandy clay loam and factor 43 higher than clay.

The difference in the response from sand and clay is further elaborated in figures 14.5 and 14.6.

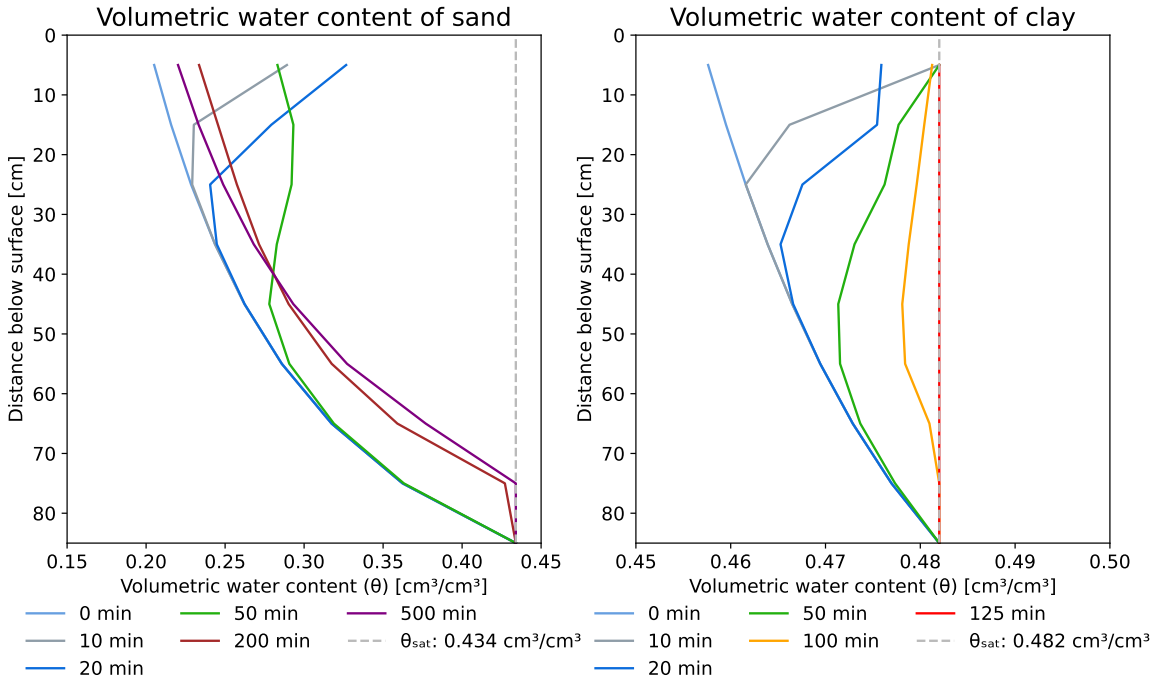

Figure 14.5: Volumetric water content of sand and clay at different simulated times in the model. As the vertical discretization is 10 cm, the values are plotted in the middle of the range, i.e. the water content from 0-10 cm is plotted at 5 cm. Notice that the x-axes differ between sand and clay. θ_{sat} = saturated volumetric water content.

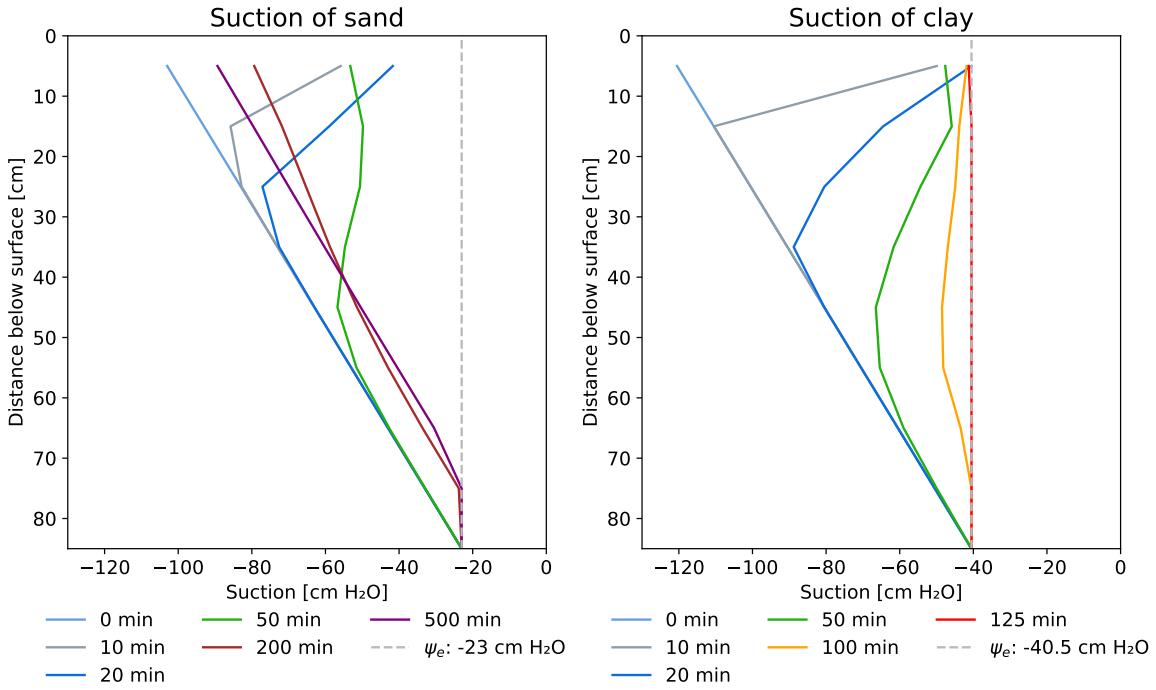

Figure 14.6: Suction of sand and clay at different simulated times in the model. As the vertical discretization is 10 cm, the values are plotted in the middle of the range, i.e. the water content from 0-10 cm is plotted at 5 cm. ψ_e = air entry suction.

Figure 14.5 shows that the change in water content relative to the saturated water content happens faster in the clay than in the sand, For instance, the entire column of clay is filled after 125 minutes, where it takes 500 min before the water content stops changing for the sand. From figure 14.6 it is evident that after 10 minutes the gradient in suction from the surface to the water front in clay is much larger than for sand which also increases the movement of the water in the clay. Despite the clay seemingly moving the water faster than the sand, the water velocity in the sand is much faster. Here, the slower overall response in groundwater increase for the sand is caused by the initial available storage capacity in the sand being much greater than in the clay as the initial available storage of the sand is 10.55 times larger than the initial available storage in the clay in the 80 cm column. Therefore, the sand has to move more water before reaching the stop criteria. This dynamics is also evident from the change in suction shown in figure 14.6.

14.3 Summary of the simplified soils' ability to replicate dynamics from Beder

The initial analysis of replicating data from Beder showed that a 30 mm rain yielded the closest groundwater increase to what was observed in monitoring boring B6 in Beder where a 40 mm rain event occurred. This comparison with data from Beder will be further discussed in chapter 16. However, from the analysis above it can be determined that the 1D model which is the engine behind the screening tool showed clear differences in the dynamics of the simplified soils in both phase 1 and phase 2 of the 1D model. These differences in dynamics are further shown in the results of the screening tool in chapter 15.

15 | Results from using the developed screening tool in Beder

This chapter presents the results from the screening tool. Here, the screening tool was run for rain depths of 15 mm, 20 mm, 30 mm and 40 mm and the area was divided into 25x25 m grid cells with the classifications "high risk", "medium risk" and "low risk" of groundwater infiltration. The quantification of the risks are explained in section 13.1.2.

15.1 The initial risk assessment before adding rain

Due to the surface near groundwater level of Beder 851 grid cells out of a total of 1181 were already classified as high risk before adding the rain and are therefore shown as a separate category in the figures and were not included in the tables showing data for the different soil types.

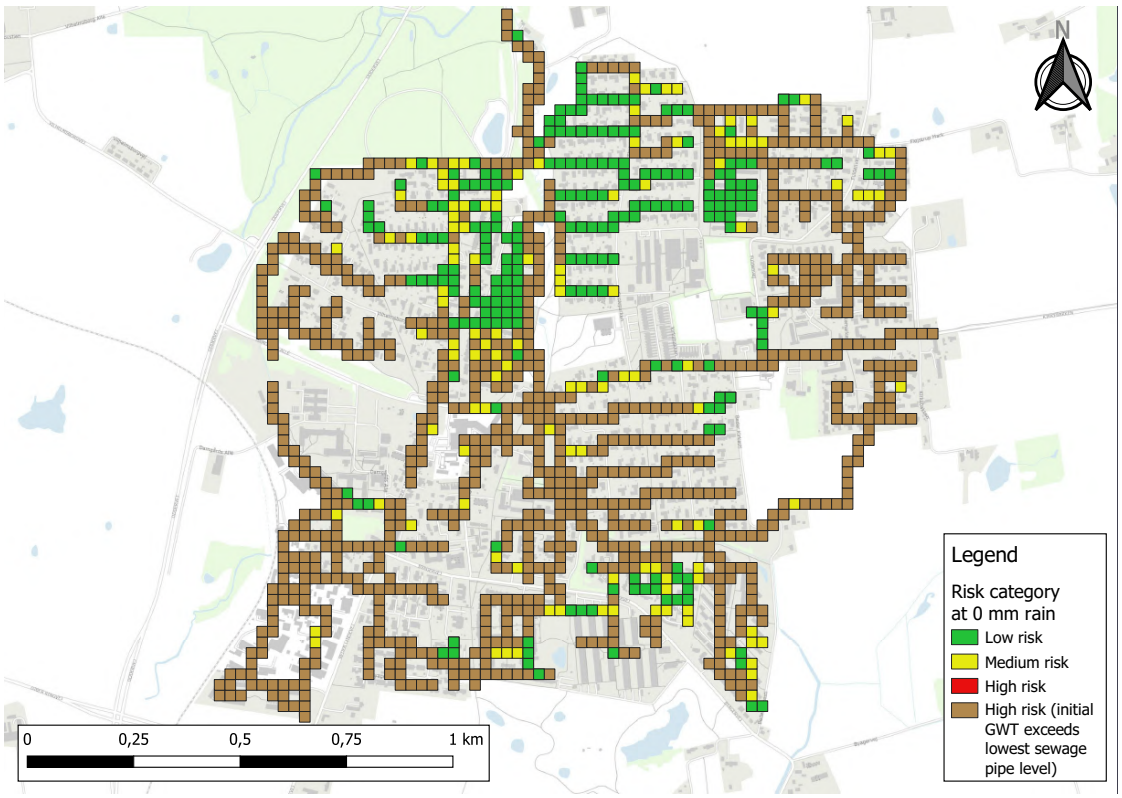

Figure 15.1: Result of the risk assessment of the sewer system in Beder in a 25x25 m grid before adding rain.

The initial risk assessment before adding rain is shown in figure 15.1. In general, many of the grid cells in the northernmost part of Beder are classified as low risk. More than half the area is classified as high risk even before adding rain.

The distribution of grid cells between the simplified soils are shown in table 15.1.

Soil type	**Amount of grid cells [#]**
Clay	4
Sandy clay loam	73
Loamy sand	6
Sand	252

Table 15.1: Amount of calculated grid cells within the different soil types. The grid cells which were classified as high risk before adding rain were not included in the calculations and therefore not shown in this table.

As shown in table 15.1 the most prevalent soil type in the calculations was sand. This was due to the areas with sandy clay loam having a groundwater table which already exceeded the lowest pipe level and therefore were excluded in the calculations.

15.2 The risk assessment at different rain depths

This section presents the results of the risk assessment at various rain depths. Due to the small changes in risk classification between the simulated rain events being difficult to notice in the figures a summary is shown in table 15.2. The distribution of the different risk categories is shown in table 15.2 in the format low/medium/high risk for the different soil types. Here, the grid cells which were already high risk before adding rain were not included in the table.

Soil type	**0 mm**	**15 mm**	**20 mm**	**30 mm**	**40 mm**
Clay	3/1/0	1/2/1	1/2/1	1/2/1	1/2/1
Sandy clay loam	23/50/0	18/38/17	11/34/28	10/32/31	8/23/42
Loamy sand	5/1/0	5/1/0	4/2/0	4/2/0	4/2/0
Sand	184/68/0	184/68/0	184/68/0	183/65/4	158/82/12
Total	215/120/0	208/109/18	200/106/29	198/101/36	171/109/55

Table 15.2: Amount of grid cells within each soil type with the different risk categories in the format low/medium/high risk. I.e. 3/1/0 means 3 low risk, 1 medium risk and 0 high risk grid cells within that soil type.

In figures 15.2 through 15.5 the results of the risk assessments of different rain depths in Beder can be seen. Here, increasing the applied rain depth also increases the amount of grid cells classified as medium and high risk. In general, the classification of the grid cells containing sandy clay loam increase to a higher risk at a greater rate compared to the sand with increasing rain depth. For instance, when comparing figure 15.3 at 20 mm of added rain with the initial scenario before adding rain, it is seen that 29 grid cells changed to a high risk classification. Of these, 28 grid cells lie within the sandy clay loam.

Many of the grid cells in the northernmost part of Beder where the predominat soil type is sand do not change from a low risk classification. As evident from figure 15.5 which shows the risk at 40 mm rain there is a larger concentration of high risk grid cells in the central part of Beder.

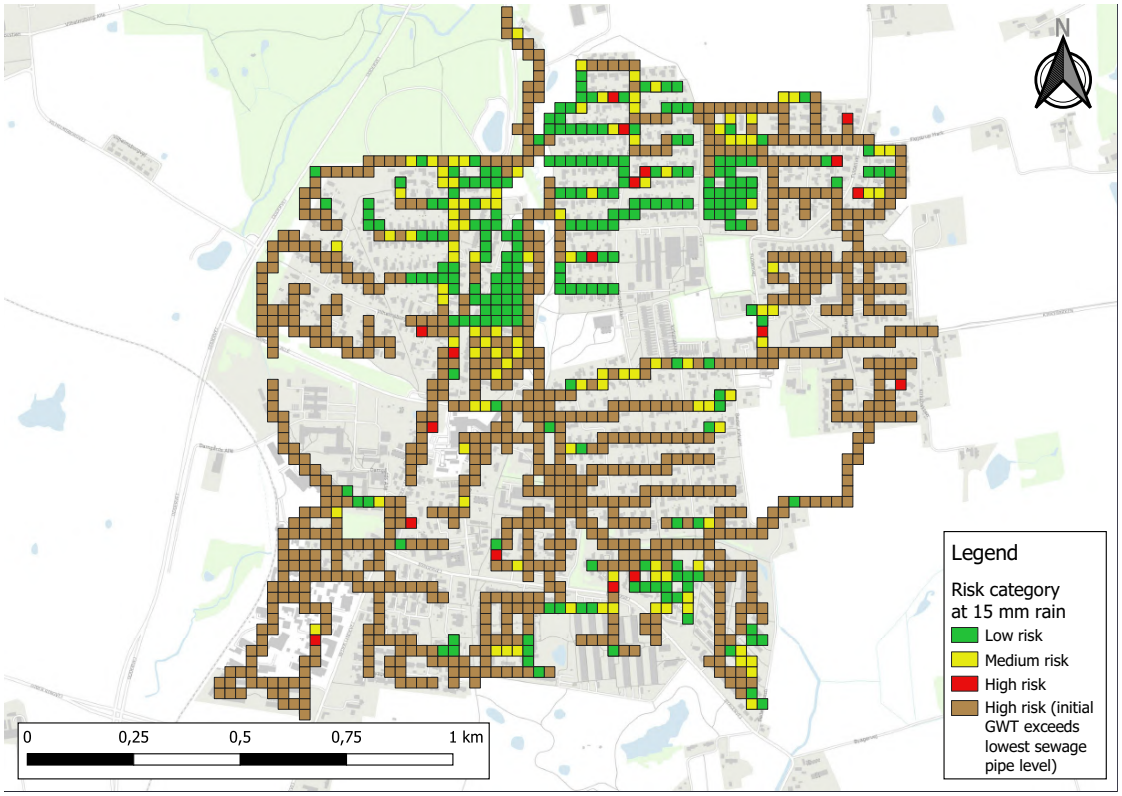

Figure 15.2: Result of the risk assessment of the sewer system in Beder in a 25x25 m grid at 15 mm rain.

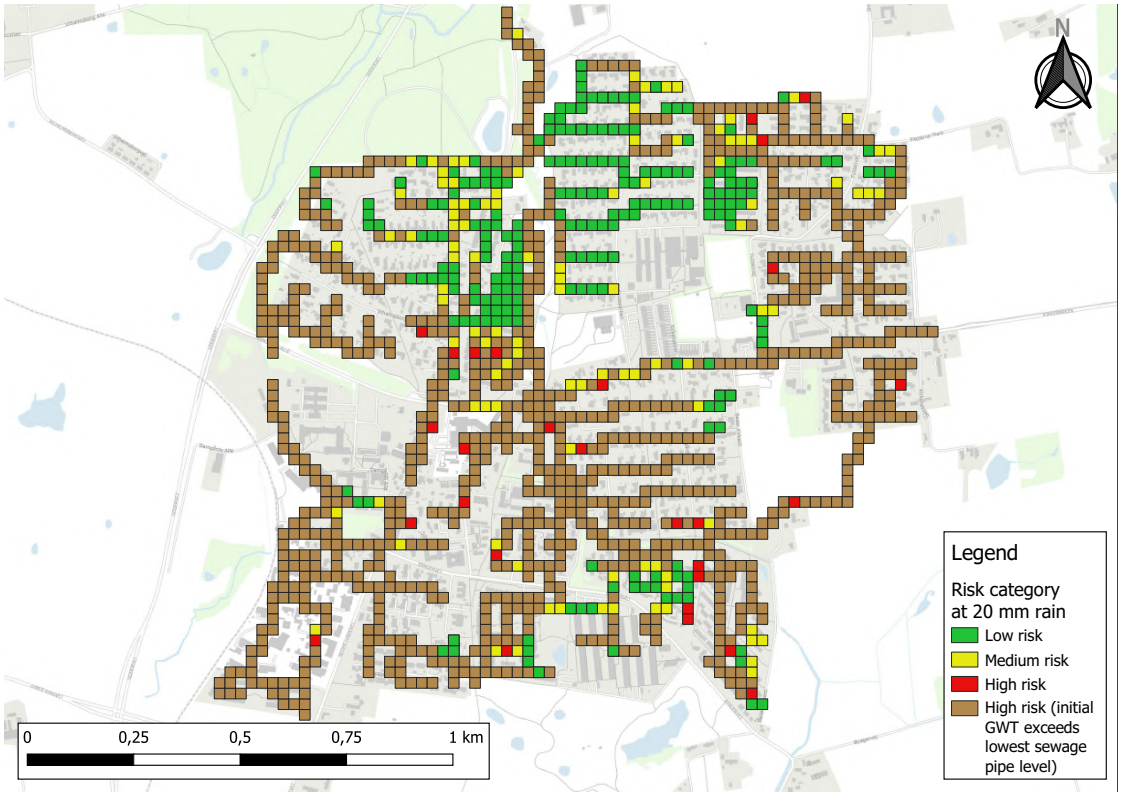

Figure 15.3: Result of the risk assessment of the sewer system in Beder in a 25x25 m grid at 20 mm rain.

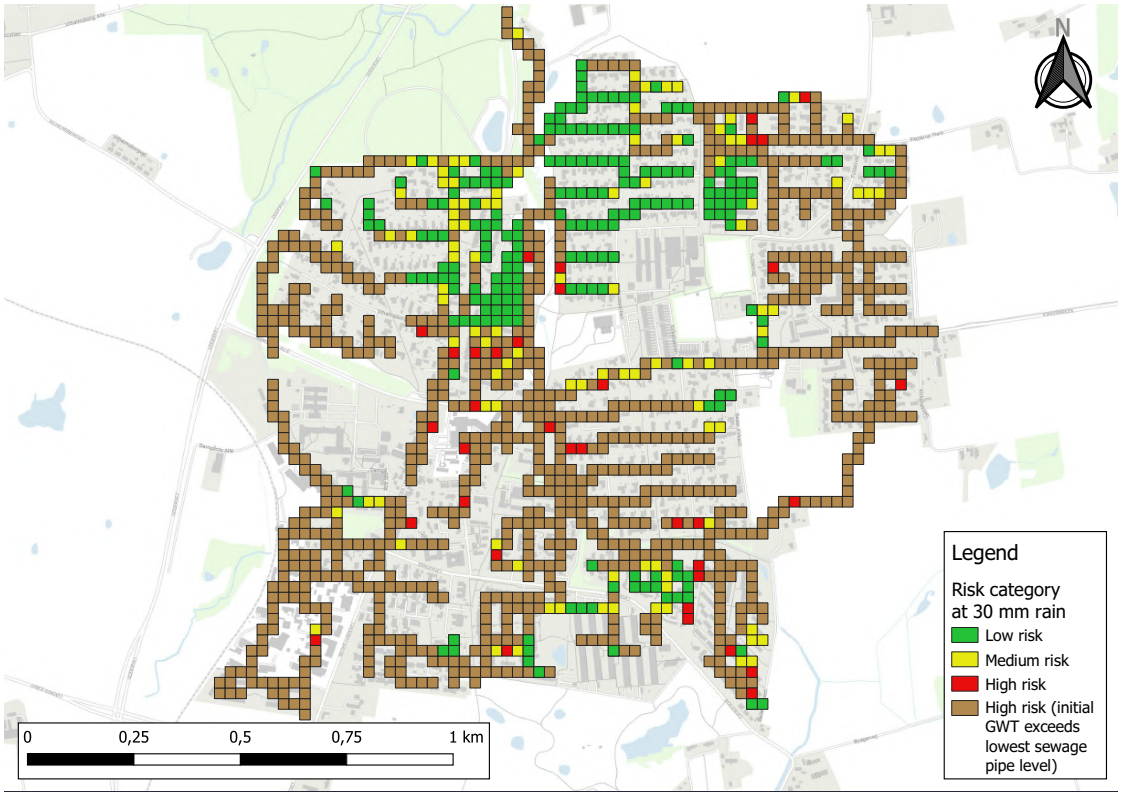

Figure 15.4: Result of the risk assessment of the sewer system in Beder in a 25x25 m grid at 30 mm rain.

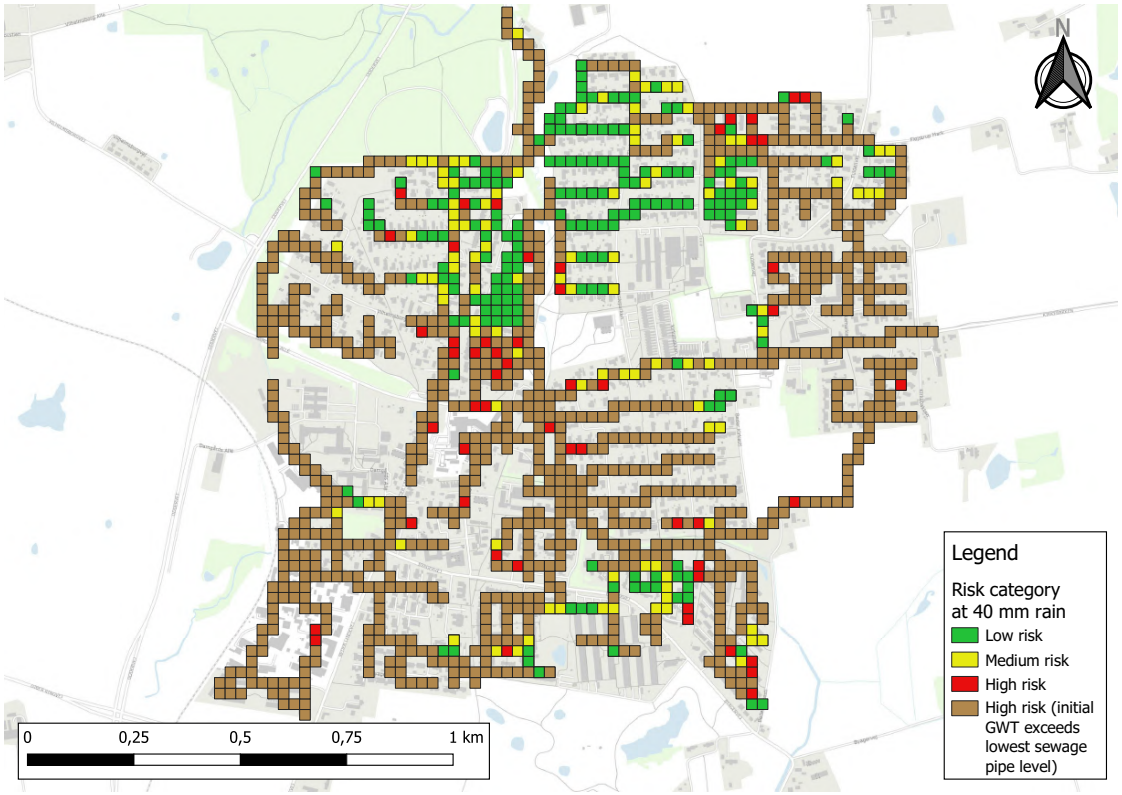

Figure 15.5: Result of the risk assessment of the sewer system in Beder in a 25x25 m grid at 40 mm rain.

15.3 Using the screening tool on a smaller grid

Figures 15.2 through 15.5 give insight into which areas of Beder has a risk of groundwater infiltration. However, further understanding of the classification of the risks necessitates a finer grid. Figure 15.6 show the screening tool with a 10x10 m grid applied to an area in the central part of Beder. This was done to evaluate whether a finer grid resolution would yield another risk category across the grid. The chosen area was not the most critical area but was selected because it contains many cells that change when rain is applied in the screening tool.

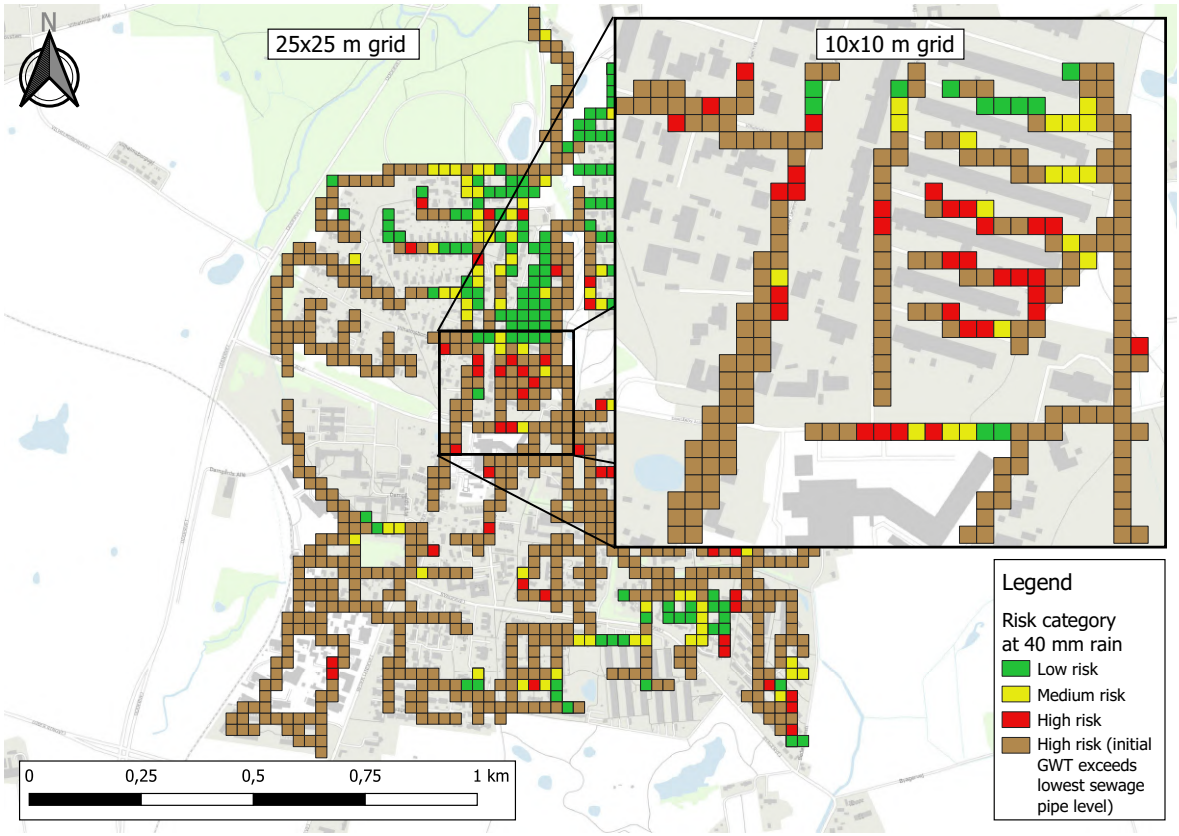

Figure 15.6: Result of the risk assessment made using the screening tool for Beder at 40 mm rain with a 25x25 m grid compared to a 10x10m grid.

The highlighted area with a 10x10m grid is mostly classified as high risk when a rain depth of 40 mm is applied. In general the 10x10m grid fits well with the 25x25m grid. Here, the finer resolution of the grid allows for a more detailed risk assessment in relation to the specific location of the pipes as these are more clearly shown in the 10x10 m grid than in the 25x25 m grid. However, the 10x10m cells do not necessarily constitute their equivalent 25X25m cell, here e.g a green 25x25m cell becomes a mixture of brown, red and yellow 10x10m grid cells.

The results of the risk assessments presented in this chapter are discussed in the following chapter along with the screening tool inputs and assumptions.

16 | Discussion of the development and results of the screening tool

In this chapter the results from the screening tool presented in chapter 15 are discussed. Here, the focus will be on answering the fourth question: *"How can the risk of groundwater infiltration into the sewer system in Beder be assessed by integrating the 1D model into a screening tool?"*.

16.1 Evaluation of the chosen case area and screening tool result

The screening tool was developed in order to aid decision-makers in evaluating areas which have a high risk of groundwater infiltration due to a rain induced increase in the groundwater table. Here, the screening tool quantifies the risk of groundwater infiltration based on whether the pipes of the sewer system become submerged. Therefore, it does not quantify whether infiltration occurs as this would require knowledge of the condition of the pipes.

As Beder was the area focused on by Ternært Vand project group [2024], this area was used for developing the screening tool. However, as obvious from the risk classification before adding water, more than half of the grid cells already showed the lowest pipe level being submerged. Therefore, Beder was not the ideal area for a risk assessment at various rain depth scenarios, due to a large part of the area not being included in the calculations. Therefore, if the purpose of using the screening tool in Beder was to decide which areas to prioritize when renovating the sewer system, the scenario without added rain would likely be the only relevant scenario as decision-makers would probably prioritize areas which are always submerged and not just submerged due to a rain event. This assessment could be made without adding the 1D model engine into the screening tool. Still, the screening tool succeeded in mapping the areas where a high risk of groundwater infiltration occurs in Beder.

The results from the screening tool showed that the changes in risk category compared to a 0 mm scenario predominantly occurred within the grid cells classified as sandy clay loam. This dynamics was also reflected in the results from the evaluation of the simplified soil types which showed a difference in response based on the particle size distribution of the soil type, where the soils with larger clay fractions showed a higher increase in groundwater table compared to the more sandy soils. Here, the clay showed the largest increase, which is also reflected in the rain scenarios of the screening tool. This is despite only calculating 4 grid cells with clay due to the rest of the cells already exceeding the lowest pipe of the sewer system.

The increase mostly occurring in the grid cells with sandy clay loam is both explained by the smaller storage capacity in the sandy clay loam than the sand resulting in a larger groundwater increase, but also by the initial groundwater table lying closer to the surface in the grid cells with sandy clay loam than the grid cells with sand. Here, a smaller initial distance to the surface will result in a larger increase in the groundwater table due to the available storage in the capillary fringe decreasing as the groundwater table nears the surface. This also highlights

the importance of the uncertainty related to the assumption of using the surface geology for the entire depth of the modelled column as well as the groundwater data used from the HIP model.

16.2 Uncertainty of the input data and its effect on the model result

The screening tool results are highly reflected by the quality of the input data, which plays a crucial role in determining the performance of the screening tool. For instance, the HIP data used for the groundwater had an uncertainty of +2 m for surface near groundwater. This is a considerable uncertainty when compared to the increases modelled with the screening tool and the resulting risk categories. Here, an uncertainty of 2 m has a significant impact on the result, as the modelled increase in groundwater is highly dependant on the initial distance to the surface. Moreover, the HIP model was also only based on a few calibration and validation data points in and around Beder, which further raises the question of whether the used groundwater table was representative of the groundwater level in Beder [Dataforsyningen 2024b].

Another uncertainty of the screening tool was the soil type in the entire soil column being sampled by the surface soil. From the established monitoring borings by Ternært Vand project group [2024] it was evident that the soil types in the bore profiles varied with the depth. This simplification of the soil layers could result in the model both under and overestimating the groundwater increase depending on the soil heterogeneity. For instance, if there was a sand layer overlying a clay layer, the entire column would be modelled as sand. However, due to the smaller storage capacity of clay, the result would be expected to yield a higher increase in groundwater table if the underlying clay layer was included. This would be possible in the screening tool, however it would require detailed bore profiles to achieve sufficient knowledge of the varying geology in an area. This would make the use of the screening tool labor intensive and expensive to use.

16.3 Assessment of screening tool simplifications and assumptions

Besides the uncertainty from the input data, the calculations of the screening tool were also simplified in several ways which affects the results of the risk assessment. For instance the simplification of the data into a 25x25 m grid. Here, the method used to sample the input data for a grid cell varied between data types as the surface level and groundwater table were average values, while the pipe level was based on the lowest point of the sewer system. This could possibly create conflicting situations, for instance if a grid cell covers a slope where the sewer system is located in the highest part of the terrain. Here, using the average surface level with the lowest point of the sewer system can result in the pipe being modelled closer to the surface than it is and even in some cases the pipe might be above ground according to the model. This is evidently not realistic and can result in the pipe being classified as a lower risk category than it should be. Conversely, if the pipe is located in the lowest part of a grid cell covering a slope the average groundwater table might be located at the level of the pipe or above which would result in the cell being wrongly classified as a high risk area. If this scenario occurred in a grid cell with sand the actual risk category of the cell could possibly remain at low risk or medium risk even after large rain depths were applied.

The uncertainties occurring due to the sampling of data can possibly be amplified along the boundaries between the different geologies. For instance, the HIP groundwater level varies with several meters within a 25 m distance in Beder along the boundary between sand and sandy clay loam. Additionally, due to the grid cell geology being assigned based on the dominant surface geology, the placement of the grid cell can greatly affect the result. Here, the result would be affected if another placement of the grid would change the geology in a grid cell from sandy clay loam to sand. This can be mitigated by decreasing the grid discretization as the modelled grid could be both smaller or greater than 25x25 m. This would instead demand a finer resolution of the rest of the input data. However, as shown with the 10x10 m grid the risk classification also change when increasing the resolution of the grid. Therefore, the screening tool should be run with the finest possible resolution if the results were to be used to identify areas with high risk of groundwater infiltration on a small scale.

Another simplification of the screening tool is the lack of removal of water and therefore all added rain is assumed to contribute to either an increase in the groundwater table or in the water content of the capillary fringe. This both includes the assumption of a drainage coefficient of 0 meaning a lack of removal by pipes but also no dispersion of the water due to horizontal gradients. This might explain why the 53 cm increase observed in Beder at 40 mm rain was best replicated with a 30 mm rain in the 1D model of the screening tool. Here, the analysis of the ability of the simplified soils to replicate the observation from boring B6 in Beder suggested that the soils do not accurately predict the dynamics. However, it might also be explained by the 40 mm rain not being measured directly above the monitoring boring, why the amount of precipitation, evapotranspiration and resulting infiltration into the boring are all unknown. This also means that whether the screening tool accurately predicts the groundwater increases in Beder was not validated. Here, a validation could be conducted with comparisons of more monitoring borings, which would yield a more certain conclusion. Ideally, several of the rapid responses across the monitoring borings could be attempted replicated with the 1D model of the screening tool. Here, the drainage of water could be implemented into the 1D model of the screening tool again. However, since the exact soil properties of the geology in Beder are unknown, the specific drainage which should be applied would require a comprehensive analysis. This is also why only one initial comparison was made with the simplified soils and the measurements from Beder.

The ability of the simplified soils to accurately predict the dynamics from Beder was inconclusive due to incomplete knowledge of the conditions in Beder. Still, the screening tool was clearly able to predict the differences expected from the different soil types and from the varying initial distances from the groundwater to the surface. This was evident from the analysis of the behavior of the simplified soils when adding 30 mm rain, but also from the results of the screening tool. Moreover, the engine of the screening tool was based on the same 1D model as used for modelling the sandbox experiments, where the 1D model also was able to replicate the increases in groundwater table. Still, the applicability of the screening tool could be further expanded, but overall the goal of developing a screening tool for risk assessment of groundwater infiltration was deemed successfully achieved.

16.4 Potential application of the screening tool by decision-makers

The screening tool was a proof of concept for assessing areas with high risk of groundwater infiltration. As the screening tool did not include the conditions of the pipes, it cannot quantify the actual risk of groundwater infiltration. Therefore, the screening tool is not a standalone program but rather the initial investigation of an area.

The results from the screening tool could for instance be applied when renovating a sewer system where decision-makers could use the result of the screening to identify which parts of the sewer system are most exposed to rising groundwater. Here, the division of Beder into 25x25 m and 10x10 grids showed a difference in applicability of the screening tool. The 25x25 m grid showed a general overview of which parts of Beder were high and low risk. Due to a large part of the area being classified as high risk the decision-maker would still have to prioritize which area contributes to the greatest amount of extraneous water, which the screening tool does not quantify. Therefore, the results of the screening could be supplemented with more data from the case area to identify areas which might contribute the most to the infiltration. The supplemental data could for instance be measurements of flow in the pumps and pipes, video footage of the conditions of the pipe or the direction of groundwater flow. Here, high risk areas with a large groundwater inflow should be prioritized. These areas could then be further analyzed with a finer resolution as demonstrated with the 10x10 m grid. Here, the finer grid helps identify specific stretches of the sewer system which are high risk. This combination of data would further improve the assessment of risk of groundwater infiltration.

The screening tool could also be used for mitigation of extraneous water. One of the issues with extraneous water is the additional water at the wastewater treatment plant which was not included when designing the plant. Therefore, during the design of a new sewer system the screening tool could be applied to assess how often the pipes would become submerged. The placement of the pipe could then be reevaluated based on the result or mitigation methods such as drain or granular capillary breaks could be installed along with it. Moreover, if inputting a climate projected rain, knowledge might be gained of the future return periods of submersion of the sewer system.

For further improvement of the screening tool, it could be relevant to use a case area with surface near groundwater which only periodically experiences submersion of the sewer system. Here, the screening tool could be used to assess which rain events are the most critical for submersion of the pipes.

Hypothetically if the results from Beder are trusted they could be used to determine where actions should be taken in order to reduce the amount of extraneous water originating from Beder. From the result it can be seen that the central and southwestern part of Beder are the most critical. Here, either the whole system could be renovated or further measurements of the sewer system could be conducted to analyse which specific part is the most critical. This would result in the screening tool being used to either directly identify which areas need improvement or which areas to do further measurements in.

16.5 Summation of the development of the screening tool

This part of the Master's thesis set out to answer the fourth question; *"How can the risk of groundwater infiltration into the sewer system in Beder be assessed by integrating the 1D model into a screening tool?"*

The development of the screening tool showed large parts of Beder being classified as having a high risk of groundwater infiltration. Here, the results of the screening tool showed that the areas with a water retaining surface geology combined with groundwater that was close to the surface had the highest risk of groundwater infiltration. Therefore, the classification of the tool is also highly dependant on representative data of especially the geology and initial distance from groundwater to surface. Though the screening tool was not validated for Beder due to a lack of knowledge of the soil, the screening tool did reproduce the expected dynamics from the inputted soil types. Therefore, the screening tool was deemed capable of modelling the variations in the risk of groundwater infiltration due to different conditions. Thus, the tool could be used by decision-makers e.g. to identify areas of the sewer system which contribute to extraneous water or for mitigation of groundwater infiltration when planning a new sewer system.

Part V :

Conclusion of the Master's thesis and future work

17 | Conclusion

This Master's thesis set out to improve knowledge of the underlying dynamics behind disproportionate groundwater rise causing groundwater infiltration into leaky sewer systems as observed in the city of Beder, Denmark. This was done by answering the problem statement; "*How can capillary fringe induced disproportional groundwater rise and subsequent infiltration be replicated experimentally and numerically, and how can the numerical model be utilized to evaluate the risk of infiltration into a sewer system?*" Here, the work was based on the second hypothesis by Ternært Vand project group [2024] which states that water only infiltrates due to a groundwater rise from below the pipe.

Through literature studies this Master's thesis deduced that the disproportionate increases of the groundwater table as observed in Beder occurs in shallow groundwater tables where the capillary fringe is either truncated or close to the surface. Here, the limited available storage of the capillary fringe causes rapid increases in groundwater table even at low amounts of rain. This dynamics was replicated through 5 sandbox experiments. Here, one of the experiments showed a clear disproportionate rise. The remaining four experiments were also considered to have shown disproportionate increases, however the experimental setup rendered it difficult to quantify. Due to water infiltrating into the drain pipe before the groundwater table reached the pipe in the water level meters in three out of five experiments the hypothesis of water infiltrating from below was not confirmed. Here, the infiltration was assumed to be caused by the formation of a secondary groundwater table around the pipe.

From the sandbox experiments it was further determined that inclusion of the capillary fringe is important when modelling groundwater due to its significance in determining groundwater levels. Thus, the sandbox experiments were successfully replicated with both a 1D and 2D numerical model of groundwater rise and unsaturated flow which were based on the Mean Moving Slope model. Here, the 1D model was able to replicate the total increase in groundwater table based on a specific amount of rain, where the 2D model was further able to quantify the amount of water drained through the leaky pipe.

The 1D model was implemented into a screening tool for risk assessment of rain induced groundwater infiltration into the sewer system in Beder. The risk assessment showed a strong dependance on the input data being representative of the geology and initial distance from the groundwater table to the surface. Despite the screening tool not being validated against data from Beder, it was concluded to be capable of replicating the differences in dynamics expected from the different soil types used in the screening.

18 | Ideas for future work

In this chapter several ideas and improvements that emerged during the course of this Master's thesis will be presented. Due to time constraints or the scope of the thesis these concepts were not fully explored. Nevertheless, they hold significant potential and are therefore outlined here in order to inspire possible future work.

18.1 Improvements to the sandbox experiments

It proved difficult to conclude whether the hypothesis treated by Hedevang and Sørensen [2023] of water infiltrating from below could be confirmed, since the sandbox experiment showed signs of deterioration. Ideally, the sandbox would have been repacked and three experiments would have been conducted with same methodology as for experiment C2. Then it would be expected that the experiments would not show infiltration before the groundwater table reached the pipe.

To improve the estimation of the disproportional increase an experiment with closed lower boundaries and rain over the entire area of the sandbox could be conducted. Here, all of the added water would contribute to the groundwater rise which would be more uniform. However, this setup would still contain the drain pipe and the more ideal approach would be a column experiment if only a disproportionate increase should be quantified and not the infiltration volume. Here, it could be interesting to measure the disproportionate groundwater rise for different initial distances to the groundwater table and for different soils.

18.2 Further applications of the 1D and 2D numerical models

Both the 1D and 2D version of the MMS-model can run vertically inhomogeneous simulations. However, this feature has not been used in this Master's thesis. Since pipes are usually embedded in some type of roadway structure, a homogeneous model will likely wrongly estimate the groundwater rise near the pipe. Therefore, an interesting application of the MMS-model would be to model the effect of a granular capillary break. In addition, it could be interesting to apply a real rain event to the 1D model since the model so far has only used box rains. With the inclusion of drainage the model could then be used to see the effects of coupled rain events.

18.3 Improvements to the screening tool and further development

The screening tool is highly dependant on its input data being representative. For instance the screening tool showed that half of the sewer system in Beder was submerged when employing the HIP groundwater data. This result is uncertain for a decision-maker to base decisions upon due to the uncertainty of the representativeness of the groundwater level. However, if the screening tool was applied using a more local validated groundwater model, thereby reducing

the uncertainty of the input data, the result of the screening tool could become more relevant. Likewise, the screening tool uses the surface geology map in combination with soil mean values of soil measured by Clapp and Hornberger [1978]. These soils are just estimations, hence measurements of the soil properties found in Beder would likely give a better estimation as it did in the sandbox experiment. This would also validate whether the simplified soils were representative of the expected dynamics.

Lastly the screening tool could be improved by adding two modules. The first could take into account that only part of the water from a rain event infiltrates to the groundwater. Here, the screening tool could utilize the calculation of water flow to the sewer system from the program MIKE URBAN. The remainder of the water that does not flow to the sewer system must infiltrate to the groundwater table (excluding evapotranspiration). Secondly, the screening tool could be coupled with data from tv-inspections or other extraneous water analyses such as the DRAINMAN project. This would allow the screening tool to further assess the risk based on both submersion of the sewer system due to a groundwater increase and whether the conditions of the pipe allows infiltration.

Bibliography

Aarhus Kommune (2024). *BorgerGIS*. Accessed: 04-04-2024. https://webkort.aarhuskommune.dk/spatialmap?favoritename=spildevandsplan_vedtaget.

— (2022). *Spildevandsplan 2021-2026*. Teknik og Miljø Aarhus Kommune.

Aarhus Vand (2023). *"Den forsvundne bro" forebygger oversvømmelser i Viby*. Accessed: 15-12-2023. https://www.aarhusvand.dk/nyheder/den-forsvundne-bro-forebygger-oversvoemmelser-i-viby/.

Andersen, L. T., K. L. Anthonsen, and P. R. Jakobsen (2023). *Danmarks Digitale Jordartskort 1:25.000 Version 7.0*. Accessed: 21-05-2024. https://data.geus.dk/pure-pdf/GEUS-R_2023-29_web.pdf.

Andersen, S. H. and D. Getreuer (2018). *Bedre viden om uvedkommende vand*. Grundvand og drikkevand nr. 2. Miljøstyrelsen. ISBN: 978-87-93710-21-4.

Awad, A., E. Holm, N. S. Aarøe, T. B. Sørensen, N. V. Bjerregaard, and K. Bjørno (2018). *Vand i tal*. DANVA.

Bassø, L., M. Rasmussen, S. Lindberg, D. K. Bak, O. H. Pjengaard, R. Pourmoayed, C. Schou, P. D. Simonsen, L. L. Kraglund, and S. B. Ploug (2021). *DRAINMAN - Uvedkommende vand og det intelligente spildevandssystem*. MUDP rapport. Miljøstyrelsen. ISBN: 978-87-7038-341-7.

Brorsen, M. and T. Larsen (2009). *Lærebog i hydraulik*. Aalborg Universitetsforlag. ISBN: 978-87-7307-978-2.

Campbell, G. (1974). "A Simple Method for Determining Unsaturated Conductivity From Moisture Retention Data". In: *Soil Science* 117(6), pp. 311–314.

Clapp, R. B. and G. M. Hornberger (1978). "Empirical Equations for Some Soil Hydraulic Properties". In: *Water Resources Research* 14(4), pp. 601–604.

Dakša, G., S. Dejus, and J. Rubulis (2022). "Assessment of Infiltration from Private Sewer Laterals: Case Study in Jurmala, Latvia". In: *Water* 14(18), 2870, pp. 1–12.

Dataforsyningen (2024a). *Dataforsyningen*. Accessed: 20-05-2024. https://dataforsyningen.dk.

— (2024b). *Hydrologisk informations- og prognosesystem*. Accessed: 13-05-2024. https://hip.dataforsyningen.dk.

De Bénédettis, J. and J. L. Bertrand-Krajewski (2005). "Infiltration in sewer systems: comparison of measurement methods". In: *Water Science and Technology* 52(3), pp. 219–227.

EHC-AAU (2023). *Experimental Hydrology Course*. Course provided by: Dept. of the Built Environment, Aalborg University. Data collected by groups attending the course in fall 2022 and 2023.

ESSG-AAU (2022). *Environmental Soil Science and Geostatistics*. Course provided by: Dept. of the Built Environment, Aalborg University.

GEUS (2024). *National boringsdatabase (Jupiter)*. Accessed: 20-05-2024. `https://www.geus.dk/produkter-ydelser-og-faciliteter/data-og-kort/national-boringsdatabase-jupiter/`.

Gillham, R. W. (1984). "The Capillary Fringe and its Effects on Water-Table Response". In: *Journal of Hydrology* 67(1), pp. 307–324.

Guo, S., Y. Yang, and Y. Zhang (2017). "An approximate model on three-dimensional groundwater infiltration in sewer systems". In: *Water Science and Technology* 75(2), pp. 306–312.

Guymon, G.L. (1994). *Unsaturated Zone Hydrology*. Prentice Hall. ISBN: 9780133690835.

Hansen, L. (1976). "Soil Types at the Danish State Experimental Stations". In: *Tidsskrift for planteavl*, pp. 742–758.

Hedevang, B. T. and F. B. Sørensen (2023). *Infiltration of unwanted water into sewage systems - Numerical and experimental quantification*. Master's thesis, Dept. of the Built Environment, Aalborg University.

Heliotis, F. D. and B. Dewitt (1987). "Rapid Water Table Responses to Rainfall in a Northern Peatland Ecosystem". In: *Water Resources Bulletin* 23(6), pp. 1011–1016.

Henriksen, H. J., S. J. Kragh, J. Gotfredsen, M. Ondracek, M. van Till, A. Jakobsen, R. J. M. Schneider, J. Koch, L. Troldborg, P. Rasmussen, E. Pasten-Zapata, and S. Stisen (2020). *Sammenfatningsrapport vedr. modelleverancer til Hydrologisk Informations- og Prognosesystem*. GEUS.

Jury, W. A. and R. Horton (2004). *Soil Physics*. 6th ed. John Wiley & Sons. ISBN: 9780471059653.

Karpf, C. and P. Krebs (2013). "Modelling of groundwater infiltration into sewer systems". In: *Urban Water Journal* 10(4), pp. 221–229.

— (2004). *Sewers as drainage systems – quantification of groundwater infiltration*. 5th int. conference NOVATECH, Lyon.

Khaled, I. M., M. Tsuyoshi, N. Kohei, N. Taku, and I. Hiromi (2011). "Experimental and Modeling Investigation of Shallow Water Table Fluctuations in Relation to Reverse Wieringermeer Effect". In: *Journal of Soil Science,* 1, pp. 17–24.

Koch, J., H. Berger, H. J. Henriksen, and T. O. Sonnenborg (2019). "Modelling of the shallow water table at high spatial resolution using random forests". In: *Hydrology and Earth System Sciences* 23(11), pp. 4603–4619.

Lehmann, P., F. Stauffer, C. Hinz, O. Dury, and H. Flühler (1998). "Effect of hysteresis on water flow in a sand column with a fluctuating capillary fringe". In: *Journal of Contaminant Hydrology,* 33(1), pp. 81–100.

Lissard, Ben J. (2017). *Field Observations of Soil-Water Tension throughout a Capillary Fringe in New Iberia, Louisiana*. University of Louisiana at Lafayette.

Loll, P. and P. Moldrup (2000). *Soil Characterization and Polluted Soil Assessment*. https://www.moodle.aau.dk/course/view.php?id=44113.

Magdoff, F. and H. van Es (2021). *Building Soils for Better Crops - Ecological Management for Healthy Soils*. 4th ed. Sustainable Agriculture Network handbook series. The Sustainable Agriculture Research and Education (SARE) program. ISBN: 9781888626193.

Mangangka, I. R. (2008). "The Decline of Soil Infiltration Capacity Due to High Elevation Groundwater". In: *Civil Engineering Dimension* 10(1), pp. 35–39. ISSN: 1410-9530.

Maxim Integrated (2018). *DS18B20 Datablad*. Accessed: 08-01-2024. https://minielektro.dk/amfile/file/download/file/4/product/172/.

Miljøstyrelsen (1992). *Uvedkommende vand i afløbssystemer*. Spildevandsforskning fra Miljøstyrelsen nr. 48. Miljøstyrelsen. ISBN: 87-7810-060-7.

— (2004). *Videreudvikling af ådalstypologi - Grundvand - Overfladevand Interaktion (GOI)*. Arbejdsrapport fra Miljøstyrelsen nr. 16. Accessed: 21-05-2024. https://www2.mst.dk/udgiv/publikationer/2004/87-7614-492-5/html/helepubl.htm.

Minasny, B. and F. Cook (2011). *Sorptivity of Soils*. Encyclopedia of Agrophysics. Springer. ISBN: 978-90-481-3585-1.

Miyazaki, T., M. K. Ibrahimi, and T. Nishimura (2012). "Shallow Groundwater Dynamics Controlled by Lisse and Reverse Wieringermeer Effects". In: *Journal of Sustainable Watershed Science & Management* 1(2), pp. 36–45.

Moldrup, P., D. E. Rolsten, and J. AA. Hansen (1989). "Rapid and Numerically Stable Simulation of One-Dimensional, Transient Water Flow in Unsaturated, Layered Soils". In: *Soil Science* 148(3). ISSN: 0038-075X.

Morris, D. A. and A. I. Johnson (1967). "Summary of Hydrologic and Physical Properties of Rock and Soil Materials, as Analyzed by the Hydrologic Laboratory of the U.S. Geological Survey 1948-60". In: *Water-Supply Paper* 1839(D), pp. D1–D42.

Nimmo, J. R. (2005). "Unsaturated Zone Flow Processes". In: *Encyclopedia of Hydrological Sciences* 13, pp. 2299–2322.

Nosetto, M. D., E. G. Jobbágy, R. B. Jackson, and G. A. Sznaider (2009). "Reciprocal influence of crops and shallow ground water in sandy landscapes of the Inland Pampas". In: *Field Crops Research* 113(2), pp. 138–148.

Novakowski, K. S. and R. W. Gillham (1988). "Field investigations of the nature of water-table response to precipitation in shallow water-table environments". In: *Journal of Hydrology* 97(1), pp. 23–32.

Olesen, M., K. S. Madsen, C. A. Ludwigsen, F. B., T. C., J. Cappelen, O. B. Christensen, K. K. Andersen, and J. H. Andersen (2014). *Fremtidige klimaforandringer i Danmark*. Danmarks Klimacenter rapport nr. 6. Danmarks Meteorologiske Institut. ISBN: 978-87-7478-652-8.

Onset (2018). *HOBO U20 Water Level Logger (U20-001-0x and U20-001-0x-Ti) Manual*. https://www.onsetcomp.com/sites/default/files/resources-documents/12315-J%20U20%20Manual.pdf.

Petkov, P. (2021). *Using the double-ring infiltrometer to evaluate key unsaturated and saturated hydrological properties*. Master's thesis, Dept. of the Built Environment, Aalborg University.

Phillips, J. D. (2021). *Landscape Evolution*. Elsevier. ISBN: 978-0-12-821725-2.

Pojmark, P. (2011). *Tracing water movement in the capillary fringe*. TVVR11/5005. Master's thesis, Dept. of Building and Environmental Technology, Lund University.

Random Nerd Tutorials (2024). *Guide for DS18B20 Temperature Sensor with Arduino*. Accessed: 08-01-2024. `https://randomnerdtutorials.com/guide-for-ds18b20-temperature-sensor-with-arduino/`.

Rasmussen, P., J. Kidmose, A. J. Kallesøe, P. B. E. Sandersen, R. Schneider, and T. O. Sonnenborg (2022). "Evaluation of adaptation measures to counteract rising groundwater levels in urban areas in response to climate change". In: *Hydrogeology Journal* 31, pp. 35–52.

Richter, J. (1980). "A simple numerical solution for the vertical flow equation of water through unsaturated soils". In: *Soil Science* 129(3). ISSN: 0038-075X.

Sørensen, I. (2019). *Ingeniørgeologi*. 1th. Praxis. ISBN: 978-87-571-2918-2.

Styrelsen for dataforsyning og infrastruktur (2023). *Vejledning om lov og bekendtgørelse om Ledningsejerregistret*. Accessed: 16-05-2024. `https://ler.dk/Files/Vejledning_til_LER-lov.pdf`.

Taylor, R. G., B. Scanlon, P. Döll, M. Rodell, R. van Beek, Y. Wada, L. Longuevergne, M. Leblanc, J. Famiglietti, M. Edmunds, L. Konikow, T. R. Green, J. Chen, M. Taniguchi, M. F. P. Bierkens, A. MacDonald, Y. Fan, R. M. Maxwell, Y. Yechieli, J. J. Gurdak, D. M. Allen, M. Shamsudduha, K. Hiscock, P. J. F. Yeh, I. Holman, and H. Treidel (2012). "Ground water and climate change". In: *Nature Climate Change* 3(1), pp. 322–329.

Ternært Vand project group (2024). *Ternært Vand projektet*. Accessed: 04-06-2024. `https://ternert.dk/index.html`.

Thorndahl, S., J. D. Balling, and U. B. B. Larsen (2016). "Analysis and integrated modelling of groundwater infiltration to sewer networks". In: *Hydrological Processes* 30(18), pp. 3228–3238.

Turluck, N. S. (2019). *An Exploration into the Controls and Extent of Capillary Rise in Fine-Grained Sand*. Master's thesis. 4731, Dept. Geological and Environmental Sciences, WMU.

Weeks, E. P. (2002). "The Lisse Effect Revisited". In: *Ground Water* 40(6), pp. 652–656.

Werner, A. D. and D. A. Lockington (2003). "Influence of hysteresis on tidal capillary fringe dynamics in a well-sorted sand". In: *Advances in Water Resources* 26(11), pp. 1199–1204.

Wittenberg, H. and H. Aksoy (2010). "Groundwater intrusion into leaky sewer systems". In: *Water Science and Technology* 62(1), pp. 92–98.

Zheng, Y., H. liu, and M. Yang (2022). "The Effects of Truncating the Capillary Fringe on Water-Table Dynamics During Periodic Forcing". In: *Water Resources Research* 58(1), pp. 1–12.

Part VI :

Appendix

Appendix A | Sandbox dimensions

Figure A.1 shows the dimensions of the sandbox experiment setup from the front and above, accordingly. Every measurement at the water level meters was done according to the datum. The datum was chosen to be 49 mm above the bottom of the sandbox since it was the most accessible point to measure at. Figure A.2 shows the dimensions of one of the rain trays. The measurements shown were used throughout the project.

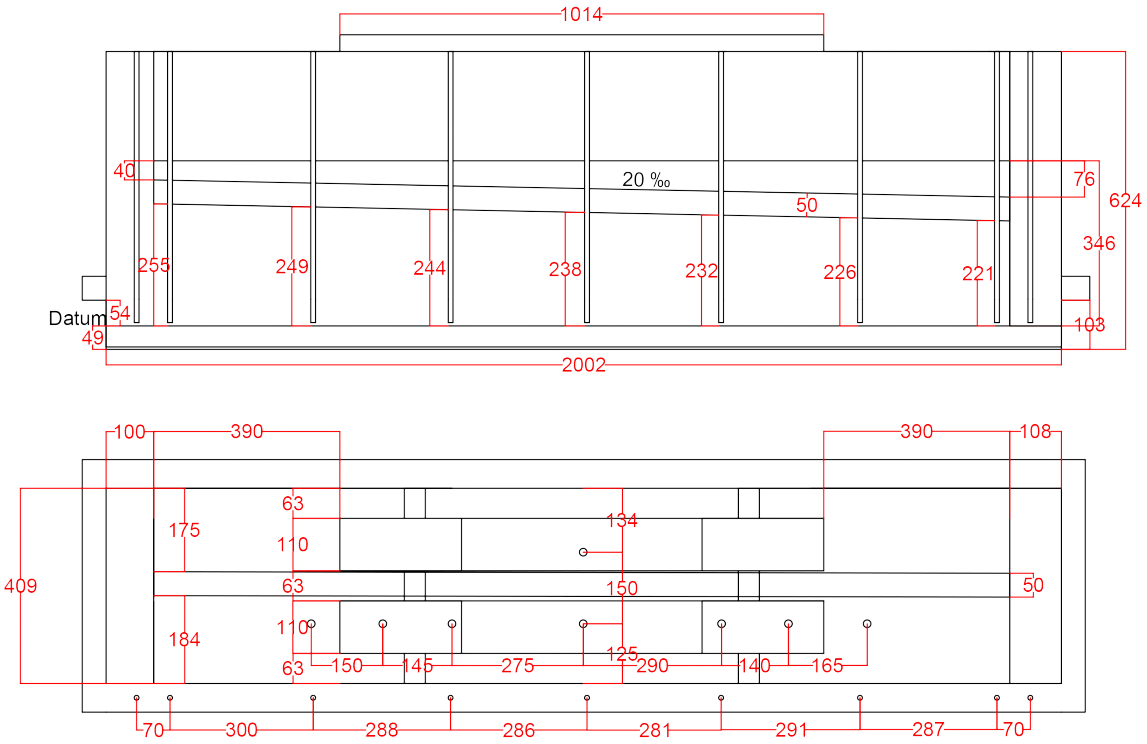

Figure A.1: Dimensions of the sandbox seen from the front (topmost figure) and seen from above (lowermost figure). Notice that the pipe is drawn with its ideal position and not the position found after excavation. Measurements in mm.

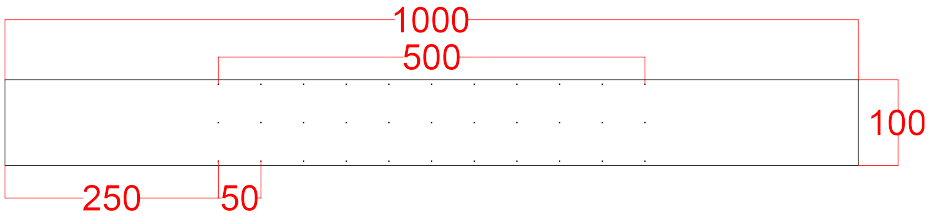

Figure A.2: Internal dimensions of the rain trays. The tray contains 33 holes with a diameter of 1 mm. The holes are placed 5 mm from the tray edge. Measurements in mm.

Appendix B

Estimation of equivalent membrane conductivities used in the numerical models based on experimental data

Figure B.1, B.2, B.3 and B.4 shows the results of the calculations of the equivalent membrane conductivities. Looking at the results it is noticed that the equivalent conductivity through the membrane is not constant and depends on the flow, where a higher flow increases the conductivity. Looking at just figures B.2 and B.3 a linear tendency can be seen. This can also be seen in figure B.1 to a certain degree. The mean was used in the 2D model, however determining it based on the flow would have been more correct. This would have necessitated iterative calculations of flow and membrane conductivity in each time step and would have increased the calculation time. Therefore, the mean values were used to limit calculation times.

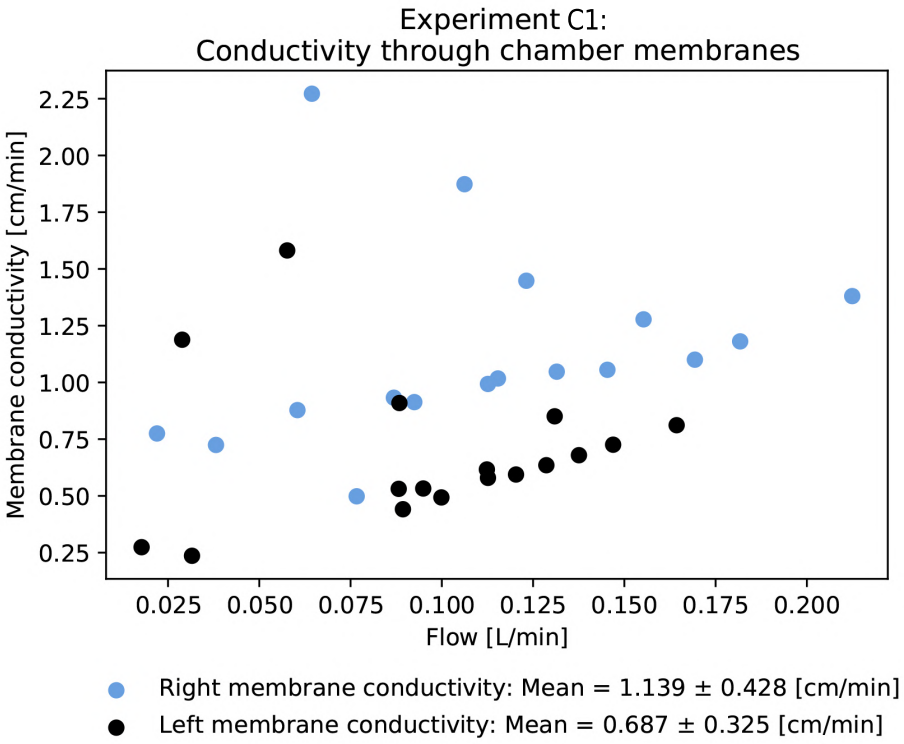

Figure B.1: Analysis of the membrane conductivity through the chambers in Cold experiment 1 (C1).

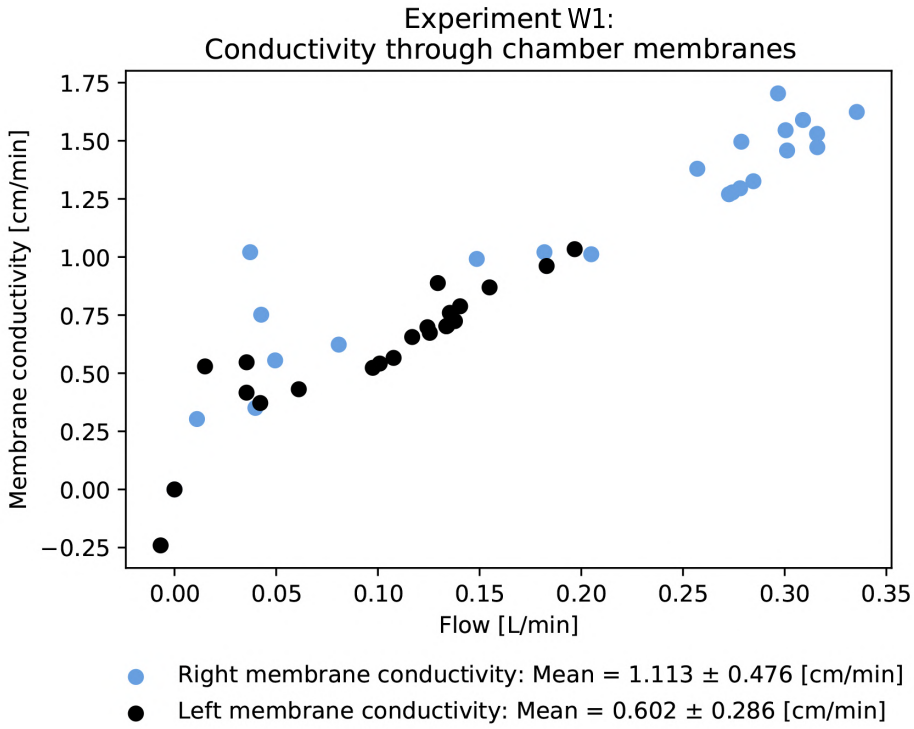

Figure B.2: Analysis of the membrane conductivity through the chambers in Warm experiment 1 (W1).

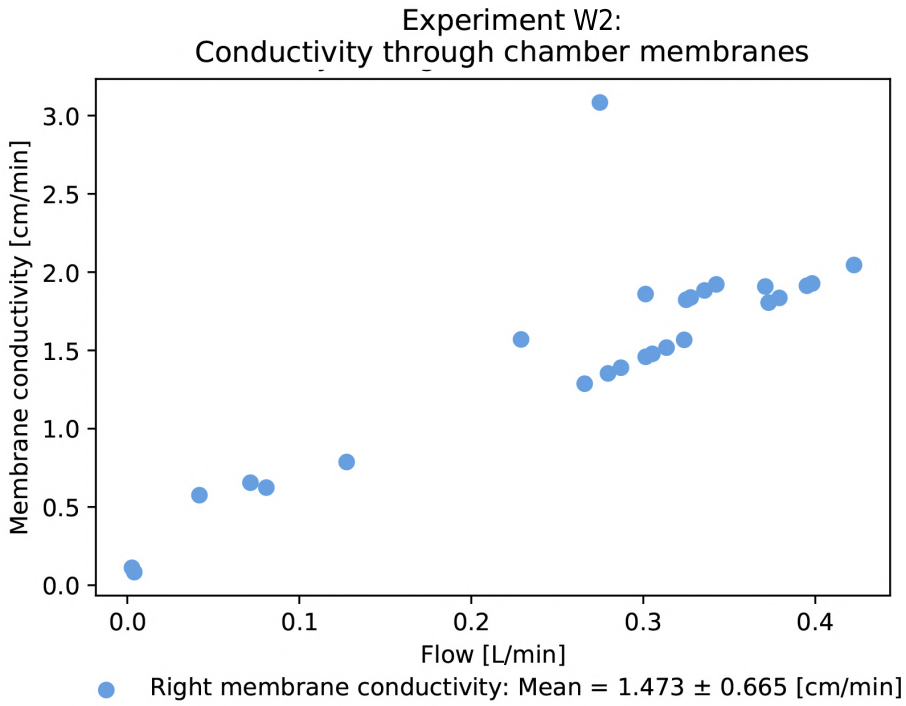

Figure B.3: Analysis of the membrane conductivity through the right chamber in Warm experiment 2 (W2). No data was available for the left side as the water level logger failed.

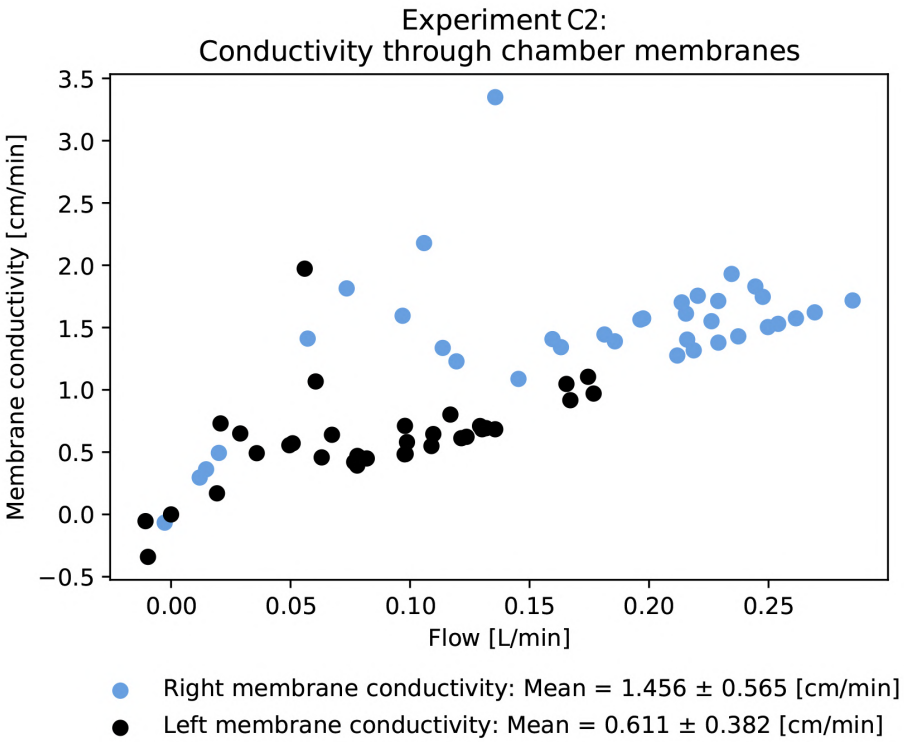

Figure B.4: Analysis of the membrane conductivity through the chambers in Cold experiment 2 (C2).

Appendix C

Derivation of the integrated version of the Darcy flow equation for horizontal flow

This appendix contains the derivation of equation 10.9 on page 95.

The Darcy flux for a transient situation and 1D horizontal flow through a unit cross-sectional area is given as:

$$v = -K\left(\frac{dH}{dx}\right) = -K\left(\frac{d\psi}{dx} - \frac{dz}{dx}\right) = -K\left(\frac{d\psi}{dx} - 0\right) = -K\left(\frac{d\psi}{dx}\right)$$

1. Derivation of $\frac{\mathrm{dK}}{\mathrm{dx}} + \alpha \cdot \mathrm{v} = 0$

Given:

$$v = -K\left(\frac{d\psi}{dx}\right) \tag{C.1}$$

$$K = K_s \cdot e^{\alpha \cdot \psi} \tag{C.2}$$

Equation (C.2) is differentiated with respect to x obtaining:

$$\frac{dK}{dx} = \frac{dK_s \cdot e^{\alpha \cdot \psi}}{dx} = \frac{dK_s \cdot e^{\alpha \cdot \psi}}{d\psi} \cdot \frac{d\psi}{dx} \tag{C.3}$$

Equations (C.1) and (C.3) are combined:

$$v = -K\left(\frac{1}{K \cdot \alpha} \cdot \frac{dK}{dx}\right) = \frac{-1}{\alpha} \cdot \frac{dK}{dx} \Leftrightarrow$$

$$\frac{dK}{dx} + \alpha \cdot v = 0 \tag{C.4}$$

Assumption used: ψ is a differentiable function of x

2. Derivation of $-\frac{\mathrm{K}}{\mathrm{v}} = \alpha \cdot \mathrm{x} + \mathrm{c}$

Given equation (C.4):

$$\frac{dK}{dx} + \alpha \cdot v = 0$$

$$I : \frac{dK}{dx} + \alpha \cdot v = 0 \Leftrightarrow$$

$$\frac{1}{\alpha \cdot v} \cdot dK = -dx$$

$$II : \frac{d}{dK} \cdot [\alpha \cdot (-K)] = -\alpha \Leftrightarrow$$

$$dK = -\frac{1}{\alpha} \cdot d[\alpha \cdot (-K)]$$

$$I + II : \frac{1}{\alpha \cdot v} \cdot \left(-\frac{1}{\alpha}\right) \cdot d[\alpha \cdot (-K)] = -dx \Leftrightarrow$$

$$\frac{1}{\alpha \cdot v} \cdot d[\alpha \cdot (-K)] = \alpha \cdot dx \Leftrightarrow$$

$$\frac{1}{\alpha \cdot v} \cdot \int d[\alpha \cdot (-K)] = \alpha \cdot \int dx \Leftrightarrow$$

$$\frac{1}{\alpha \cdot v} \cdot \alpha \cdot (-K) + c' = \alpha \cdot x + c'' \Leftrightarrow$$

$$-\frac{K}{v} = \alpha \cdot x + c \tag{C.5}$$

where c, c' and c" are constants

Assumption used: v is constant

Check of above calculation:

$$K = -v \cdot \alpha \cdot x - v \cdot c \Leftrightarrow$$

$$\frac{dK}{dx} = \frac{d}{dx} \cdot (-v \cdot \alpha \cdot x - v \cdot c) \Leftrightarrow$$

$$\frac{dK}{dx} = -v \cdot \alpha$$

Since the check yielded equation (C.4) the solution to the differential equation is accepted.

3. Derivation of equation: (10.9) $v_{i,n+1/2} \rightarrow \quad = -\frac{K_N e^{\alpha_N \psi_{i,n+1}} - K_N e^{\alpha_N \psi_{i,n}}}{\alpha_N \Delta x}$

Assumption used: The velocity of flow v is constant between consecutive horizontal nodepoints n and n+1 within a timestep

Given equation (C.5):

$$-\frac{K}{v} = \alpha \cdot x + c \Leftrightarrow$$

$$-c = \frac{K}{v} + \alpha \cdot x \tag{C.6}$$

Equation (C.6) is transformed using the conditions $K = K_n$ for $x = x_n$ and $K = K_{n+1}$ for $x = x_{n+1}$ obtaining:

$$I : -c = \frac{K_n}{v} + \alpha \cdot x_n \quad \text{for } x = x_n$$

$$II : -c = \frac{K_{n+1}}{v} + \alpha \cdot x_{n+1} \quad \text{for } x = x_{n+1}$$

Combining I and II yields:

$$-c = -c \Leftrightarrow$$

$$\frac{K_n}{v} + \alpha \cdot x_n = \frac{K_{n+1}}{v} + \alpha \cdot x_{n+1} \Leftrightarrow$$

$$K_n + v \cdot \alpha \cdot x_n = K_{n+1} + v \cdot \alpha \cdot x_{n+1} \Leftrightarrow$$

$$v \cdot \alpha \cdot x_n - v \cdot \alpha \cdot x_{n+1} = K_{n+1} - K_n \Leftrightarrow$$

$$v \cdot \alpha \cdot (x_n - x_{n+1}) = K_{n+1} - K_n \Leftrightarrow$$

$$v \cdot \alpha \cdot (-\Delta x) = K_{n+1} - K_n \Leftrightarrow$$

$$v = -\frac{K_{n+1} - K_n}{\alpha \cdot \Delta x} \tag{C.7}$$

The average values of K between the consecutive node point are calculated using the MMS-model fromMoldrup, Rolsten, and Hansen [1989]. If the terms from the MMS-model is inserted in equation (C.7) with the 2D notations in figure 10.1 on page 93 yields equation (C.8)

$$v_{i,n+1/2} \rightarrow \quad = -\frac{K_N e^{\alpha_N \psi_{i,n+1}} - K_N e^{\alpha_N \psi_{i,n}}}{\alpha_N \Delta z} \tag{C.8}$$

□